Formability of Magnesium AZ80

Muhammad Waseem Soomro

A thesis submitted to Auckland University of Technology in fulfilment of the requirements for the degree of Doctor of Philosophy (PhD)

2016

School of Engineering, Computer and Mathematical Sciences

Declaration

I hereby declare that this submission is my own work and that to the best of my knowledge and belief, it contains no material previously published or written by another person (except where explicit has been defined in the acknowledgements), nor material which to a substantial extent has been submitted for the award of any other degree or diploma of a university or other institution of higher learning.

Auckland 2016

Muhammad Waseem Soomro

Abstract

Economical and fuel-efficient vehicles are a current topic of interest worldwide, due to increasing fuel costs and environmental concerns. The most strident demand from various auto-sector stakeholders is to reduce emissions from vehicles and keep the environment clean. To solve this issue we need to reduce vehicle weight to lower fuel consumption. In this context, magnesium alloys can be considered as an alternative for sheet metal components, as they are 35 percent lighter than aluminium alloys and 78 percent lighter than steel.

The AZ magnesium alloy series is widely used by the modern light metal industry. In this research, AZ80 magnesium alloy was selected. AZ80 is an important structural wrought-magnesium alloy with a high aluminium content of about 8 wt. %. AZ80 is the main subject of this study because it offers higher strength and greater hardness than the more widely used AZ31.

In this research, magnesium AZ80 alloys with two different grain sizes were considered, that is fine grain AZ80 (grain size ≈ 10 µm) and coarse grain AZ80 (grain size ≈ 60 µm). These grain sizes were chosen for investigations of the effect of grain size at higher temperatures and to observe changes in mechanical and forming capabilities with respect to grain size.

To investigate the formability characteristics of magnesium alloys, various tensile tests and deep drawing tests were performed at different temperatures, test speeds and grain sizes to understand the nature of the material. Anisotropy of material, strain sensitivity index and flow stress were also determined by varying all of these parameters. Moreover, load-displacement diagrams, forming-limit diagrams and the effects of variations in various pre-and-post processing parameters were also examined.

A further part of this research was to examine microstructure changes through the use of microscopic images at high magnification by utilising optical and scanning electron microscopes. It was observed that the microstructure of magnesium alloys was extremely sensitive to processing parameters in tensile tests and deep-drawing tests.

The final part of the research was the verification of mathematical modelling and simulation of metal forming processes by using the commercial FEA software package Abaqus.

Contents

Abstract……………...i

List of figures……………………………………………………………………...........x

List of tables…………………………………………...……………………......xvii

List of symbols……………………………………...………………………..…xviii

Acknowledgement…………………………………………………………………......xxi

Chapter 1 1

Introduction..1

1.1 Definition of the problem..1

1.2 Selection of material 4

1.3 Testing equipment, calibration and standards...6

1.4 Forming issues at elevated temperatures..7

1.4.1 Experimental setup development 8

1.4.2 Examination of the basic forming parameters and results from literature...........8

1.4.3 Construction of forming limit curves (FLC)...9

1.5 Research limitations..11

1.6 Scope and aspirations..11

Chapter 2 15

Characteristics and Properties of Magnesium Alloys...15

2.1 Magnesium Alloys 15

2.2 Classification and designations..16

2.2.1 Cast magnesium alloys...18

2.2.2 Wrought magnesium alloys 22

2.3 Role and influences of alloying constituents 25

2.3.1 Aluminium 25

2.3.2 Zinc 26
2.3.3 Manganese 28
2.4 Deformation theories for HCP materials 29
2.4.1 Slip 29
2.4.2 Twinning 33
2.5Texture development in magnesium alloys 35
2.6 Superplasticity 37
2.7 Diffusion creep 40
2.8 Grain boundary sliding 42
2.9 Recrystallisation in magnesium alloys 45
2.10 Grain growth 45
2.11 Cavitation 46
2.12 Conclusion 47

Chapter 3 48

Formability of magnesium alloys 48

3.1 Introduction 48
3.2 Problems of elevated temperature processing 48
3.2.1 Sensitivity of elevated temperature forming towards strain rate 49
3.2.2 Grain size effects on SPF of magnesium alloys 50
3.2.3 Influence of temperature on SPF of Mg alloys 53
3.3 Formability of magnesium alloys 54
3.3.1 Experimental setup development 55
3.3.2 Examination of the basic forming parameters and results 56
    3.3.2.1 Influence of punch speed in forming of magnesium alloys 58
    3.3.2.2 Influence of the punch force in forming magnesium alloys 59
    3.3.2.3 Influence of the blank holder force in forming magnesium alloys 60
    3.3.2.4 Influence of the texture (anisotropy) in forming of magnesium alloys 60

3.3.2.5 Influence of temperature in forming magnesium alloys 61

3.3.2.6 Temperature distribution during forming of magnesium alloys 62

3.3.2.7 Thickness distribution during forming of magnesium alloys 63

3.3.2.7 Spring-back properties in forming of magnesium alloys 64

3.3.2.8 Tooling geometries influences in forming magnesium alloys 65

3.3.2.9 Other influences 66

3.4 Construction of forming limit curves (FLC) 66

3.5 Strain measurement 71

3.6 Constitutive analysis 71

3.6.1 Phenomenological models 72

3.6.2 Physical or material relying models 72

3.6.3 Artificial neural network models 72

3.7 Mechanics of material flow 73

3.7 Yield criterion 74

3.7.1 Isotropic yield criterion 75

3.7.1.1 Tresca Criterion 75

3.7.1.2 Von Mises Criterion 75

3.7.1.3 Hosford yield criterion 76

3.7.2 Anisotropic yield criterion 76

3.8 Formability prediction models 78

3.8.1 Swift's diffused instability criterion 78

3.8.2 Hill's criterion for confined necking 79

3.8.3 Marciniak-Kuczinski (M-K) model 80

3.8.4 Vertex model 81

3.9 Conclusion 82

Chapter 4 84

Ductility of AZ80 Magnesium Alloys 84

4.1 Introduction 84
4.2 Uniaxial tensile testing issues 85
4.2.1 Tensile testing machine 86
4.2.2 Gripping issues 87
4.2.3 Geometric issues 88
4.2.4 Measurement issues 89
4.2.5 Material flow and expansion issues 90
4.2.6 Testing time issues 91
4.3 Experimental Procedure 91
4.4 Design of experiments 92
4.5 Results and discussion 93
4.5.1 Room temperature tests 93
4.5.2 Higher temperature tests 100
4.6 Sensitivity of both alloys to variation in temperature 105
4.7 Influence of strain rate 108
4.8 Influence of grain size 109
4.9 Fracture strain 110
4.10 Flow Stress and strain rate sensitivity index 111
4.11 Anisotropy effects 111
4.12Two-stage deformation 118
4.13 Conclusion 120
Chapter 5 123
Formability of Magnesium AZ80 123
5.1 Introduction 123
5.2 Experimental setup 124
5.2.1 Round tool setup 124
5.2.2 Rectangular-tool tests 127

5.2.2.1 Tool design and manufacturing....127

5.2.2.2 Assembling and checking of heating and measurement equipment....132

5.3 Strain Measurement....136

5.4 Problems during warm deep-drawing....139

5.5 Sample sizes and standards....140

5.6 Grid printing....142

5.7 Test procedure....143

5.8 Results and discussion....147

5.8.1 Forming limit curves....147

5.8.2 Pre-processing parameter characteristics....152

5.8.2.1 Influence of temperature....152

5.8.2.2 Influence of blankholder force....156

5.8.2.3 Influence of blank notch width....156

5.8.2.4 Influence of punch velocity....159

5.9 Conclusions....159

Chapter 6....162

Microstructure analysis....162

6.1 Introduction....162

6.2 Methodology....163

6.2.1 Sample preparation....163

6.2.2 Optical and electron microscopes....164

6.3 Results and discussion....165

6.3.1 Surface morphology....165

6.3.2 Twinning....168

6.3.3 Grain growth....172

6.3.4 Dynamic recrystallisation and gliding....177

6.3.5 Cavitation and filaments....180

6.4 Deep-drawn cups microstructure 192

6.5 Conclusions 196

Chapter 7 198

Simulation and Modelling 198

7.1 Introduction 198

7.2 Constitutive analysis 199

7.3 Phenomenological models 200

7.3.1 Johnson and Cook (J – C) model 200

7.3.2 Arrhenius model 207

7.4 Finite Element Simulations 217

7.5 Formulations Algorithms 218

7.6 FEA formulations 218

7.6.1 Discretisation 218

7.6.2 Meshing 219

7.7 Results and discussion 220

7.8 Conclusions 225

Chapter 8 227

Conclusion and Future Work 227

8.1 Conclusion 227

8.1.1 Tensile behaviour investigations 227

8.1.2 Deep-drawing behaviour investigations 228

8.1.3 Microstructure investigations 229

8.1.4 Mathematical modelling and finite element simulations 230

8.2 Future Work 231

List of Publications from this Project 233

References 234

Appendix A: Tensile test curves 277

Appendix B: Tensile test microstructure results at strain of 0.2 279

List of figures

Figure 1. Vehicle approximate mass distribution by sub-systems [2] 1

Figure 2. Increase in weight of vehicles over different decades [4] 2

Figure 3. Comparison of density against Young’s modulus for different materials [19] 5

Figure 4. Forming limit diagram [41] 10

Figure 5. Dissertation layout 14

Figure 6. HCP crystal structure illustrating three layers and lattice parameters [44] 15

Figure 7. Distribution of consumption of raw magnesium until 2010 [63] 19

Figure 8. Various applications of magnesium cast alloys [64] 20

Figure 9. Comparison of cast and wrought alloys [77] 22

Figure 10. Binary phase diagram of aluminium and magnesium [68]...........................26

Figure 11. Phase diagram of zinc and magnesium [90] 27

Figure 12. Phase diagram of manganese and magnesium [93].....................................28

Figure 13. Phase diagram of magnesium with manganese content of up to 5% mass [93] 29

Figure 14. HCP crystals with various slip systems, (a) basal, (b) prismatic, (c) first order pyramidal, (d) second order pyramidal, and (e) tension twinning [98].................31

Figure 15. Variation in CRSS with respect to temperature for various slip systems [100] 32

Figure 16. Twinning as function of grain size and temperature in AZ31 [102] 34

Figure 17. Microstructure of magnesium AZ31 [109]..36

Figure 18. Sigmoidal relationship between flow stress and strain rate [127] 38

Figure 19. Superplastic behaviour of materials in various regions [128] 38

Figure 20. Deformation map of AZ31 [133]..40

Figure 21. Deformation mechanism governed by (a) GBS (b) Diffusional creep [144]42

Figure 22. Dynamic recrystallisation model in magnesium alloys [157] 45

Figure 23. Influence of strain rate and temperature on mechanical properties of AZ61 [169]...50

Figure 24. Process diagram of deep-drawing tests at higher temperatures [36] 55

Figure 25. Comparison of four magnesium sheets at different punch speeds [220]......59

Figure 26. Drawing depth of magnesium AZ31 at different temperatures [246] 61

Figure 27. Prediction of exact location of thinning area by FEA [254].........................64

Figure 28. Forming limit diagram [268] 66

Figure 29. (a) Nakazima test setup (b) Marciniak test setup [269] 68

Figure 30. FLC curves of AZ31 for Nakazima and Marciniak tests [273] 70

Figure 31. Schematic diagram of Artificial Neural Network [296] 73

Figure 32. Schematic representation of stress strain curve [300] 74

Figure 33. Comparison of maximum shear stress and maximum distortion energy criterion [302] 76

Figure 34. Representation of test sample for M-K model [323] 80

Figure 35. Hounsfield H50KS Universal tensile testing machine 87

Figure 36. Special grips for Hounsfield H50KS Universal tensile testing machine 88

Figure 37. Dog bone tensile sample 89

Figure 38. Stress strain curves of AZ80-O (Fine) at room temperatures and various strain rates (a) 0^0 (b) 45^0 (c) 90^0 94

Figure 39. Stress strain curves of AZ80-F (Coarse) at room temperatures and various strain rates (a)0^0 (b) 45^0 (c) 90^0 95

Figure 40. Comparison of AZ80 fine and coarse grain materials at room temperature. 99

Figure 41. Comparison of AZ80 in LD at various temperatures and strain rates (a)Fine grain (b) Coarse grain 102

Figure 42. Comparison of elongation to failure in AZ80 – O vs (a) Temperature (b) Strain rate. 103

Figure 43. Comparison of elongation to failure in AZ80 – F vs (a) Temperature (b) Strain rate 104

Figure 44. Fracture strain variations in AZ80 – O (a) vs Temperature (b) Strain rate 106

Figure 45. Fracture strain variations in AZ80 – F (a) vs Temperature (b) Strain rate . 107

Figure 47. Flow stress as a function of strain rate at a strain of 0.1, (a) AZ80 – O, (b) AZ80 – F 112

Figure 47. Flow stress as a function of temperature at a strain of 0.1, (a) AZ80 – O, (b) AZ80 – F 113

Figure 48. Anisotropy effects in AZ80 – O (a) 200^0C and 10^{-3} sec^{-1} (b) 200^0C and 10^{-4} sec^{-1} (c) 300^0C and 10^{-3} sec^{-1} (d) 300^0C and 10^{-4} sec^{-1} and AZ80 – F (e) 200^0C and 10^{-3} sec^{-1} (f) 200^0C and 10^{-4} sec^{-1} (g) 300^0C and 10^{-3} sec^{-1} (h) 300^0C and 10^{-4} sec^{-1} 117

Figure 49. Two stage stretch forming in AZ80 – O, (a) 60% strained at 200^0C, 40% at 400^0C and $2x10^{-4}$ sec^{-1}, (b) 60% strained at 200^0C and $2x10^{-4}$ sec^{-1}, 40% at 400^0C and $2x10^{-4}$ sec^{-1} 119

Figure 50. Two stage stretch forming in AZ80 – F, (a) 60% strained at 200^0C, 40% at 400^0C and $2x10^{-4}$ sec^{-1}, (b) 60% strained at 200^0C and $2x10^{-4}$ sec^{-1}, 40% at 400^0C and $1x10^{-4}$ sec^{-1} 120

Figure 51. Schematic deep-drawing setup of Nakazima test 125

Figure 52. Erichsen formability tester 125

Figure 53. Accessories of Erichsen formability tester, (a) heating furnace for die and blank-holder assembly, (b) heating elements with temperature controller 126

Figure 54. Surface temperature distribution with the offset setup after 20 min (left) and the radial setup after 60 min (right) [341] 129

Figure 55. Assembly of the heated deep-drawing tool with drawbeads 129

Figure 56. Assembly of the heated deep-drawing tool 130

Figure 57. Schematic deep-drawing setup of Marciniak test 131

Figure 58. Manufactured tool parts 131

Figure 59. Circuit diagram of heating and controlling equipment 132

Figure 60. Set-up for heating and controlling 133

Figure 61. Temperature distribution on the surface after 4, 10 and 16 minutes, at a set temperature of 100 °C 134

Figure 62. Temperature distribution on the surface after 10, 20 and 36 minutes at a set temperature of 200 °C 135

Figure 63. Temperature rise at the surface temperature measuring point at a set temperature of 200 °C 136

Figure 64. CCD camera image capturing methodology 137

Figure 65. Installation setup of CCD cameras above the tooling, along with 4 ultra-high beam LED lights. 138

Figure 66. Standard sample sizes that were used for deep-drawing of AZ80, ... 141

Figure 67. Grid painting, (a) Grid painting setup, (b) Specimens after grid painting .. 143

Figure 68. A view of the heat shield used to protect cameras from heat. 146

Figure 69. View of strain paths generated by Autogrid software for various blank widths at RT and 1mm/min (Nakazima tests), (a)15mm, (b) 100mm 148

Figure 70. Round Punch samples of various widths (Nakazima tests) (a)10mm (b)20mm (c)35mm (d)50mm at RT and 1mm/min speed 149

Figure 71. Forming limit curves of AZ80 – F at various temperatures (Nakazima tests) 150

Figure 72. Forming limit curves of AZ80 – O at various temperaturestemperatures (Nakazima tests) 150

Figure 73. Effect of punch velocity on forming limit curves of AZ80 – O at 200^{0}C (Nakazima tests) 151

Figure 74. Anisotropy effects on forming limit curves of AZ80 – O at 200^{0}C (Nakazima tests) 151

Figure 75. Formed cups at various temperature and at speed of 1mm/min (Marciniak tests). 153

Figure 76. Load displacement curves for deep-drawing tests for magnesium AZ80 – O at various temperatures (Marciniak tests) 154

Figure 77. Variation in Limit Drawing Ratio (LDR) with temperature at punch speed of 1mm/min for magnesium AZ80 – O (Marciniak tests)... 154

Figu**Figure 78.** Effect of Blank holder force at 150^{0}C and 1mm/min. (a) 50 kN, (b) 75kN, (c) 100kN, (d) 75kN and 200^{0}C, (e) 100kN and 200^{0}C (Marciniak tests)......... 157

Figure 79. Load displacement curves for deep-drawing tests for magnesium AZ80 – O at various blank holder forces (Marciniak tests) 158

Figure 80. Load displacement curves for deep-drawing tests of magnesium AZ80 – O for various blank notch widths (Marciniak tests)... 158

Figure 81. Load displacement curves for deep-drawing tests for magnesium AZ80 – O for various punch velocities (Marciniak tests) 159

Figure 82. Hitachi SU – 70 scanning electron microscope 164

Figure 83. Surface morphology of (a) AZ80 – O and (b) AZ80 – F at room temperature at 1 x 10^{-3} sec^{-1} 165

Figure 84. Surface morphology of (a) AZ80 – O at 200^{0}C, (b) AZ80 – F at 200^{0}C, (c) AZ80 – O at 300^{0}C, (d) AZ80 – F at 300^{0}C, (e) AZ80 – O at 400^{0}C and (f) AZ80 – F at 400^{0}C at 1 x 10^{-3} sec^{-1} 167

Figure 85. Surface morphology of AZ80 – O at (a) 200^{0}C and (b) 300^{0}C (c) 400^{0}C at 1 x 10^{-3} sec^{-1} showing dense dimples 167

Figure 86. Surface morphology of AZ80 – O at (a) 200^0C and (b) 300^0C showing dense dimples 168

Figure 87. Effect of twinning on both magnesium (a) AZ80 – O and (b) AZ80 – F at room temperature and 1 x 10^{-3} sec^{-1} 169

Figure 88. Effect of variation in strain rate on twinning in AZ80 – O (a) $10^{-2}sec^{-1}$, (b) $10^{-3}sec^{-1}$, (c) $10^{-4}sec^{-1}$ 169

Figure 89. Effect of variation in temperature on twinning in AZ80 – O (a) room temperature, (b) 200^0C, (c) 300^0C and (d) 400^0C at $10^{-4}sec^{-1}$........ 170

Figure 90. Grain size increments with varying temperature in AZ80 – O at gauge (a) room temperature (b) 200^0C (c) 300^0C and (d) 400^0C at $10^{-3}sec^{-1}$ 173

Figure 91. Microstructure of magnesium AZ80 – O at 300^0C and $10^{-3}sec^{-1}$ (a) gauge section (b) grip 174

Figure 92. SEM micrographs of nucleated grains at $10^{-4}sec^{-1}$ (a) AZ80 – O at 300^0C (b) AZ80 – F at 300^0C (c) AZ80 – O at 400^0C AZ80 – F at 400^0C 175

Figure 93. SEM micrographs of nucleated grains at $10^{-4}sec^{-1}$ (a) AZ80 – O at 300^0C (b) AZ80 – F at 300^0C (c) AZ80 – O at 400^0C AZ80 – F at 400^0C 175

Figure 94. Grain aspect ratio of AZ80 – O as function of strain........ 176

Figure 95. Grain aspect ratio of AZ80 – F as function of strain 176

Figure 96. Dynamic grain growth at 300^0C and 1x10^{-3} sec^{-1} (a,c) AZ80 - O (d,e) AZ80 - F........ 179

Figure 97. Dynamic grain growth at 400^0C and 1x10^{-3} sec^{-1} (a) AZ80 – O, (b) AZ80 – F 179

Figure 98. Various cavities shown at 300^0C and 10^{-4} sec^{-1} at 60% of strain (a) AZ80 – O and (b) AZ80 – F........ 181

Figure 99. OP micrographs showing cavities at 300^0C and 10^{-4} sec^{-1} at 60% of strain (a) AZ80 – O and (b) AZ80 – F........ 181

Figure 100. OP micrographs showing cavities at 300^0C and 10^{-4} sec^{-1} at 60% of strain (a) AZ80 – O and (b) AZ80 – F........ 182

Figure 101. SEM micrographs showing cavities at 300^0C and 10^{-4} sec^{-1} at 60% of strain (a) AZ80 – O and (b) AZ80 – F 183

Figure 102. SEM micrographs showing filaments at 3500C and 10-4 sec-1 at 60% of strain (a) AZ80 – O and (b) AZ80 – F 183

Figure 103. SEM micrograph showing locations for EDS analysis on AZ80 – O 184

Figure 104. EDS analysis showing position at 60% of strain (a) X, (b) Y, and (c) filaments 186

Figure 105. Evidence of pre-existing cavities at grain boundaries with size 0.1 - 0.3µm at 200^0C and 10^{-4} sec^{-1}........ 187

Figure 106. SEM micrographs of AZ80 – F at 60% strain (a) room temperature, (b) 200^0C, (c) 300^0C (d) 400^0C........ 188

Figure 107. SEM micrographs of AZ80 – F at 60% strain (a) room temperature (b) 200^0C (c) 300^0C(d) 400^0C........ 189

Figure 108. Comparison of the number of cavities as a function of percentage of strain at 400^0C and 10^{-4} sec^{-1} for both magnesium materials........ 190

Figure 109. Comparison of the number of cavities as a function of percentage of strain at 400^0C and 10^{-4} sec^{-1} for AZ80 – O for conventional and two-stage forming. 190

Figure 110. Measured areas in deep-drawn cup........ 193

Figure 111. SEM micrographs of deep-drawn cup at 100^0C for magnesium AZ80 – O (a) Flange (b) Wall (c) Bottom........ 194

Figure 112. SEM micrographs of deep-drawn cup at 200^0Cfor magnesium AZ80 – O(a) Flange (b) Wall (c) Bottom 195

Figure 113. Plot of ln (ϭ – Y) vs ln ε at 200^0C and 10^{-4} sec^{-1} for both magnesium materials 203

Figure 114. Plot of ϭ / (Y + Hε^n) vs ln $\acute{\varepsilon}_r$ at 200^0C and 10^{-4} sec^{-1} for both magnesium materials 204

Figure 115. Plot of ln [1-{ϭ / (Y + Hε^n)}] vs ln T* at 300^0C and 400^0C and 10^{-4} sec^{-1} for both magnesium alloys........ 205

Figure 116. Stress strain diagrams for magnesium AZ80 – O, predicted vs experimental results (a) 0.1 sec^{-1}, (b) 0.01 sec^{-1}, (c) 0.001 sec^{-1} 206

Figure 117. Stress strain diagrams for magnesium AZ80 – F, predicted vs experimental results (a) 0.1 sec^{-1}, (b) 0.01 sec^{-1}, (c) 0.001 sec^{-1} 207

Figure 118. Plot for evaluation of material constants (a) ln(σ) vs ln($\acute{\varepsilon}$) yields 'n*', (b) σ vs ln($\acute{\varepsilon}$) results β, (c) ln sinh (ασs) vs ln($\acute{\varepsilon}$) provides n and (d) ln sinh ($\alpha\sigma_s$) vs 1000 / T results Q for AZ80 – O........ 210

Figure 119. Plot for evaluation of material constants (a) ln(σ) vs. ln($\acute{\varepsilon}$) yields 'n*', (b) σ vs. ln($\acute{\varepsilon}$) results β, (c) ln sinh (ασs) vs. ln($\acute{\varepsilon}$) provides n and (d) ln sinh ($\alpha\sigma_s$) vs. 1000 / T results Q for AZ80 – F 211

Figure 120. Stress strain diagrams for magnesium AZ80 – O, predicted vs. experimental results (a) 0.1 sec^{-1}, (b) 0.01 sec^{-1}, (c) 0.001 sec^{-1} 213

Figure 121. Stress strain diagrams for magnesium AZ80 – F, predicted vs. experimental results (a) 0.1 sec^{-1}, (b) 0.01 sec^{-1}, (c) 0.001 sec^{-1} 214

Figure 122. Sensitiveness of material constants towards strain (a) α, (b) Q, (c) n, (d) ln A for AZ80 – O 215

Figure 123. Sensitivity of material constants to strain (a) α, (b) Q, (c) n, (d) ln A for AZ80 – F 216

Figure 124. FEA model of deep-drawing setup 218

Figure 125. FEA quarter model of deep-drawing setup with mesh of blank 219

Figure 126. Quarter model of deep-drawing tools with meshes (a)punch, (b)die and (c) blank holder... 220

Figure 127. FEA analysis of deep-drawn cup at 100^0C with 10kN force for magnesium AZ80 – O (a) Von Mises stress distribution, (b) Principal stress distributions, (c) Pressure distributions 222

Figure 128. FEA analysis of deep-drawn cup at 250^0C with 10kN force for magnesium AZ80 – O (a) Von Mises stress distribution, (b) Principal stress distributions, (c) Pressure distributions 223

Figure 129. Thickness distribution of specimen with a blankholder force of 10 kN at 250^0C for magnesium AZ80 – O 223

Figure 130. Temperature distribution of specimen with a blankholder force of 10 kN and at 250^0C for magnesium AZ80 – O (Simulation results) 224

List of tables

Table 1. Designated letters for alloying elements in magnesium [56] 17

Table 2. Various heat treatment designations [56] 18

Table 3. Mechanical properties of cast alloys at room temperature 21

Table 4. Physical properties of cast alloys at room temperature 21

Table 5. Physical properties of common wrought alloys at room temperature [80] 24

Table 6. Various slip systems and their CRSS values at room temperature [99] 32

Table 7. Various twinning modes along with their dislocations [106] 35

Table 8. Summary of different grain boundary sliding models 44

Table 9. Summary of different elevated temperature tests in commercial magnesium alloys 52

Table 10. Summary of limit drawing ratios (LDR) for magnesium AZ31 alloy 57

Table 11. Different sample geometries for Nakazima and Marciniak tests [130] 69

Table 12. Chemical composition of AZ80 as fraction of mass (%) 92

Table 13. Mechanical properties of AZ80 – O and AZ80 – F at room temperature (RT) and 1x10^{-3} sec^{-1} 96

Table 14. Mechanical properties of AZ80 – O and AZ80 – F at room temperature (RT) and 1x10^{-4} sec^{-1} 96

Table 15. Mechanical properties at room temperature (RT) and 1x10^{-3} sec^{-1} 100

Table 16. Mechanical properties and r – values of 45^{0}RD sample at 300^{0}C 110

Table 17. Mechanical properties and r – values 117

Table 18. Various material constants in Johnson – Cook model for magnesium AZ80 – O and AZ80 – F 207

Table 19. Various material constants in Arrhenius model for magnesium AZ80 – O and AZ80 – F. 216

Table 20. Various polynomial curve fitting material constants in the Arrhenius model for magnesium AZ80 – O. 216

Table 21. Various polynomial curve fitting material constants in the Arrhenius model for magnesium AZ80 – F 217

List of symbols

A	structure dependent constant
a	material constants
B	burger vector
b	material constant
c	material constant
d	grain size
D_{gb}	grain boundary diffusivity
D_L	lattice diffusivity
D_p	dislocation pipe
D_{chem}	chemical diffusivity
D_{IPB}	interfacial phase boundary
D_L	coefficient of lattice diffusion
D_{gb}	coefficient of grain boundary diffusion
E	modulus of elasticity
F	material constant
G	material constant
H	material constant
h	average individual cavity growth
I_2	second invariant of stress
k	boltzman constant
K	material constant
L	material constant
M	material constant
m	strain rate sensitivity
N	material constant
n*	grain size exponent
p	material constant

Q	activation energy
r	lankford coefficient
r_{avg}	average anisotropic ratio
S	flow stress
s	strain hardening exponent
T	absolute temperature
T_m	stands for melting temperature
T_r	reference temperature
T''	homologous temperature
t	thickness
V	cavity volume,
V_0	volume at specific strain
x	grain-aspect ratio
Y	material constant
Z	stress coeffiecient
α	material constant
α_ε	ratio of strains in different directions
β	material constant
γ	scalar factor,
δ	grain boundary width,
$\acute{\varepsilon}$	strain rate
ε	applied strain
ε_y	applied yield strain
ε^p	strain in the plastic zone
ε_{cr}	critical major strain
ϕ	potential yielding function
$Ϭ_0$	threshold stress
σ	applied stress
$\sigma_{1,2,3}$	principal stresses

σ_s	shear stress in yielding

Acknowledgements

I dedicate this thesis to my parents, my late mother (Mrs. Mukhtiar Soomro), and my father Prof. Dr. Muhammad Saleh Soomro, my wife Mrs. Rabia Soomro my children Khadija Soomro and Muhammad Adil Soomro, My brothers Muhammad Kaleem Soomro and Muhammad Naeem Soomro who encouraged and motivated me throughout.

I am very grateful to my supervisor Prof. Dr. Thomas Neitzert, for his continuous, extraordinary support and guidance. He inspired me in work and in my daily life. I was fortunate to have him as a supervisor, he understands student problems and offers extreme support. I express my gratitude to Assoc. Prof. Dr. Timotius Pasang, Dr. Maziar Ramezani, Mr Holger Heinzel, Dr. Shamzin Yazdanian, Prof. Dr. Zhan Chen and Assoc. Prof. Dr. Sarat Singamneni for their enormous support and cooperation throughout my studies.

My sincere acknowledgement and appreciation goes to Dr. Matthias Weiss, (Institute of Frontier Materials, Deakin University) for giving his precious time from his busy schedule and greatly assisting me in their forming facilities.

I am thankful to AUT University for providing me excellent facilities, an exceptional learning environment, and outstanding support. My sincere thanks to our lab technicians, Mark Masterton, Patrick Conor, Tim Luton, Ross Jamieson and Jim Crossen who trained me and assisted me throughout my studies.

Chapter 1

Introduction

1.1 Definition of the problem

The automotive industry is currently growing extensively through increasing consumer demand. As well as this growth, the sector is also facing several challenges from environment-conscious agencies. The most strident request from these agencies is to reduce the emissions from vehicles and keep the environment cleaner [1]. Automotive experts and researchers have suggested numerous solutions to this problem, which include variations in aerodynamic vehicle shape, increasing use of alternative fuels or boosting the production of hybrid vehicles and lastly abating the weight of vehicles. An analysis of vehicle mass distribution is shown in Figure 1[2].

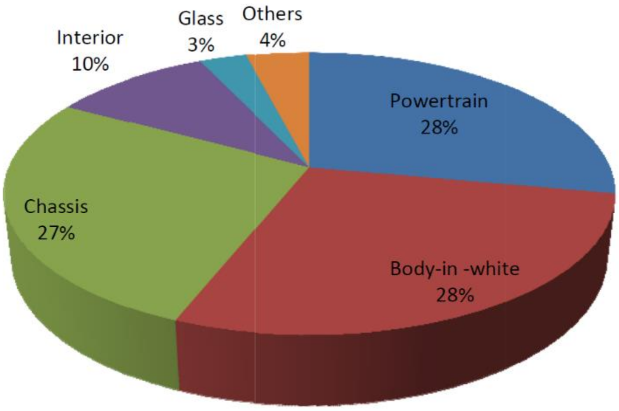

Figure 1. Vehicle approximate mass distribution by sub-systems [2]

Given all these solutions, a first step was taken to control weight. After several studies, it is now an established fact that more than 50 percent of fuel consumption is mass-dependent [3], and an increase in features demanded by customers is adding more weight to vehicles, which ultimately results in an overall decrease in fuel efficiency, as shown in Figure 2. Numerous light-weight materials were considered to reverse the trend such as aluminium alloys (e.g. 7475 and 5083) and titanium (e.g. Ti-6Al-2Sn-4Zn-2Mo and Ti-6Al-4V), as well as various magnesium alloys (e.g. AZ31, AZ31B, ZK60, ZE10) [4].

For structural applications in aerospace and outer space components, magnesium alloys are the preferred choice because they carry the least density of all commercially used structural metals. Magnesium's density of 1.74 g/cm^3 is 35 percent lighter than aluminium (2.70 g/cm^3), and 78 percent lighter than steel (7.85 g/cm^3) [5,6]. Moreover, magnesium alloys also possess enhanced damping characteristics when compared with aluminium. These numbers highlight the great weight-saving potential promised by the metal (and its alloys), if it can be effectively and productively utilised in particular areas [7].

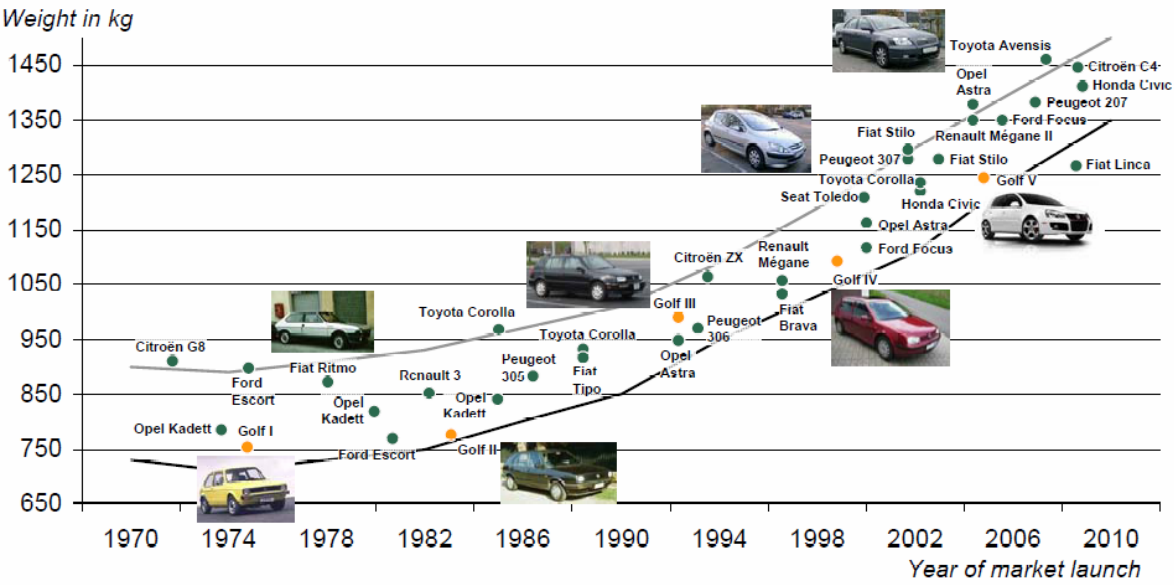

Figure 2. Increase in weight of vehicles over different decades [4]

The use of magnesium started shortly after World War II, when Volkswagen utilised it in the clutch housing of its famous Beetle model. Later, Toyota, Mazda and Porsche also employed it. In the last ten years, magnesium use has increased from one to four kg per vehicle and many researchers estimate that it could climb to 100 kg per vehicle in the near future [8]. At present, General Motors, Ford and Chrysler are using magnesium in their latest models, such as the GMT 800. General Motors is a leading company in the utilisation of magnesium in its mirror brackets, transfer cases, instrument panels and steering wheels. Besides all these developments, the current use of magnesium is about four kg per vehicle, compared with aluminium which is reaching 123 kg per vehicle [9].

To simplify its manufacture, different variations have been created in its material properties, as well as casting and forming parameters. The attractive features of magnesium are: extended specific strength, increased damping capacity and high corrosion resistance. Due to its low density, thicker sections can be formed easily without using any extra stiffening [10].

Magnesium cast alloys such as AM50, AM60, AS41 and AZ91 have been in use for decades for automotive components, housing and electrical components, through die casting, permanent mould casting and investment casting processes. But research on wrought magnesium alloys such as AZ31, AZ61 ZE10 and AZ80 is still very limited [11].

The main hindrance to a wider application is the hexagonal close-packed (HCP) crystal system with a limited number of operative slip systems, and thus cold-forming of magnesium alloys is restricted to small deformations with a generous bend radius. Therefore, hot extrusion and hot rolling are the most popular techniques for producing commercial magnesium plates and rods [12].

The AZ magnesium alloy series is widely used by the light metal industry. In this research, AZ80 magnesium alloy was selected. The chemical composition of this alloy is 7.8%-Al, 0.2%-Zn, 0.12%-Mn, 0.10%-Si, 0.05%-Cu, 0.005%-Ni and 0.005%-Fe. AZ80 is an important structural wrought magnesium alloy with a high aluminium content of about 8 wt. %. AZ80 will be the main subject of this study, because it offers higher strength and higher hardness than the widely used AZ31, but its stronger solid solution hardening, and its forming ability is not well understood [13].

In this research, the magnesium AZ80 alloy with two different grain sizes was considered, that is fine grain AZ80 (grain size ≈ 10 µm) and coarse grain AZ80 (grain size ≈ 60 µm). These grain sizes were chosen to investigate the effect of grain size at a higher temperature and to observe changes in mechanical and forming capabilities with respect to grain size.

This research adds to knowledge of a new alloy in the wrought magnesium alloy series for formability applications in the light metal industry.

The AZ80 magnesium alloy has already proven its properties as cast and extruded bars, which show excellent properties when compared with AZ31, AZ61 and ZK60 alloys. Until now there has been no data available related to formability parameters, deformation mechanisms including grain boundary sliding and cavitation, forming limit curves, flow stress values, texture variations and effect of grain sizes for thin magnesium AZ80 sheets. This research covers all these issues and provides a comprehensive knowledge-base for thin AZ80 wrought magnesium alloy.

In summary, this research will assist the use of magnesium in the light metal industry as a wrought alloy. As magnesium AZ80 has already proven its properties as a cast alloy, but its application as wrought alloy are yet to be explored. This research will investigates its various forming characteristics as a high strength wrought alloy.

1.2 Selection of material

Magnesium is the lightest engineering construction metal with a lower density than aluminium and steel, as shown in Figure 3 [14]. Moreover, it has ductility, good recyclability, and improved vibration and noise characteristics compared with other structurally used metals. Forming characteristics are also satisfactory as acknowledged by the sheet metal industry, for commercial production [15]. In addition to that, magnesium is stronger than polymers and electromagnetic interference (EMI) shielding, as well as its heat dissipation being much higher than polymers [16]. Magnesium alloys can be categorised into two parts: cast magnesium alloys and wrought magnesium alloys.

The focus in this project is confined to wrought magnesium alloys, because of their increasing application in the sheet metal industry. Some of the best-known series in this category are AZ, ZK, WE and ZE. To improve the characteristics of the pure wrought magnesium, several alloying elements are used, such as in the AZ series, aluminium and zinc are added to strengthen the workability of these alloys. Similarly, in the ZE series rare earth elements such as cerium, yttrium and neodymium are added, along with zinc, to increase the ductility of the material [17].

Despite these advantages, there are some barriers to the wide use of magnesium in the commercial sheet metal industry. The biggest obstacle is its limited ductility at room temperature, compared with aluminium and iron, because of its HCP structure, along with low numbers of operative slips systems. This also reduces the melting point and makes it less resistant to corrosion [18].

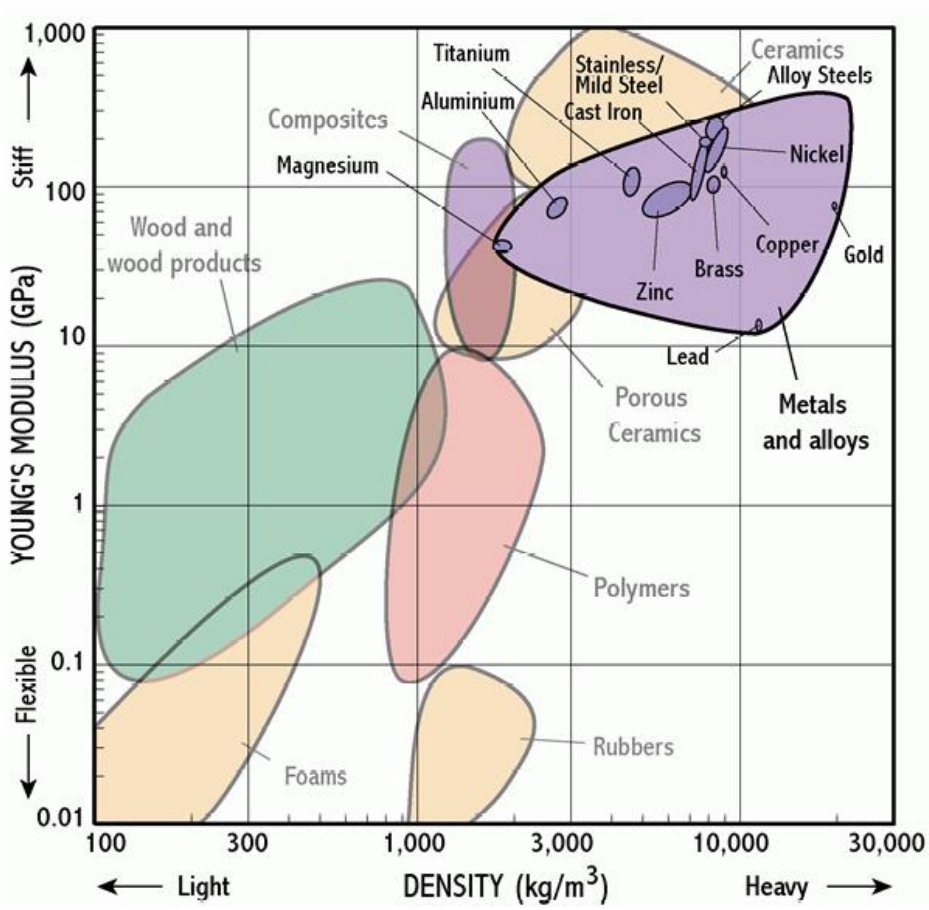

Figure 3. Comparison of density against Young’s modulus for different materials [19]

To overcome these problems, different techniques are presented, based on research on magnesium. The most widely accepted solution appears when the inferior ductility of this metal becomes high ductility at an elevated temperature. This revolutionises the light metal industry, and is similar to aluminium and titanium alloys, which also show excellent ductility at higher temperatures.

Elevated temperature formability can nevertheless be further improved. A fine-grained material is of assistance, which to produce long elongations before failure. The second option is slower strain rates, which range from 10^{-2} to

$10^{-4}s^{-1}$. The operating temperature should be approximately equal to $0.5T_m$ (where T_m is the melting temperature of the given material) [20].

The AZ80 magnesium alloy is the focus of this study for several reasons:

i. Commercially available in sheet form
ii. Good room-temperature mechanical properties
iii. High strength-to-weight ratio compared with many competitive steel, aluminium and magnesium alloys
iv. Exhibits superplastic behaviour at elevated temperatures

Until now, there have been very few references [21]–[25] available related to AZ80 sheets. Most of the authors have focussed on cast slabs of AZ80 [26] -[29]. The thin sheet properties of AZ80 still need a lot of investigative work. This research discovered the elevated temperature properties of thin sheets of magnesium AZ80 alloy. These properties include its mechanical and formability characteristics in uniaxial and multiaxial tests at various strain rates, temperatures and in two different grain sizes. Finally, its microstructural properties will be discussed and explained for various process parameters.

1.3 Testing equipment, calibration and standards

The selection of standard procedures for testing plays a vital role for meaningful and consistent results. Due to long elongations at extremely slow speeds and at elevated temperatures, standard sample testing time increased to more than 24 hours per sample. Unfortunately, the commonly used standards do not mention any specimen geometry of samples that produce results in a reasonable timeframe and with acceptable accuracy level for uniaxial tests. To overcome this, ASM standards were used for mini tensile samples, which gave favourable results within eight hours of testing for a single sample.

The equipment used for uniaxial tensile tests is a universal tensile testing machine, along with an electrical heating furnace (chamber) that can accommodate a maximum temperature of 1200^0C with an accuracy of ±1 ^{0}C. Special grips are used to hold the specimen at higher temperatures and reduce any slipping. Specimens are heated at different temperatures and a pre-set load was maintained to allow the test samples to expand and to acquire an equilibrium strain.

Forming tests were performed at the National Center for Metal Forming at AUT University, with an 80-ton Bipel Press equipped with a data-logging computer, and at the Institute for Frontier Materials at Deakin University, Australia, with a 60-ton Erichsen formability tester, also with a data-logging computer. Six specimens for each forming limit curve were prepared according to NF EN ISO 12004.

Microstructural images were obtained by using a Scanning Electron Microscope (SEM) and optical microscopes at AUT University.

1.4 Forming issues at elevated temperatures

Formability is the ability of a material to undergo plastic deformation without damage or fracture. The plastic formability of several alloys, such as HCP metals, is quite limited in industrial applications [30]. The main hindrance to its use has been its low ductility at room temperature. Stamping magnesium alloys is a more challenging task than with other light metals, as it cannot be formed extensively at room temperature [31] - [32].

Most of the researchers have confined their studies to AZ31, which is the most common commercial magnesium alloy. Most of the studies are related to uniaxial tensile tests at different temperatures, and based on these many researchers have made predictions about its forming behaviour.

The warm deep-drawing process is quite complex, as it depends on a number of parameters that control it [32]. Warm stamping ductility and formability has not been investigated in detail for many new magnesium alloys. One reason might be the requirement of a large number of tests (i.e. uniaxial, biaxial and multiaxial) to accurately predict their behaviour.

The investigation of formability of a material can be divided in general into three stages [33]:

i. Experimental setup development

ii. Examination of the basic forming parameters
iii. Construction of forming limit curves (FLC)

These three stages were all conducted in this project.

1.4.1 Experimental setup development

Warm deep-drawing, as already stated, is a complex process to control. The heating of the blank is an additional step in this process. Two methods are used for blank heating, that is external heating and internal heating [34].

External heating, which is commonly performed in an external oven, is not effective in laboratory procedures as heat losses can be great. However, for industrial applications, an integrated conveyor system can be used, in which heat losses will be minimised.

Internal heating is the preferred method, as heat can be homogeneously distributed in the blank. The blank needs to be clamped by the blank holder for a short time to distribute the heat evenly.

The drawing setup also involves setting different processing parameters such as temperature, punch velocity, ram stroke, die geometry and blank holder force (BHF). The drawing gap between the sheet and the die should usually be 1.2 times the sheet thickness [35].

1.4.2 Examination of the basic forming parameters and results from literature

Formability of magnesium alloys has been a topic of interest for a number of decades because of global warming and environmental issues. An increased drawing capacity for magnesium sheets not only indirectly addresses environmental issues, but also enhances productivity and parts quality. Very few studies are available regarding the drawing of magnesium sheets, but some are by Doege and Droder [37] - [38], who have performed limiting drawing ratio (LDR) experiments to examine the formability of AZ31 sheets at different temperature states, and they managed to form 100 mm diameter cups with a

LDR of 2.5 at a forming temperature of 200^0C. They also mentioned investigating the forming of magnesium alloys in rectangular pans and achieving a maximum height of 65mm at 225^0C. One common factor in both rectangular and round cups is that wrinkles during drawing will decrease with an increase in temperature up to a certain limit.

Heat treatment processes also influence the formability of magnesium alloys. Yang et al. [39] investigated the cold-forming deformation behaviour of magnesium AZ31 by performing uniaxial tensile tests and deep-drawing tests. They used a sheet thickness of 0.5mm and annealed these sheets at different temperatures, varying from 400^0C to 550^0C for one to three hours, and achieved an LDR of 1.72. They also found that anisotropy effects are dominant during cold forming and vary material flow into the die cavity, resulting in different thicknesses at the flanges for different orientations.

All these results indicate magnesium alloys can be commercially used as an alternative material for aluminium and steel by considering the above techniques and parameters. After reviewing these formability data in-depth, extensive research started on the optimisation of process parameters and factors that affect the formability of AZ80 magnesium alloy, so that this alloy can compete with existing metals in the field of sheet metal forming, especially in the automotive and aerospace industries. These factors are: the influence of the punch speed, punch force, blank holder force, texture, temperature, temperature distribution during warm forming at different sections of the formed part, thickness distribution during warm forming, spring-back properties, tool geometry, and the lubrication system of the tool and blank. Finally an exact prediction of the flow of material during forming was undertaken by mathematical modelling.

1.4.3 Construction of forming limit curves (FLC)

Formability of sheet metal is often assessed by forming limit diagrams (FLD). A forming limit diagram is a plot of maximum principal strains. The concept of forming limit diagrams was introduced by Keeler and Backofen in 1964 [40]. The FLD forming limit curve (FLC) represents the maximum major principal strains that can be reached in sheet materials at given minor principal strains, prior to the onset of localised necking.

A forming limit diagram is a plot of planar strains that combines major and minor strains generated during different types of tests such as uniaxial, bi-axial and deep-drawing tests [41]. It also indicates different zones of uniform deformation, plastic instability and necking, which ultimately lead to failure [41]. In other words, it can be said that FLC actually highlights the boundary between safe and unsafe forming regions of an FLD as shown in Figure 5. The safe region can be highlighted as the area under the curve where there is no visible necking. On the other hand, the area above the curve represents the deformed or failed region where necking can be observed.

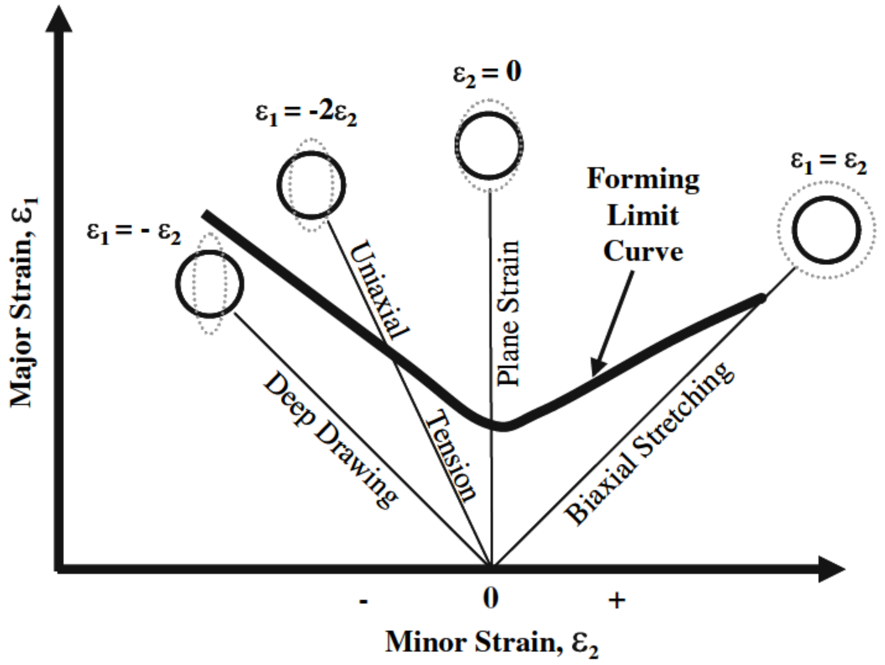
$\varepsilon_2 = 0$
$\varepsilon_1 = -2\varepsilon_2$
$\varepsilon_1 = -\varepsilon_2$
$\varepsilon_1 = \varepsilon_2$
Forming Limit Curve
Major Strain, ε_1
Uniaxial
Tension
Plane Strain
Deep Drawing
Biaxial Stretching
-
0
+
Minor Strain, ε_2

Figure 4. Forming limit diagram [41]

1.5 Research limitations

As this work is mainly experimental work on thin magnesium sheets at numerous strain rates and temperatures, a limitation is applied by restricting the temperature to 400^0C, due to the tensile testing setup and melting properties of magnesium. In addition, the strain rates were limited to 10^{-4} s^{-1}, along with the geometry of ASM mini specimens chosen to reduce the test time to eight hours per test at the lowest speed. In forming experiments the temperature is limited to 200^0C through consideration of the formability tester's limitations.

1.6 Scope and aspirations

There were five main objectives in this research.

First, determine mechanical properties. The material selected for this research is magnesium AZ80 with a sheet thickness of 0.8mm, which is a commonly used thickness value for automotive body panels. The material is further divided into two types with variation in grain sizes and tested at different strain rates and temperatures.

Second, improve formability of magnesium alloys by using elevated temperatures. To achieve this objective, pre-process and post process parameters were optimised by performing a number of experiments and theoretical simulations based on analytical formulae, as well as finite element formulations developed for future designs.

The third objective of this research was to investigate and explain the changes in the microstructure of the material used during elevated temperature processing, with respect to variations in grain sizes, strain rates and temperatures. Additionally this included the investigation of deformation mechanisms at various sections of a formed cup.

The fourth objective was the generation of constitutive equations. These equations are used to describe the stress/strain relationship in the tensile tests for sheet metal forming. Two types of models were used, one is the power law [42] and the second one is the Gavrus law [43]. The equations are produced by curve fitting techniques. The outcome of this analysis is a generalised flow stress equation for uniaxial and deep-drawing tests that can predict material behaviour at different temperatures, strain rates, textures and grain sizes.

The fifth objective was to simulate the deep-drawing process by using the mechanical properties from experimental data and applying appropriate boundary conditions to verify the results. To accomplish this objective a finite element methodology was used with the commercial software package Abaqus and results were verified experimentally.

1.7 Dissertation layout

This thesis contains eight chapters.

Chapter 1 introduces the aims and objectives for this research. It highlights the role of vehicles in affecting the environment and emphasises various means of reducing this influence. It further indicates the role of lightweight materials in cutting back the weight of vehicles. Magnesium materials are introduced as an alternate solution for structural members rather than steel and aluminium. The general properties of magnesium materials and their forming capabilities are discussed. Finally, the aims and objectives of this research project are stated.

Chapter 2 demonstrates key characteristics of magnesium alloys. These characteristics include the history and developmental stages of these alloys, along with a description of the series used. In addition, the role of distinct alloying elements in terms of mechanical and forming properties is examined. In the second half of this chapter, the literature concerning various deformation theories related to uniaxial and multiaxial deformations is discussed. These theories include the basic crystal system of magnesium alloys, slip systems available at room temperature as well as at elevated temperature, primary and secondary twinning mechanisms, grain boundary sliding (GBS), grain boundary migration (GBM) and cavitation mechanism at elevated temperatures. All these characteristics are discussed in relation to magnesium’s sensitivity to variations in temperature, strain rate and grain size.

Chapter 3 highlights the forming characteristics of magnesium alloys. The literature is reviewed, starting with tensile testing, which relates to stretch forming of magnesium alloys at various temperatures, strain rates and grain sizes. Multi-axial forming is then focused on, along with the various problems that restrict the use of magnesium in sheet metal forming. Recent developments and advances in forming are also discussed. The second part of this chapter outlines various constitutive models for tensile and forming tests that provide assistance to identify the behaviour of materials. The anisotropic effects of thin magnesium sheets are also reviewed, in order to correctly understand the material. In the last part of this chapter, various deformation theories related to the yielding of materials are compared, such as Tresca and von Mises yield criteria, Hill's anisotropy yield criterion and Hosford's anisotropy yield criterion. Theoretical forming limit criteria including the swift model, Hill's model and the M-K method are also discussed.

Chapter 4 provides the experimental results for the uniaxial tensile tests. Various tests were performed at different temperatures, test speeds and grain sizes to understand the nature of the material. Anisotropy of materials, strain sensitivity index and flow stress were also calculated by varying all of the above mentioned parameters.

Chapter 5 reports on the stamping tests conducted. The formability of magnesium alloys is examined in terms of load displacement diagrams, forming limit diagrams and the effects of various pre-and-post processing parameters.

Chapter 6 examines the microstructure of magnesium alloys. In this chapter, microscopic images of magnesium alloys are discussed in relation to varying conditions of temperature, strain rate and grain sizes. Optical and scanning electron microscopes were used to provide information. Deformation modes at various stages in tensile and stamping tests are discussed.

Chapter 7 demonstrates the simulation results. Simulations were performed by developing models and applying finite element methodology. The commercial code used was Abaqus. Simulations were performed by using the experimental load displacement data of all conditions investigated, which included variations in temperature, strain rate and grain size.

Chapter 8 summarises this work in the context of the existing literature and the insights gained.

A layout for dissertation is shown in Figure 5, which establishes link between all chapters.

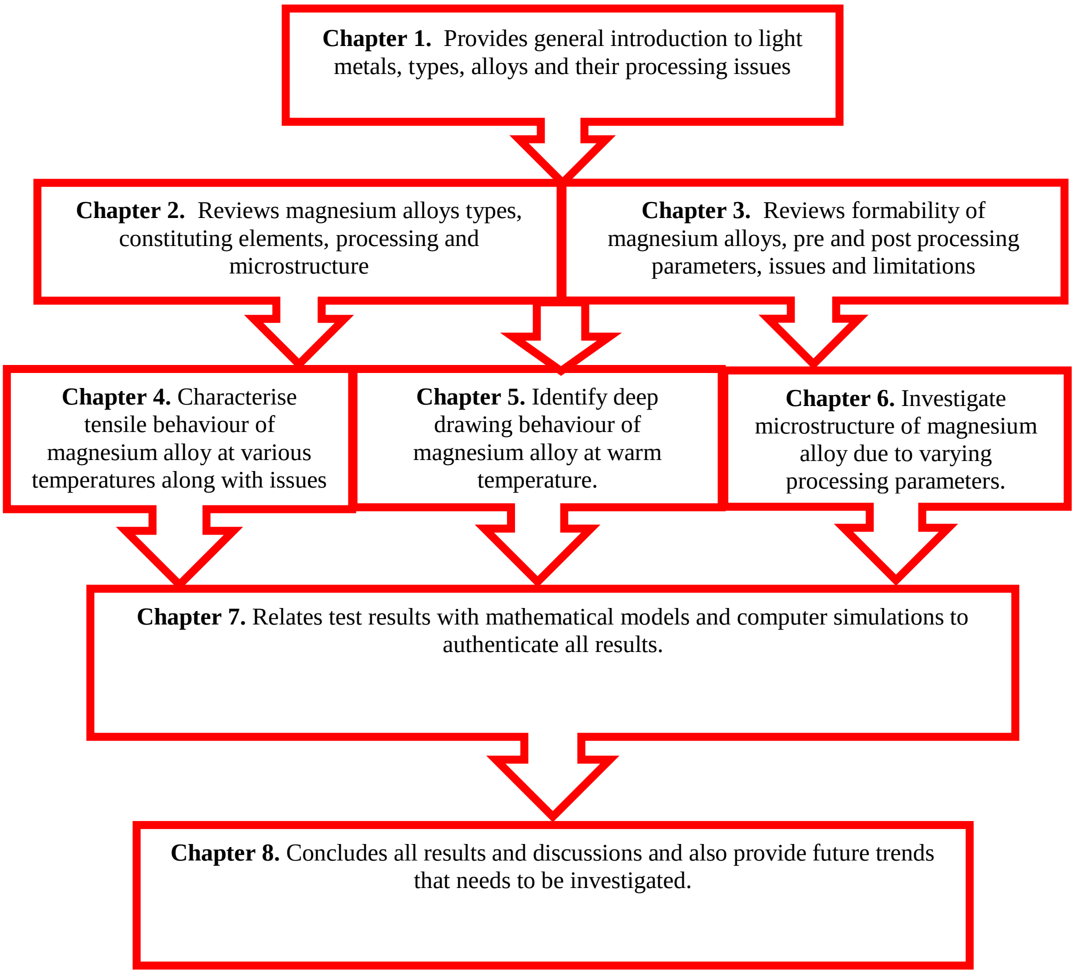

Chapter 1. Provides general introduction to light metals, types, alloys and their processing issues

Chapter 2. Reviews magnesium alloys types, constituting elements, processing and microstructure

Chapter 3. Reviews formability of magnesium alloys, pre and post processing parameters, issues and limitations

Chapter 4. Characterise tensile behaviour of magnesium alloy at various temperatures along with issues

Chapter 5. Identify deep drawing behaviour of magnesium alloy at warm temperature.

Chapter 6. Investigate microstructure of magnesium alloy due to varying processing parameters.

Chapter 7. Relates test results with mathematical models and computer simulations to authenticate all results.

Chapter 8. Concludes all results and discussions and also provide future trends that needs to be investigated.

Figure 5. Dissertation layout

Chapter 2

Characteristics and Properties of Magnesium Alloys

2.1 Magnesium Alloys

Magnesium, with its atomic number 12, belongs to the family of alkaline earth metals. It possesses a hexagonal close packed (HCP) crystal system. A unit cell of magnesium can be divided into layers 1, 2 and 3 as shown in Figure 6 [44].

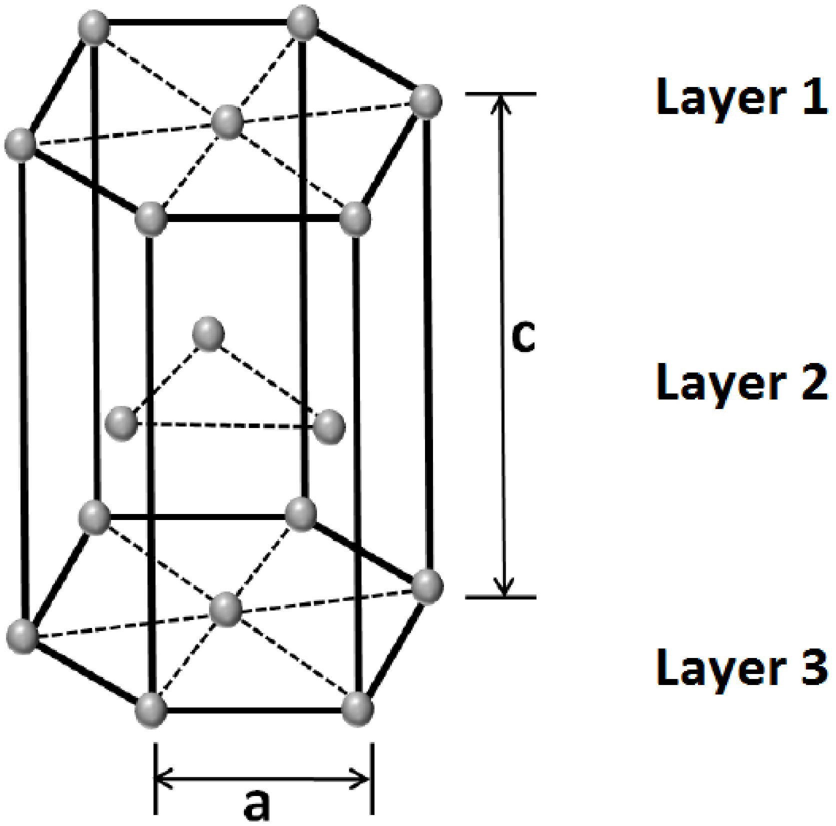

Figure 6. HCP crystal structure illustrating three layers and lattice parameters [44]

The unit crystal cell of magnesium is shown in combinations of layers as 1-2 and 2-1. Lattice parameters can be related as $a \neq c$ with c/a ratio equal to 1.622, which is quite near to the ideal c/a ratio of 1.633. This ratio of c/a plays a key role in determining the sensitivity of materials to texture. Metals with a c/a ratio higher than the ideal value of HCP crystals such as cadmium (with c/a=1.887) and zinc (with c/a=1.857), reveal a slanting of basal planes towards the rolling direction ranging from $\pm 15^0$ to $\pm 25^0$ on a rolled surface. However, on metals with c/a ratios lower than the ideal HCP c/a ratio, such as magnesium and titanium, show breaching of basal planes in transverse directions [45].

For structural applications in aerospace and outer-space components, magnesium alloys are the material of choice because they show the least density of all commercially used structural materials [46]. In addition, magnesium has better damping characteristics than aluminium. This highlights the great weight-saving potential promised by the metal (and its alloys), if it can be effectively and productively utilised in particular areas [47].

Because of its low density, it is commonly used in thicker sections so that bulky stiffening can be eliminated. To further simplify its manufacture, different variations have been produced in material properties and forming parameters [48] - [49]. The attractive features of magnesium are its high specific strength, high corrosion resistance and good damping capacity.

These features make this a very suitable choice for automotive and other structural applications [50]-[52].

The main hindrance to its usage is the hexagonal close packed (HCP) crystal system with a limited number of operative slip systems, and thus cold-forming of magnesium alloys is restricted to small deformations with a generous bend radius. To improve its workability, elements are added to make it comparable with other structural elements used in the sheet metal industry. Alloying elements are beneficial for hot extrusion and hot rolling, which are the most popular techniques for producing commercial magnesium sheets, plates and rods [53]-[54].

2.2 Classification and designations

In material selection and designation, specific standards need to be established for uniformity in testing and recording of results. The two most common classifications for magnesium alloys are wrought alloys and cast alloys.

ASTM (American Society for Testing Materials) is the most common standard used for designations of magnesium alloys [55]. The designation for magnesium alloys is a combination of two letters and two numbers. The first two letters refer to the constituent elements and the last two numbers indicate their alloying percentage by weight (% wt.). Letter codes for constituent elements are given, along with examples in Table 1. All the alloying elements are rounded to whole numbers for simplification reasons [56].

Table 1. Designated letters for alloying elements in magnesium [56]

Designated Letters	Alloy Name	Example
A	Aluminium	AZ31, AZ80
C	Copper	ZC63
E	Rare earth	ZE10, EQ21
H	Thorium	HK31
K	Zirconium	ZK40, ZK60
L	Lithium	LA141
M	Manganese	AM20, AM50
Q	Silver	QE22
S	Silicon	AS41
W	Yttrium	WE43, WE54
Z	Zinc	ZK51, ZK61

In addition to the above mentioned designation system, there are more letters often used in designating magnesium alloys. Sometimes the letters A,B, C, D and E are added to the end of an alloy designation, for example AZ31A (with 0.3% by wt. calcium), AZ31B (with 0.4% by wt. calcium), AZ31C (with 0.1% by wt. copper), AZ31D (with <0.01Si) and AZ31E (with 0.28% by wt. manganese, 0.0007% by wt. nickel and 0.0001% by wt. beryllium) [57]- [59].

The last component of the designation system is related to the heat treatment of magnesium alloys. Designations such as F, O, T4, T6 and H23 are used to represent heat treatment of material. A detailed list of various heat treatment designations is given in Table 2 [60].

Table 2. Various heat treatment designations [56]

Heat treatment Designations	Description
F	As fabricated
O	Annealed and recrystallised
T	Heat treated for stability
T2	Cooled from elevated temperature
T3	Solution heat treated and cold worked
T4	Solution heat treated
T5	Artificially aged only
T6	Solution heat treated and artificially aged
T7	Solution heat treated and stabilised
T8	Solution heat treated, cold worked and artificially aged
T9	Solution heat treated, artificially aged and cold worked
T10	Artificially aged
H	Strain hardened (wrought products only)
H1	Strain hardened only
H2	Strain hardened and partially annealed
H3	Strain hardened and stabilised
W	Solution heat treated to produce stable tempers

2.2.1 Cast magnesium alloys

Cast magnesium alloys have been in use for a few decades, reflecting the growing demand for lightweight materials in vehicles. The dominant use of magnesium alloys is in the form of cast alloys, and the most common process used for shaping is hot chamber die casting. Magnesium cast alloys were first commercially used by Professor Porsche in the Volkswagen beetle at the Institut fuer Maschinenlemente, Stuttgart [61].

Magnesium cast alloys became very popular because of their mechanical properties, which were quite comparable with aluminium and steel alloys, surface finish, ease of productivity and fine grain structure for large elongations [62].

With respect to overall usage, the main consumption of magnesium alloys is as constituent elements in various aluminium alloys. Only 36 percent of magnesium is used as die cast magnesium alloys and only 2 percent of that is used as wrought magnesium alloys, as shown in Figure 7 [63].

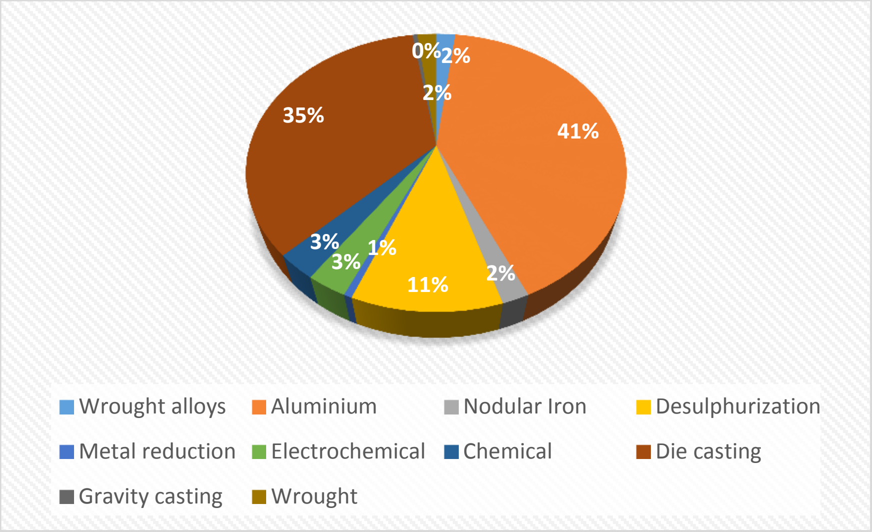

Figure 7. Distribution of consumption of raw magnesium until 2010 [63]

This distribution emphasises that magnesium alloys need a lot of focus to increase their use in various fields, where it can compete with aluminium-and steel-based metals on mechanical properties.

Die cast alloys of magnesium have various applications in the automotive industry, electronic devices and household appliances. A number of applications of magnesium cast alloys are shown in Figure 8 [64]. Some common applications in the automotive industry include engine heads and foundations, inlet and exhaust manifolds, transmission covers, wheel rims, valve covers and pistons. In addition to that the sand casting and permanent mould casting are also employed as casting processes for the production of engine blocks and alloy wheel rims.

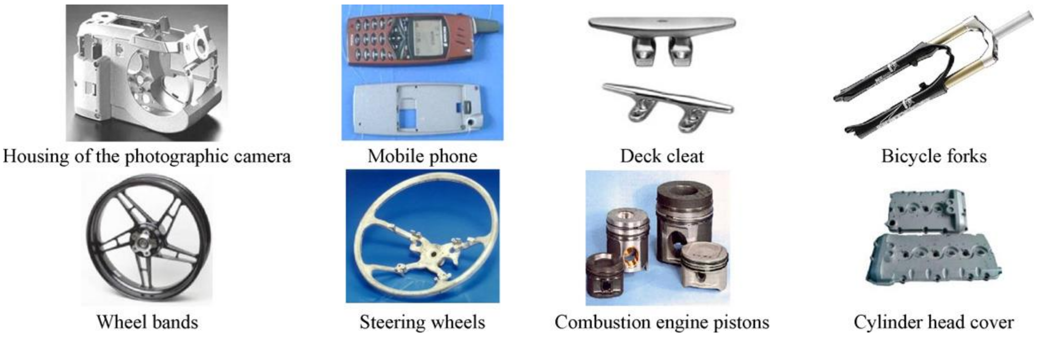
Housing of the photographic camera
Mobile phone
Deck cleat
Bicycle forks
Wheel bands
Steering wheels
Combustion engine pistons
Cylinder head cover

Figure 8. Various applications of magnesium cast alloys [64]

However, due to less accuracy than the die cast process, these processes are not so widely applied [65].

The most frequent families of alloys used for magnesium cast alloys are aluminium - zinc - manganese (AZ family), aluminium – silicon – manganese (AS family) and aluminium manganese (AM family). The AZ family is one of the most used magnesium alloys series. AZ91 is predominantly used as a cast alloy because of the increased aluminium content which provides adequate level of strength, better castability and an acceptable resistance to corrosion [66]. It is widely used in automobile parts, housings and covers, cell phones, laptops and household equipment. From the AM family, AM50 and AM60 are frequently used for commercial applications. They appear in vehicle seat frames, instrument panels, dash boards and steering wheels, due to their strength and castability [67]. AS alloys are well known for their increased creep properties. This resistance can only be maintained in a moderate temperature range that is less than 160^0C [68]. The most popular alloys are AS21, AS41 and AE42.

The properties of cast alloys can be categorised with respect to variations in microstructure. Electrical and thermal properties are less sensitive to microstructural arrangements of atoms than mechanical properties. Mechanical properties of cast alloys are reliant on the solubility of constituent elements.

The softening process of these intermetallics start from 150 - 170^0C [68] - [69]. These intermetallics abate the ability of cast alloys to exhibit long elongations before failures, ultimately decreasing the ductility of alloys. $Mg_{17}Al_{12}$ is mostly patterned at grain boundaries and provides hindrances to the sliding of grains and slippage of planes [70]. The physical and mechanical properties of a few cast magnesium alloys are listed in Table 3 and 4.

Table 3. Mechanical properties of cast alloys at room temperature

Alloy	**Ultimate strength (N/mm^2)**	**Yield Strength (N/mm^2)**	**Maximum Elongation (%)**	**Reference**
AE42	240	155	12	61
AM20	200	80	21	65
AM50	240	135	17	65
AM60	255	140	14	65
AZ91	260	140	7	63
AS21	230	110	14	70
WE43	260	165	5	71
WE54	240	150	7	72

Table 4. Physical properties of cast alloys at room temperature

Alloy	**Thermal Conductivity (W/m.K)**	**Coefficient of thermal expansion [20 – 200^{0}C] x 10-6 (K-1)**	**Electrical resistivity (n.Ω . m)**	**Specific heat capacity x 1000 (J.kg-1.K-1)**	**Reference**
AE42	83	26.8	133	1	63
AM20	94	26	155	1	65
AM50	61	26	148	1	65
AM60	65	26	148	1	65
AZ91	84	26.3	144	1	63
AS21	84	26.1	180	1	73
WE43	51	25.4	170	0.96	74
WE54	50	27.1	150	0.96	75

2.2.2 Wrought magnesium alloys

Wrought magnesium alloys had less attention in previous decades than cast magnesium alloys, due to having only moderate deformation capabilities at room temperature.

Their relative significance in practical applications is manifest in the fact that only 3 – 5 percent of pure magnesium is now consumed in the preparation of wrought products out of the total usage of magnesium [76]. Figure 9 indicates that wrought alloys have better mechanical properties than cast alloys in terms of strength and elongations. Where $Rp_{0.2}$ is proof stress at 0.2% strain and A5 is elongation symbol in DIN 50145. Guage length = $5.56x\sqrt{A_0}$, where A_0 is the original cross-sectional area.

Nevertheless, wrought alloys require extensive attention to increase their use in commercial products and make them an alternative to aluminium and steel, not to mention polymeric materials.

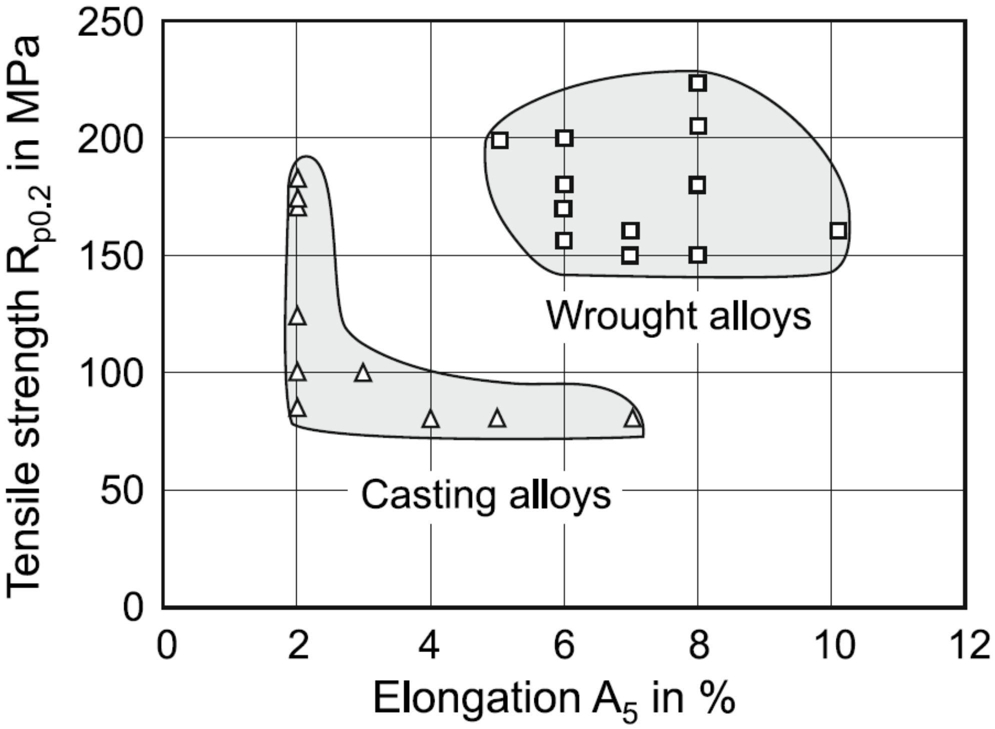

Figure 9. Comparison of cast and wrought alloys [77]

To highlight their characteristics, a detailed study would be required on deformation behaviour, process parameters and operating conditions such as temperature [77]. Typical wrought magnesium alloy products include extrusions, plates and rolled sheets, which can be further utilised in the form of tubes, rods, bars and sheets. Furthermore, their use can be extended to vehicle chassis, interior and exterior panels, and internal pillars and stiffeners by enhancing its mechanical properties and corrosion resistance [78].

In wrought alloys, the HCP structure plays a key role in limiting their use as a commercial wrought alloy. Less availability of slip systems is the main hindrance during room temperature deformation. Intermetallic particles are formed at various temperatures between alloying elements in different alloys of magnesium. This explains why, during thermo-mechanical treatments, premature melting and hot cracking often occurred [79 – 80].

There are several series used for wrought alloys. The most common series commercially applied is aluminium, zinc and manganese, with a combination of some other minor elements as well. The reason for being the most common is the presence of aluminium as the major alloying constituent, which makes a very high strength alloy. Some of the common alloys found as wrought alloys are given in Table 5.

Besides all these common families there are several other families used in industry. The first ones are magnesium – zinc – zirconium alloys (ZK30, ZK40 and ZK60). Zirconium is a sublimating ingredient that constitutes a strong and stable compound with silicon, iron and carbon. Zirconium’s solubility varies from 0.3 to 4% by mass, varying from room temperature to melting point (650^0C) [81].

The second family is magnesium - zinc - rare earth alloys (ZE10, AE42, ZK10, ZEK100 and ZEK410). Rare earth alloys are mostly used for improved creep resistance, but have low values of tensile and yield strength. Reason for having less yield and tensile strength is the absence of aluminium.

Table 5. Physical properties of common wrought alloys at room temperature [80]

Alloy	**Ultimate strength (N/mm^2)**	**Yield Strength (N/mm^2)**	**Maximum Elongation (%)**
AZ31	260	130	13
AZ61	280	195	10
AZ105	295	200	11
ZK30	320	210	9
ZK60	315	240	8
WE43	270	160	6
WE54	290	185	6

Common rare earth elements include cerium (Ce), neodymium (Nd), yttrium (Y), and praseodymium (Pr). Amongst these, yttrium has maximum solubility and cerium has the lowest solubility in magnesium [82]. Due to variations in solubility, different precipitates form along grain boundaries of rare earth magnesium alloys.

The addition of various rare earth elements to alloys is still an area of active research. The effect of rare earth alloys on the texture of magnesium alloys was studied by Ball and Pragnell [82]. In most of the rare earth elements-based rolled magnesium sheets, basal plane slip is more sensitive to transverse direction than rolling direction. Sen and Agnew [83] highlight the role of shear bands in rare earth magnesium alloy deformation.

Lithium alloys are mostly known as low density alloys. The density of these alloys becomes as low as 0.54 g/cm3. The solubility of lithium varies from 3 percent to 7 percent in magnesium [84].

2.3 Role and influences of alloying constituents

The alloying of various elements is the usual approach to upgrading the mechanical and physical properties of elements. Atomic diameter plays a vital role in the alloying of different elements. Magnesium, with a 0.32nm diameter, encourages its solution with several other elements. One of the main alloying elements is aluminium, with a 0.282nm diameter and a minor variation of approximately 13% [86]. This similarity is why aluminium is the major constituent in magnesium alloys, to provide strength. Zinc is the second most common alloying constituent, with a 0.76nm diameter [87]. This study is based on AZ alloys that are commercially used in the sheet metal industry predominantly.

2.3.1 Aluminium

As mentioned earlier, aluminium is the most preferable alloying constituent for magnesium, providing enhancement in strength and improving hardness and castability [68]. In cast magnesium alloys, an increased aluminium content will boost fluidity and augment the casting process.

In contrast, the freezing point of alloys will ultimately increase with the rise in aluminium content, thus the occurrence of shrinkage and porosity will also multiply. This is why the maximum content of aluminium in magnesium is limited to 12 percent [69].

Corrosion resistance in magnesium also improves with increased aluminium content. Usually, an 8 – 10 percent of aluminium content is enough to make magnesium alloys reasonably corrosion-resistant [70].

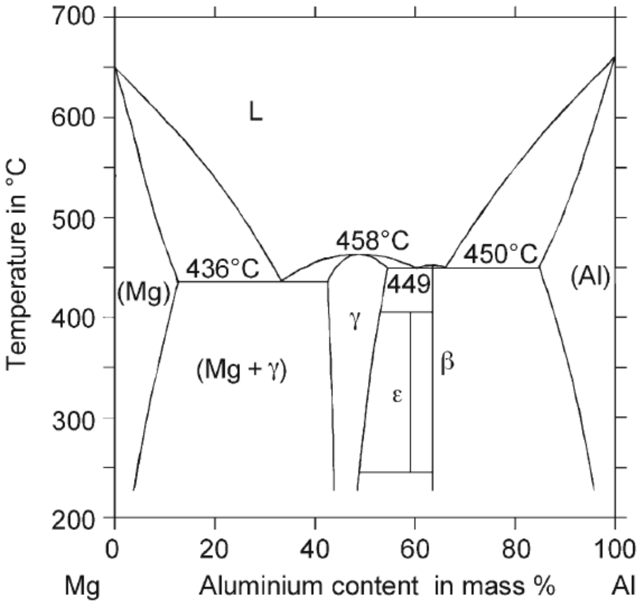

Figure 10. Binary phase diagram of aluminium and magnesium [68]

The solubility of aluminium in magnesium is shown in Figure 10. It is seen from the diagram that the maximum solubility of aluminium is 13 percent approximately, at the eutectic temperature of 436^0C. This solubility is reduced by 2 percent at room temperature, which results in precipitation of its brittle phase that is $Mg_{17}Al_{12}$. Precipitation hardening is commonly used to further enhance the strength of magnesium aluminium alloys, preferably with an aluminium content of more than 6 wt. % [88]. On the other hand, a discontinuous type of precipitation of γ-$Mg_{17}Al_{12}$is generated along grain boundaries, which ultimately reduces creep resistance of the alloy. Precipitation usually occurs in the form of coarse particles during aging along basal planes with a lamellar form and is a thermally unstable process [89].

2.3.2 Zinc

Zinc is the second most commonly used constituent in magnesium alloys. Its key role is to improve room-temperature strength of the alloy. It also boosts fluidity during casting. Another factor affecting material grain structure is critical resolved shear stress (CRSS). It is a state of stress where a material’s dislocations will start to change its position and shape after achieving a certain amount of shear stress. It increases CRSS along basal planes and decreases it along prismatic planes. Both of these effects on CRSS improve ductility and strength, mainly at room temperature. The addition of zinc is restricted to 0.5 – 2.0 percent or in other words, the total combination of aluminium and zinc should be less than or equal to 10 percent due to chances of occurrence of hot cracking [90]. Hot cracking usually decreases the ductility limit of alloys and also plays a role in the formation of γ-$Mg_{17}Al_{12,}$ which results in the formation of discontinuous precipitates along grain boundaries, as discussed in section 1.2. The influence of temperature on zinc content in magnesium alloys is shown in Figure 11. Zinc along with aluminium, refines precipitates and also facilitates overcoming corrosion, which could be increased due to the presence of iron (Fe) and nickel (Ni) [91].

Three zinc-enriched alloys are most commonly used, ZA124, ZA102 and ZA88. These alloys provide excellent results in terms of increased creep resistance and corrosion resistance because of having no γ-$Mg_{17}Al_{12}$ phase development [92]. These alloys are mainly produced for casting purposes to overcome the poor creep resistance provided by AZ91, which is the most commercially used alloy in die cast products.

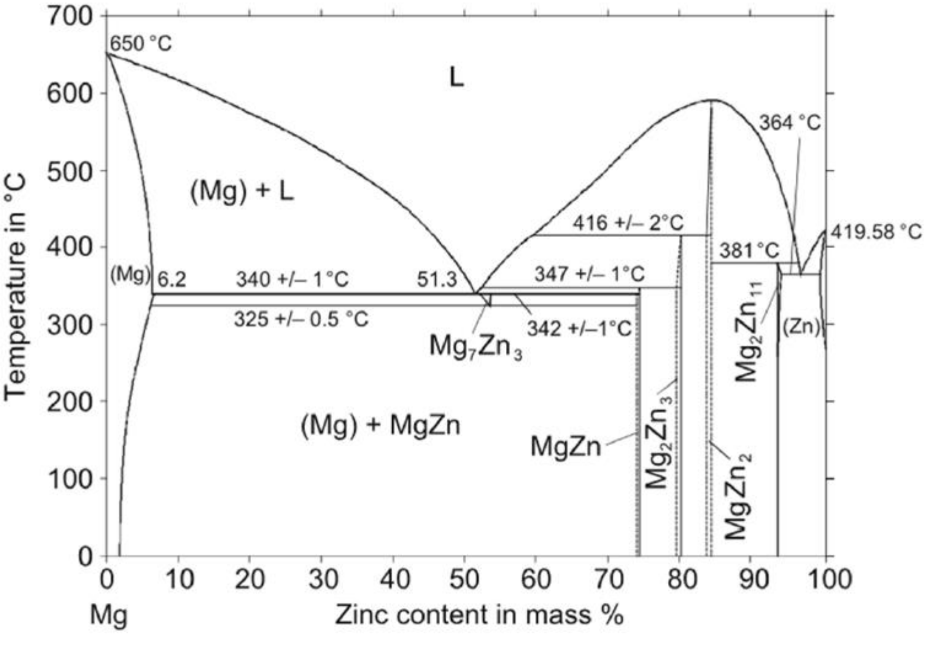

Figure 11. Phase diagram of zinc and magnesium [90]

2.3.3 Manganese

Manganese is usually added to increase corrosion resistance in magnesium alloys. Maximum solubility of manganese varies in different magnesium alloys, as shown in Figure 12.

Manganese forms coarse intermetallics with different types of impurity that can exist in magnesium alloys such as iron [93]. The average rate of pure magnesium corrosion is 10 mm/year; however, this rate doubles when magnesium alloys possess Fe particles, usually at above 45 weight ppm [94].

Manganese offers help in removing these impurities from magnesium to a certain extent, which ultimately results in an increase in corrosion resistance mainly against salt water and also improves yield strength to a minor extent [95]. The weight ratio for Fe/Mn varies from 0.01 – 0.032. If the Fe/Mn ratio is greater than this, there will be a sharp increase in corrosion of magnesium alloys.

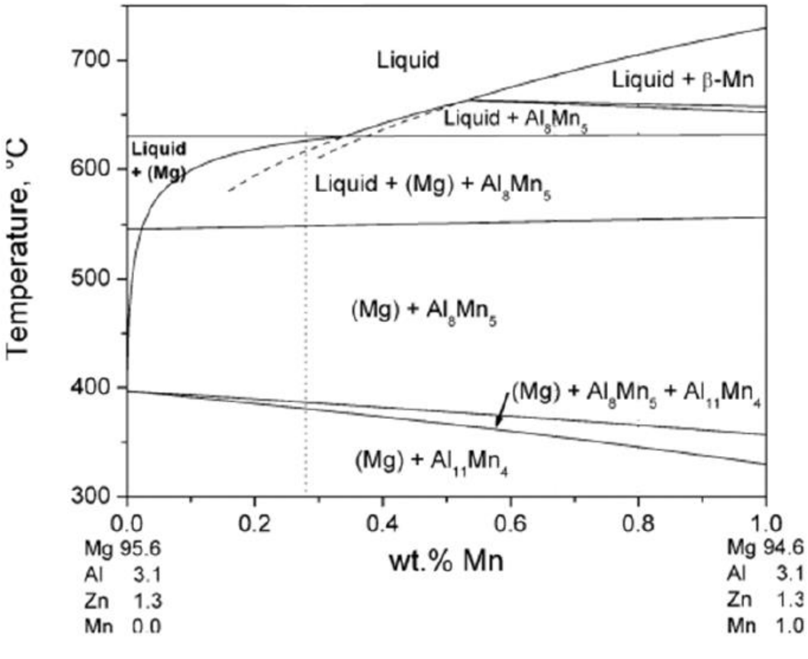

Figure 12. Phase diagram of manganese and magnesium [93]

In magnesium alloys, when manganese is combined with aluminium, it produces different precipitates, that is, MnAl, $MnAl_2$ and Mn_5Al_8. Any Fe particles will usually act as cathodes and these precipitates act as a passive phase, which ultimately results in high corrosion [96].

Figure 13 shows phases of manganese that vary with temperature in rich magnesium alloys.

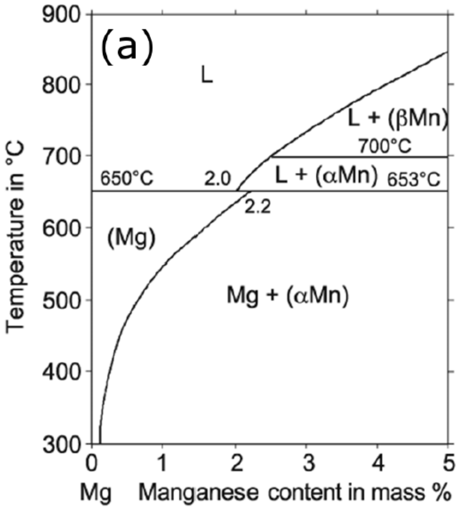

Figure 13. Phase diagram of magnesium with manganese content of up to 5% mass [93]

2.4 Deformation theories for HCP materials

Deformation in HCP metals is reduced when compared with other cubic metals, due to fewer available slip systems at room temperature. However, activation of additional slip systems at increased temperatures allows large elongations and makes them comparable with other cubic metals [30]. The deformation system involves slip, twinning, grain boundary sliding and cavitation.

2.4.1 Slip

Slip is a deformation process in which a drift of planes occurs along supportive crystallographic planes.

Slip is usually associated with migration of dislocations along crystallographic directions. This migration of dislocations frequently occurs in planes with maximum atomic compactness or density [97]. Blending of slip directions and slip planes is designated a slip system.

The slip system of a HCP crystal is categorised in various ways, i.e. basal slip, pyramidal slip and prismatic slip or basal and non-basal slip or primary, secondary and tertiary slip systems. Primary slip is assigned to the basal slip which is comprised of the (0001) basal plane and the <1120> burger vector's direction, and is particularly effective at room temperature [98].

The reason behind an initiation of a slip on the basal plane is its high atomic density, which is dependent on a minimum shear stress which develops due to an applied load. The amount of minimum shear stress required to activate any slip system is termed a critical resolved shear stress (CRSS).

CRSS plays a key role in activation of basal as well as non-basal slip systems, however, much less attention is given to this factor in the literature. Its role in the deformation process at room temperature as well as at elevated temperatures is not widely comprehended. Understanding the slip system is important because according to the von Mises principle of homogeneous deformation, five independent slip systems are necessary to produce a uniform deformation in any shape-changing process [99]. These five independent slip systems represent five components of the strain tensor out of six components (i.e. three normal and three shear strain components).

From Figure 14 it can be seen that deformation initiates with the basal slip system (0001) <1120>, which contributes two independent slip systems arrayed in three patterns, however, to satisfy the von Mises criterion two more independent slip systems are still required. With the further addition of load, prismatic slip (1010) <1120> triggers a fourth independent slip system parallel to the < c > axis in < a > direction. Later with the addition of first order pyramidal slip (1011) <1120> along the < a > axis, the requirement for a homogeneous deformation is completed. A second order pyramidal slip (1122) <1122> also takes part in deformation at a high value of CRSS [99]. All these slip systems vary according to the value of CRSS.

The critical resolved shear stress is heavily dependent on temperature. In Figure 15 various slip systems CRSS values are compared with varying temperature. It is quite clear that beyond 200^{0}C there is a sudden drop in values of CRSS. This suggests poor formability of magnesium alloys at room temperature [100].

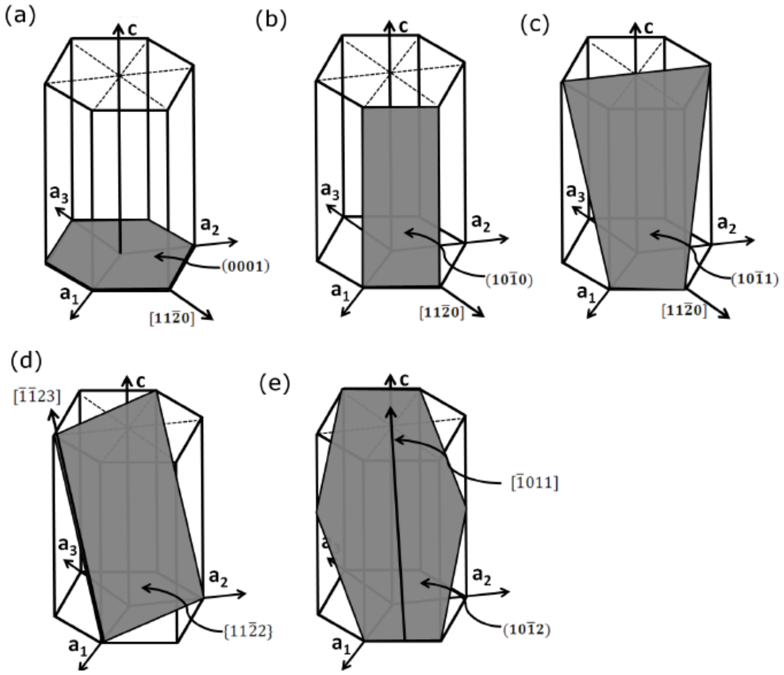
(a)
c
a$_3$
a$_2$
a$_1$
(0001)
[11$\bar{2}$0]
(b)
c
a$_3$
a$_2$
a$_1$
(10$\bar{1}$0)
[11$\bar{2}$0]
(c)
c
a$_3$
a$_2$
a$_1$
(10$\bar{1}$1)
[11$\bar{2}$0]
(d)
[$\bar{1}\bar{1}$23]
c
a$_3$
a$_2$
a$_1$
{11$\bar{2}$2}
(e)
c
[$\bar{1}$011]
a$_2$
a$_1$
(10$\bar{1}$2)

Figure 14. HCP crystals with various slip systems, (a) basal, (b) prismatic, (c) first order pyramidal, (d) second order pyramidal, and (e) tension twinning [98]

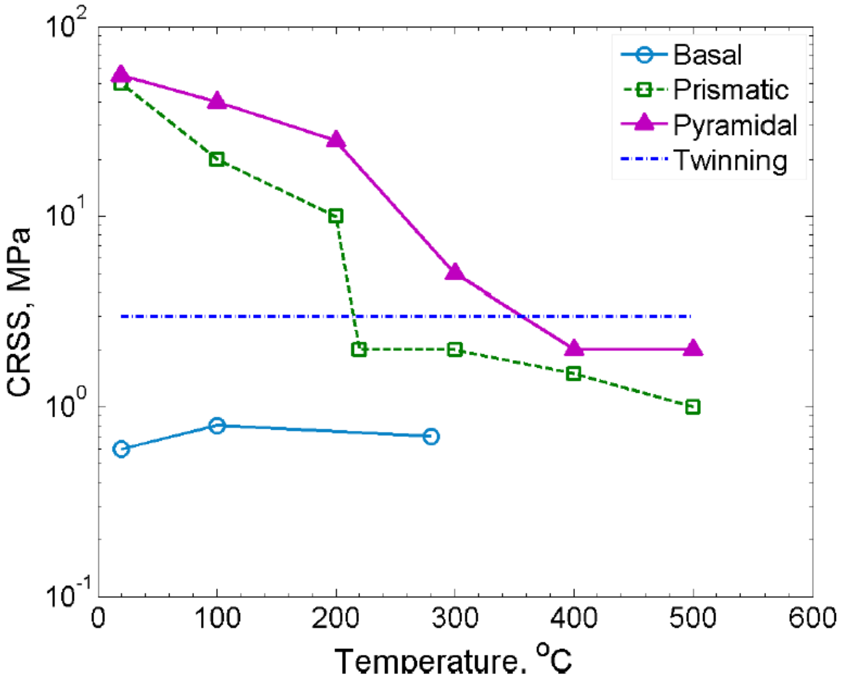

Figure 15. Variation in CRSS with respect to temperature for various slip systems [100]

To attain reasonable elongation, magnesium alloys are formed at elevated temperatures where twinning, grain boundary sliding and cavitation takes place as discussed later.

Basal slip normally activates at a CRSS value of 0.3 – 0.5MPa, however, other slip systems may reach values of 40MPa to trigger a slip system. A detailed list of all slip systems and their required CRSS values are given in Table 6.

The Burger vector plays an indispensable role in the deformation process. To accommodate deformation in the <c> axis during rolling directions a burger vector in that direction is compulsory. It is quite clear from Table 6 that only a second-order pyramidal slip can provide that deformation. As the CRSS value for the second-order pyramidal slip system is quite high, so it cannot be initiated at room temperature. In addition, the first-order pyramidal slip accommodates four independent slip systems that are the same as when we combine basal and prismatic slip systems.

Even the second-order pyramidal slip system provides five independent slip systems, but with the highest CRSS value. In summary, at room temperature only the basal slip system can be activated with only two independent slip systems not sufficient for homogeneous deformation. This is why magnesium alloys are processed at higher temperatures.

Table 6. Various slip systems and their CRSS values at room temperature [99]

Type of slip	Burger's vector direction	Total number of slip systems	Independent slip systems	CRSS (MPa)
Basal slip	< a >	3	2	0.49

Prismatic slip	< a >	3	2	50
1st order pyramidal slip	< a >	6	4	62
2nd order pyramidal slip	< c+a >	12	5	65

2.4.2 Twinning

Twinning is another deformation mode that is available to accommodate deformation along the (parallel) c-axis. In the previous section it was stated that only the second-order pyramidal slip system provides deformation along the c axis with extremely high values of CRSS. Variations in the deformation mechanism is a function of temperature and grain size, as shown in Figure 16.

The difference between slip and twinning is that slip accommodates deformation by drifting of planes and it occurs along supportive crystallographic planes, while in twinning, deformation is accommodated by reorientation of deformed portions with un-deformed ones [101]. Twinning mostly occurs from room temperature to warm temperature at coarse grain sizes, where the deformation process cannot be completed with the basal slip system only [102].

Twins are specific locations, where extension and contraction of grains is accommodated along the c axis via reorientation of crystals. There have been seven types of twin system identified by various researchers, out of which three types of twins occur mostly in magnesium alloys: {1012} extension or tension twins, {1011} contraction twins and {1011} – {1012} double twins [103]. Extension twins are observed when the load is applied parallel to the c-axis, however, in contraction the twin direction of the loading is perpendicular. Extension twins are more easily activated due to a low CRSS and are mostly observed at the onset of plastic deformation, however, contraction twins appear at the last stage of deformation to relieve stress concentration from grain boundaries. Double twins occur under specific loading conditions, when a contraction twin acts as a primary twin and a tension twin as secondary. In double twinning, crystals reorient twice, which orientates the c axis parallel to the loading axis [104]. After the second twinning further reorientation of crystals is not possible, which leads the slip to activate again and will dominate deformation until failure.

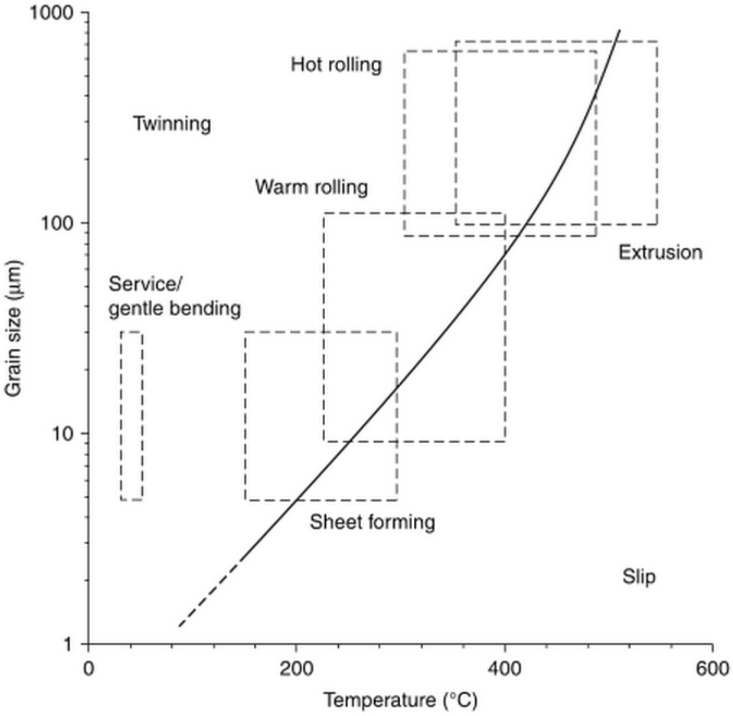

Figure 16. Twinning as function of grain size and temperature in AZ31 [102]

CRSS plays a leading role in defining the deformation mode in magnesium alloys. Extension twining usually requires a 3.5 times higher CRSS to be triggered as the dominating deformation mechanism. Barnett [105] has correlated slip and twinning modes in terms of ratios. According to him, the CRSS ratio is 1:3.5:6.5:15 for basal slip, twinning, and prismatic and pyramidal slip systems. Similarly Jonas et al. defined a ratio of 1:4.5:9:30:42 for basal, extension twinning, contraction twinning, prismatic and pyramidal slip system. The average value of CRSS starts at 2.5MPa for extension twins and will lead to 45–155 MPa for contraction twins. If we compare these values with the slip mode CRSS values given in Table 6, it will clearly indicate why extension twins are the lead deformation mode in the basal slip system [99].

Table 7. Various twinning modes along with their dislocations [106]

Type of slip		Invariants on shear Plane	Shear Direction	Rotation angle	Width	Thickness (nm)
Single twin modes	Extension Twin	{10-12}	<10-11>	86.3^0	6a	0.049
	Contraction Twin	{10-11}	<10-12>	56^0	a	0.135
Double Twin modes	I	{10-12}	<-1011>	37.5^0		
	II	{-1012}	<10-11>	30.1^0		
	IIIA	{1-102}	<-1101>	69.9^0		
	IIIB	{0-112}	<0-111>	66.5^0		
	IVA	{-1102}	<1-101>	66.5^0		
	IVB	{0-112}	<01-11>	30.1^0		

Extension and contraction twins can also be compared in terms of their rotation angle, thickness and width. Due to higher width and smaller thickness values, extension twins move more frequently than contraction twins [106]. Comparison of various twin modes is given in Table 7, along with their respective planes, directions and rotation angles.

2.5Texture development in magnesium alloys

Magnesium alloys are highly sensitive to crystallographic texture at room temperature as well as at warm temperatures (i.e. from 0^0C to 250^0C).

As commercial magnesium products are formed at warm temperatures (i.e. up to 250^0C), a clear understanding of texture influences is necessary to explain the behaviour of the material [107]. Texture is usually defined as a group of crystallographic planes arranged parallel to the rolled sheet surface or rolling direction [108].

Balance in the texture of sheets is highly recommended to produce uniform yield stress values. Kaiser et al. [109] recorded a difference of 55MPa in yield stress in transverse and longitudinal rolling directions. During rolling of magnesium sheets, grains reorient themselves by passing through various slip systems and twin modes of deformation. Pole diagrams are the conventional method for the study of variations in grain positioning and orientations, as shown in Figure 17.The most frequent type of texture appearing during hot and warm rolling is basal texture {0001} with [10-10] direction. Basal texture severely affects formability of magnesium alloys.

The shape of poles for basal texture strongly depends on temperature during the rolling process [110]. At warm temperatures, the pole shape is more likely to be oval, due to the development of contraction twins followed by re-twinning of an extension type. However, hot rolling produces a perfect distribution of planes in pole diagrams. Therefore, several efforts have been made by researchers [111] - [114] to weaken texture, which is highly recommended to increase formability of magnesium alloys.

A reduction of the effects of basal texture by a weakening process is very important for the forming behaviour of magnesium alloys. The easiest method is the addition of some alloying elements. Rare earth alloys are highly recommended as alloying constituents for minimising the basal texture effect [115].

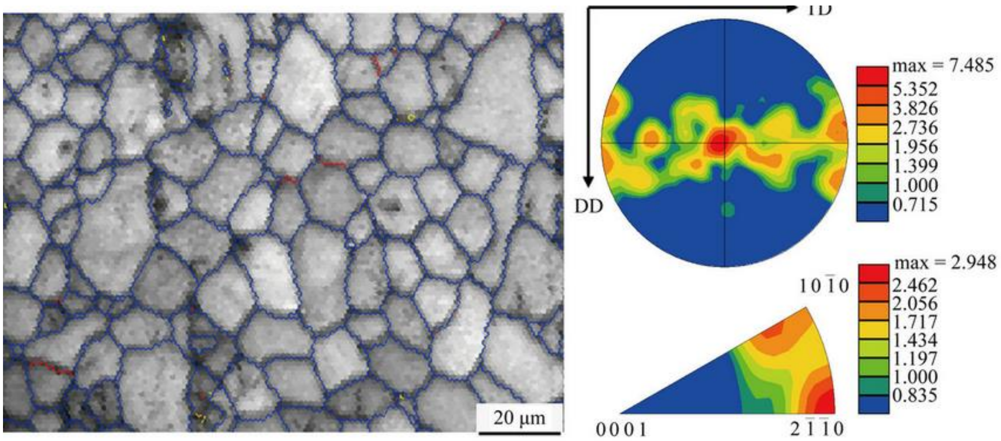

Figure 17. Microstructure of magnesium AZ31 [109]

Various rare earth elements have been suggested. Mackenzie [116] proposes the addition of Ce for magnesium lithium alloys, with a maximum lithium percentage of up to 3 percent. Barnett et al. [117] and Chino et al. [118] also focussed on the addition of Ce in pure magnesium to increase the formability of sheets. Chino et al. [118] revealed an increment in improved formability by addition of Y of up to 1.8 percent in magnesium zinc alloys. The influence of Gd and Nd was highlighted by Stanford and Hantzsche [119]. Another method is recrystallization, in which different subgrains are formed at interfaces of particles, with different orientations as compared to their parent grain. This method is known as particle stimulated nucleation (PSN) [120].

2.6 Superplasticity

Superplasticity is a mechanism for testing conditions in which large elongations can be obtained before failure. Parameters that play a key role in superplastic behaviour of materials are temperature, strain rate (test speed) and grain size. Large elongations have been reported in magnesium alloys under varying test conditions [121]. Langdon and Figueiredo [122] achieved 3040 percent elongation in ZK60 with a 0.85μm grain size at a temperature of 200^0C and a strain rate of $10^{-4}s^{-1}$.

According to Langdon [122], superplasticity is usually referred to as a condition where material undergoes at least 300 percent elongation before failure, with a strain rate sensitivity (m) equal to 0.5, and a temperature more than or equal to 50 percent of the melting temperature ($0.5T_m$). However, other studies [123]–[126] suggest that any elongation near 200 percent is seen as a superplastic behaviour.

Flow stress is the common term for defining the superplastic flow of materials. Flow stress is any stress value that is necessary to continue the plastic flow of materials [127]. Flow stress is directly proportional to grain size and inversely proportional to deformation temperatures. Flow stress also shows sigmoidal dependence, with strain rate and slope of lines indicating strain rate sensitivity (m), as shown in Figure 18. Mathematically, m can be defined as:

$$m = \ln S / \ln \dot{\varepsilon} \qquad (1)$$

Where S refers to flow stress and $\dot{\varepsilon}$ is strain rate during a test.

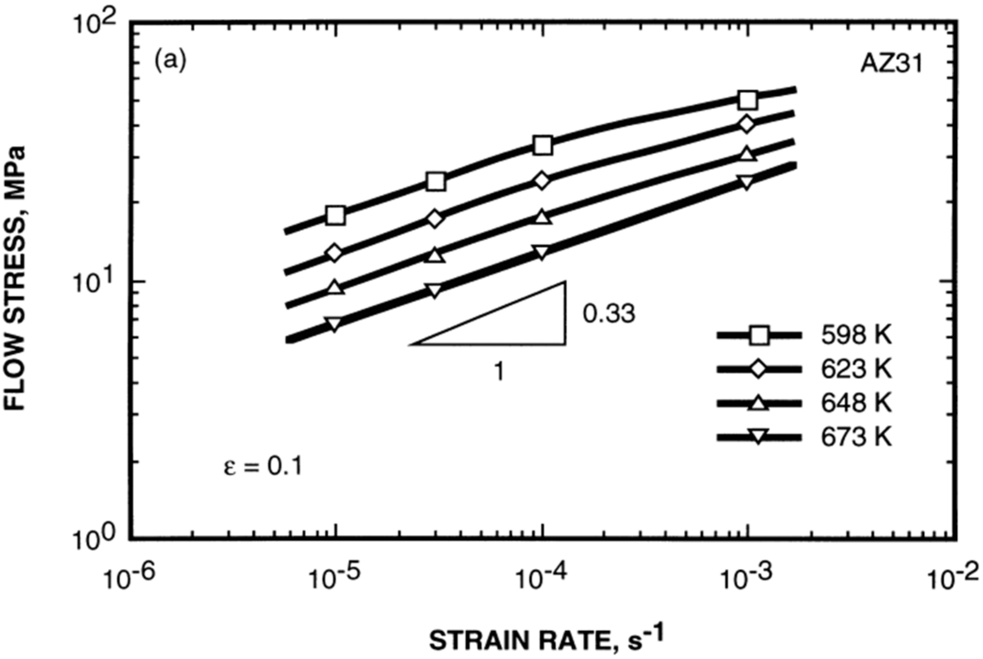

Figure 18. Sigmoidal relationship between flow stress and strain rate [127]

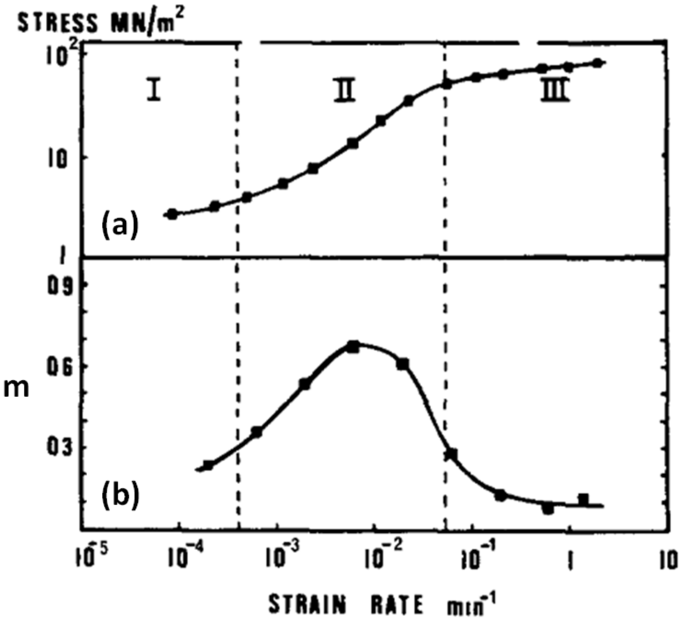

Figure 19. Superplastic behaviour of materials in various regions [128]

Based on m values and strain rate, superplastic regions were defined by Edington and Lee [128] as shown in Figure 19. The curves were divided into three regions. Region I indicate maximum m values up to 0.3, region II ranges from 0.3 to 0.7 and region III again has reduced m values.

Superplasticity is mostly observed in region II with m values above 0.5. In superplastic regions, m also strongly depends on grain size. Usually, grain sizes smaller than 10µm are preferred for perfect superplastic behaviour. Lower grain sizes minimize flow stress and ultimately increase flow rate. The relationship of grain size and strain rate was explained mathematically by Sherby and Wadsworth as:

$$\dot{\varepsilon} = d^{-n^*} \tag{2}$$

Where "d" is grain size and "n*" is grain size exponent. The grain size exponent is the slope of the line that is plotted logarithmically between strain rates with reciprocal values of grain size [129].

All three superplastic regions indicate different behaviour in the microstructure of material. In region I, there are lower values of flow stress and strain rate sensitivity is usually governed by diffusional creep. Region II is mostly dominated by grain boundary sliding. In region III, large stresses result in dislocation creep and new grain formation along grain boundaries. These changes also create various cavities at the boundaries of grains [130].

A deformation mechanism map is a common method of defining variations in governing mechanisms at the microstructure level. As explained earlier, temperature, grain size and strain rate are directly related to flow stress and ultimately decide yield strength and Young's modulus values for materials [131].

Deformation maps are drawn by considering all these factors. An example of a deformation map is Figure 20. Various regions are plotted according to deformation mechanisms, and constitutive equations are used to gain exact values for the plotting of curves. Deformation maps were initially introduced by Ashby in 1972 [132], and later Langdon [133] plotted the effects of varying grain sizes on flow stress and strain rate.

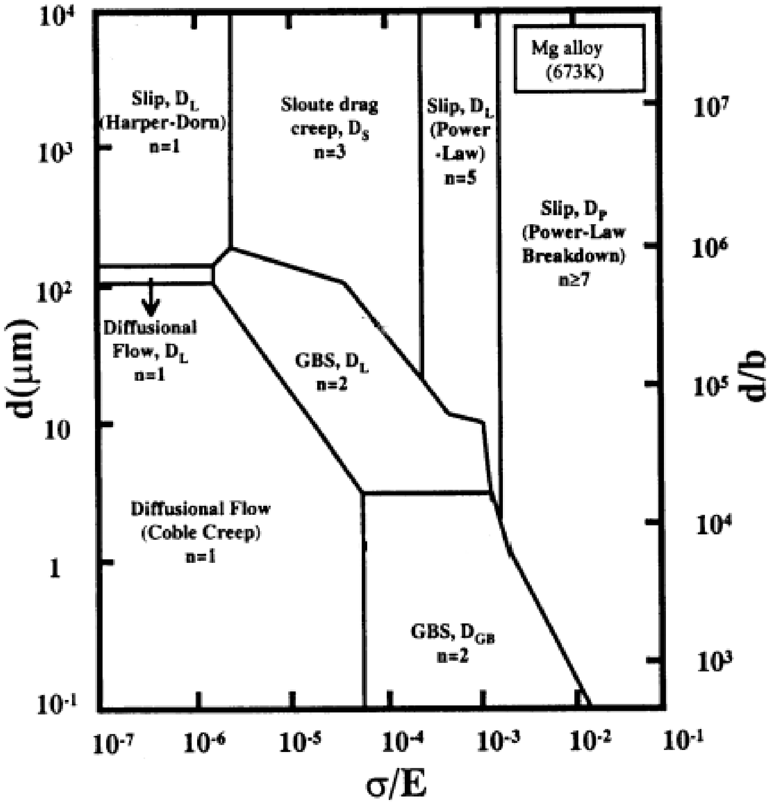

Figure 20. Deformation map of AZ31 [133]

2.7 Diffusion creep

Diffusion creep is another deformation mechanism that occurs in magnesium alloys at elevated temperatures, due to diffusion of several vacancies that develop in a material due to reorientation of grains under the application of load and temperature.

Creep strains affect materials either by dislocation creep or gliding, or by diffusional flow. Diffusional creep is a process mainly dominant in region I of superplastic flow.

In creep deformation, strains proceed due to continuous application of loads that are irreversible. In magnesium alloys, creep deformation is important when continuous loads are applied at high temperatures (close to 0.4 – $0.5T_m$), where T_m stands for melting temperature [134]. Under these conditions, creep is mostly controlled by diffusion or flow of vacancies along grain boundaries, therefore it is commonly referred to as diffusion creep or Harper Dorn creep. In addition, Nabarro-Herring and Coble are two common types of diffusional creep occurring in alloys that have a tendency to flow in a superplastic manner. The Nabarro-Herring creep is based on the volume of diffusional flow through grains, however, the Coble model is established based on the mass transport of vacancies along grain boundaries [135]. In terms of mathematical formulations, both types of diffusional creep can be described as:

For Nabarro-Herring creep

$$\dot{\varepsilon} = \mathrm{a}\,\frac{D_L}{d^2}\left(\frac{Eb^3}{kT}\right)\left(\frac{S}{E}\right) \qquad (3)$$

For Coble creep

$$\dot{\varepsilon} = \mathrm{b}\,\frac{\pi\delta D_{gb}}{d^3}\left(\frac{Eb^3}{kT}\right)\left(\frac{S}{E}\right) \qquad (4)$$

where $\dot{\varepsilon}$ is strain rate, S is flow stress, T is absolute temperature, D_L is the coefficient of lattice diffusion, D_{gb} is the coefficient of grain boundary diffusion, d is grain size, δ is grain boundary width, b is the Burger's vector, E is the modulus of elasticity, k is Boltzman constant, and a and b are material constants mainly dependant on strain rate, grain size and temperature. For magnesium alloys both constants a and b are equal to 14 [136].

Coble creep is principally dominant in fine-grain size alloys, however, Nabarro-Herring governs coarse magnesium alloys, as suggested by Lee [137]. Watanabe [138] reported that at extreme low strain rates (10^{-4} sec^{-1}) and high temperatures Coble creep is the main diffusional creep mechanism. Cao [139] highlighted Nabarro-Herring creep in magnesium lithium alloys at a temperature of 573K and a strain rate of 1.67 x 10^{-3} sec^{-1}. Srivastava [140] examined creep behaviour of AZ61 wrought alloy at a grain size of 25µm and a temperature range of 250 – 350^0C. He also verified that Coble is the dominating creep mechanism. Similar results were produced by Watanabe et al. [141] and Kim et al. [142] Watanabe explained the variation in values of strain rate sensitivity index of 0.14 at high speeds and warm temperatures, which increased to 0.25 by decreasing test speeds and increasing temperature.

Creep deformations have received less attention due to less dominancy in the overall deformation mechanism of magnesium alloys. In addition, due to high stresses and less elongation in region I, researchers mostly focus on the superplastic region governed by grain boundary sliding.

2.8 Grain boundary sliding

A mechanism by which drifting of grains occurs due to the application of load and temperature is termed grain boundary sliding or shearing (GBS). The drifting of grains mainly occurs through stress concentrations produced at the boundaries of grains via applied load and temperature. This stress concentration generates inter-granular cracks, or vacancies between grains [143]. The flow of these vacancies during GBS is accommodated or governed by diffusional creep as a secondary deformation process. GBS mainly governs deformation mechanisms in superplastic flow of materials that is in region II in Figure 19 [128]. A change in the mode of deformation from region I to region II is heavily dependent on the amount of stress, grain size, and temperature. A comparison of the GBS mechanism and diffusional creep in grains is given in Figure 21 [144].

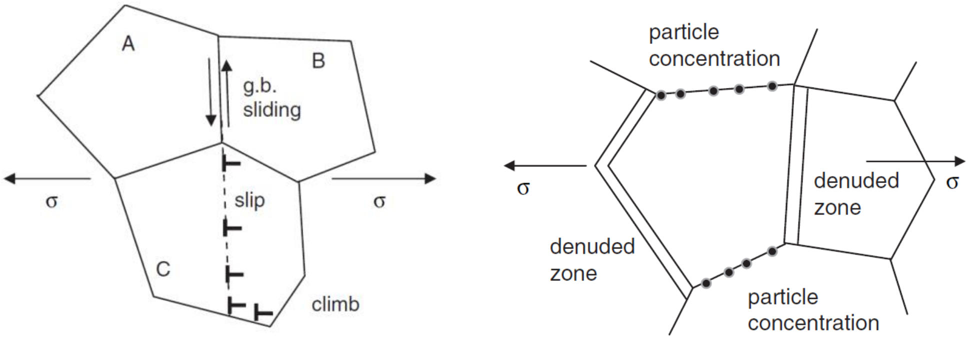

(a) (b)

Figure 21. Deformation mechanism governed by (a) GBS (b) Diffusional creep [144]

Langdon and Gifkins [145] concluded that GBS cannot occur at room temperature and rejected a model presented by Hauser et al. [146]. Hauser observed scribed lines at room temperature and at 100^0C in pure magnesium and deemed them a GBS mechanism. Langdon and Gifkins claimed that these scribed lines are the result of localisation of shear between various adjacent grains.

Several models related to GBS are presented in various research publications. Ball and Hutchison [147] proposed the first GBS model by dividing grains into various groups, and then modelled their behaviour. Later Langdon [148] presented a modified model of GBS and claimed that stress concentrations produced at a triple junction of grains changed GBS to a coupled mechanism that is always accompanied by some secondary deformation mechanism such as diffusional slip or dislocation slip. Mukherjee [149] highlights the role of ledges in GBS. He modified Ball and Hutchison's GBS model and suggested that dislocations generated via movement of grains will accumulate on opposite sides of other grains and block further movement of grains. Gifkins [150] proposed a new constitutive model by further modifying Mukherjee's GBS equation. According to him, dislocations that accumulate on grain boundaries restrict movement of grains to penetrate other grains, and later with the further addition of load they can glide or climb into grain boundaries to rotate whole grains and generate new grain boundaries. A summary of various GBS models is given in Table 8.

It is quite clear that in superplastic deformations GBS is the dominating deformation mechanism that is accompanied by various types of accommodating mechanisms which act as secondary deformation mechanisms just like diffusional creep or dislocation creep. Various models have been proposed to predict the behaviour of GBS mechanisms by calculating the optimum strain rates at which deformation mechanisms switch from twinning and slip to GBS, but it is still a point of discussion. Certainly much more work is required to verify these models for the exact prediction of parameters during high temperature tests.

Table 8. Summary of different grain boundary sliding models

Reference	Equation	Remarks
Ball and Hutchison [147]	$έ = K_1 (b/d)^2 D_{gb} (б/E)^2$	Sliding group of grains
Langdon [148]	$έ = K_2 (b/d)^2 D_L (б/E)^2$	Dislocation movement near grain boundary
Mukherjee [149]	$έ = K_3 (b/d)^2 D_{gb} (б/E)^2$	Individual grain slide
Gifkins [150]	$έ = K_5 (b/d)^2 D_{gb} (б/E)^2$	Accumulation occurs at triple point
Hayden et. al. [151]	$έ = K_4 (b/d)^2 D_p (б/E)^2$	Grain boundary's sliding rate is controlled by slip
Gittus [152]	$έ = K_6 (b/d)^2 D_{IPB} \{(б - б_0) /E\}^2$ $έ = K_7 (b/d)^2 D_L (б/E)^2$	Accumulation occurs at inter-phase boundary
Arieli-Mukherjee [153]	$έ = K_8 (b/d)^2 D_{gb} (б/E)^2$	Individual dislocation climb
Sherby-Wadsworth [154]	$έ = 6x10^8 (b/d)^3 (D_{gb}/b^2) (б/E)^2$ $έ = 2x10^9 (b/d)^2 (D_L/b^2) (б/E)^2$	$T = 0.4 - 0.6 T_m$
Kaibyshev et al. [155]	$έ = (A/k_9T) (b/d)^2 \{(б - б_0) /G\}^2$	Recovery and hardening behaviour of dislocations at GBS
Fukuyo et al. [156]	$έ = K_{10} (b/d)^2 D_{chem} (б/E)^2$	Accommodation of GBS via dislocation climb

Where, K_1 to K_{10} are material constants, T is temperature, $Ϭ_0$ is threshold stress, D_{gb} is grain boundary diffusivity, D_L is lattice diffusivity, D_p is dislocation pipe, D_{chem} is chemical diffusivity and D_{IPB} is interfacial phase boundary.

2.9 Recrystallisation in magnesium alloys

Recrystallisation is a process by which texture and grain size can be controlled. In refinement of grains during a rolling process, energy is stored inside materials and is relieved through migration of boundaries, and this is termed recrystallisation. When alloys are subjected to large deformations, recrystallisation occurs and this is termed dynamic recrystallisation (DRX). A simple model for DRX is shown in Figure 22 [157].

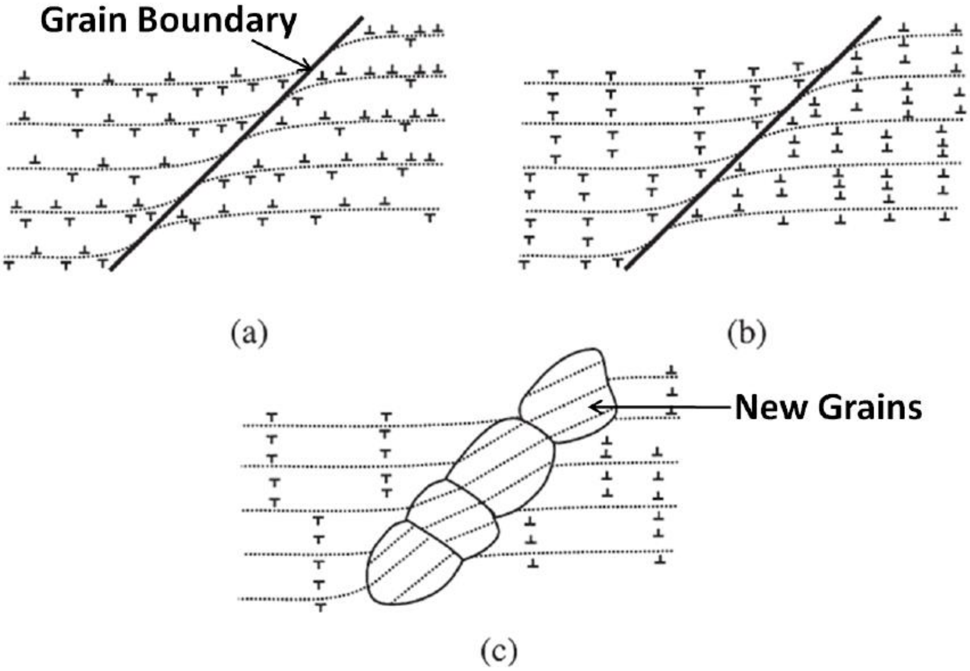

Figure 22. Dynamic recrystallisation model in magnesium alloys [157]

2.10 Grain growth

Grain growth is an important factor in high temperature deformations. Two types of grain growth occur in magnesium alloys. The first type of growth is static grain growth (SGG), which is mainly due to annealing of material at a certain temperature, inside or outside of a testing machine.

The second type of grain growth is dynamic grain growth, which occurs due to continuous strain being produced in a material with the application of load, and temperature [158]. This latter type is mostly important in magnesium alloys, as they are mostly formed at high temperature and subject to large strains.

The importance of dynamic grain growth is highlighted by many observations of researchers.

Bate [159] suggests that dynamic grain growth also acts as a secondary deformation mechanism during GBS, and in migration of grain boundaries due to dislocation creep. Clarke [160] relates the hardening behaviour of material during deformation with dynamic grain growth and points to it as the main reason for hardening of material.

Grain growth in magnesium alloys is also dependent on process parameters. Strain rate, temperature and grain size play a leading role in the amount of growth during deformation.

2.11 Cavitation

After the deformation phase, the last stage is failure. Failure in magnesium alloys can occur in two ways. One is necking, which results from plastic flow (usually in an unstable state) and the second is cavitation. Failure due to necking produces a fine neck, however failure dominated by cavitation generates a rough surface [161]. Due to high temperatures, grain growth occurs through recrystallisation, which enhances hardening behaviour in the gauge area of samples. This hardening phenomenon reduces the chances of localisation of strain (effect of strain on specific area), which leads to necking and ensures long elongation before failure [162]. Cavitation occurs due to nucleation of voids, produced in the material at grain boundaries. These voids are actually unattended cavities which were produced in the material due to movement and growth of grains, and are not entertained or accommodated by any secondary deformation process such as diffusional or dislocation creep during grain boundary sliding [163].

Cavitation is mostly reported in tensile tests, however, very few researchers have highlighted its role during compression and stamping tests.

Strain rate sensitivity, temperature and grain size are leading parameters that affect the volume of cavities. Mathematically the cavity volume can be represented as:

$$V = V_0 \exp (h \varepsilon) \qquad (5)$$

Where V refers to cavity volume, V_0 is volume at specific strain, h is average individual cavity growth and ε is applied strain [164].

Cavitation restricts the formability of magnesium alloys due to failures caused by the interlinkage of cavities. Cavities not only decrease the formability of Mg alloys, but also degrade the mechanical properties of formed parts [165]. Therefore, it is important to reveal the cavitation mechanism during the deformation of Mg alloys in order to suppress the formation of cavities through improving the materials or processing conditions.

2.12 Conclusion

The microstructure of magnesium alloys has not been fully understood in relation to the various forming operations. As it is discussed in previous sections the mode of deformation and failure varies continuously due to variation of load and strain rate. Individual studies are available on magnesium alloys’ behaviour during heat treatment and tensile tests, however, a detailed study is required to analyse the deformation and failure behaviour of magnesium alloys in relation to pre-and-post forming parameters. In this study the magnesium alloy AZ80 is explored, with variations in grain size, temperature, strain rate and texture.

Incorporating fine grain as well as coarse grain material varies the behaviour of AZ80, whose properties as a wrought alloy have not yet been widely explored. The role of grain boundary sliding, diffusional creep as an accommodating or secondary mechanism, grain growth and finally, failure through cavitation are analysed in the light of uniaxial and multi-axial deformation processes.

Chapter 3

Formability of magnesium alloys

3.1 Introduction

Magnesium alloy processing and manufacturing is attracting the attention of the sheet metal industry due to its light weight and reasonable strength. A certain degree of ductility is observed in magnesium, which has attracted the attention of many researchers in the past. Several magnesium alloys reveal high ductility at elevated temperatures. Titanium and aluminium alloys have also been processed by means of high temperature forming, but few findings have been published for magnesium [166]. As discussed in section 2.1, due to their HCP structure, magnesium alloys need to be processed at an elevated temperature to activate additional slip planes during a deformation process. This technique offers numerous advantages over conventional forming methods; the ability to produce rather complicated shapes from hard-to-form metals in one single step is definitely the most attractive. As magnesium is difficult to form, elevated temperatures bring new possibilities and open more opportunities to use magnesium in sheet metal applications [167].

3.2 Problems of elevated temperature processing

The forming of metals is a very complex process, due to the implications of various processing parameters and multi-axial deformations. As mentioned in the previous section, magnesium alloys can barely be formed at room temperature because of the limited slip systems available. It was observed that elevated temperature processing will provide additional slip systems and through this reasonable ductility can be achieved that will make magnesium alloys comparable to steel, aluminium and other alloys used in the sheet metal industry. However, this technique has been confronted with a number of obstacles and issues that limit its extensive use on a larger scale, the most critical of which are limited predictability, speed limitations and lack of comprehensive data about deformation and failure. Also, there is a lack of accurate models to describe the behaviour of magnesium materials during deformation at elevated temperatures and thereby predict their failure point. Therefore, most of these processes are carried out by trial and error routines [168]. Since elevated temperature deformation is rate-dependent, it is a common practice to avoid premature failure by forming at lower strain rates, which consequently, makes forming of magnesium a rather slow process. But in the highly competitive automotive sector, where the production rate is of prime interest, problems related to high temperature forming need to be addressed, if the process should be used to form automotive sheet-metal components in larger numbers.

From above discussion it is quite clear that elevated temperature forming is a complex process to control, due to the involvement of various pre-and-post processing parameters. These parameters include both mechanical and material factors that need to be optimised to attain maximum formability. There are three main factors in achieving good ductility in magnesium before failure to exhibit reasonable formability:

i. Slow strain rates
ii. Fine grain size
iii. High temperature

3.2.1 Sensitivity of elevated temperature forming towards strain rate

Magnesium alloy processing is commonly deemed as a quasi-static process in relation to strain rates. The speed of the punch during elevated temperature forming plays a vital role in the distribution of load and strains on the surface of a sheet. Strain rate is an important parameter that affects the amount of elongation before failure occurs in metals. Strain rates used in various tests have varied from 10^{-1} to 10^{-4} sec^{-1}. The selection of strain rates is also an intricate process as extremely slow strain rates are not recommended for the commercial production of sheet metal parts, and extremely high rates will result in non-uniform formability. Therefore 10^{-2} to 10^{-3} sec^{-1} are the recommended strain rates for forming magnesium alloys [169].

On the other hand, high strain rate superplasticity (HSRS) has also been achieved by some researchers. HSRS was first defined by the Japanese standards association as superplasticity at a strain rate equal to or greater than 10^{-2} s^{-1} [170]. They also explained that higher strain rate superplasticity is only achievable by reducing the grain size as much as possible.

Slower strain rates at high temperatures affect material characteristics and mechanical properties as shown in Figure 23. With extremely slow rates, the increased heating time results in cavitation in magnesium alloys, as discussed in section 2.8. Due to increased heating time, premature failure occurs in magnesium, degrading its mechanical properties, which results in poor formability. Therefore moderate strain rates are usually recommended for commercial production.

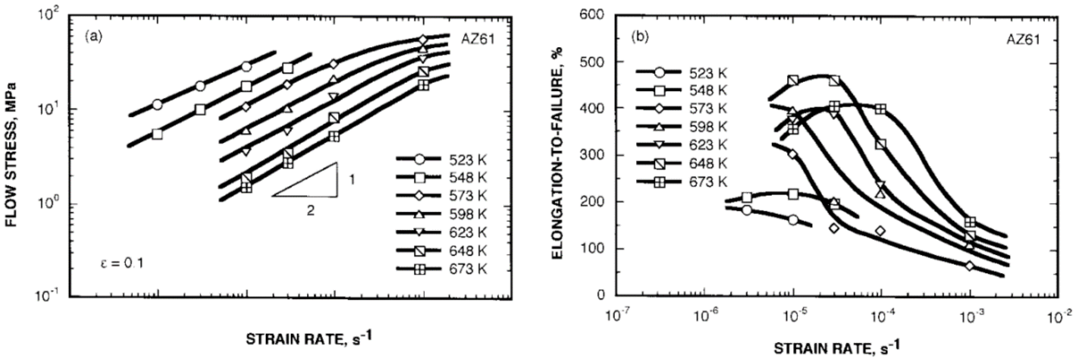

Figure 23. Influence of strain rate and temperature on mechanical properties of AZ61 [169]

3.2.2 Grain size effects on SPF of magnesium alloys

Grain size is considered the most important factor in producing superplasticity in metallic alloys. Materials formable at elevated temperatures, such as steel, aluminium, magnesium and titanium, generally have grain sizes in the range of 3–5µm. Fine-grained ductility normally requires that the grain size should be homogeneously distributed over the entire surface and be below10 – 15 µm, without significant growth during deformation. To avoid grain growth during deformation variable temperature forming is suggested [171].

Grain size affects material and mechanical properties. Mechanical properties such as yield strength, work hardening and flow stress are key parameters that are very much influenced by a variation in grain size. The flow stress, proof stress and hardening rate decreases when the grain size becomes finer, reducing the force required for deformation. Also at a given strain rate, stress decreases as grain size decreases. With regard to material properties, twinning is more dominant with coarse grain size alloys; however, as grains become finer the slip system overtakes twinning.

There are a number of means through which grain refinement can be achieved. The most common methods used for grain refinement are: severe plastic deformation (SPD), equal channel angular pressing (ECAP) [172], high pressure torsion (HPT) [173], accumulative roll bonding (ARB) [174], large strain hot rolling (LSHR) [175], extrusion [176], the most recently developed technique friction stir processing (FSP) based on friction stir welding (FSW), and others [177].

A finer grain size is normally preferred in producing extensive superplasticity in metals, because it is easier for these grains to rotate and slide over each other and accommodate larger strains before failure.

Superplasticity in magnesium alloys can nevertheless be achieved by a coarse grain size, as shown in Table 9. Higashi and his co-researchers [178] indicate an elongation of 604 percent in hot rolled AZ91 with an initial grain size of about 39.5 µm. A similar type of experiment was also conducted by Xin Wu [179] in the USA, in which he used AZ31 with an initial grain size of up to 300 µm. After grain refinement to 25 µm, he achieved an elongation of 320 percent at a temperature of 500^0C along with a rate of 10^{-3} s^{-1}.

Table 9. Summary of different elevated temperature tests in commercial magnesium alloys

Alloy	**Processing Method**	**Grain Size (μm)**	**Test Temperature (^0C)**	**Strain Rate (s^{-1})**	**Elongation (%)**	**Reference Number**
AZ80	Extrusion	35	350	1.31×10^{-4}	200	188
			430	6.56×10^{-4}	239	
ZE10	Extrusion	5	350	4.8×10^{-3}	330	189
			350	5.55×10^{-4}	364	190
AZ91	Conventional	-	250	3.3×10^{-3}	110	
	Casting +		275		180	
			300		170	
	RS + extrusion	-	250		>500	
			275		>1000	
			300		>1000	
AZ91	PM +	1.4	300	1×10^{-2}	280	191
	IM + extrusion	4.1	250	4×10^{-3}	430	
AZ91	ECAP	1	175	6×10^{-5}	326	192
			175	2×10^{-4}	180	
			200	6×10^{-5}	661	
			200	1×10^{-4}	400	
		1.4	300	1×10^{-2}	280	
		4.1	250	3×10^{-4}	430	
AZ91	Extrusion	7.6	300	1×10^{-5}	310	193
		15.4			150	
		66.1			<30	
AZ91	Extrusion	2.5	300	1×10^{-3}	1200	194
AZ91	Reciprocal	-	300	1×10^{-3}	1000	195
AZ105	PM + extrusion		200	2×10^{-3}	53	196
			300	2×10^{-3}	400	
			300	2×10^{-2}	900	
			200	2×10^{-3}	75	
			300	2×10^{-3}	120	
AZ31	Extrusion	5	325	1×10^{-4}	608	197
AZ31	Extrusion	15	177	1×10^{-5}	120	198
AZ31	Extruded rod	-	450	1×10^{-5}	596	199
	Extruded sheet	-	375	6×10^{-5}	200	
ZK60	IM + extrusion	3.3	325	1×10^{-2}	544	200
			350	1×10^{-3}	420	
	PM +	6.5	200	3×10^{-6}	430	
ZK60	Extrusion	3.2	300	4×10^{-3}	730	201
ZK61		1.8	350	1×10^{-1}	450	
ZK60	Extrusion	3.3	325	1×10^{-5}	370	203

			325		544	
			325		130	
			350		420	
			350		320	
			350		150	
ZK60	Extrusion + annealing	6.5	200	1 x 10^{-5}	240	204
			225		430	
ZK61	PM + extrusion	0.5	200	1 x 10^{-3}	659	205
					283	

3.2.3 Influence of temperature on SPF of Mg alloys

It is recognised that good formability of magnesium alloys is associated with higher temperatures and smaller grain size, with a low strain rate as shown in Table 9. Controlling temperature during heating tests can be quite complex. Table 9 summarises from the literature various elongations of different commercial AZ, ZE and ZK Mg alloys, along with their processing means.

To achieve large elongations before failure, strain rates are reduced, which can result in a drop in tool temperature. To maintain a temperature continuous heating during a process is required. McNelley [180] and Valiev [181] showed that metals can exhibit acceptable elongations at low temperatures and medium strain rates.

For achieving long elongations before failures at elevated temperatures, the strain rate sensitivity of the material at any combination of the temperature and strain rate is reflected by the strain rate sensitivity index m, represented by the slope of the flow curve at a given point. In most experiments, m is equal to 0.5. In addition, McNelley [182] and Valiev [183] showed that m was 0.4 – 0.5 for both low and high temperature elongations. On the other hand, Pu [184 – 185] showed that m was about 0.3 for low temperature superplasticity of Al-Li alloys.

Nevertheless, achieving a high percentage of superplasticity in magnesium alloys is reported by a number of different authors. For example, Mabuchi [186] - [187] achieved a 661% elongation in AZ91 at 473K, which is about $0.51T_m$ with a strain rate sensitivity of about 0.3.

Variation in temperature governs deformation mechanisms, as discussed in section 2.3. At room temperature, poor formability is a result of a low number of independent slip systems, as recognised by the von Mises criteria. Additional slip systems activated through an increased temperature are the cause for long elongations before failure.

3.3 Formability of magnesium alloys

As discussed, the forming characteristics of magnesium alloys are rarely studied as they are difficult to deform. The majority of researchers have confined their studies to AZ31, which is the most common commercial magnesium alloy. Most of these studies are related to uniaxial tensile tests at different temperatures, based on these many researchers have made predictions about magnesium alloys forming behaviour.

The warm deep-drawing process is quite complex, as it depends on a number of parameters that control it [208]. The warm stamping ductility and formability of magnesium alloys has not been investigated in detail, as this requires a large number of tests (uniaxial, biaxial and multi-axial) and analysis to predict their behaviour accurately.

The investigation of formability of a material can be divided into three stages [209]:

i. Experimental setup development
ii. Examination of the basic forming parameters
iii. Construction of forming limit curves (FLC)

These three stages can be successfully achieved by experimental tests and advanced numerical simulations.

3.3.1 Experimental setup development

Warm deep-drawing, as already stated, is a complex process to control, as shown in Figure 24. Heating the blank is an additional step in this process. Two methods are used for blank heating, that is, external heating and internal heating [210].

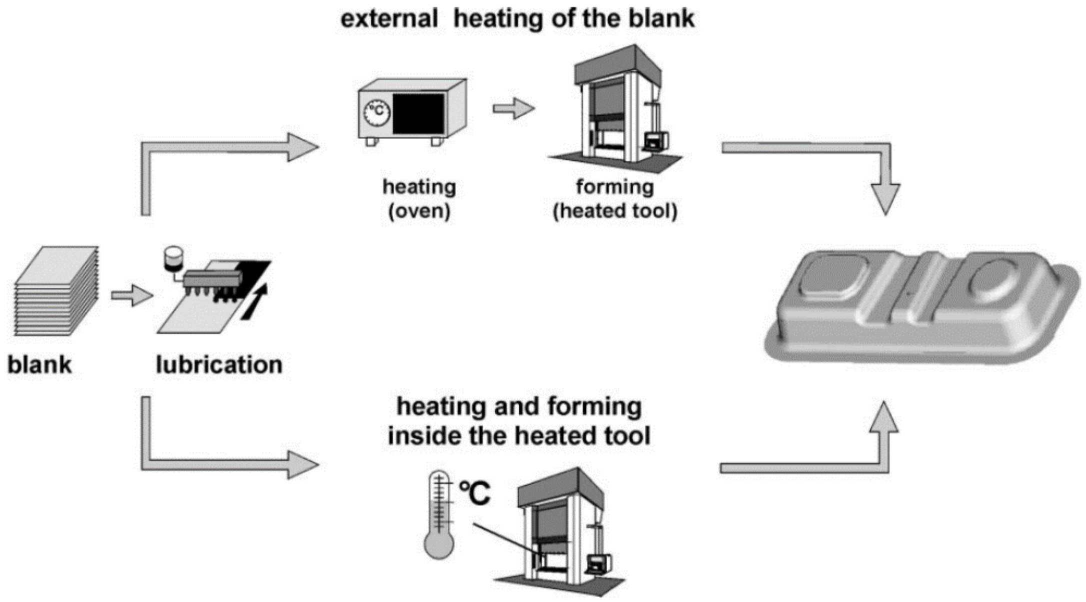
external heating of the blank
heating (oven)
forming (heated tool)
blank
lubrication
heating and forming inside the heated tool
°C

Figure 24. Process diagram of deep-drawing tests at higher temperatures [36]

External heating, which is commonly performed in an external oven, is not effective in laboratory procedures as heat losses can be great. However, for industrial applications a conveyor system can be used, through which heat losses will be minimised.

Internal heating is the preferred method as heat can be homogeneously distributed in the blank. The blank needs to be clamped by the blank holder for a short time to distribute the heat evenly.

The drawing setup also involves setting different processing parameters such as temperature, punch velocity, ram stroke, punch diameter, die diameter and blank holder force (BHF). The drawing gap between the sheet and the die should usually be 1.2 times the sheet thickness [211].

3.3.2 Examination of the basic forming parameters and results

Formability of magnesium alloys has been a topic of interest for a number of decades because of global warming and environmental issues. The increased drawing capacity of magnesium sheets not only indirectly tackles environmental issues but also enhances productivity and parts quality.

Only a few studies are available regarding the drawing of magnesium sheets, including Doege and Droder [212], who performed limit drawing ratio (LDR) experiments to examine the formability of AZ31 sheet at different temperatures, and they state, it is possible to form 100 mm diameter cups with an LDR of 2.5 at a forming temperature of 200^0C. They also mentioned investigating the forming of magnesium alloys in rectangular pans and achieving a maximum height of 65mm at 225^0C. One common fact that was found in both rectangular and round cups is that wrinkles during drawing will decrease with an increase in the temperature, up to a certain limit. Droder and Doege [80] also found that an increase of the formability of magnesium alloys is possible by establishing high temperatures at the tool corners and low temperatures at the tool straight edges. By implementing this technique, they formed a 110mm x 220mm x 1.0mm sheet with a drawn depth of 98mm. This is an increase from their previous publication [213], which also drew the same size of cup with a height of 65mm.

Yoshihara [214], T.B Huang [215] and Yoshihara [216] have suggested a new combination of a local heating and cooling system to increase the formability of magnesium sheet. Yoshihara [217] has achieved an LDR of 5 by using a combination of blank holder pressure (BHP) and a local heating/cooling system.

Heat treatment processes influence the formability of magnesium alloys. Yang et al. [218] investigated the cold forming deformation behaviour of magnesium AZ31 by performing uniaxial tensile tests and deep-drawing tests. They used a sheet thickness of 0.5mm and annealed these sheets at different temperatures, varying from 400^0C to 550^0C for one to three hours, and achieved an LDR of 1.72. They also found that anisotropy effects are dominant during cold forming and varied material flow into the die cavity, resulting in different thicknesses at the flanges at different orientations.

All these results indicate that magnesium alloys can be commercially used as an alternative material for aluminium and steel through considering the above techniques and parameters. After reviewing all these formability data, shown in Table 10, this research started with the optimisation of process parameters and factors that affect the formability of magnesium alloys, so that these alloys can compete with existing metals in the field of sheet metal forming, especially in the automotive and aerospace industries. These process factors are:

a) Influence of the punch speed
b) Influence of punch force
c) Influence of blank holder force
d) Influence of texture
e) Influence of temperature
f) Temperature distribution during warm forming
g) Thickness distribution during warm forming
h) Spring-back properties
i) Tool design
j) Lubrication system for tool and blank
k) Exact prediction of the flow of material during forming by mathematical modelling

Table 10. Summary of limit drawing ratios (LDR) for magnesium AZ31 alloy

Processed	Temperature (^{0}C)	Thickness	Punch Speed	LDR	Reference
Rolled	50	1.0	100 mm/sec	1.5	221
	100			1.68	
	150			2.3	
	200			2.5	
	250			2.3	
	300			2.2	
Rolled	380 (453K)	2.5	5 mm/min	2.2	222
Cross rolled + annealed	150	0.6	4 mm/min	2.0	223
	150 – 200		15 mm/min	2.5	
	200 – 300		15 mm/min	3.0	
????	200	0.58		2.63	224

Hot rolled + annealed	180	0.7	30mm/min	2.2	225
	180		15mm/min	2.5	
	180		6mm/min	3.25	
	230		30mm/min	2.8	
	230		15mm/min	2.8	
	230		6mm/min	3.375	
Rolling+	400	0.5	200 mm/min	5	226
	224 (498K)	0.83	3mm/sec	3.0	227
Hot rolled	RT	0.8	30mm/min	1.3	
	50			1.5	
	100			1.7	
	150			2.2	
	200			2.65	
	250			2.3	
Extrusion + annealing	200	0.8	1000 mm/min	1.8	228
	216			2.0	
	226			2.2	
	236			2.15	
	300			2.1	
Casting + hot rolling	250	0.5	30 mm/sec	2.3	229
	300			2.7	
	350			2.3	
Rolling	100	0.6		1.4	230
	150			1.9	
	200			2.3	
	250			2.1	
	300			2.0	
Repeated unidirectional bending (RUB)	RT			1.3	
	50			1.4	
	100			1.75	
	150			1.9	
	200			2.2	
	250			2.0	
	300			1.9	

3.3.2.1 Influence of punch speed in forming of magnesium alloys

Different factors that affect formability have been investigated by many researchers, such as the effect of strain rate on drawing by Zhang [219], who conducted deep-drawing at three punch speeds, 7.5, 30 and 72 mm/min, and proved that at increased strain rates the ductility of magnesium alloys decreases drastically and causes draw-in of the flange, which ultimately decreases its formability.

Doege and Droder [220] also focussed on this issue and made a comparison of four magnesium materials and their LDR trend against punch velocity at 200^0C, as shown in Figure 25. The four magnesium sheets showed a similar trend, that is, a decline in LDR as the punch velocity increases. The reason for this decline is the generation of high stresses at low strain values.

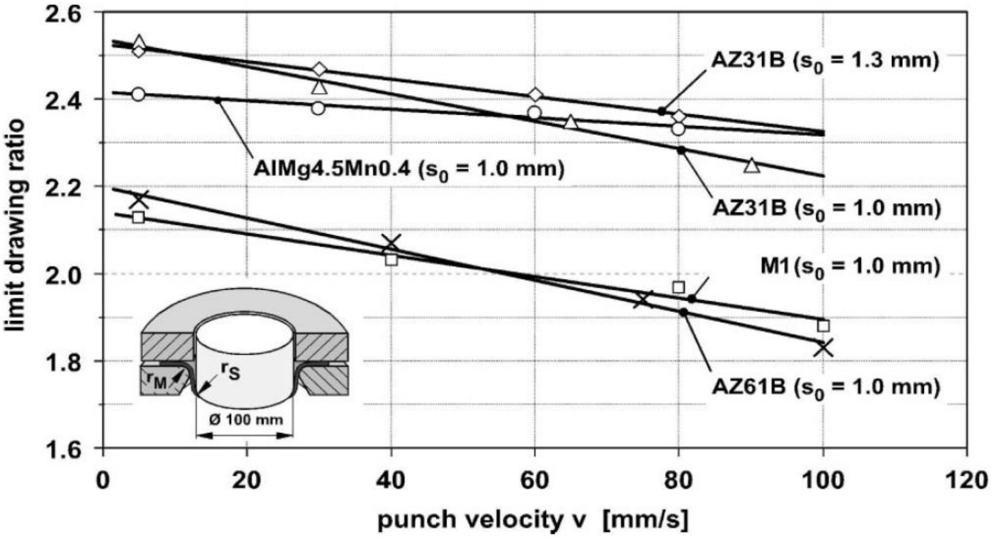

Figure 25. Comparison of four magnesium sheets at different punch speeds [220]

This trend also indicates that magnesium alloys are more sensitive to punch speed /velocity than aluminium alloys. This is exactly the same behaviour that is also proved by uniaxial tests in this project's preliminary results sections.

3.3.2.2 Influence of the punch force in forming magnesium alloys

There are several factors that affect the punch force, such as temperature, stroke and blank diameter. The best formability is achieved when the punch force is less than the strength of the cup. Tyng et al. [231] described how by following the above condition, successful flow of the blank in the die cavity can be achieved. They and M. Jain et al. [232] also emphasised that punch force increases with the increase in the blank diameter.

3.3.2.3 Influence of the blank holder force in forming magnesium alloys

Blank holder force (BHF) is also an important parameter that influences the forming of magnesium sheets. It has been confirmed by several researchers that whenever the blank holder force is too high or too low, fracture and wrinkles may occur, respectively [233]. S. Yoshihara [234] proposed a new strategy of variable blank-holder force against a constant blank-holder force, and reported an improvement in the LDR, that is, from 2.09 to 2.14 at 300^0C. It has also been reported that thickening and thinning are both suppressed when compared with a constant BHF in which thinning starts from the punch shoulder and extends to the wall, and thickening occurs at the ends of the drawn cups.

3.3.2.4 Influence of the texture (anisotropy) in forming of magnesium alloys

The fourth factor is considered by Hua Zhang [235] as the effect of texture on the formability of magnesium sheets. It is suggested by many researchers, such as Watanabe et al. [236] and Huang et al. [237], that magnesium alloys possess a strong basal texture that directly affects ductility as well as formability of these alloys. To improve ductility and formability, Iwanaga et al. [238] suggested that with reduction in the texture of the basal plane (0 0 0 2), formability of the magnesium improved extensively from room temperature to 175^0C. Hua Zhang et al. [239] suggested a new method, called repeated unidirectional bending (RUB) processing, to weaken the strength of magnesium AZ31. In this they rolled a sheet several times on a long cylindrical rod with the help of supports and motors. After deep-drawing tests, he concluded that the LDR of the sheets improved, as shown in Table 10. He also proposed that the anisotropy ratio (r-value), which is quite low at higher temperatures (as it is also shown in uniaxial tests), is a possible reason for a declining LDR after 200^0C, because relating to the r-value local thinning of the sheet occurred near the die corner. It was further explained by Sanbong et al. [240], that mechanical anisotropy affects the formability of magnesium sheets extensively. They found that most of the grains have their c-axes in the normal direction of the sheets in the basal type texture. Thus when load is applied in the normal direction, this will restrict the activity of the <a> dislocation slips and make magnesium sheets difficult to form. These results also confirm our tensile test results, which show that magnesium has strong anisotropy effects from room temperatures up to 200^0C.

Several further ways, other than repeated unidirectional bending, have been suggested by Sanbong [241], Kocks [242], Philippe [243] and Styczynski [244] - [245] to tackle the anisotropy problem in magnesium sheets. One common method is to induce large shear deformation during rolling with the help of asymmetric rolling, which makes the texture quite weak.

3.3.2.5 Influence of temperature in forming magnesium alloys

This is the fifth factor that affects the formability of magnesium alloys. L.M. Ren et al. [246] highlight the variation in the drawing depth with temperature as shown in Figure 26.They explain that drawn depth increases with an increase in temperature up to 250^0C, and thereafter it declines, which results in local thinning in the formed cup, as shown in Figure 26.

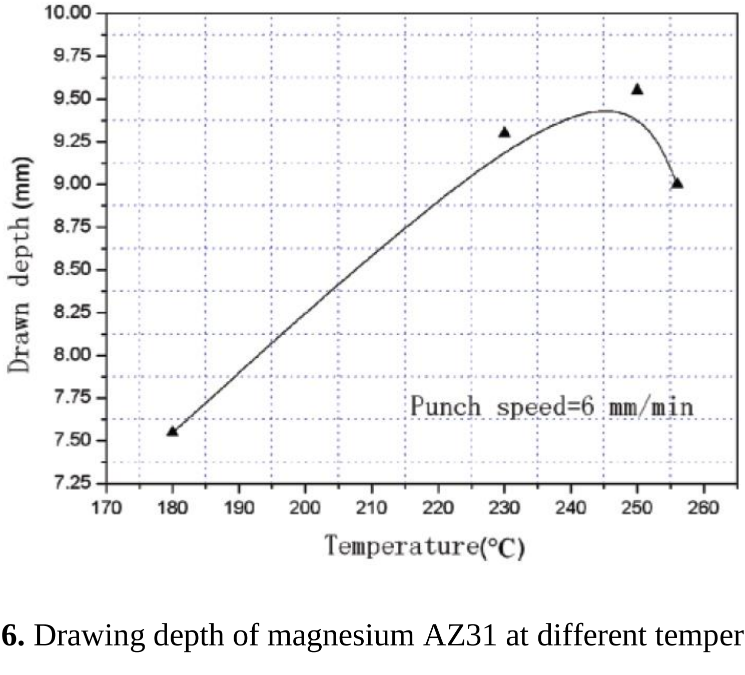

Figure 26. Drawing depth of magnesium AZ31 at different temperatures [246]

A possible reason for this declining trend in drawn depth against temperature is the lower work-hardening exponent of the AZ31 sheets at higher forming temperatures. Chen et al. [247] stated that an optimum temperature for most magnesium sheets exists between 200^0C to 250^0C.

3.3.2.6 Temperature distribution during forming of magnesium alloys

Temperature distribution and its understanding is an important part of the forming process. Understanding is necessary to predict the thinning and thickening of the sheet during forming. In the warm forming process, when the punch travels towards the cavity in the die, the contact of the blank with the punch increases, while contact with the die decreases [248]. Due to this contact, the blank loses some of its heat energy to the punch. As a result, the blank has a minimum temperature at the shoulder radius of the punch and an increased temperature at the shoulder radius of the die. Another reason for this is the low specific heat capacity and high thermal conductivity value of magnesium alloys, which result in a significant difference in the punch and the blank temperature [249].

Droder and Doege [250] and Yoshihara [251] also state that due to this low temperature in the wall, flow stress increases, so temperature controls are also an important parameter in the formability of magnesium alloys. A similar temperature distribution was investigated by Hariharasudhan et al. [252], who conducted forming tests of round shapes of magnesium AZ31B at 200^0C. They observed an additional increase in the temperature of the flange, which was set to 200^0C. The reason stated for this increase is the amount of heat generation during plastic work. This also supports the above reason, that high flange temperature and low temperature in the wall are necessary for proper drawing of magnesium alloys, as this will increase the flow stress and enable the cup wall to bear more stress at the punch corner. This strategy will also avoid localised necking in the material. They further explained that the punch should always be kept at a lower temperature than the blank, because the punch temperature will automatically increase during the forming operation.

It is necessary to mention here that the blank temperature is always highest at its corners because of a smaller available area for convection than the temperature along its surface area, where a minimum temperature is observed because of losses due to a large convection area and contact with the punch [253]. This also helps the forming operation. As we described earlier, flow stress always increases with a decrease in temperature. Therefore, an increased temperature at the corners avoids fractures and a large drawn-depth can be achieved.

3.3.2.7 Thickness distribution during forming of magnesium alloys

Understanding thickness distribution is very important in predicting a material’s behaviour during warm forming. Hariharasudhan et al. [254] investigated the thickness distribution of round and rectangular cups. In the case of round cups, they observed maximum thinning in the cup wall, both experimentally and in simulations. This is quite contrary to ordinary room temperature forming processes in which the maximum amount of thinning is usually observed at the punch radius. The reason they gave for this different behaviour is the existence of non-uniformity in the strength of the cup walls in warm forming, as compared with ordinary cold stamping processes. This strength variation in the cup wall is caused by the variation in temperature distribution in the cup wall, as explained above. As said, the temperature is increased at the die corner radius as opposed to the punch corner radius, which results in a lowering of the yield strength at the cup wall as opposed to the material portion that is in contact with the punch corner, which ultimately results in thinning of the material at the walls.

Hariharasudhan et al. [254] also predicted and stated via FEA simulations that when the thinning of the material exceeds 25 percent, the specimen is considered a failure. Comparisons of thinning regions at different temperatures are shown in Figure 27 below.

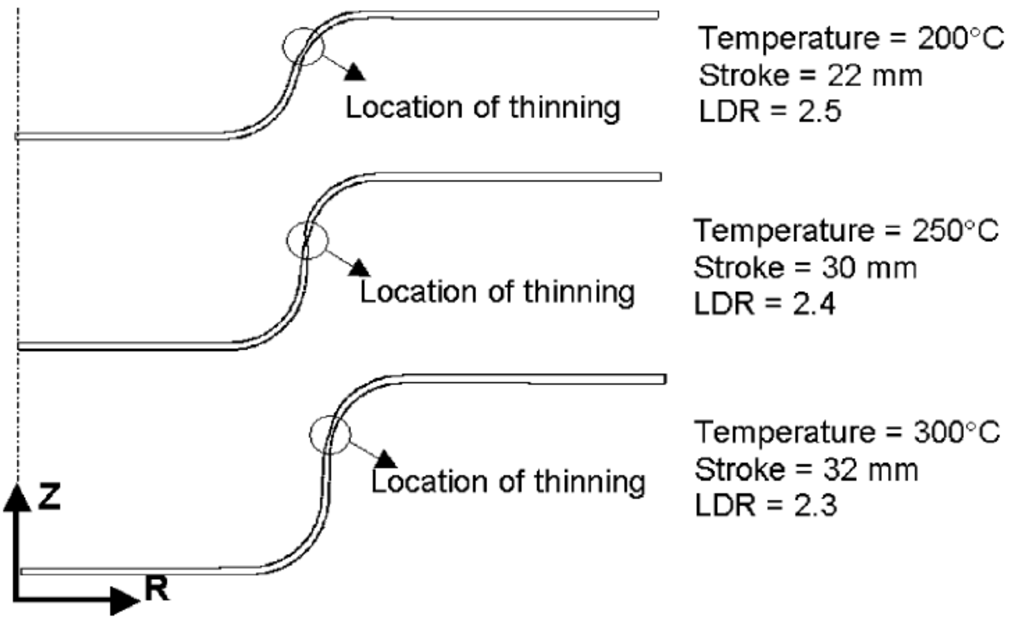
Temperature = 200°C
Stroke = 22 mm
LDR = 2.5
Location of thinning
Temperature = 250°C
Stroke = 30 mm
LDR = 2.4
Location of thinning
Temperature = 300°C
Stroke = 32 mm
LDR = 2.3
Location of thinning
Z
R

Figure 27. Prediction of exact location of thinning area by FEA [254]

3.3.2.7 Spring-back properties in forming of magnesium alloys

Spring-back effects are very critical when conducting hot forming processes. There are very few researchers who have investigated spring-back effects for magnesium alloys. Spring-back occurs on removal of load after completing the deep-drawing process. The basic reason for its occurrence is elastic deformation before the yield limit and it is greater with low elastic moduli. There are several other factors that contribute to this effect such as sheet thickness, material geometry, strain rate sensitivity, work hardening, yield stress and forming conditions [255].

Prediction of spring-back before the forming process starts is important because spring-back creates dimensional inaccuracy, which can create problems during assembly of parts [256]. Several yield criteria can be used to predict the spring-back effect, such as von Mises, Hill quadratic, Barlat three parameters and Barlat 1996 [257]. Li et al. [258] and. Gau et al. [259] highlight the influence of the Bauschinger effect on the accuracy of the spring-back and proposed a new hardening model for prediction of the behaviour of the material. It has also been confirmed by several authors that the amount of spring-back will reduce with an increase in temperature, and almost vanishes at 300^0C [260]. A possible reason for this is the decrease in flow stress and therefore elastic behaviour with increases in temperature.

The effect of the texture was also investigated by a few researchers such as Gomes et al. [261] and Ragai et al. [262]. All agree that the amount of spring-back increases with an increase in the angle of rolling direction in aluminium and steels. This effect of texture on the amount of spring-back has not been considered by any researcher for magnesium alloys. So this is an area which requires the attention of researchers in the future.

Takayuki et al. [263] investigated spring-back characteristics in draw-bending of magnesium AZ31B sheets. They observed that the amount of spring-back decreases with an increase in temperature and blank holder force (BHF), but temperature influences dominate the BHF factor.

Hyung et al. [264] performed draw-bending experiments with two different approaches, isothermal tests and non-isothermal tests. In the isothermal tests they achieved a thermal equilibrium between blankholder, punch and die, while in the non-isothermal tests, die and blank holder are heated to a desired temperature but the punch was not heated. They concluded after the tests that the spring-back effect is negligible at 200^0C only in isothermal tests, but it does not vanish in non-isothermal tests even at 200^0C or above. Therefore, while conducting non-isothermal draw-bending tests, the spring-back effect must be taken into account during the design of experiments.

3.3.2.8 Tooling geometries influences in forming magnesium alloys

Tooling geometries include die clearances and punch radii. Proper die clearances are very important, especially for thin sheets. In the case of smaller clearances, fractures occur most commonly, while wider clearances lead to the appearance of wrinkles in the blanks [265].

It has also been reported that by using smaller punch radii, formability of magnesium alloys is reduced because smaller radii restrict material flowing simultaneously in different directions, which ultimately leads to fracture because of an increase in major strains [266].

3.3.2.9 Other influences

Other factors including lubrication, initial blank shape and tooling geometry also have a strong influence on the formability of magnesium alloys.

The above factors all indicate that optimisation of all these factors will lead to an increase in the formability of magnesium alloys. Therefore this is a wide area available for future researchers to vary all the above parameters to achieve increased formability of magnesium alloys.

As well as this, more alloys need to be researched and their processing customised so that a maximum number of alternatives can be produced by the magnesium industry beside aluminium and steel.

3.4 Construction of forming limit curves (FLC)

A forming limit diagram is a plot for planar strains and combines major and minor strains generated during different types of test such as uniaxial, bi-axial and deep-drawing tests, as shown in Figure 28.

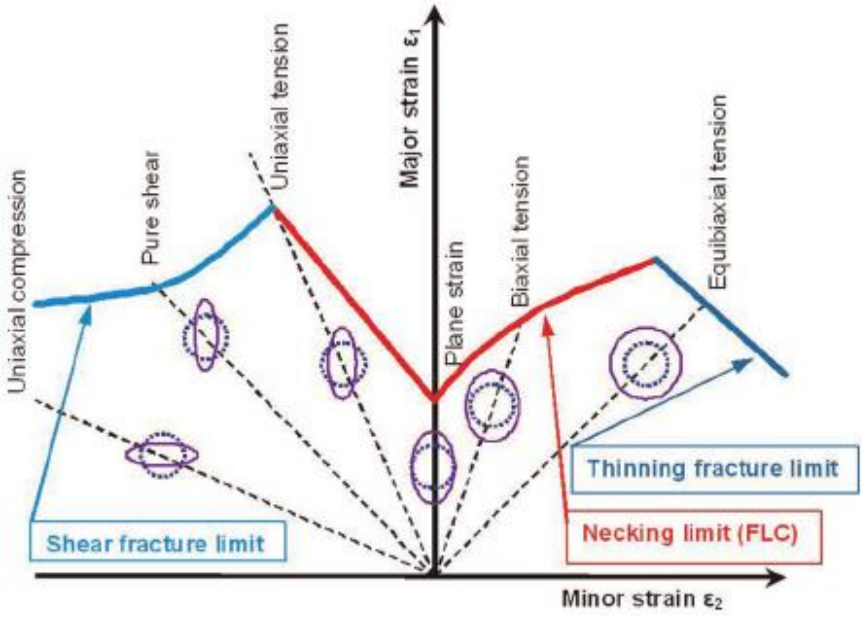
Uniaxial compression
Pure shear
Uniaxial tension
Major strain ε1
Plane strain
Biaxial tension
Equibiaxial tension
Thinning fracture limit
Necking limit (FLC)
Shear fracture limit
Minor strain ε2

Figure 28. Forming limit diagram [268]

It also indicates different zones of uniform deformation, plastic instability and necking, which ultimately lead to failure [267 - 268]. In other words, it can be said that an FLC actually highlights the boundary between safe and unsafe forming regions of an FLD. The safe region can be regarded as the area under the curve where there is no visible necking, whereas the area above curve represents the deformed or failed region where a visible neck can be observed.

The FLC represents strain limits in the FLD that predict the deformation of the materials along strain paths. These strain paths are ranging from uniaxial to multi-axial tests. A linear path actually indicates a constant ratio between minor strains (ε_2) to major strains (ε_1), usually represented by β.

$$\beta = \varepsilon_2 / \varepsilon_1 \tag{6}$$

The values of the strain paths are divided according to the type of tests:

$-0.5 < \beta < 0$	(Indicates deep-drawing of the sheets)
$\beta \approx 0$	(Indicates plane strain condition)
$0 < \beta < 1$	(Indicates bi-axial stretching of the material)

To check the formability of materials, two types of test are used that is, the Nakazima test (Limit Dome Height test or LDH test) [269] and the Marciniak test. These tests are also called out-of-plane and in-plane forming tests. This is because in Nakazima tests, strains are measured on the outer plane of the samples, which is quite difficult, while in the Marciniak tests the strains are measured on the inner surface of the material. Marciniak tests are very simple but several industries still also use Nakazima tests.

There are two further major differences in these two tests, as shown in Figure 29. In the Nakazima test, a hemispherical punch with a draw bead is used to form the blank. The beads are uses to control the sliding motion of the blank. However the Marciniak test uses a hollowed cylindrical shape with a flat head. In addition to this, a specific blank is used with a drilled-hole (pole region) at its centre, also called the driving blank. Due to this hole the force of the punch is concentrated at the centre of the blank as tensile (expansion) stress.

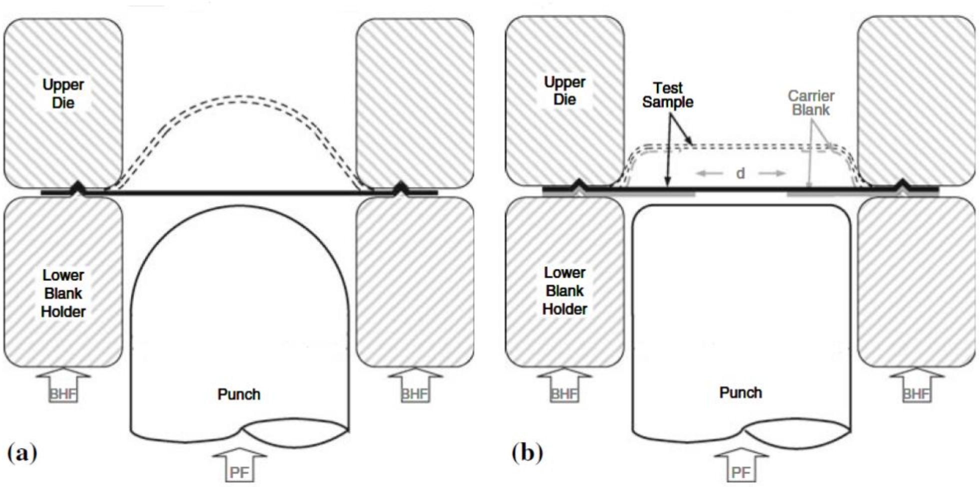
Upper Die
Lower Blank Holder
BHF
Punch
BHF
PF
(a)
Upper Die
Test Sample
Carrier Blank
d
Lower Blank Holder
BHF
Punch
BHF
PF
(b)

Figure 29. (a) Nakazima test setup (b) Marciniak test setup [269]

Both tests have their own merits and demerits and both tests should be conducted to check the formability variations by varying sample types. Emilie et al. [270] performed both tests on aluminium alloys and reported that LDH tests are more complex than Marciniak tests, as they involve strain gradients due to bending, normal loading and friction simultaneously.

Different types of samples have been used by researchers to obtain strain paths for developing the forming limit curves. The most commonly used sample sizes were proposed by Raghavan [271], as shown in Table 11. The narrowest samples are used for generating strain paths in uniaxial directions, while the widest samples are used to generate strain paths in multiaxial directions.

Table 11. Different sample geometries for Nakazima and Marciniak tests [130]

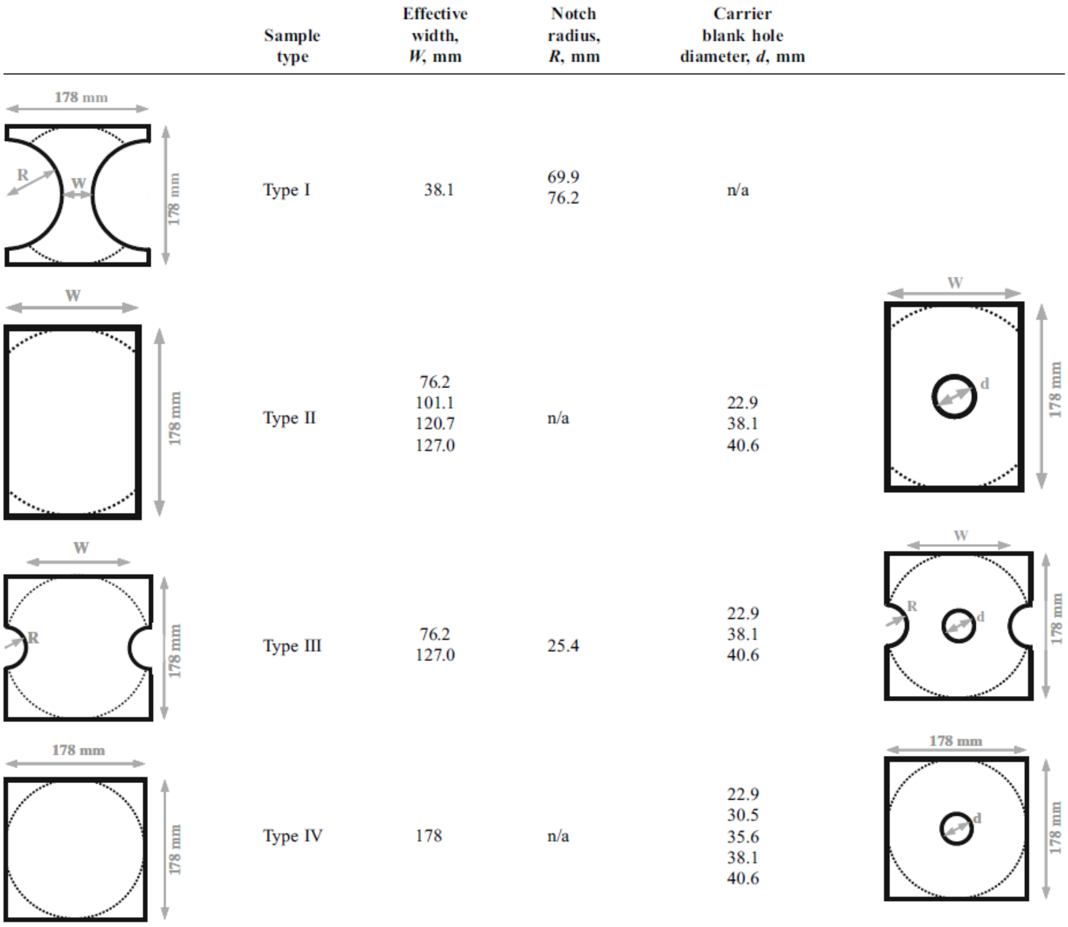

178 mm
R
W
178 mm
W
d
178 mm

	Sample type	Effective width, *W*, mm	Notch radius, *R*, mm	Carrier blank hole diameter, *d*, mm
	Type I	38.1	69.9 76.2	n/a
	Type II	76.2 101.1 120.7 127.0	n/a	22.9 38.1 40.6
	Type III	76.2 127.0	25.4	22.9 38.1 40.6
	Type IV	178	n/a	22.9 30.5 35.6 38.1 40.6

Emilie et al. [273] performed both in-plane and out-of-plane measurements on magnesium AZ31B and obtained an enhanced ductility at elevated temperature. It is also reported that a 67 percent plane strain forming limit was obtained at 300^{0}C. They also concluded that it is difficult to perform out-of-plane (LDH) tests because of bending strain, frictional effects and normal pressure acting on the magnesium sheets.

These effects mean that LDH tests always show higher forming limits, as displayed in Figure 30 and Marciniak tests are the preferred method for identifying forming limits. However strain localisation and the occurrence of fractures near the pole are difficult to achieve in Marciniak tests.

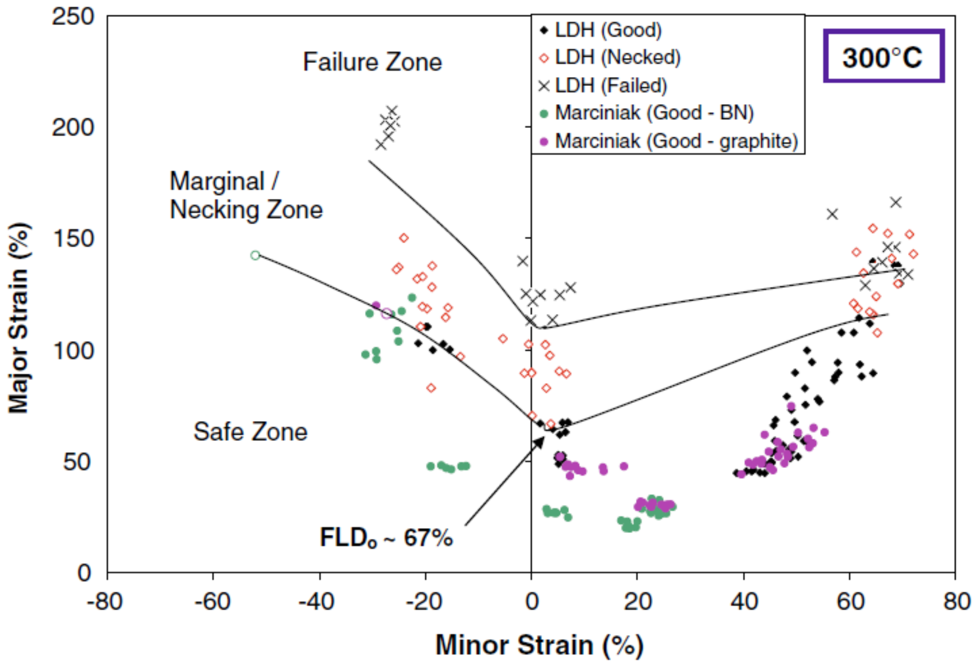

Figure 30. FLC curves of AZ31 for Nakazima and Marciniak tests [273]

Therefore there is still a research gap to develop a methodology in which fracture and strain localisation should be forced to occur near the pole. This can be done by optimising the tool geometry parameters and temperature distributions in an experimental setup to perform FLD tests related to magnesium alloys.

Similarly, Palumbo et al. [274] investigated the forming properties of magnesium by varying the temperature and strain rate, based on the Marciniak method. They observed that by reducing the strain rate from 0.02 s^{-1} to 0.002s^{-1}, the forming limit curve of the magnesium alloy shifts upwards by about 35 percent at 200^{0}C. Huang et al. [275] also reported that an FLC of magnesium alloys shifts upwards with an increase in temperatures which indicates improvement of stretch formability. They also investigated the effect of repeated unidirectional bending, which further improved the forming characteristics.

All these references indicate that temperature, strain rate and other parameters have a strong influence on forming limit curves and their behaviour. There is a strong need to optimise these parameters to predict the exact behaviour of magnesium alloys to identify the fracture and safe zones. This could create a more suitable alternative for the sheet metal industry than aluminium and steel.

3.5 Strain measurement

Strain measurement is one of the most important steps in determining the strain paths for an FLD. The most common method of determining strains are printed grids of circles imposed on the sheet materials with electrochemical etching or silk screen printing. After deformation, the deformed grids are measured and matched with original circle sizes to obtain the principal strains in different directions [272].

3.6 Constitutive analysis

Material flow prediction during hot tests is a topic of interest. Unlike with room temperature, the effects of temperature enable materials to exhibit long elongations before failure. This elongation is heavily dependent on strain rate, grain size and temperature. Prediction of this elongation would help to modify process parameters and improve material flow [274]. Variations in thermo- mechanical parameters would not only affect mechanical properties but also influence the kinetics of metallurgical characteristics as well. Constitutive modelling is considered an effective way to predict the flow behaviour of materials by using mathematical formulations. Numerical simulations also rely on these constitutive models. A comparison of all these formulations would lead to an effective prediction.

In ideal conditions, it is usually expected that any constitutive model should consider effects of variations in strain rate, temperature, grain size, work hardening behaviour et cetera and based on these, it will calculate instantaneous flow stresses. However, it is impossible to practically accommodate all these parameters in a single equation [275]. Therefore, several constitutive equations have been presented by researchers that can be categorised in three ways.

3.6.1 Phenomenological models

The most widely used constitutive equations or models are discussed in the following. Phenomenological models are mostly used to predict flow stress by considering the effect of temperature and strain rates. They are simple to use, as they do not consider the physical history of the material's behaviour and material's characteristics. Therefore, a fewer constants are employed in these models. Some of the most frequently used models are the Johnson & Cook (JC) model [276], the Khan, Liang & Farrokh (KLF) model [276],the Arrhenius equation [276–279], the Molinari & Ravichandran (MR) model [280], the Khan & Huang (KH) model [281], the Fields & Backofen(FB) model [282], the Khan, Huang & Liang (KHL) model [283–285], the Voce & Kocks (VK) model [285 – 286], and a few others[287].

3.6.2 Physical or material relying models

Physical or material relying models are slightly more difficult to use than phenomenological models. They were developed by considering the effect of microstructure changes such as the number of activated slip systems and dislocation movements with the inclusion of high temperatures and strain rates which are neglected in phenomenological models. A few examples of these models can be mentioned, such as the Zerilli & Armstrong (ZA) model [288], the Preston, Tonks & Wallace (PTW) model [289], the dynamic recrystallisation (DRX) model [290], the Voyiadjis & Almasri (VA) model [291], the Bonder & Partom (BP) model [292], the Rusinek & Klepaczko (RK) model [293], the Cellular Automaton (CA) model [294], and a few others[295].

3.6.3 Artificial neural network models

An Artificial neural network (ANN) is based on the processing by many nonlinear units called neurons. Neural networks are used for modelling, regulating, optimising and diagnosing of material models. The ANN methodology is based on signal processing between neurons divided into three types of layers: input layer, hidden layer and output layer, as shown in Figure 31 [296].

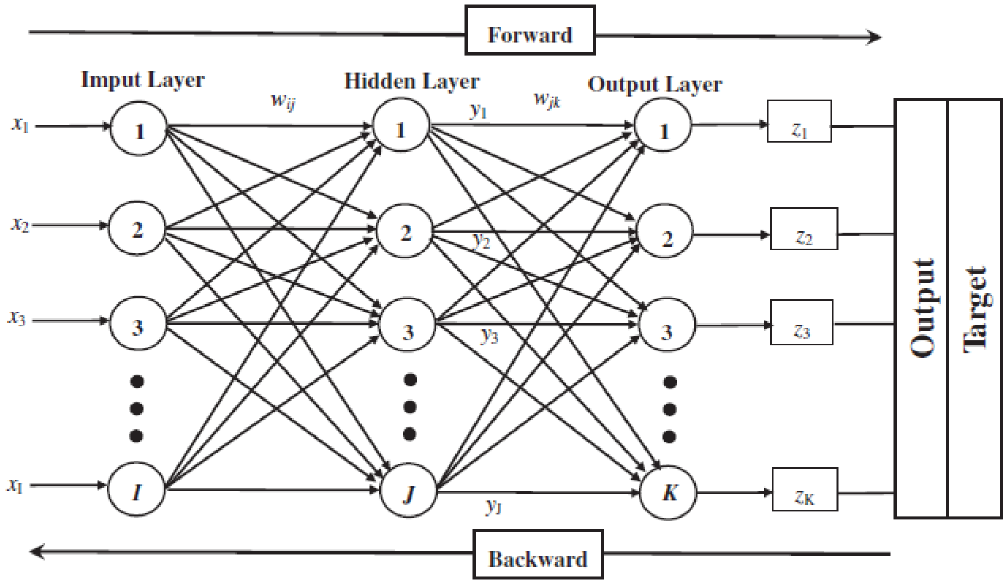

Figure 31. Schematic diagram of Artificial Neural Network [296]

ANN models were used by Bariani et al. 2001 [297] to predict the deformation behaviour of nickel-based alloys. They used Gleeble tests and successively compared compression test data at various strain rates with predicted ANN results. Jamal et al. [298] developed material models in ANN and compared them with the experimental results of Al 7075-T6. They proved that ANN models took less time to develop than conventional mathematical models.

3.7 Mechanics of material flow

When a material is undergoing stress, the flow of material initiates within the elastic region and further addition of load takes it into the plastic region. In the plastic region, material exhibits increments in plastic strain without any further addition of load [299]. This flow of material under yielding conditions can be defined mathematically as

$$d \in_y{}^p = d\gamma \frac{d\emptyset}{d\sigma} \tag{7}$$

Where $\in_y$ is yield strain in plasticity, p is a material constant, γ is a scalar factor, $\emptyset$ is the potential yielding function and σ is the applied stress in the plastic region.

Equation 7 indicates a proportional relationship between plastic strain and yield function. This is also called flow rule, which is mostly used for sheet metals.

3.7 Yield criterion

Yield behaviour prediction is important in the deep-drawing process to avoid cracks and wrinkles.

Yielding, as described earlier, is a continuous increase in strain without any further addition of load. Any material which achieves this state or simply when $\sigma = \sigma_y$is calledthe yield criterion,where σ is applied stress and $\sigma_y$is yield stress. A simple example of the yield criterion in one-dimensional space is given in Figure 32 [300].

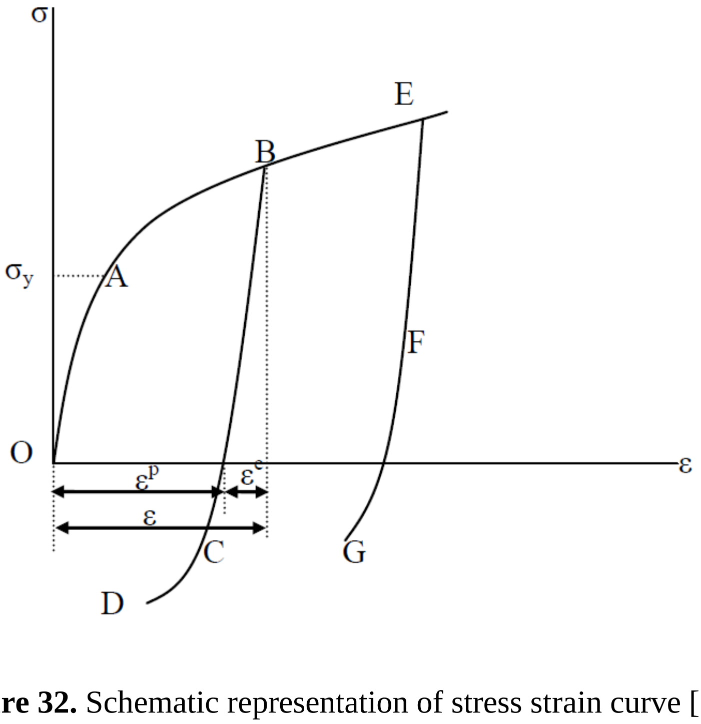

Figure 32. Schematic representation of stress strain curve [300]

3.7.1 Isotropic yield criterion

3.7.1.1 Tresca Criterion

Tresca's yield function, also known as maximum shear stress criteria, is one of the oldest yield criteria and was established by Henri Tresca in 1864 for ductile materials [301]. It was developed on experimental grounds, in which he performed various experiments on extrusion of metals. He finally concluded that when the maximum applied shear stress attains a critical value equivalent to the yield strength of the material, it starts to flow plastically. The criterion is based on the difference between two principal stresses and can mathematically be expressed as:

$$\max(|\sigma_1 - \sigma_2\,|\,,|\sigma_2 - \sigma_3|,|\sigma_3 - \sigma_1|) = \ \sigma_s \tag{8}$$

Where σ_1, σ_2 and σ_3 are principal stresses and σ_s is shear stress in yielding.

3.7.1.2 Von Mises Criterion

Von Mises in 1913 suggested another yield criterion, also known as a maximum distortion energy criterion, in which he explained the yield function's dependence on stress invariants [302]. He stated that a material will fail when its energy reaches a critical yield stress function energy level.

Later, Hencky and Nadai interpreted its physical definition by correlating yield strength with distortion strain energy density (work done per unit volume by the deviatoric part of a stress tensor) and claimed that yielding will only occur when distortion strain energy attains a critical value. Later, Nadai in 1933 [303] compared the Tresca and von Mises criterion by drawing their yield surfaces as cylinderical and hexagonal shapes respectively, as shown in Figure 33. Mathematically the von Mises criterion is expressed as:

$$(\sigma_1 - \sigma_2\,)^2 + (\sigma_2 - \sigma_3)^2 + \ (\sigma_3 - \sigma_1)^2 = \ 2{\sigma_s}^2 \tag{9}$$

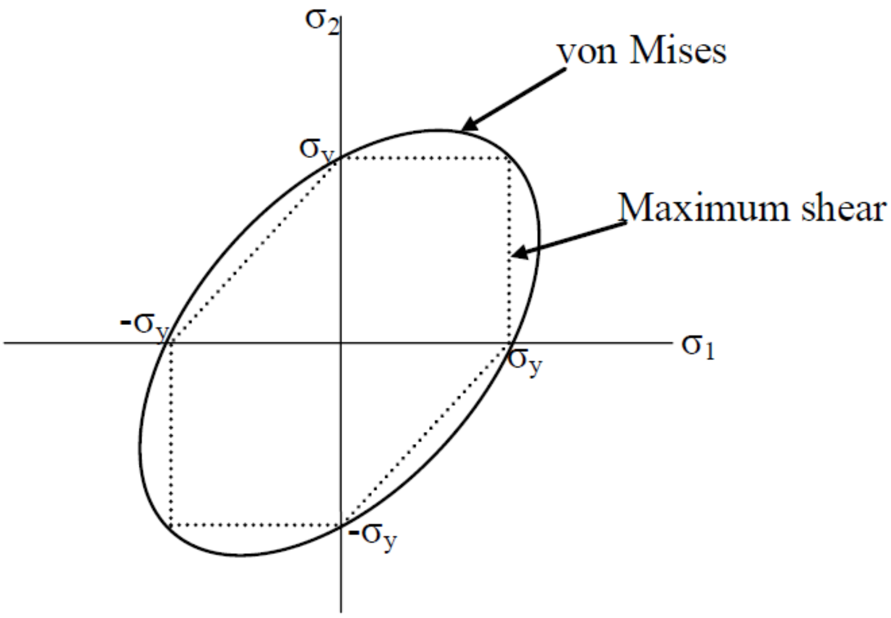

Figure 33. Comparison of maximum shear stress and maximum distortion energy criterion [302]

3.7.1.3 Hosford yield criterion

Hosford [304] also modified the von Mises yield criterion along with Hershey and proposed an isotropic criterion for orthotropic materials as:

$$\frac{1}{2}|\sigma_1 - \sigma_2|^z + \frac{1}{2}|\sigma_2 - \sigma_3|^z + \frac{1}{2}|\sigma_3 - \sigma_1|^z = \sigma_s{}^n \tag{10}$$

Where z is a material constant that when equivalent to 1 turns it into a maximum shear stress criterion and when equal to 2 leads to a maximum distortion energy criterion.

3.7.2 Anisotropic yield criterion

Anisotropy in magnesium alloys plays a significant role at room temperature and moderate temperatures. However, its effect becomes negligable at higher temperatures, that is at 300^0C and 400^0C. These above yield criteria did not consider the effect of anisotropy. Hill in 1948 [305] presented the concept of anisotropy in forming of sheet metal components. He extended the concept of the von Mises criterion and introduced a modified form of it by considering varations in properties of materials in different directions.

$$\begin{aligned} F\left(\sigma_{yy}-\sigma_{zz}\right)^2 + G(\sigma_{zz}-\sigma_{xx})^2 + \; H\left(\sigma_{xx}-\sigma_{yy}\right)^2 \\ +2\left(L\sigma_{xy}{}^2 + M\,\sigma_{yz}{}^2 + N\,\sigma_{zx}{}^2\right) \;=\; \sigma_s{}^2 \end{aligned} \qquad (11)$$

Where *F,G,H,L,M* and *N* are referred to as material constants obtained in different rolling directions. This quadratic yield criterion is only valid for ferrous materials. In 1990 Hill, [306] suggested a yield criterion for non-quadratic functions to predict flow behaviour of non-ferrous materials. He represented a planar isotropy expression for the plane stress condition.

$$|\sigma_1+\sigma_2\,|^z + (1+2\mathrm{r})^z|\sigma_1-\sigma_2|^z = 2\;(1+r)\;\sigma_s{}^n \qquad (12)$$

Where σ_1 and σ_2 are principal stress components, r is the so-called Lankford coefficient that varies according to the rolling direction of the material.

Several other models were also created by considering various different effects, such as Brain and Lian [307] anticipating orthotropic sheet behaviour by considering planar anisotropy under the folding effects of sheets. Barlat also introduced his law in 1991 [308] by considering tri-axial loading, and distributed the yield function into six components. His model is represented as:

$$\begin{aligned} (3I_2)^{\frac{c}{2}}\{\;[2\;Cos\;\left(\frac{2\theta+\;\pi}{6}\right)]^c + \left[-2\;cos\;\left(\frac{2\theta-3\;\pi}{6}\right)\right]^c \\ +[2\;cos\;\left(\tfrac{2\theta+\;5\pi}{6}\right)]^c\;\} = 2\;\sigma_s{}^c \end{aligned} \qquad (13)$$

Where, c is material constant, I_2 is the second invariant of stress and θ is the angle that depends on the second and third invariants of stress.

Barlat et al. [309] proposed a generalised model for the plasticity yield function by using a binary magnesium-aluminium sheet with varying microstructure in 1997. In addition to this, Barlat et al. in 2003 [310] used the Cauchy stress tensor and multiple linear transformations to predict the yield function that accurately describes the anisotropic nature of sheet. Yoon et al. in

2004 [311] described a comparison of yield surfaces with r values for aluminium alloys. Barlat et al. in 2005 [312] proposed yield function relationships with the stress deviator by using linear transformations.

Further, various other contributions added to yield prediction models. Barlat and Yoon [313] focussed on directionalities in yield stress functions in 2011. Other contributions include Ghavam et al. in 2010 [314], Bagheriasl et al. in 2011 [315], Desmorat and Marull Paquet et al. in 2012 [316], Segurado et al. in 2012 [317] and Abedrabbo in 2013 [318]. These references indicate that yield criteria play a significant role in predicting material behaviour at room temperature as well as at higher temperatures.

3.8 Formability prediction models

Formability prediction is important in planning experiments and production processes. It is therefore important to have some useful numerical relationships. Several factors like geometry, mechanical set-up, materials etc. [319] are involved in a theoritical prediction. Among several available models, four models are most commonly used. Swift’s diffused instability criterion and Hill’s localised instability criterion are sensitive to work-hardenning factors, but cannot provide an accurate prediction for heated tests. A further two models are the Marciniak-Kuczinski’s model and the Maximum Force Criterion [320].

3.8.1 Swift’s diffused instability criterion

Swift’s maximum force criterion is one of the oldest formability prediction models. It was developed by H.W. Swift in 1952 [321]. The concept of the limit-drawing ratio as a measurement of formability of material was also proposed by Swift,where he described a linear relationship between drawing force and drawing ratio.

Swift’s model is based on diffused necking,which is a phenomenon in sheet materials where all material is made to concentrate at a narrow width of a sample due to the applied load. After the start of diffused necking, strains ceases linear relationship with stresses. In this work-hardening zone, the stress/strain relationship is represented by a power law that can be mathematically represented as:

$$\sigma = Z (\varepsilon^{p})^{s} \tag{14}$$

Where Z is a stress coeffiecient, ε^{p} represents the amount of strain in the plastic zone and s is the leading strain hardening exponent.

Swift's model for diffused necking in sheet metal parts is represented as:

$$\mathcal{E}_{cr} = \frac{2s\,(1 + \alpha_{\varepsilon} + \alpha_{\varepsilon}^{2})}{(\alpha_{\varepsilon} + 1)(2\alpha_{\varepsilon}^{2} - \alpha_{\varepsilon} + 2)} \tag{15}$$

Where $\mathcal{E}_{cr}$ is critical major strain and α_{ε} represents the ratio of strains in different directions. As this model is based on strain ratios in various directions in the necked area, chances of inaccuracy increase on the left side of the FLD where the width of samples is smallerthan the right side.

3.8.2 Hill's criterion for confined necking

Hill proposed his criterion for confined necking in 1952 [322]. He introduced the concept of zero extension or elongation in the confined necked region. His criterion is based on the following assumptions:

a. The ratio of strain in various directions (α_{ε}) is constant until the onset of necking in a confined zone
b. The inclination of confined bands is constant with zero elongation in all loading directions
c. Material should be rigid and plastic.

Based on these assumptions, the ratio of critical strains can be defined as:

$$\mathcal{E}_{cr} = \frac{s}{(\alpha_{\varepsilon} + 1)} \tag{16}$$

The angle of confined bands is represented as:

$$\mathcal{E}_{cr} = tan^{-1}\frac{1}{\sqrt{\alpha_{\varepsilon}}} \tag{17}$$

3.8.3 Marciniak-Kuczinski (M-K) model

The M-K model was proposed by Marciniak and Kuczinski in 1967 [323] and is the most widely accepted model for the prediction of FLCs of various materials.

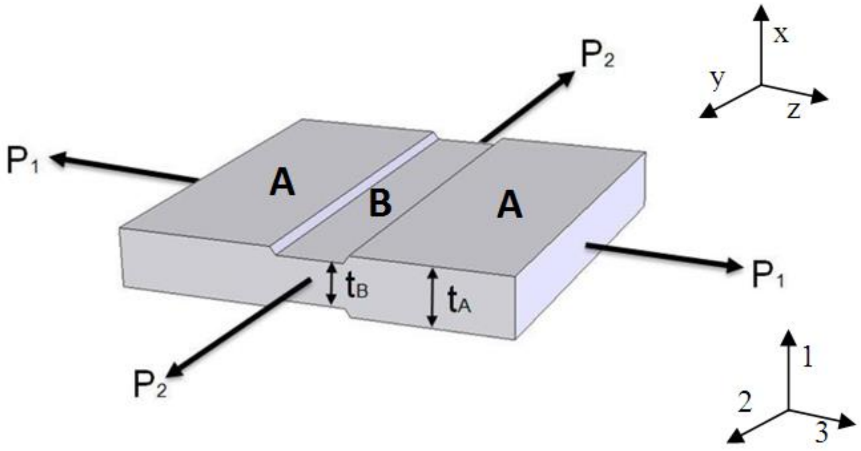

Figure 34. Representation of test sample for M-K model [323]

This model is based on the assumption of inhomogeneity with a groove (or imperfection) is present in a sample. A view of that imperfection is shown in Figure 34.

According to this model, several imperfections are present in sheet materials including geometrical imperfections such as thickness variations or structural imperfections with several types of gaps and inclusions. As a result, under applied loads these imperfections progress accordingly and plastic deformation is confined to these special zones, which result in the appearance of a necking band. The model was widely used because of its relatively accurate formability prediction of various materials. However, several researchers have also found that it overestimates imperfections or inhomogenity parameters and is more sensitive to constitutive equations.

According to the M-K model, a sample is divided into two regions with ‘A’ as the homogeneous region and ‘B’ as the inhomogeneous region. Defining x,y,z as three rolling directions and 1,2,3 representing the principal directions, the ratio of strains in various directions is defined by the imperfection parameter or coefficient of non-homegenity (ζ), which can be determined as grooved thickness (t_B) to original sample thickness (t_A).

$$\zeta = \frac{t_B}{t_A} \tag{18}$$

Straining of an inhomegenious sheet is defined by the ratio of principal strains of sections 'A' and 'B'. Principal strains in two zones are defined by $\varepsilon_{1,A}$, $\varepsilon_{2,A}$ and $\varepsilon_{1,B}$,$\varepsilon_{2,B.}$ So when strain in section 'B' exceeds section 'A' ($\varepsilon_{1,B} >> \varepsilon_{1,A}$ or $\varepsilon_{1,B} > 10\varepsilon_{1,A}$), the material is assumed to be cracked.

Several researchers have implemented this model for the construction of FLCs. The shape of the yield locus (drawn by ratio of strains in two sections) was higlighted by Banabic (2012) [324]. Texture-based models were also tested initially by Bate in 1984 and recently by Wu et al. in 2013 [325]. Amongst all available FLCs prediction models, the M-K model is the most popular and accurate.

3.8.4 Vertex model

The vertex model is another FLC prediction model, based on the combined concept of flow localisation and vertex generation of the yield surface. The vertex model was presented by Storen and Rice in 1975 [326]. According to them, confined flow in a grooved region (B) starts simultaneously with vertex generation on the yield surface. This theory mainly focussed on rate-independent materials. Zhu, Weinnen and Chandra in 2001 [327] modified this mathematical form to enable it to be used in a higher-order yield criterion.

Based on these assumptions, the ratio of critical strains can be defined in two ways: one when the strain ratio is positive and the other when it is less than zero as, then the equations are:

$$\varepsilon_{cr} = \frac{3\alpha_\varepsilon{}^2 + s\,(2 + \alpha_\varepsilon)^2}{2(1 + \alpha_\varepsilon + \alpha_\varepsilon{}^2)} \tag{19}$$

where $\alpha_\varepsilon \geq 0$,

and for $\alpha_\varepsilon < 0$

$$\varepsilon_{cr} = \frac{2s}{(1-s)(\,1+\ \alpha_\varepsilon) + \sqrt{[(1+s)(1+\alpha_\varepsilon)^2 - 4s{\alpha_\varepsilon}^2}} \tag{20}$$

3.9 Conclusion

In this chapter, magnesium formability was discussed along with its pre-forming and post-forming characteristics. It can be concluded that magnesium alloys have good formability at elevated temperatures and at lower punch speeds. However, different process parameters can be varied to improve formability.

Despite all the above discussions, magnesium alloys are still difficult to form at a commercial level. To improve its formability, a study is now being conducted by the author into microstructural characteristics to understand the behaviour and flow of the material to maintain a uniform temperature and thickness distribution during forming. Process parameters need stronger control during forming. It should also be noted that by varying the blank-holder force, further enhancement of the formability is possible. The punch temperature should always be kept lower than the sheet temperature and the recommended difference is 50^0C to 90^0C for non-isothermal deep-drawing tests. This will also reduce flow stress in the flange of the formed part. Spring-back effects are important at warm temperatures especially in non-isothermal tests.

Texture effects during forming need more attention to improve formability. Basal-type texture has a strong influence on the formability of AZ series wrought magnesium alloys, and basal plane inclination is a major factor that needs to be examined accurately to improve formability. For more accuracy in drawing of forming limit curves, a more detailed study is required into frictional effects and bending strains in both in-plane and out-of-plane test methods.

Various types of yield criteria were also discussed and compared to predict yielding, so that material behaviour can be modelled accurately. Similarly, prediction of formability is also quite necessary to forecast crack initiation, so that during the actual forming process it can be avoided.

In Chapter 5, the experimental results of tests of formability of magnesium AZ80 will be discussed in light of this literature review and discussion.

Chapter 4

Ductility of AZ80 Magnesium Alloys

4.1 Introduction

Tensile testing, a simple type of stretch forming, as discussed in chapter 3, is a basic step to revealing material behaviour under various test conditions. In this chapter, the tensile characteristics of magnesium AZ80 are discussed at various temperatures, strain rates, grain sizes and rolling directions. Later, these characteristics are matched with multi-axial forming characteristics and some valid conclusions are drawn. Magnesium AZ80 was analysed by considering two grain sizes: coarse and fine. Fine-grain AZ80 was received after annealing and hot rolling and was therefore named as AZ80 – O, with an average grain size of 10µm, while a coarse-grain alloy was received and symbolised as AZ80 – F, with a grain size of 35 µm. The purpose of selecting two grain sizes was to study the effect of grain size on the mechanical, material and forming characteristics of magnesium AZ80. As discussed in section 2.3.2, grain size has a strong influence on the deformation mechanism, and a comparison of changes in the deformation mechanism with respect to grain size and temperature is shown in Figure 15 [102]. A distinction between twinning and slip regions is clearly visible with variations in grain size and temperature. In addition, the effect of grain size was analysed in relation to enhancing ductility up to the superplastic range, in section 2.3.

In this chapter, various issues with tensile testing are discussed relative to machine performance, gripping of samples, heating of samples at higher temperatures such as 400^0C, maintaining and measuring continuous temperatures, geometrical problems, heating time and availability of testing standards. Various parameters such as proportional limit, yield strength and fracture strain were obtained through stress strain curves at room and at elevated temperatures. Other observations, including variation in flow stress, fracture strain, percentage elongation with respect to strain rate and temperature, strain rate sensitivity index (m), and anisotropy characteristics were also investigated with respect to variation in grain size. A brief discussion of deformation mechanisms at room temperature as well as at higher temperatures is also given. Details of these are discussed along with SEM and TEM micrographs in Chapter 6.

Despite previous background studies, the mechanical properties of magnesium alloys are still not very well understood. For example, the effect of grain size has not been analysed in relation to failure mechanisms, anisotropy and ductility. In this chapter, regular tensile tests are performed with various grain sizes, temperatures, strain rates and rolling directions. Load displacement curves were obtained and analysed under test conditions. Moreover, two stage tensile tests were performed to minimise the effect of cavitation at higher temperatures, as described in section 2.8, and the effects of grain size and rolling direction were analysed in accordance with test conditions. Due to two-stage tensile test deformations, the amount of cavitation was reduced significantly, which leads to an increase in the ductility of materials and failure typically occurred because of necking instead of cavitation. Flow stress curves were also generated at a strain rate of 0.1 to obtain a strain rate sensitivity index without any grain growth influences.

4.2 Uniaxial tensile testing issues

Tensile tests are quite simple and swift at room temperature, but very challenging when done at high temperatures. This is due to the rapid variation in microstructure, which enhances strains generated in the material. There are several studies available of high temperature tensile testing, but none of them have clearly highlighted the effects while heating the materials. In addition, most of the available testing standards such as ASTM, ASME and ASM do not provide detailed testing procedures and geometric shapes for high temperature testing of materials. JIS standards were first to publish a few guidelines related to superplastic testing in JIS H7501 [328], and later on similar procedures were published by ASTM, with ASTM E21 [329] and ISO 783 [330] in 2005 and 2007 respectively. ASM [331] also published their book related to tensile testing, but again, it lacks key issues faced during high temperature testing. In spite of these standards, most researchers do not follow them because they do not adequately nor authentically provide solutions to elevated temperature tensile testing.

This also explains why there are huge variations in results of experiments, and most of the available data is scattered and not replicable. Custom-made procedures have been adopted in most studies, which are not justified according to standards that are suitable at room temperature. When dealing with high temperatures (up to 400^0C), several issues are encountered which can be classified as follows:

i. Tensile Testing Machine issues
ii. Clamping issues
iii. Geometric issues
iv. Measurement issues
v. Material flow and expansion issues
vi. Testing time issues

All these need to be addressed in standards that provide guidelines related to elevated temperature testing.

4.2.1 Tensile testing machine

The tensile tests were performed at the Engineering Research Institute (ERI) in the Centre for Advanced Manufacturing Technologies of AUT. A Hounsfield universal tensile testing machine (UTM) was used, along with a separate split heating chamber from Jinan Testing equipment in China, as shown in Figure 35. The UTM has a maximum load capacity of 50kN with a speed accuracy of 0.05% and force accuracy of 0.5%. The crosshead speed was maintained at 10mm/min, 1mm/min and 0.1 mm/min. The heating chamber has a maximum heating capacity of 1200^0C with PID control. It is equipped with three K-type thermocouples to monitor temperatures in upper, middle and lower zones, with an accuracy of ± 3^0C. It also contains a water pump that can be used for the circulation of cooling water in case of excessive heat. The major issue faced concerning the tensile testing machines was the heating of load cells when heating time increased due to a slow strain rate. To tackle this issue, separate insulated pads were used that restrict the effect of heat transfer to load cells.

4.2.2 Gripping issues

Firm gripping of samples in a tensile testing machine is necessary for accuracy of results. Slippage in tensile testing is a common issue during high temperature heating. If slippage occurs on the shoulders of test specimens, an abrupt decrease will be observed in stress strain values.

Once again, aforementioned standards were unable to provide specific designs for grips that can be adapted to high temperature testing. The original grips were a pair. Both were wedge-shaped, with knurled marks on it to hold the specimens' shoulders. These grips were quite useful for room temperature tests but unable to hold samples at elevated temperatures, because at high temperature the material may soften and the gripping pressure is reduced suddenly.

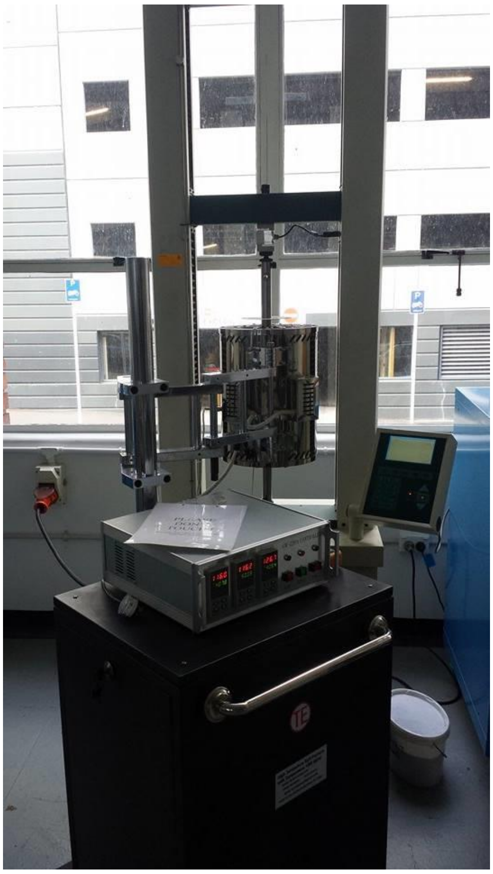

Figure 35. Hounsfield H50KS Universal tensile testing machine

Another problem with these grips is that they apply pressure on surface areas which restrict material flow into the gauge area. Therefore, special sample holders were machined with holes at the ends instead of wedge-shaped edges, as shown in Figure 36. Samples could be held with simple pins. These holders allowed quick and easy mounting and removal of samples from tensile testers.

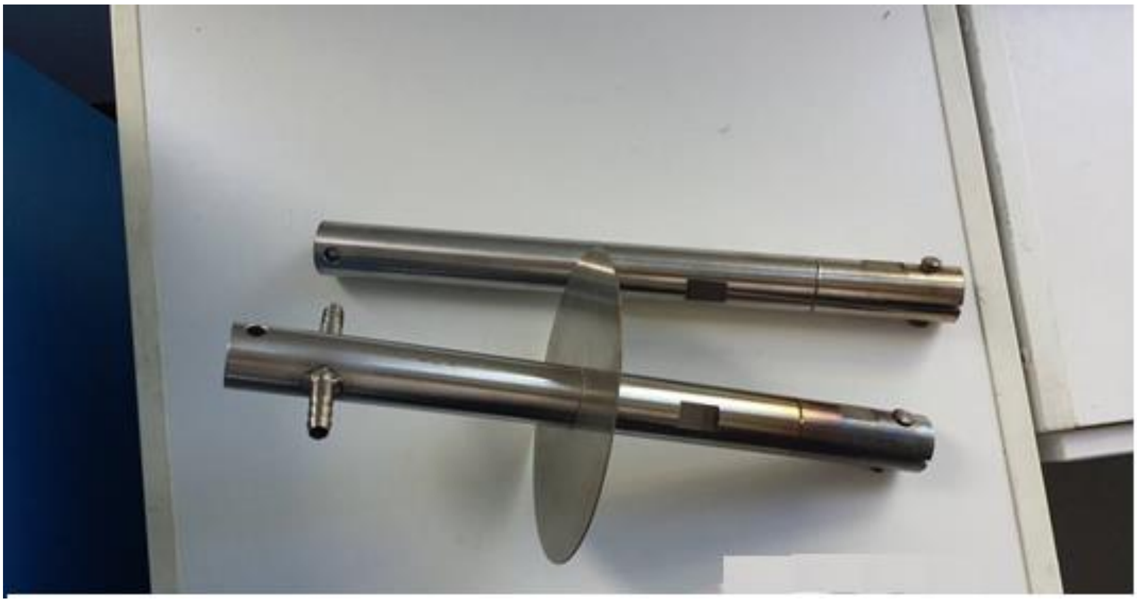

Figure 36. Special grips for Hounsfield H50KS Universal tensile testing machine

They are designed in such a way that the number of moving parts is reduced to avert slippage issues at higher temperatures, and so that a minimum load will be applied on the surfaces of specimens.

4.2.3 Geometric issues

The geometry of test samples directly affects the time required during tests and strain measurements of material. Standard lengths, as defined by ASTM E21, will take more than 48 hours for a single test at a strain rate of 10^{-4} sec^{-1}. This could be damaging for grips and machinery, because they can’t bear that much continuous heat. In addition, much energy will be wasted if large numbers of samples are tested using that design. ISO and JIS standards also do not address these issues of specific lengths of samples at unique strain rates to avoid long testing times. ASM standards define minimum sizes that can be machined for the samples, where larger lengths cannot be machined. The gauge length selected was 15mm with a gauge width of 3mm. Typical dimensions are given in Figure 37. Samples were CNC-machined and holes were drilled in shoulders to grip them securely.

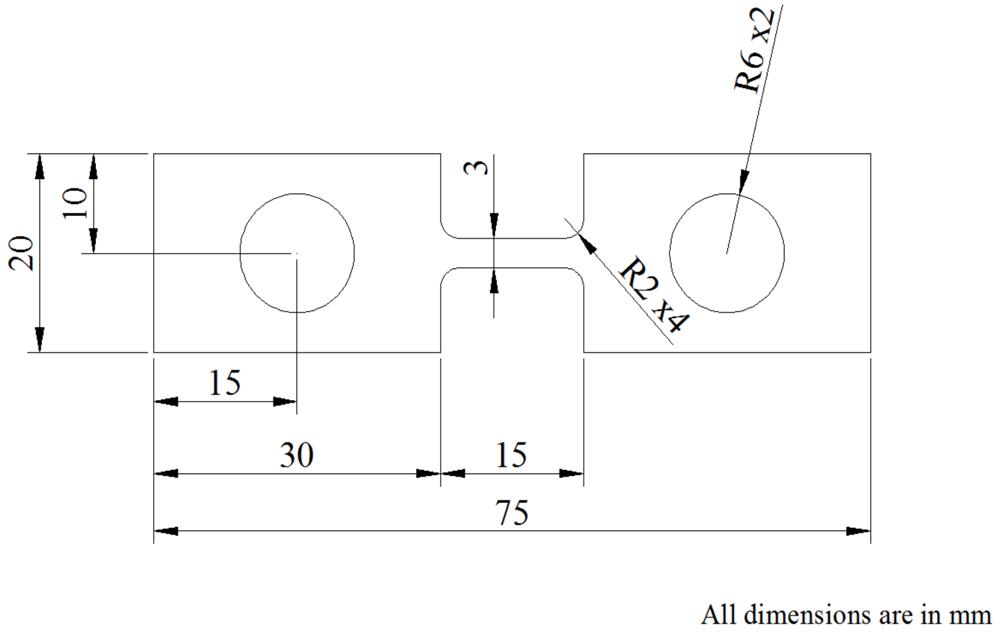

Figure 37. Dog bone tensile sample

4.2.4 Measurement issues

The measurement of accurate values is one of the major issues that can also occur during high-temperature tensile tests.

Initially, a dual input thermometer was used along with thermocouples. A K-type thermocouple was attached to the gauge section with aluminium tape to accurately measure the temperature of the specimen at different intervals, in order to monitor any temperature drop during tests.

In low strain rate tests, load cells continuously bore heat from the heating chamber, which could affect the accuracy of results. It was noticed that when a sample broke and two pieces were quite separate, the load cell was still showing a reading of 5 to 10N in various tests, however, after rechecking at room temperature, they were working accurately and reading a zero value.

An increment of 10N at 400^0C and 10^{-4} sec^{-1} is approximately equal to 0.4MPa of true stress (or 13% of flow stress). Therefore, separate insulators were placed on load cells to minimize the effect of heating and increase the accuracy of results. In addition, a small fan was used to blow heat away from load cells.

4.2.5 Material flow and expansion issues

Material flow occurs from shoulders to the gauge area exclusively at higher temperatures. Slippage is also a common problem in these conditions, as mentioned previously. To tackle this, special grips were manufactured with 10mm holes. A disc was also welded on top, to preserve heat inside the heating chamber. Similar holes of 10.5mm diameter were drilled in specimens' shoulders so that a proper grip could be taken and ease of material flow could also be provided at high temperatures.

Thermal expansion of specimens is also a unique problem faced during testing. Most standards adopt two types of procedure related to thermal expansion [332]. ISO 783, JIS H7501 and ASM suggest heating a specimen while it is clamped with grips inside the heating chamber, however ASTM E21 recommends heating a specimen in a separate furnace. The latter is preferred by only a few researchers because it is quite difficult to transfer a heated specimen from a furnace to the tensile testing machine and then grip it firmly [333]. Another problem is the microstructure changes that can occur in a specimen due to moving the specimen from a furnace to the tensile testing machine. On top of that, additional time would be required to attain thermal equilibrium between the specimen and grips [334]. The first option is quite simple and also suggested by most standards, however, no standard addresses problems that occur from continuous heating. In some studies [335], it was reported that with continuous heating, compressive stresses develop in the material that could lead specimens to buckle. But this is still quite simple to handle and that is why heating within the testing machine is adopted by most standards.

To avoid any slip and thermal expansion as described earlier, the test specimen was gripped only from the top side and held freely from the lower side, so that any compressive stresses could be reduced before testing. Once the specimen had acquired the specific temperature, the lower side of the specimen was clamped and the test was started. Usually a specimen took about 15 – 20 minutes to achieve the required temperatures.

Moreover, the thermal coefficient of magnesium AZ80 is lower than the one of steel and aluminium, so it barely influences strain values. The thermal expansion coefficient of magnesium AZ80 is 28.9 x10^{-6} (mm / (mm K)) from room temperature to 450^0C. According to the ASM handbook of tensile testing at 400^0C, only 1.1% variation in gauge length occurs, which is approximately 0.2mm over a gauge length of 15mm. At 200^0C and 300^0C, increments of gauge length vary from 0.62% to 0.80%. Therefore thermal expansion of specimens during heating inside the chamber is ignored.

4.2.6 Testing time issues

Testing time is usually referred to as the amount of time spent for heating and testing of materials. Heating time includes heating of a specimen as well as time that is spent for achieving the equilibrium of specimens inside the grips. As mentioned earlier, to reduce testing time ASM standards were adopted and micro specimens were machined on a CNC mill with a 15mm gauge length and 3mm gauge width. In addition, 15 to 20 minutes were spent on each specimen to attain thermal equilibrium inside the heating chamber, so that the accuracy of results could be improved.

4.3 Experimental Procedure

AZ80 sheets with variations in grain size were sourced from Doo Won Industrial Company, Limited, Korea. Sheets were manufactured in two types, one with fine grain size (10µm) and the other with coarse grain size (35 µm). Coarse grain-size sheets of AZ80 – F were as extruded and cold rolled, however, to cultivate a fine grain-size additional heat treatment was provided at 200^0C and referred to as AZ80 – O. All sheets had a thickness of 0.8 ± 0.02mm. The chemical composition of magnesium AZ80 is given in Table 12. Samples were designed with a CAD package with gauge dimensions of 15 x 3 x 0.8 mm^3, as shown in Figure 37.

Table 12. Chemical composition of AZ80 as fraction of mass (%)

Al	Zn	Mn	Fe	Si	Cu	Ni	Mg
8.9	0.54	0.22	<0.006	<0.02	<0.01	<0.001	balance

To investigate anisotropy in materials, specimens were taken in three different rolling directions (RD), one along the rolling direction of the sheet at 0^0 termed loading direction (LD), the second at an angle of 45^0 to RD (AD) and the third in a transverse direction (TD) at 90^0 to the rolling direction of the sheet. After taking these samples they were machined in a dog-bone shape on a CNC mill instead of conventional milling, to avoid any changes in microstructure during machining, because the CNC machine is fast and accurate. The gauge radius was kept at 2mm, while 10.5mm holes were machined on shoulders to hold the samples firmly in grips.

4.4 Design of experiments

Tests were designed to thoroughly examine tensile characteristics. The aim of the tests was to identify yield stress, elastic strength, fracture strain, a strain rate sensitivity index (m), anisotropy ratio and effects of texture on material properties. All these properties were examined at four temperatures, that is, from room temperature to 400^{0}C. Test conditions were limited to a temperature of 400^{0}C due to apparatus limitations and also the melting point of magnesium of around 650^{0}C. A series of repeated tests (3 tests at every temperature and strain rate) were performed to ensure the accuracy of results. In addition, three strain rates were selected according to the commercial production-speed limits of sheet metal parts. The crosshead speed was maintained at 10mm/min., 1mm/min. and 0.1 mm/min. Strain rates were calculated accordingly, by using the gauge length and strain rate that are 1x10^{-2} sec^{-1}, 1x10^{-3} sec^{-1} and 1x10^{-4} sec^{-1}. Further, to investigate the effect of texture in warm and hot conditions, the anisotropy ratio was measured on textured specimens at the above mentioned temperatures and strain rates.

4.5 Results and discussion

4.5.1 Room temperature tests

Tensile tests were carried out at room temperature to examine mechanical properties and initial anisotropy. As discussed previously in chapter 2, magnesium alloys exhibit less ductility at room temperature due to the limited availability of slip systems, according to the von Mises criterion of independent slip systems required for homogeneous deformations. Furthermore, a strong (influence of) basal texture plays a key role in limiting the ductility of magnesium alloys as compared with other sheet metal materials.

To study material properties over a wide range, specimens were divided according to variations in grain sizes: fine (AZ80 – O) and coarse grain (AZ80 – F) materials, which were further subdivided into three families, associated with their rolling directions; that are 0^0 (LD), 45^0 (AD) and 90^0 (TD). Tests were performed at three speeds, and later speeds were converted to strain rates by using the gauge dimensions of samples. The selected strain rates were $1x10^{-2}$ sec^{-1}, $1x10^{-3}$ sec^{-1} and$1x10^{-4}$ sec^{-1}.

Figures 38 – 39 show stress strain curves of both AZ80 – O and AZ80 – F in all three rolling directions at room temperature. It is quite obvious that AZ80 – O exhibits greater elongation than AZ80 – F, due to its fine grains and additional thermo-mechanical processing, i.e. rolling at elevated temperatures.

Also with an increase in the number of passes of rolling and of heat treatment, strain hardening is more significant due to a reduced domination of basal slips, as discussed in section 2.3.1 Therefore, fine-grain alloys are more ductile than coarse-grain ones.

The summary of the results is shown in Tables 13 and 14. A comparison of yield strength, tensile strength and fracture strain is given amongst specimens with different rolling directions and at two strain rates. 0.2% proof stress is obtained by graphical methods. Results clearly indicate that 0.2% proof strength shows inversely proportional behaviour with grain size.

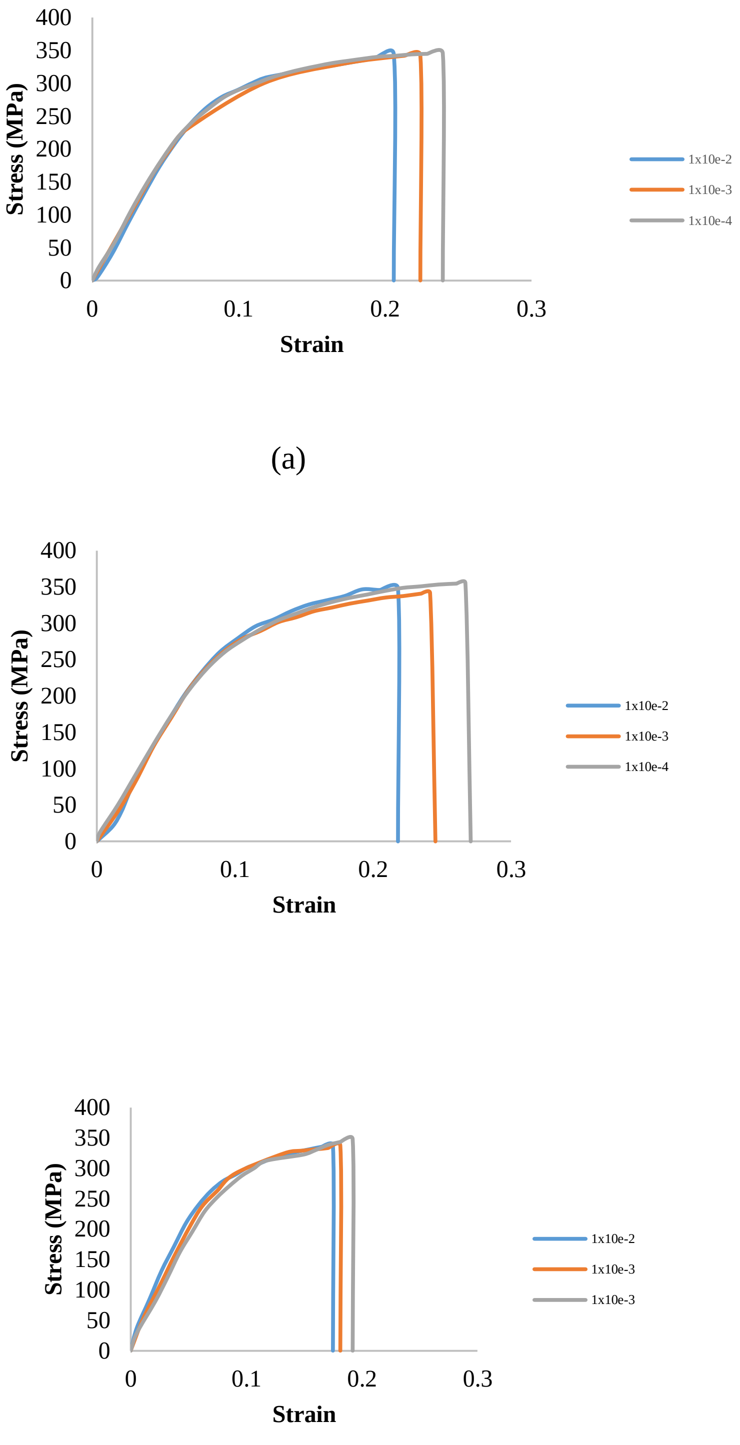

(a)

(b)

(c)

Figure 38. Stress strain curves of AZ80-O (Fine) at room temperatures and various strain rates (a) 0^0 (b) 45^0 (c) 90^0

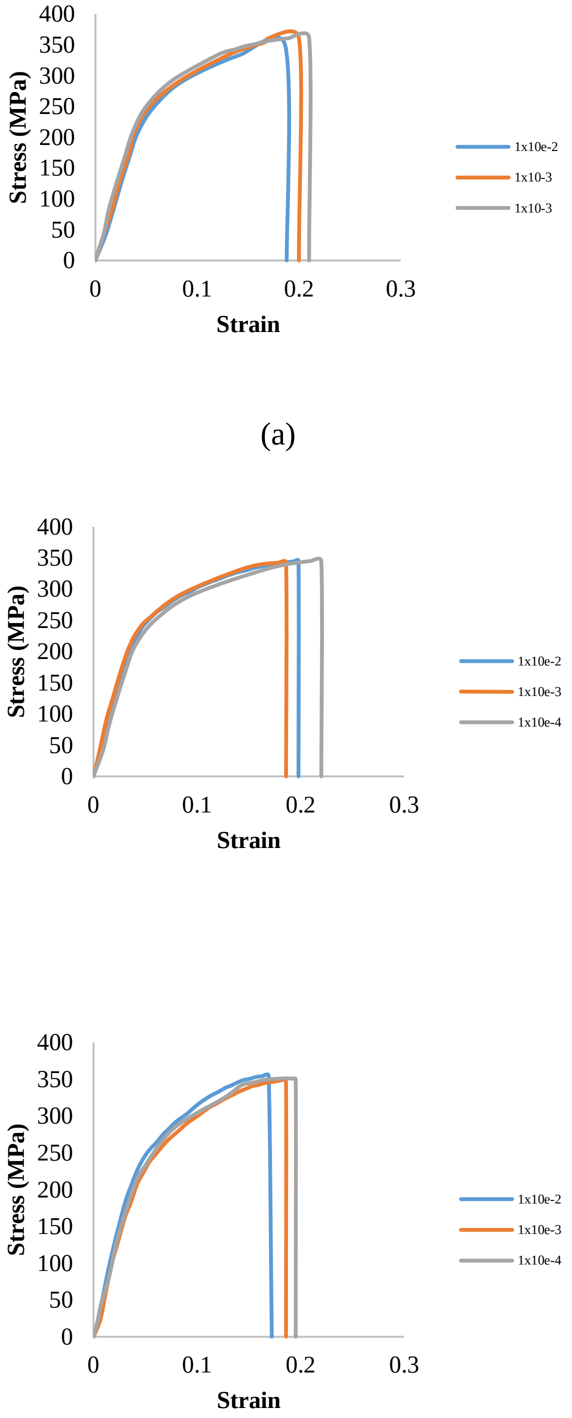

(a)

(b)

(c)

Figure 39. Stress strain curves of AZ80-F (Coarse) at room temperatures and various strain rates (a)0^0 (b) 45^0 (c) 90^0

Table 13. Mechanical properties of AZ80 – O and AZ80 – F at room temperature (RT) and 1x10^{-3} sec^{-1}

Material	Orientation	Proportional Limit [MPa]	Yield Strength [MPa]	Ultimate Tensile Strength [MPa]	Fracture Strain
AZ80-O	**0^{0}RD**	180	200	341	0.22
	45^{0}RD	215	230	340	0.24
	90^{0}RD	195	218	355	0.26
AZ80-F	**0^{0}RD**	225	235	360	0.2
	45^{0}RD	235	250	355	0.186
	90^{0}RD	215	235	365	0.185

Table 14. Mechanical properties of AZ80 – O and AZ80 – F at room temperature (RT) and 1x10^{-4} sec^{-1}

Material	Orientation	Proportional Limit [MPa]	Yield Strength [MPa]	Ultimate Tensile Strength [MPa]	Fracture Strain
AZ80-O	**0^{0}RD**	175	195	325	0.24
	45^{0}RD	195	212	338	0.26
	90^{0}RD	190	215	347	0.19
AZ80-F	**0^{0}RD**	214	220	361	0.21
	45^{0}RD	195	210	345	0.22
	90^{0}RD	175	183	350	0.19

Similarly 45^0 RD samples show more elongation before failure at both strain rates, due to the reduced effect of basal slip at room temperature as compared with the other two directions.

The second factor examined was the influence of variation in strain rates on mechanical characteristics. As discussed, magnesium alloys are quite sensitive to strain rates. This sensitivity was highlighted here by plotting load-displacement data curves, at three strain rates. In all curves variations in strain rate impose a considerable increase in percentage elongation and fracture strains in both coarse and fine grain alloys as shown in Figures 38 and 39. It is also worth noting that peak stresses and yield strength show inversely proportional behaviour with strain rates, because of an increased number of twins at slower speeds, as discussed in section 2.4.2 [101]. According to Tables 13 and 14, the proportional limit decreases from 5 to 9 percent for coarse grain and up to 18 percent for fine grain, similarly yield strength reduces by 22 percent, tensile strength lowers by 5 percent and fracture strain increases up to 18 percent of total strain. These figures indicate that strain rate greatly affects process parameters in processing magnesium alloys. However, its influence on mechanical characteristics will drastically increase at elevated temperatures, when the deformation mechanism will be governed by GBS instead of twinning [104]. Details of elevated temperature tests are discussed in the next section of this chapter.

The third significant effect considered here is anisotropy. Anisotropy plays a vital role in magnesium alloys at room temperature, however, its effects are reduced when magnesium alloys are processed at high temperatures. Anisotropy usually occurs in materials due to texture. Its effect can be minimised by controlling basal-slip textures in specified rolling directions, which is a strong governing mechanism in the deformation of magnesium alloys at room temperature. Anisotropy reduces the mechanical formability of alloys, mainly at room and warm temperatures.

Anisotropy of materials can be measured by the r value (also known as Lankford co-efficient), as discussed in section 3.3.2.4. As noted earlier, three rolling directions were considered here and their anisotropic characteristics are portrayed in Figure40. Stress strain curves are plotted for AZ80 – O and AZ80 – F at room temperature and various strain rates.

Three rolling directions curves are plotted: in 0^0RD, 45^0RD and 90^0RD with respect to fine and coarse grain at various strain rates. Each of these samples are stretched at three strain rates that vary from $1x10^{-2}$ sec^{-1} to $1x10^{-4}$ sec^{-1}, to check variations in mechanical characteristics over a wide range of strain rates at room temperature.

It is quite obvious that 45^0RD specimens show more elongation until failure than the other two directions, in both fine and coarse grain material. Both alloy variations show high peak stresses with high yield stresses. A strain-hardening region is also quite visible and dominating. A comparison of proportional limit, yield stress, ultimate tensile stress and fracture strain is listed in Tables 13 and 14, for strain rates of $1x10^{-3}$ sec^{-1} to $1x10^{-4}$ sec^{-1}. For AZ80 – O, the proportional limit varies from 215 to 180 MPa at $1x10^{-3}$ sec^{-1}, while the values show a smaller reduction at $1x10^{-4}$ sec^{-1} that ranges from 190 to 170MPa. Similarly, yield stress, ultimate tensile stress and fracture strain values show little reduction with a reducing strain rate. AZ80 – F also follows analogous behaviour at both strain rates.

Anisotropy of the sheets can be expressed as r-value (strain ratio):

$$r = \varepsilon_w / \varepsilon_t \tag{21}$$

Where ε_w is the strain in width and ε_t is the strain in thickness. Considering incompressibility, the strain in thickness can be calculated as:

$$\varepsilon_t = -(\varepsilon_l + \varepsilon_w) \tag{22}$$

$$r = - \varepsilon_w / (\varepsilon_l + \varepsilon_w) \tag{23}$$

Average r values (r_{avg}) can be calculated by using the following formula:

$$r_{avg} = \frac{r_0 + r_{90} + 2r_{45}}{4} \tag{24}$$

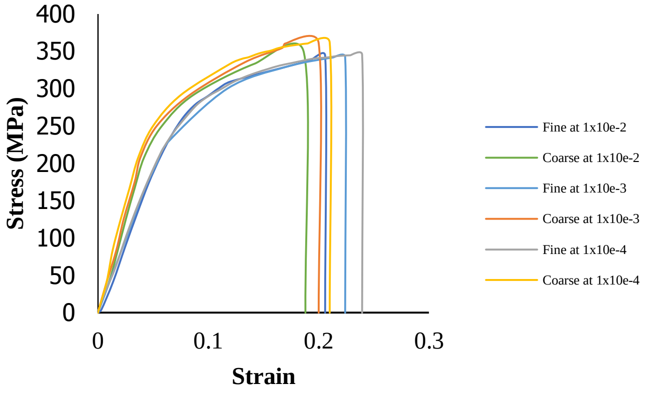

(a)

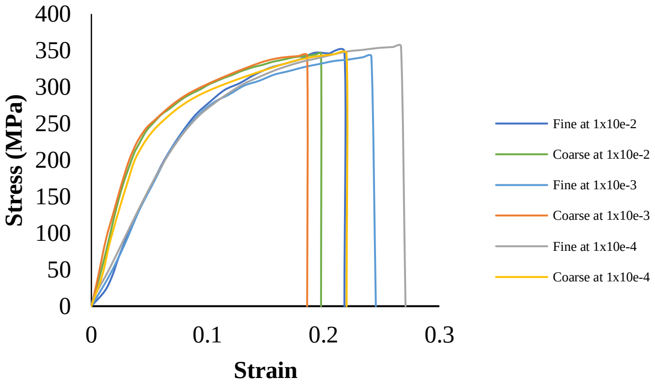

(b)

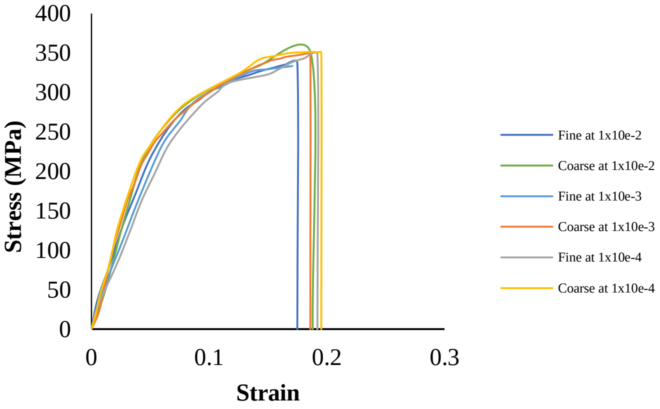

(c)

Figure 40. Comparison of AZ80 fine and coarse grain materials at room temperature.

Where r_0, r_{90} and $r_{45}$are r values in all three rolling directions respectively. A comparison of r values is given Table 15.

Table 15. Mechanical properties at room temperature (RT) and 1x10^{-3} sec^{-1}

Material	**Orientation**	**r – value**
AZ80-O	**0^0RD**	1.2
	45^0RD	1.6
	90^0RD	1.5
AZ80-F	**0^0RD**	1.8
	45^0RD	2.5
	90^0RD	2.1

To achieve improved formability, higher r – values are recommended. Measurement of anisotropy characteristics is necessary to reduce plastic deformation instability that is generated during tensile and compressive loads. Tensile instability normally refers to poor signs of necking before failure, and as mentioned, at room temperature magnesium alloys show low elongation, that is from 15 – 17 percent with minor indications of necking. Table 15 indicates r – values for both fine and coarse material.

Higher values of AD samples indicate that basal texture is quite strong in the 45^0 RD direction when compared with0^0 RD and 90^0 RD, for both fine and coarse grain alloys. It also indicates that critical resolved shear stress (CRSS) values are also higher in 45^0 RD than the other two.

4.5.2 Higher temperature tests

As discussed in the previous section, magnesium alloys exhibit poor ductility at room temperature, due to strong basal-slip dominance and absence of independent slip systems. It is therefore necessary to investigate their characteristics at elevated temperatures, along with other processing parameters, strain rate, grain size and texture. Careful selection of parameters is quite significant here as they will be relevant in deep-drawing processes.

In addition, the range of temperatures should be selected to cover most characteristics of magnesium alloys that are useful for enhanced ductility and also to maintain a significant distance from the melting temperature. In this research, three temperatures were selected: 200^0C, 300^0C and 400^0C, so that variation in ductility, flow stress, fracture strain and strain rate sensitivity, work hardening and amount of elongation could be examined. However, the strain rates used are similar to room temperature tests, so their characteristics can be compared in analogous conditions.

Anisotropy was examined at 0^0RD, 45^0RD and 90^0RD of samples. The influence of grain size was probed by having fine and coarse material. A new technique of two-stage tensile testing was introduced. In this technique, strain samples were tested, initially at 200^0C for a strain of 60% and later, the temperature was increased from 200^0C to 400^0C for the rest of elongations of 40%, so that effects of cavitation could be reduced in materials and failure of materials would be purely due to necking. In addition, strain rate was also varied along with temperature. Variable temperature increased the ductility of AZ80 – O from 153 percent at constant temperature of 400^0C to 205 percent with varying temperature for fine grain, while the coarse grain alloy's percentage elongation increased up to 186 percent with varying temperature as compared with the previous 140 percent at constant temperature of 400^0C and 10^{-4} sec^{-1}. Furthermore, a variation of strain rate from 1 x 10^{-4} sec^{-1} to 2 x 10^{-4} sec^{-1} along with variation in temperature in two-stage tensile testing gave an additional increase in elongation that is about 7 – 9 percent, which brought this alloy into the zone of superplastic alloys.

The results of the elevated temperature tests are shown in Figure 41. Figures 42 and 43 summarise the results of percentage elongation with respect to temperature and strain rate for AZ80 – O and AZ80 – F respectively. Both materials were tested from 200^0C to 400^0C at three different strain rates. As discussed, the AZ80 – O alloy shows more elongation than AZ80 – F did. Additional experimental curves of tensile tests are plotted in Appendix 1.

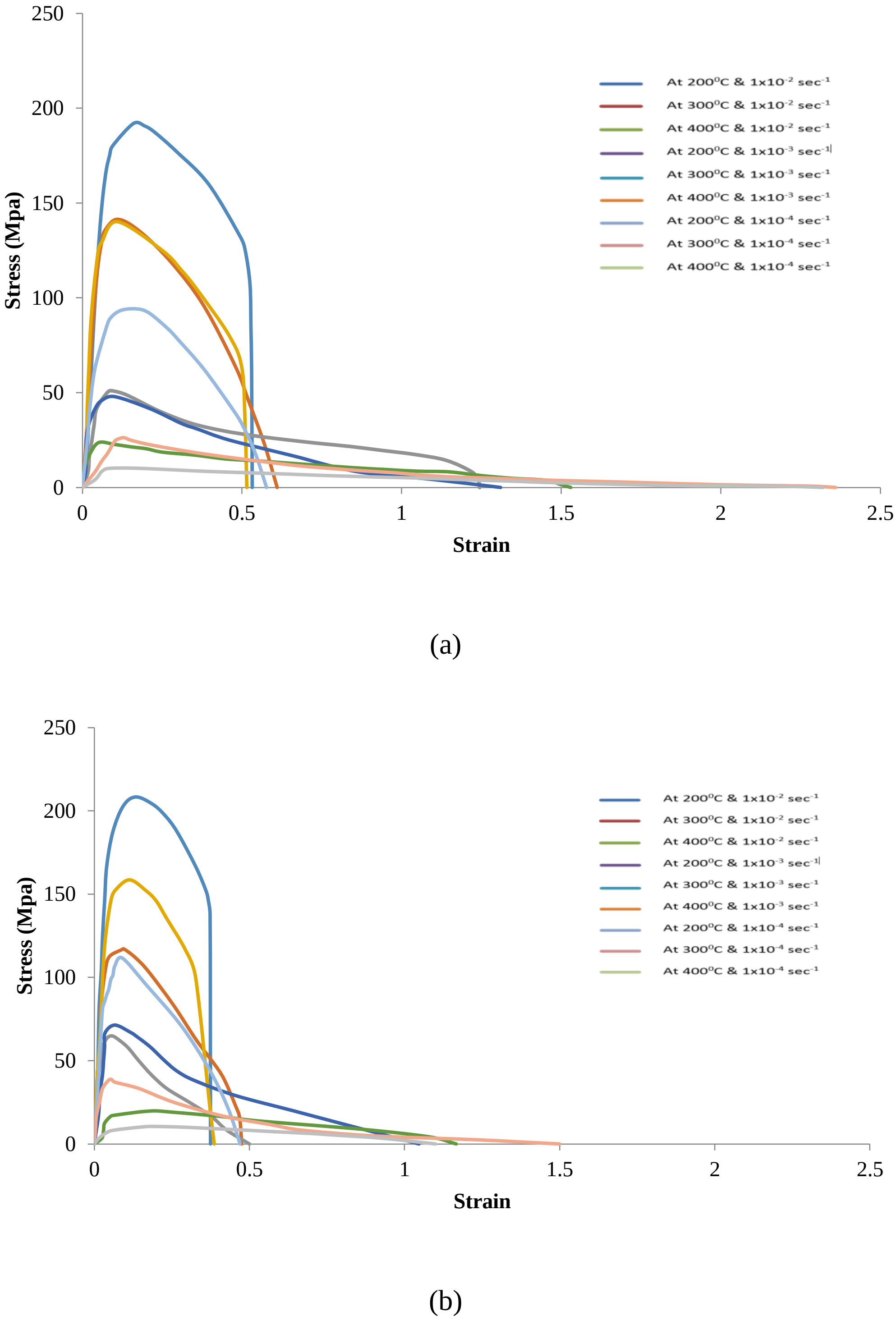

(a)

(b)

Figure 41. Comparison of AZ80 in LD at various temperatures and strain rates (a)Fine grain (b) Coarse grain

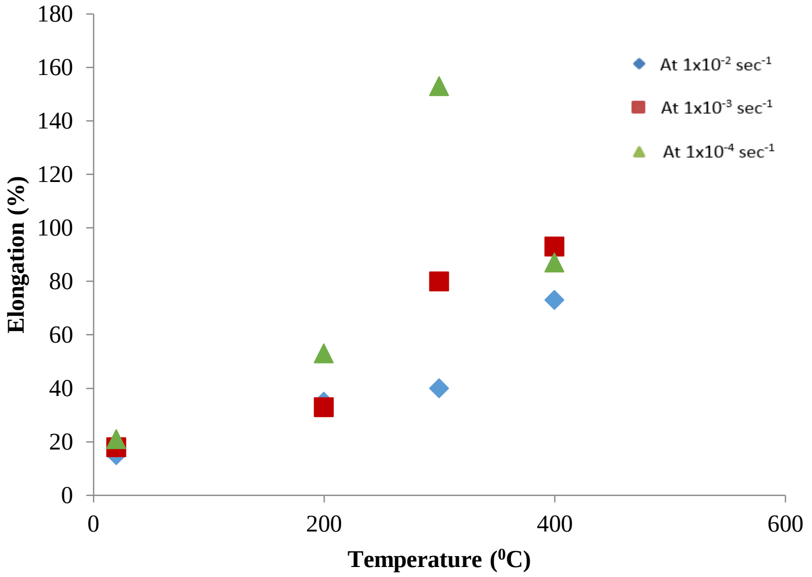

(a)

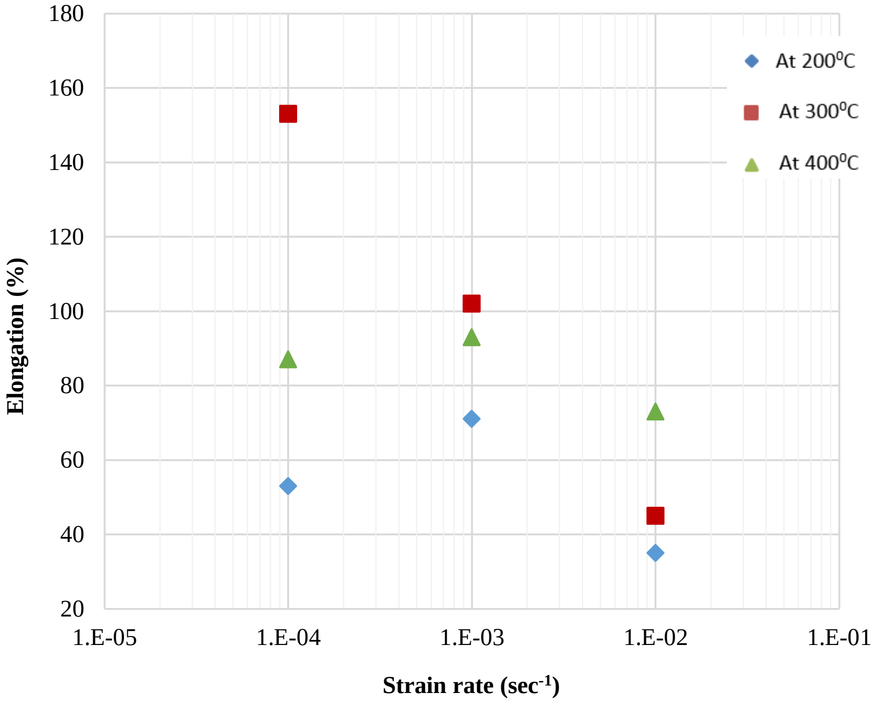

(b)

Figure 42. Comparison of elongation to failure in AZ80 – O vs (a) Temperature (b) Strain rate.

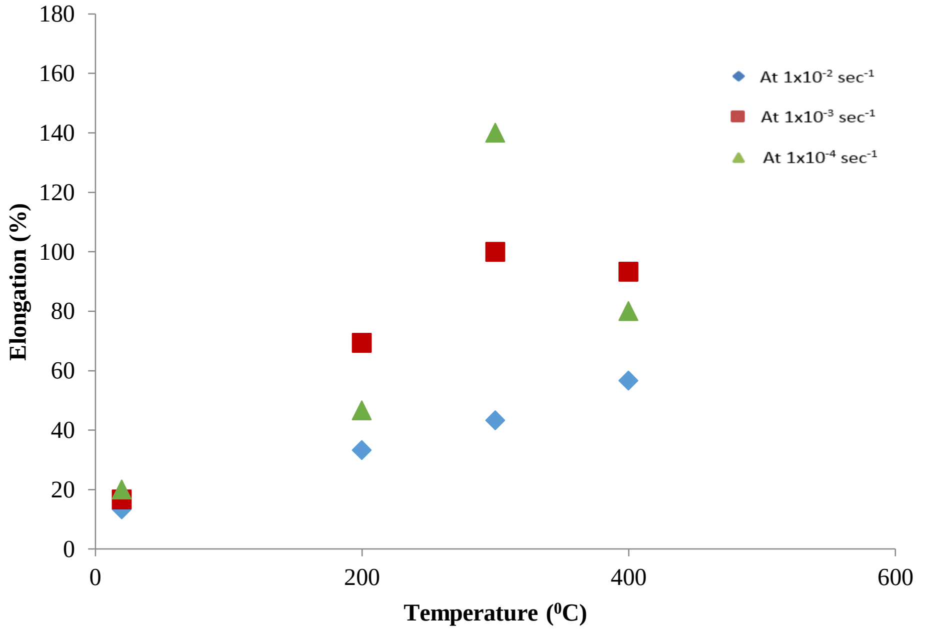

(a)

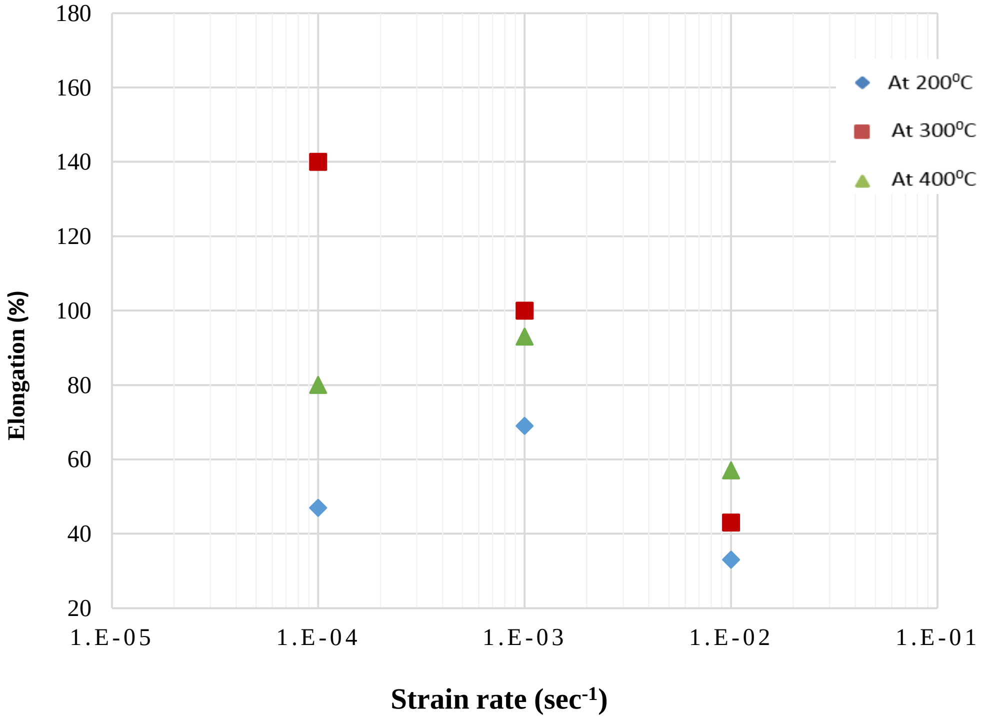

(b)

Figure 43. Comparison of elongation to failure in AZ80 – F vs (a) Temperature (b) Strain rate

4.6 Sensitivity of both alloys to variation in temperature

Both alloys showed strong sensitivity to temperature. Figure 41 shows stress strain curves of both alloys with respect to temperature and strain rate in LD. It is clear from Figure 42 that as we are increasing the temperature, the ductility of both materials is enhanced and both elongate more, as shown in Figure 42 and 43. Compared to room temperature tests, there is a visible decrease in ultimate tensile strength, flow stress and yield strength with increase in temperature, and all three characteristics show an inverse proportional relationship with temperature.

The most likely reason for this is activation of additional slip systems at elevated temperatures, which fulfils the von Mises criterion for uniform deformation as discussed in section 2.3.1. In line with an increase of ductility, percentage elongation and fracture strain shows positive proportionality to temperatures as shown in Figure 42 – 45.

A comparison of percentage elongation is plotted in Figures 42 and 43, which indicates that the elongation percentage increases 57% compared with room temperature at 10^{-2} sec^{-1}. This figure increases to 100 percent at $1x10^{-3}$ sec^{-1} and up to 140 percent in $1x10^{-4}$ sec^{-1} in coarse-grain AZ80 – F. In addition, elongation increases exponentially in the fine-grain alloy AZ80 – O. In AZ80 – O percentage elongation increases from 15 percent at room temperature to 73 percent at 400^0C at a uniform strain rate of $1x10^{-2}$ sec^{-1} which increases to 93 percent at $1x10^{-3}$ sec^{-1}, and is further enhanced to 153 percent at 10^{-4} sec^{-1}.

If we compare room temperature elongations in fine and coarse grain material, they vary from 15 – 18 percent to 13 – 16 percent in fine and coarse grain alloys respectively, however, this figure increases to 140 and 153 percent at 300^0C. This shows strong influence of temperature on magnesium alloys.

An interesting fact to consider here is that both materials demonstrate their maximum elongation at 300^0C instead of 400^0C, at 10^{-4} sec^{-1}. This is due to cavitation that generates premature failure in both at high temperatures. Details of these failures are discussed with micrographs in chapter 6.

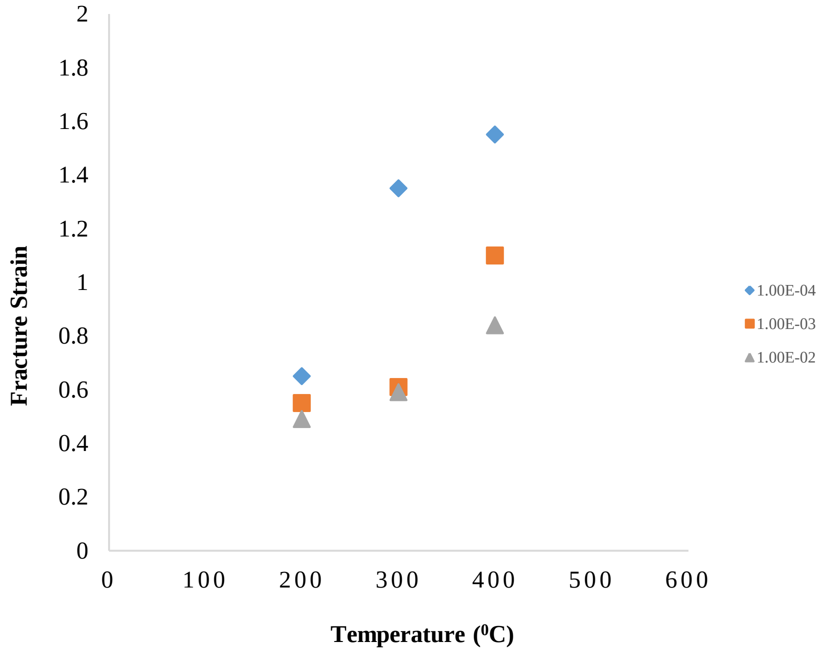

(a)

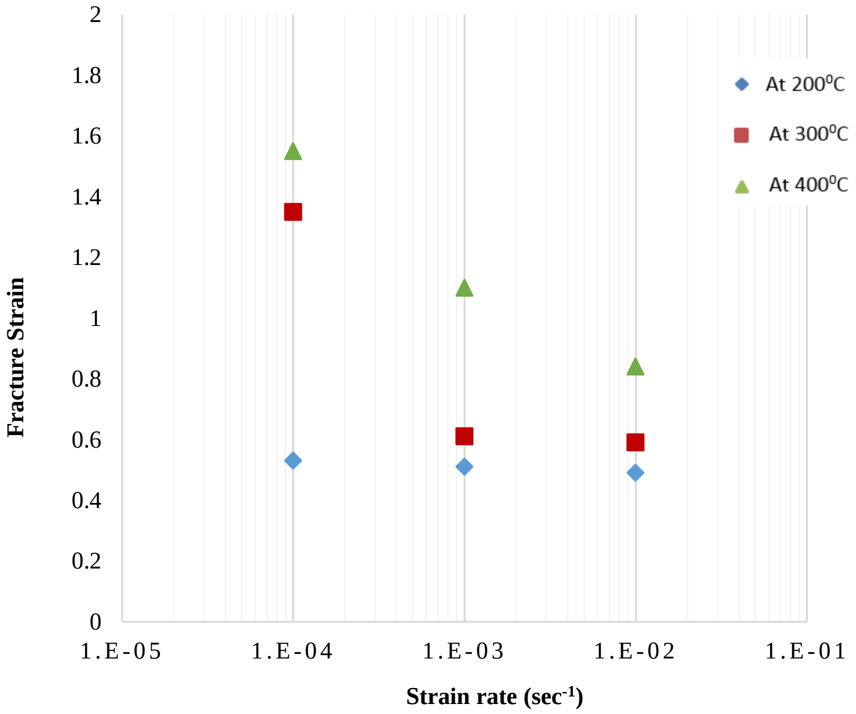

(b)

Figure 44. Fracture strain variations in AZ80 – O (a) vs Temperature (b) Strain rate

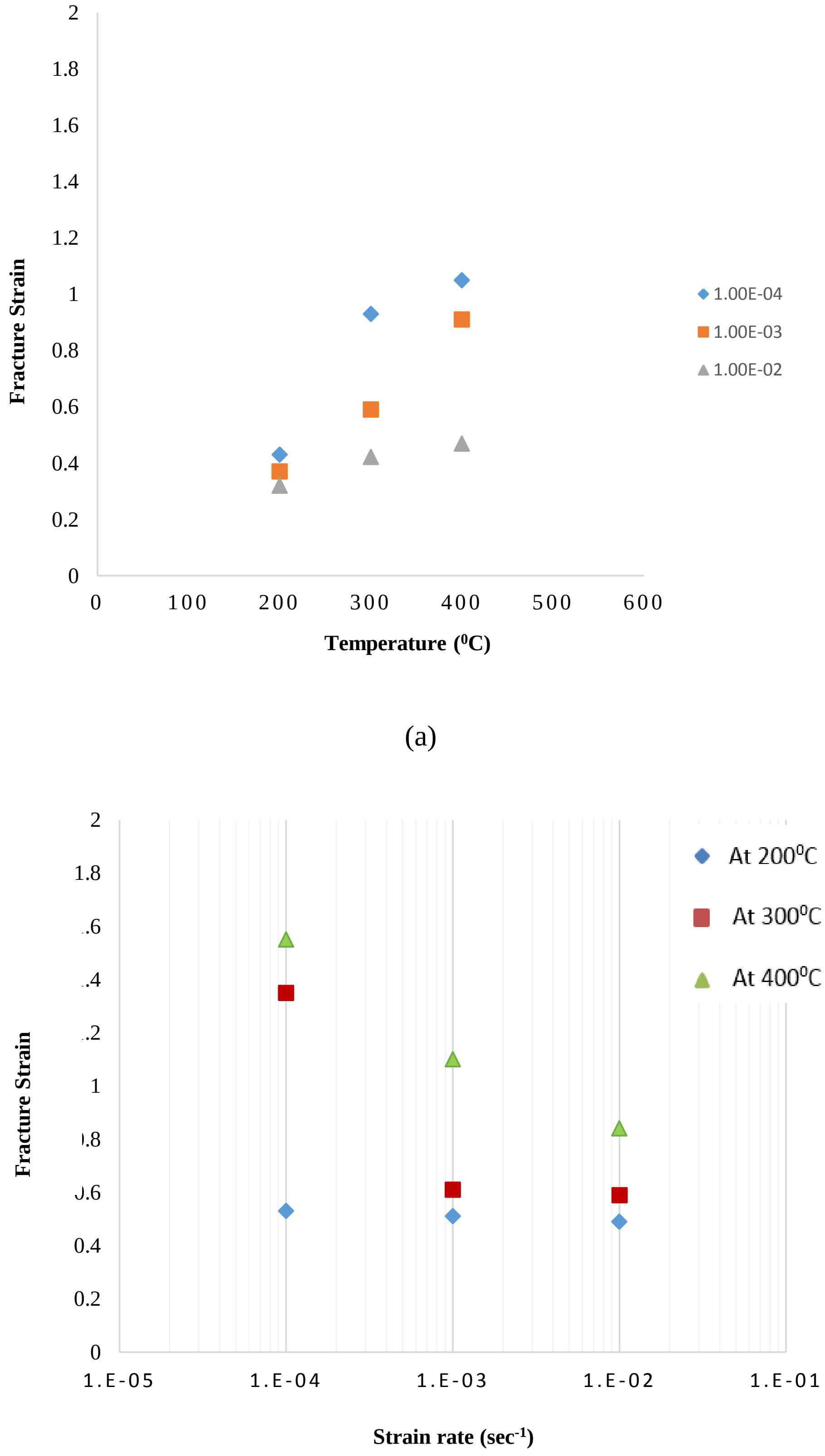

(a)

(b)

Figure 45. Fracture strain variations in AZ80 – F (a) vs Temperature (b) Strain rate

It also indicates that exceeding a temperature of 400^0C is not beneficial, as this will not increase elongation further.

The reason for this reduction in elongation at 400^0C and 1x10^{-4} sec^{-1}, as compared to 300^0C, is a reduction in the strain rate sensitivity index (m), which is discussed in the next section. Fine-grain size magnesium shows more ductility due to the easy movement of grains during deformation and recrystallisation that occurs at higher temperatures. Ultimate stress and 0.2% proof stress of material reduces significantly with increases in temperature, due to a reduction in the CRSS of pyramidal and prismatic slip. Further details of CRSS are discussed in Chapter 6.

4.7 Influence of strain rate

Three values of strain rates were selected as described earlier. In the Figures 41 – 45, both materials show their sensitivity towards strain rate at an elevated temperature. Percentage of elongation is plotted against strain rate on a logarithmic scale for both fine-and coarse-grain AZ80. Both alloys exhibit similar behaviour at various strain rates. Maximum elongation is achieved at 300^0C and 10^{-4} sec^{-1}. In the logarithmic plot, percentage elongation curves for 200^0C and 400^0C behave similarly for both fine and coarse alloys. Initially, both curves start accelerating upwards at 10^{-2} sec^{-1} and after showing a peak at 10^{-3} sec^{-1} they decline for 10^{-4} sec^{-1}. However, the 300^0C curve achieves its maximum peak at 10^{-4} sec^{-1}. Therefore, following the behaviour of the other two curves, the 300^0C curve is also expected to drop at even slower strain rates.

A summary of mechanical characteristics influenced by the strain rate of both materials is given in Table 15. Both AZ80 – O and AZ80 – F values in Table 15 are at 300^0C, with strain rates of 10^{-3} sec^{-1} and 10^{-4} sec^{-1} for LD specimens. A significant reduction in yield and ultimate stress is visible at an elevated temperature when compared with room temperature. It can be concluded that the amount of elongation has an inverse relation with strain rate. It can also be observed that both materials are showing strain softening with a decreasing strain rate, and this will then convert into strain hardening with a decline in strain rate. The reason for reduction in ultimate stresses and yield stresses at slower strain rates is that dislocations gather at grain boundaries, which result in dynamic recrystallisation in grains and most of the grains gain additional time for growth and the recrystallisation processes. Guo [336] termed this phenomenon the ‘necklace’ type of dynamic recrystallisation (DRX).

It was discussed earlier that dynamic recrystallisation at slower strain rates is usually classified as continuous and discontinuous types. Continuous recrystallisation is mostly referred to as a recovery phenomenon for boundary deformations, however, nucleation of new grains at pre-existing boundaries is mostly controlled by the discontinuous type. This type of discontinuous dynamic recrystallisation process is mostly affected by a decrease in strain rate, which results in favourable elongation at 400^0C at 10^{-4} sec^{-1}.

4.8 Influence of grain size

To investigate the effect of grain size, two types of AZ80 alloys were used: fine-grain size (10μm) and coarse-grain size (35μm), as mentioned earlier. Both alloys exhibit similar behaviour, but the amount of elongation varies drastically at higher temperatures, however, at room temperatures the difference is quite small, as shown in Figures 38 - 39.

Yield stresses and ultimate tensile stresses are higher in coarse-grain alloy as opposed to fine-grain as shown in Table 16. The amount of elongation in fine-grain is about 153 percent compared with 140 percent in coarse-grain as shown in Figure 41.

Grain refinement usually provides relaxation in internal stresses that are generated during rolling. It also provides space for generation of new grains in twin-bounded areas as well as at grain boundaries.

As it was discussed earlier, basal texture and twins usually restrict large elongations in magnesium alloys and their effects can also be minimised by grain refinement.

Due to strong twins, dislocations accumulate that minimise large elongations and increase ultimate tensile stress at warm temperatures.

Table 16. Mechanical properties and r – values of 45^0RD sample at 300^0C

Material	Strain rate [sec^{-1}]	Proportional limit [MPa]	Yield Strength [MPa]	Ultimate Tensile Strength [MPa]	Fracture Strain
AZ80 – O	$1x10^{-4}$	23	25	27	0.85
	$1x10^{-3}$	62	69	75	0.71
AZ80 – F	$1x10^{-4}$	32	36	37	0.67
	$1x10^{-3}$	65	72	79	0.65

Fine-grain alloys usually have weaker basal textures than coarse-grain alloys, therefore to achieve maximum elongations before failures a fine grain size is preferred.

4.9 Fracture strain

Fracture strain is another parameter that indicates the amount of ductility in magnesium alloys. Fracture strain is plotted against temperature and strain rates with varying conditions in Figures 44 and 45. Values of fracture strain range from 0.49 to 1.5 for AZ80 – O, however, for AZ80 – F they vary from 0.39 to 1.1. A summary of the variation in fracture strain with respect to strain rate at 300^0C is also tabulated in Table 16. To show the variation in behaviour of fracture strain, curves are drawn on a logarithmic scale for variable strain rates. Both fine and coarse material follow similar behaviour for fracture strain. It is also quite clear that fracture strain increases with an increase in temperature, however, it follows a reverse trend with strain rate. These trends indicate an activation of additional slip systems at low strain rates and high temperatures.

4.10 Flow Stress and strain rate sensitivity index

Flow stress is plotted in Figures 46 and 47 for AZ80 – O and AZ80 – F at various strain rates and temperatures. Values are plotted on a logarithmic scale to cover a wide range of data points.

Flow stress is measured at a strain of 0.1 to avoid the effects of grain growth during high-temperature deformation. In Figure 46, flow stresses are plotted against strain rates, which show increases in flow-stress values with an increase in strain rate for both fine-and coarse-grain alloys. However, curves of flow stress are plotted against temperature at various strain rates in Figure 47. The slopes of these flow lines indicate a strain rate sensitivity index (m) that varies from 0.2 to 0.35 at various temperatures, which is a clear indication of superplasticity at extreme slow strain rates and high temperatures.

Low strain-rate sensitivity values at room and warm temperature indicate a great influence from basal texture and twinning. As we increase temperature and decrease strain rate, grain-boundary sliding starts, which supports sensitivity values and enhances the material’s ductility which leads to superplasticity.

Both materials show a similar behaviour of flow stress and strain-rate sensitivity at lower strain values such as 0.1, that is, the effect of grain size is quite negligible. However, if we increase the strain from 0.1 to 0.5 or above, a clear variation can be found.

4.11 Anisotropy effects

As mentioned earlier, to check anisotropy effects three samples in different rolling directions were used. Samples were divided according to varied grain sizes: fine (AZ80 – O) and coarse grain (AZ80 – F) materials further subdivided into three families, associated with their rolling directions 0^0 (LD), 45^0 (AD) and 90^0 (TD). Tests were performed at three speeds, and later these speeds were converted to strain rate by using the gauge dimensions of the samples.

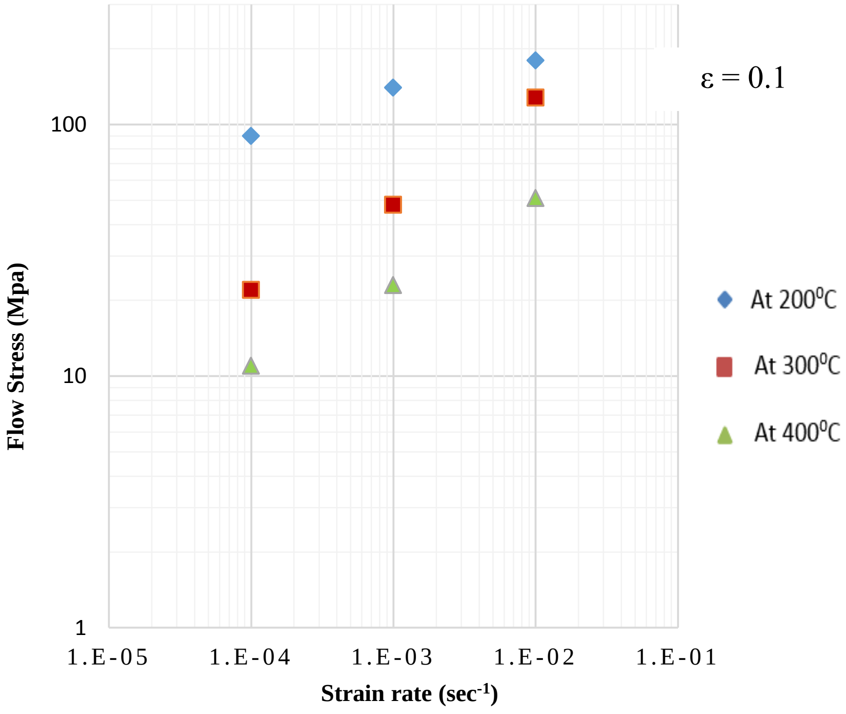

(a)

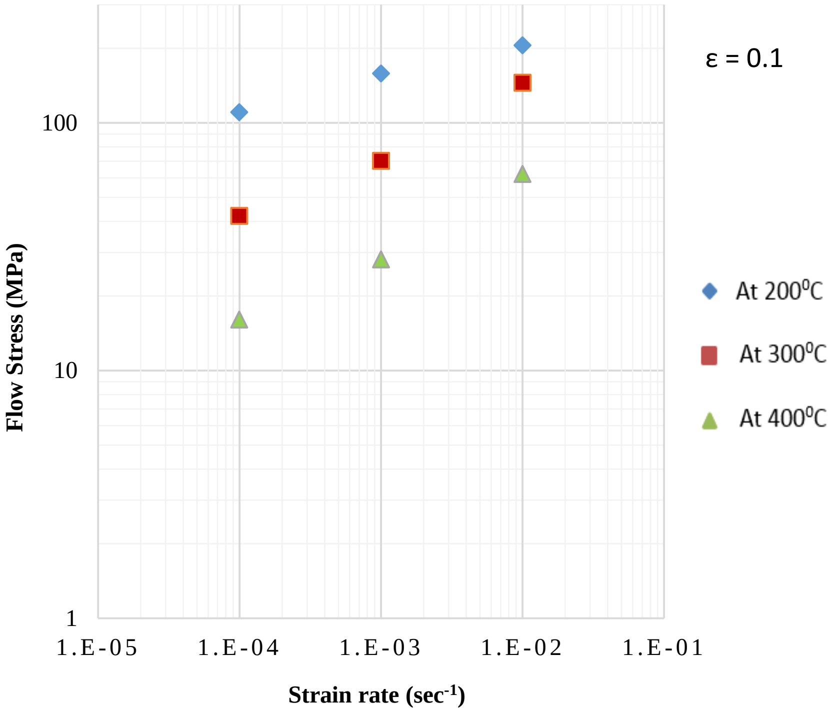

(b)

Figure 46. Flow stress as a function of strain rate at a strain of 0.1, (a) AZ80 – O, (b) AZ80 – F

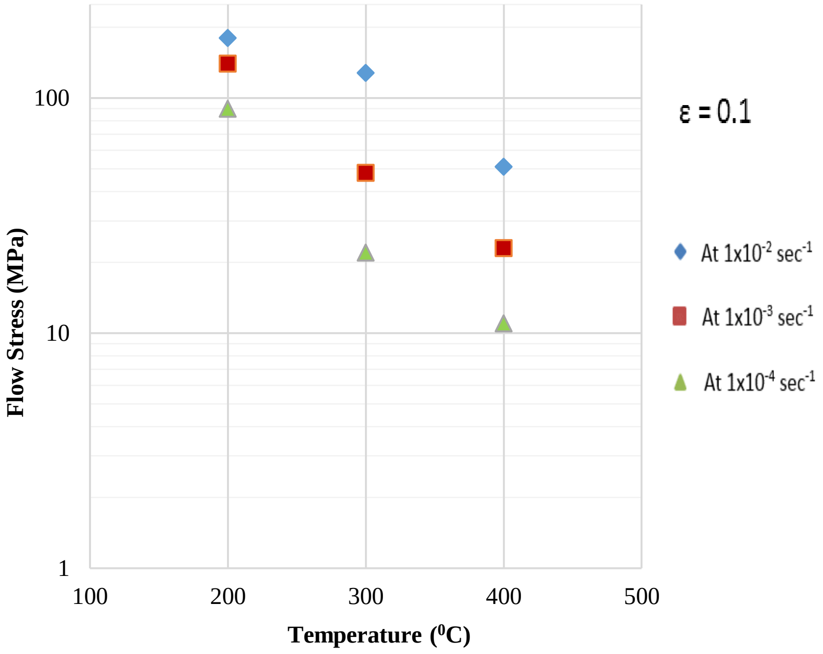

(a)

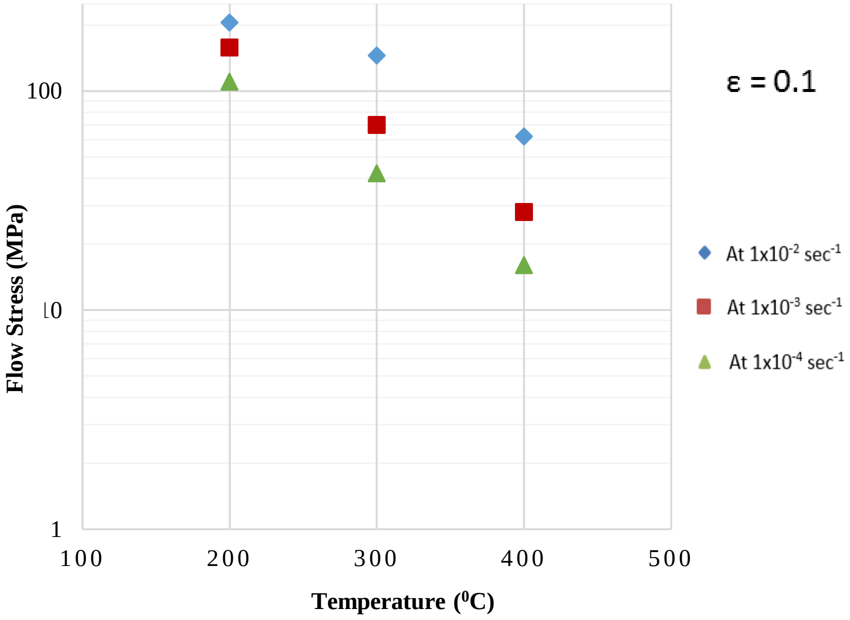

(b)

Figure 47. Flow stress as a function of temperature at a strain of 0.1, (a) AZ80 – O, (b) AZ80 – F

Selected strain rates were $1x10^{-2}$ sec^{-1}, $1x10^{-3}$ sec^{-1} and $1x10^{-4}$ sec^{-1} as shown in Figure 48. As noted earlier, anisotropy of materials can be measured by r values. Table 17 indicates r – values of both fine and coarse grain alloys at 300^0C and 400^0C at $1x10^{-3}$ sec^{-1}. By comparing values it is quite clear that r – values at 300^0C are quite high when compared with 400^0C.

It was mentioned in section 2.3 that prismatic slip in <a> direction usually controls width strains, however, thickness strains are governed by pyramidal slip <c+a> and twinning. Twinning only plays a vital role up to warm temperatures. Therefore smaller r – values indicate a weak basal-texture hold in AD samples at 400^0C and $1x10^{-3}$ sec^{-1}, which supports basal-slips occurring during high temperature deformation processes.

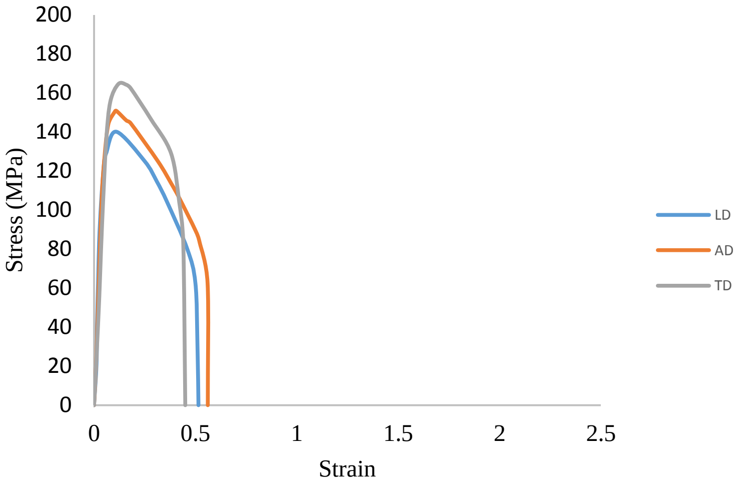

(a)

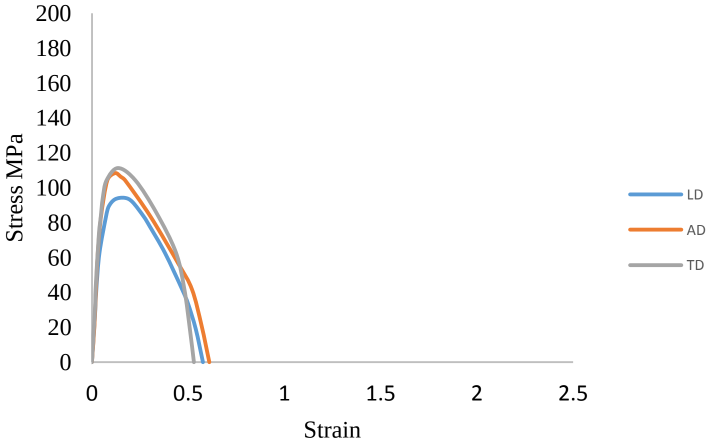

(b)

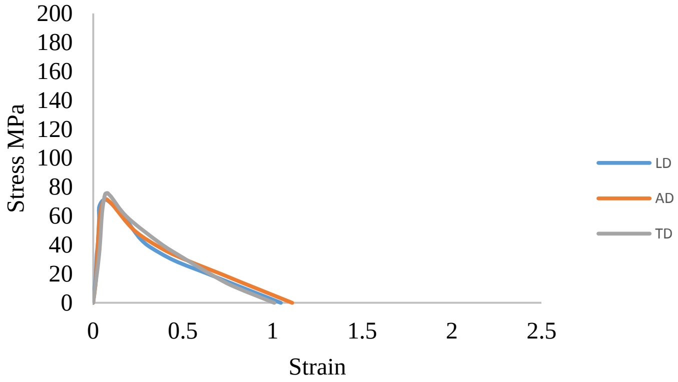

Stress MPa
200
180
160
140
120
100
80
60
40
20
0
0
0.5
1
1.5
2
2.5
Strain
LD
AD
TD

(c)

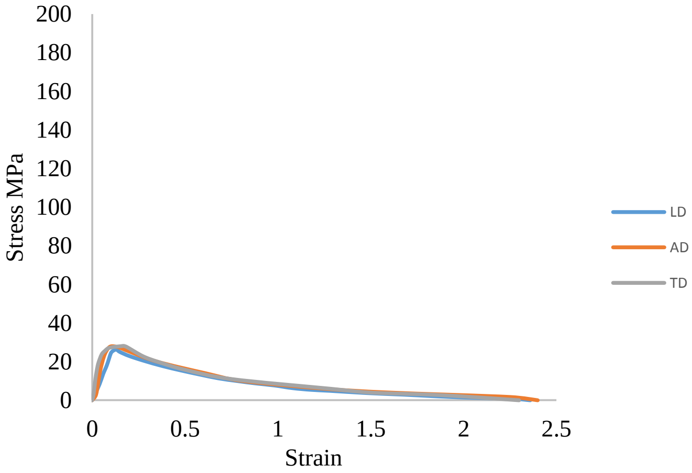

Stress MPa
200
180
160
140
120
100
80
60
40
20
0
0
0.5
1
1.5
2
2.5
Strain
LD
AD
TD

(d)

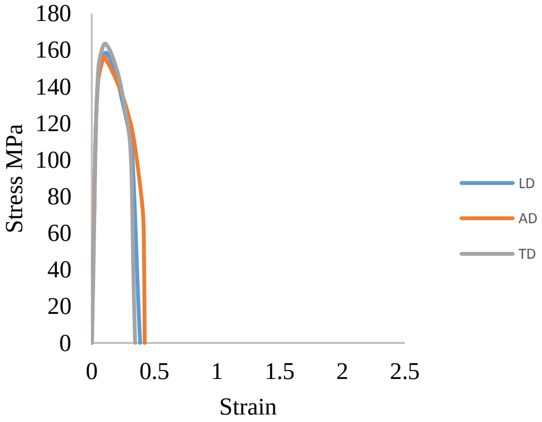

Stress MPa
180
160
140
120
100
80
60
40
20
0
0
0.5
1
1.5
2
2.5
Strain
LD
AD
TD

(e)

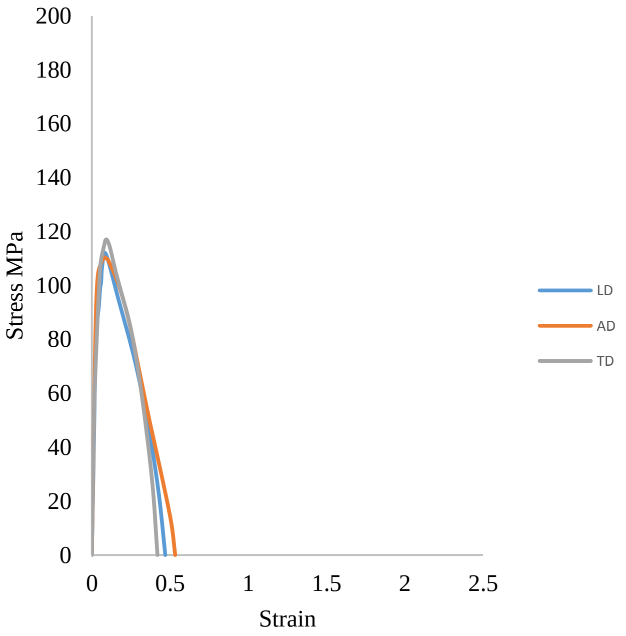
Stress MPa
200
180
160
140
120
100
80
60
40
20
0
0
0.5
1
1.5
2
2.5
Strain
LD
AD
TD

(f)

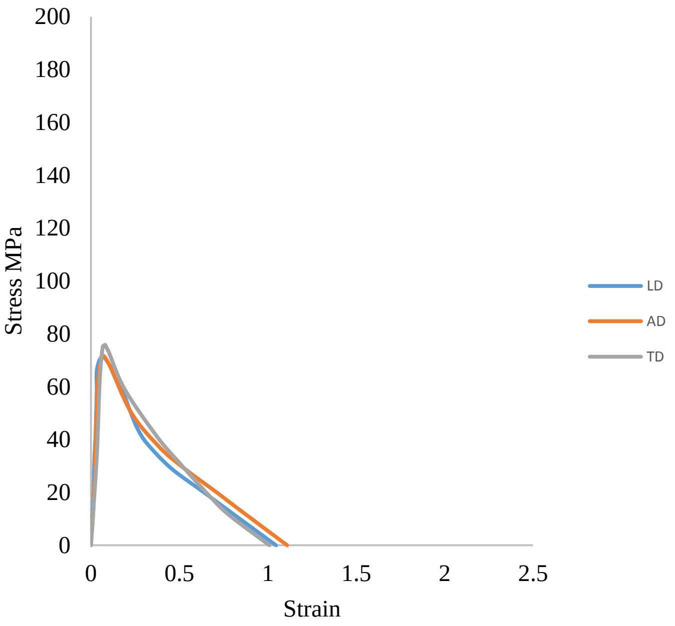
Stress MPa
200
180
160
140
120
100
80
60
40
20
0
0
0.5
1
1.5
2
2.5
Strain
LD
AD
TD

(g)

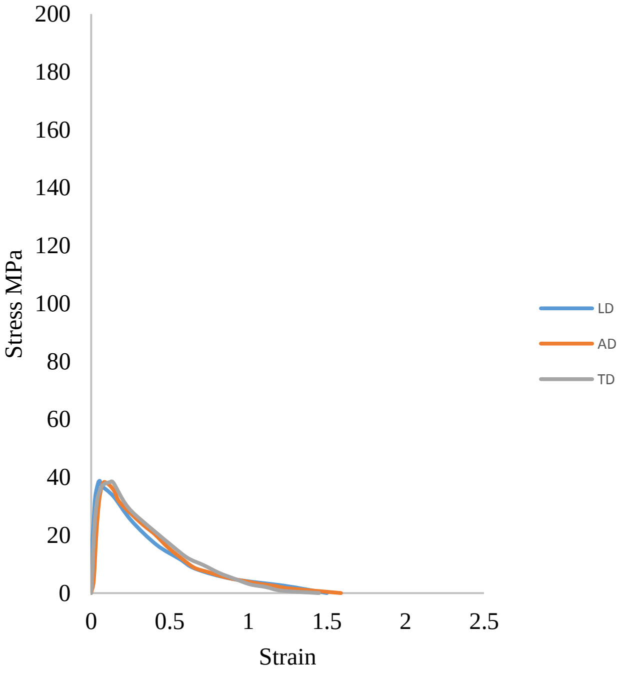

(h)

Figure 48. Anisotropy effects in AZ80 – O (a) 200^0C and 10^{-3} sec^{-1} (b) 200^0C and 10^{-4} sec^{-1} (c) 300^0C and 10^{-3} sec^{-1} (d) 300^0C and 10^{-4} sec^{-1} and AZ80 – F (e) 200^0C and 10^{-3} sec^{-1} (f) 200^0C and 10^{-4} sec^{-1} (g) 300^0C and 10^{-3} sec^{-1} (h) 300^0C and 10^{-4} sec^{-1}

Table 17. Mechanical properties and r – values

Material	**Orientation**	**r – value**	
		Temperature	
		300^0C	**400^0C**
AZ80-O	0^0RD	2.1	1.2
	45^0RD	2.4	1.6
	90^0RD	2.2	1.4
AZ80-F	0^0RD	2.2	1.4
	45^0RD	2.6	1.8
	90^0RD	2.3	1.5

4.12Two-stage deformation

Two-stage forming is used here to produce large elongations before failure. Previously it was stated that basal slip plays a leading role in low elongations at room temperature. When similar samples were tested at 200^0C, a significant difference in elongation was observed. The explanation for this elongation is the activation of additional slip systems, which are required for homogeneous deformation according to the von Mises criterion of independent slip systems.

Twinning is observed as a major deformation mechanism that takes place in warm temperature conditions. When temperatures rise further, the GBS mechanism starts dominating the deformation process along with recrystallisation and grain growth.

A phenomenon was seen when the temperature reached 400^0C at $2x10^{-4}$ sec^{-1}: the amount of elongation started reducing instead of increasing further, as shown in Figures 42 and 43. The reason behind this is cavitation, which was discussed in section 2.5. Cavities usually are voids that occur in HCP materials due to high temperature and slower strain rates; the occurrence of these cavities is called cavitation.

These cavities inflict premature failure on materials, instead of deformation through necking. Further discussion on cavitation, along with SEM and TEM micrographs, is presented in detail in Chapter 6.

To avoid this premature failure of samples, a new technique was used, two-stage deformation. In two stage-deformation, samples are initially strained under warm conditions with a constant strain rate, and then the temperature is raised to a maximum value, to achieve pure plastic deformation through necking instead of cavitation. Two values of temperature were chosen: 200^0C and 400^0C for two-stage tensile testing. To achieve this, it is necessary to know at what level of strain the temperature needs to be increased from 200^0C to 400^0C. Several tests were conducted with different combinations of strain at stage 1 to strain at stage 2: 20% / 80%, 40% / 60%, 50% / 50%, 60% / 40% and 80% /

20% at a strain rate of $2x10^{-4}$ sec^{-1}. Finally a maximum elongation was achieved at 60% / 40%.

Based on these observations a sample was initially strained at 200^0C at $2x10^{-4}$ sec^{-1}, then at 60% of strain the test was initially stopped and the temperature was increased to 400^0C at a constant strain-rate for both AZ80 – O and AZ80 – F, as shown in Figure 49. Significant variations in characteristics were observed as UTS decreased by 93 percent for AZ80 – O and 91percent for AZ80 – F. Fracture strain increased by 15 percent, while elongation before failure reached to 195% compared with153percent at 400^0C and $2x10^{-4}$ sec^{-1}. Similarly for AZ80 – F, fracture strain increased by 11% while elongation before failure reached to 186percent compared with 140percent at 400^0C and $2x10^{-4}$ sec^{-1}, as shown in Figure 49.

A further addition was made in these two-stage tensile tests by decreasing the strain rate in stage 2 from $2x10^{-4}$ sec^{-1} to $1x10^{-4}$ sec^{-1}. This gave an additional elongation of 7% for AZ80 – O, and elongation before failure reached to 205 percent, as shown in Figure 50. AZ80 – F touched a maximum value of 189 percent. The ultimate load also reduced to 8 percent and 6 percent for AZ80 – O and AZ80 – F respectively.

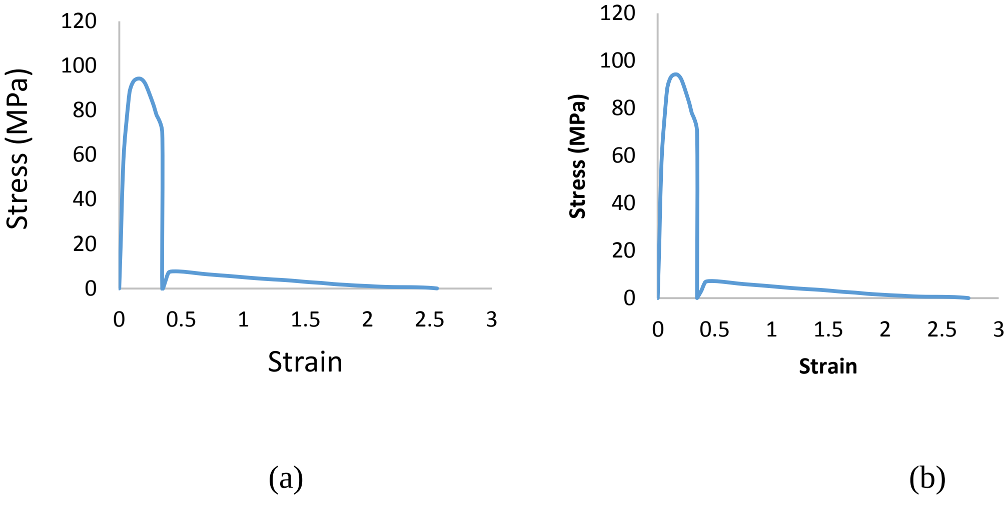

Figure 49. Two stage stretch forming in AZ80 – O, (a) 60% strained at 200^0C, 40% at 400^0C and $2x10^{-4}$ sec^{-1}, (b) 60% strained at 200^0C and $2x10^{-4}$ sec^{-1}, 40% at 400^0C and $2x10^{-4}$ sec^{-1}

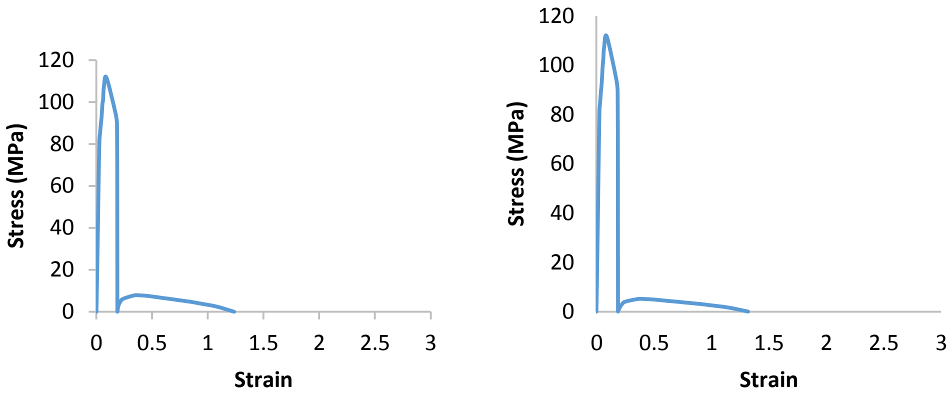

(a) (b)

Figure 50. Two stage stretch forming in AZ80 – F, (a) 60% strained at 200^0C, 40% at 400^0C and $2x10^{-4}$ sec^{-1}, (b) 60% strained at 200^0C and $2x10^{-4}$ sec^{-1}, 40% at 400^0C and $1x10^{-4}$ sec^{-1}

Samples showed clear indications of failure through necking rather than of cavitation, due to the initial stage straining. It is a slow process, but quite useful in forming magnesium alloys at high temperatures. Detailed micrographs are shown in Chapter 6.

4.13 Conclusion

In this chapter, the tensile characteristics of magnesium AZ80 – O and AZ80 – F were discussed in detail. Various problems that were faced in the pre-testing and post-testing phases were highlighted. Influences of temperature, strain rates and grain size were shown with the help of stress strain curves at room temperature as well as at higher temperatures. Mechanical characteristics were also gathered such as proportional limit, yield stress, hardening behaviour, and fracture strain and percentage elongation. Logarithmic graphs were used to explain variations in flow stress, fracture strain and percentage elongation, while covering a wide range of strain rates. Anisotropy of material was explained with the help of dividing specimens in three rolling directions. The anisotropy ratio at room temperature was also established, as well as at high temperature, to have information about its effects on formability of sheets. Finally two stage tensile testing was executed to achieve additional elongation and to establish the material's behaviour as a superplastic alloy. Several conclusions can be drawn such as:

1) Unavailability of a standard procedure for high temperature tensile testing was a major problem in the variation of results from different studies.
2) Testing time can be reduced by using small gauge-length samples.
3) At room temperature, strain rate was a major parameter affecting elongation percentage.
4) Anisotropy plays a major role at room temperature, however 45^0 RD samples showed more anisotropy than the other two.
5) Percent elongation at strain rate of 1 x 10^{-2} sec^{-1} at room temperature was 13% which increases to 57% at temperature of 400^0C at a constant strain rate for magnesium AZ80 - F. Similarly percent elongation of magnesium AZ80 - O increase from 17 percent (at room temperature) to 73% (at temperature of 400^0C) at constant strain rate of 1 x 10^{-2} $sec^{-1.}$ Maximum elongation achieved were 153 percent and 140 percent for magnesium AZ80 – O and AZ80 – F respectively at temperature of 3000C and strain rate of 1 x 10^{-4} sec^{-1}.

6) Fine grain-size magnesium shows more ductility due to the easy movement of grains during deformation, and recrystallisation that occurs at higher temperatures.
7) Yield stresses and ultimate tensile stresses are higher in coarse grain as compared to fine grain at 200^0C to 400^0C. The amount of elongation of fine grain is about 153 percent compared with140 percent in coarse grain.
8) Fracture strain increases with increase in temperature, however it follows a reverse trend with strain rate.
9) It was also indicated that exceeding 400^0C is not required as it will not further increase elongation.
10) r – Values at 300^0C are relatively high compared with 400^0C.

11) The strain-rate sensitivity index (m) varies from 0.2 to 0.35 at various temperatures, which is a clear indication of having superplasticity at extreme slower strain rates and high temperatures.
12) In two-stage deformation, elongation at a constant strain-rate before failure reaches 195 percent, compared with 153 percent at 400^0C and $2x10^{-4}$ sec^{-1}. Similarly for AZ80 – F, fracture strain increased by 11 percent while elongation before failure was raised to 186 percent compared with 140 percent at 400^0C and $2x10^{-4}$ sec^{-1}.
13) In two-stage deformation at varying strain-rates, an additional elongation of 7 percent was achieved for AZ80 – O, and elongation before failure reached to 205 percent. While AZ80 – F touched a maximum value of 189 percent. The maximum or ultimate load also reduced by up to 8% and 6percent for AZ80 – O and AZ80 – F respectively.

Chapter 5

Formability of Magnesium AZ80

5.1 Introduction

The forming characteristics of latest magnesium alloys have not been widely investigated. As described in Chapter 3, formability is the ability of a material to undergo plastic deformation without damage or fracture. The reduced plastic formability of several alloys such as HCP structured metals, limits their use in industrial applications [337]. Most researchers have confined their studies to AZ31, which is the most common commercial magnesium alloy. Most of the studies are related to uniaxial tensile tests at different temperatures, based on which, many authors have made predictions about the forming behaviour of magnesium alloys. The warm deep-drawing process is quite complex, as it depends on a number of parameters that control it [338], and requires a large number of tests (i.e. uniaxial, biaxial and multi-axial) and analyses to predict behaviour.

In this chapter, the formability of magnesium AZ80 is examined. Round tool and rectangular tool tests were performed on both AZ80 – O and AZ80 – F. Round tool tests were performed at the Institute of Frontier Materials (IFM) at Deakin University, Geelong, Australia, with a round punch 45mm in diameter and temperatures ranging from room temperature to 200^0C at various strain rates. However, some rectangular tests were conducted at the National Centre for Metal Forming at the Engineering Research Institute of AUT University in New Zealand. Various parameters such as punch force, blank holder force, strain distribution and effects of punch velocity were examined and analysed with respect to variation in grain size and temperature. Load-displacement diagrams were plotted and data examined by comparing them with tensile tests reported in the previous chapter.

As discussed, Forming Limit Diagrams (FLD) are well recognised maps to explore the formability of metals. Therefore, FLDs were plotted for round tool tests using Autogrid software at IFM, Deakin University. All FLDs are drawn for round tool tests because the setup was not available for rectangular tool tests. Major strains were examined as a function of the minor strains. Various blank sizes were machined according to ISO 12004 – 2, to establish forming limit curves (FLCs) at various temperatures, strain rates and blank holder forces. A series of repeated tests (3 tests at every temperature and strain rate) were performed to ensure the accuracy of results. Strain distribution and length measurements were also recorded, before and after failure, to investigate the effect of processing parameters on the formability of AZ80 at room temperature as well as at elevated temperatures. AZ80 – O showed better formability than AZ80 – F due to a fine-grain size and additional heat treatment. Furthermore, a comparison of the load displacement curves was also made using Nakazima and Marciniak tests regarding variation in tooling shapes. The influence of lubrication on the formability of magnesium AZ80 was also examined by varying the lubrication medium and its thickness.

5.2 Experimental setup

Formability of magnesium AZ80 was quantified by establishing two common types of deep-drawing setups, the Nakazima (round tool) and Marciniak (rectangular tool) tests. Both tests have their own merits and demerits and therefore, both tests should be conducted to check the formability variations by varying sample sizes. Droder et al. [339] performed both tests on aluminium alloys and reported that Limit Dome Height (LDH) tests are more complicated than Marciniak tests, as they involve strain gradients due to bending, normal loading and friction being conducted simultaneously.

5.2.1 Round tool setup

Round-tool setup tests were conducted at the Institute of Frontier Materials (IFM) at Deakin University, to quantify forming characteristics. A schematic diagram of the round-tool setup is shown in Figure 51. An Erichsen formability tester was used with a 600 kN maximum load for the hemispherical deep-drawing tests, as shown in Figure 52. The machine was electrohydraulically driven, with an embedded PLC system. Tooling was designed to attain a maximum temperature of 900^0C. The blank holder force was also hydraulically maintained, with a maximum capacity of 300 kN. The punch stroke and drawing speed can be raised to a maximum limit of 150 mm and 750 mm/min respectively, with a stroke resolution of 0.1mm and accuracy of ±1%.

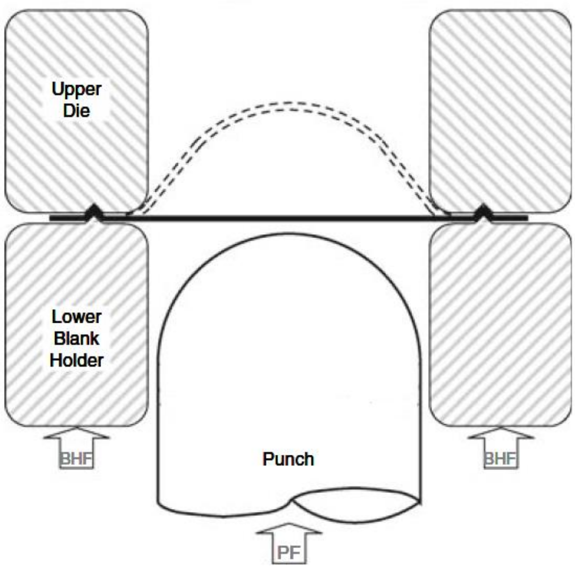

Figure 51. Schematic deep-drawing setup of Nakazima test

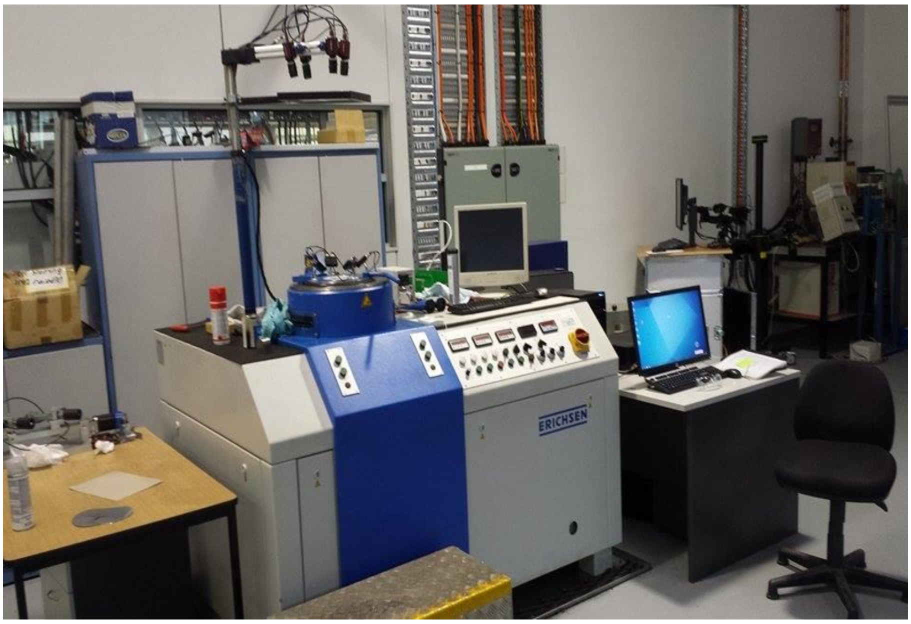

Figure 52. Erichsen formability tester

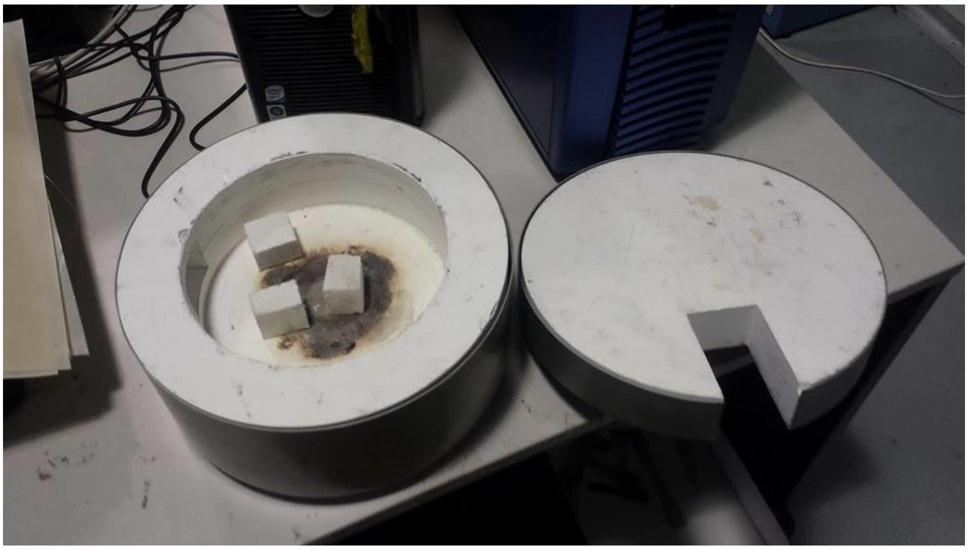

(a)

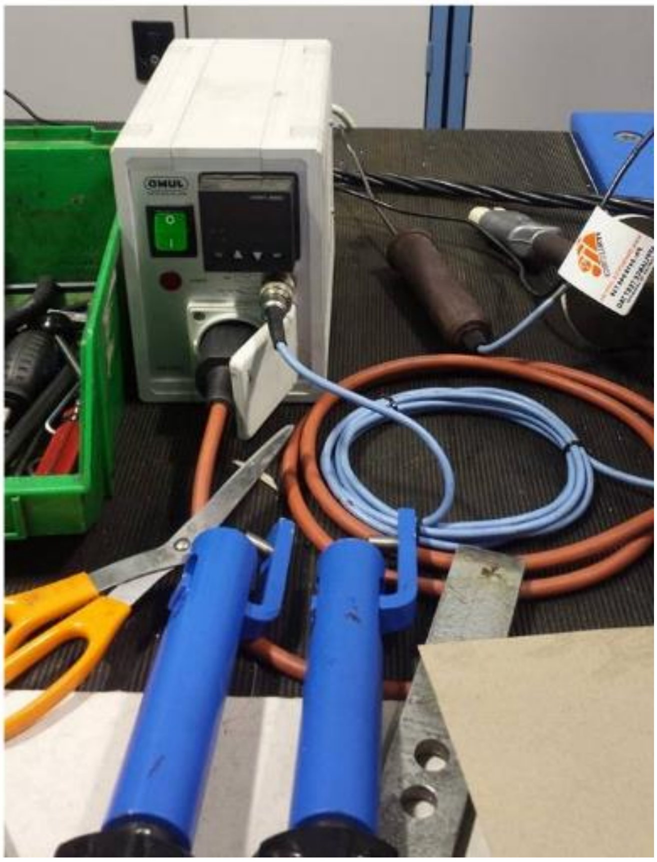

(b)

Figure 53. Accessories of Erichsen formability tester, (a) heating furnace for die and blank-holder assembly, (b) heating elements with temperature controller

The machine was equipped with a locking sensor and a handle on the top lid so that accidents could be avoided. A round die and blank holder were used with an outer diameter of 140mm and a 55mm diameter inner hole. The punch had a length of 80mm and a front nose of 15mm. The diameter of the punch was 45mm, leaving a clearance of 10mm from the die and blank holder.

The stretch-forming test setup was also equipped with two furnaces. A round furnace was used to heat the die and blank holder assembly, while a furnace was used for the punch. Temperature controllers were installed beside the furnaces to maintain a compatible temperature between forming tools, as shown in Figure 53(b). A separate computer loaded with Erichsen formability-tester special software and Universal software for controlling the machine and measuring data curves was used.

5.2.2 Rectangular-tool tests

Rectangular-tool tests were performed with a rectangular flat-base punch. The rectangular tool tests were conducted at the National Centre for Metal Forming in the Engineering Research Institute at AUT University, Auckland, New Zealand.

5.2.2.1 Tool design and manufacturing

While planning and designing the deep-drawing tool for tests at elevated temperatures, the following requirements had to be taken into account:

- suitable dimensions for assembling the tool to suit the existing adjoining tool parts
- deep-drawing of rectangular magnesium parts with a thickness of 0.8 mm
- heating up the die and blank-holder to around 200 °C
- measuring and controlling the temperature in the die and blank-holder
- sufficient heat insulation between the heated and adjoining tool parts

The maximum possible size of the rectangular punch is defined by an existing tool. Therefore, a cross-section of 80 x 60 mm with a corner radius of 10 mm was chosen. According to ISO 12004 – 2, the minimum corner radius for rectangular parts made of magnesium sheet is h/20 where h is the drawing depth [340]. In addition, the minimum punch radius is $3s_0$, where s_0 is the blank thickness, which is 0.8 mm. With this, the chosen punch radius is much greater than the minimum radius required.

The die radius is 10 mm and the clearance between punch and die is around 0.87 mm. The maximum drawing depth is defined by the maximum stroke of the drawing cushion of around 100 mm. With this, the resultant minimum corner radius is 5 mm and smaller than the chosen radius of 10 mm.

For heating the die and blankholder, straight heating cartridges with a length of 100 mm, a diameter of 15.8 mm and an electric power of 280 W were used. These have the following advantages over other heating elements:

- easy machining of holes in die and blankholder
- due to thermal expansion of heating cartridges, a tight fit is guaranteed to ensures a maximum heat transfer
- the power maximum of up to 280 W per cartridge provides a high heating rate and a relatively short heating time
- heating cartridges are made of high quality ceramics and have a high strength, damage tolerance and protection by stainless steel for high durability

A tool for drawing a circular cup was designed with two different configurations of the abovementioned heating cartridges, namely an offset and a radial setup. The temperature development in the die and blank holder during the heating process was analysed with Abaqus.

Figure 54 shows the surface temperature distribution, with the offset setup after 20 minutes and the radial setup after 60 minutes of heating. It can be seen that the surface temperature is more evenly distributed with the offset setup and, additionally, a higher heat flux is possible due to a larger contact surface between the cartridges and tool. This comparison confirms a more even and faster heating with the offset setup, which is why this configuration was chosen for the tool design used in this study.

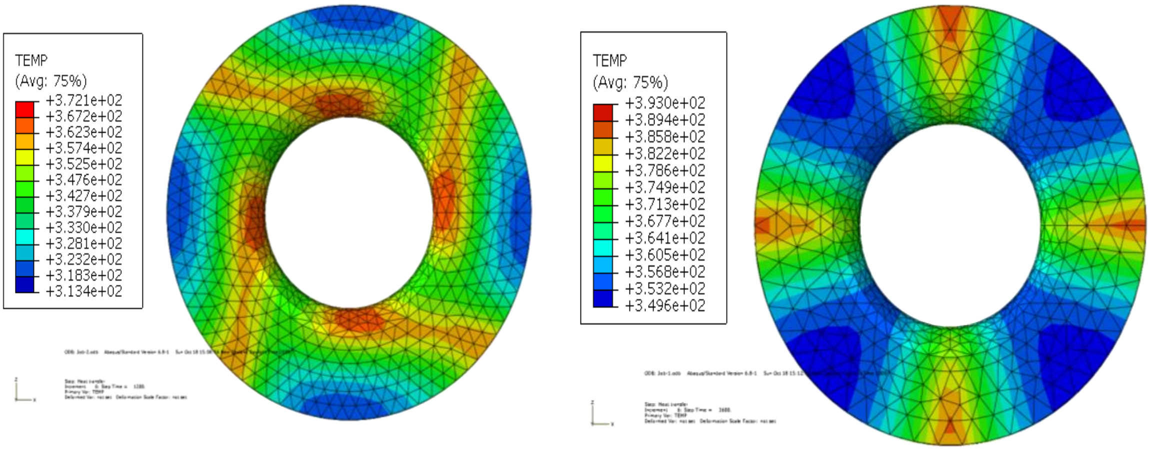

Figure 54. Surface temperature distribution with the offset setup after 20 min (left) and the radial setup after 60 min (right) [341]

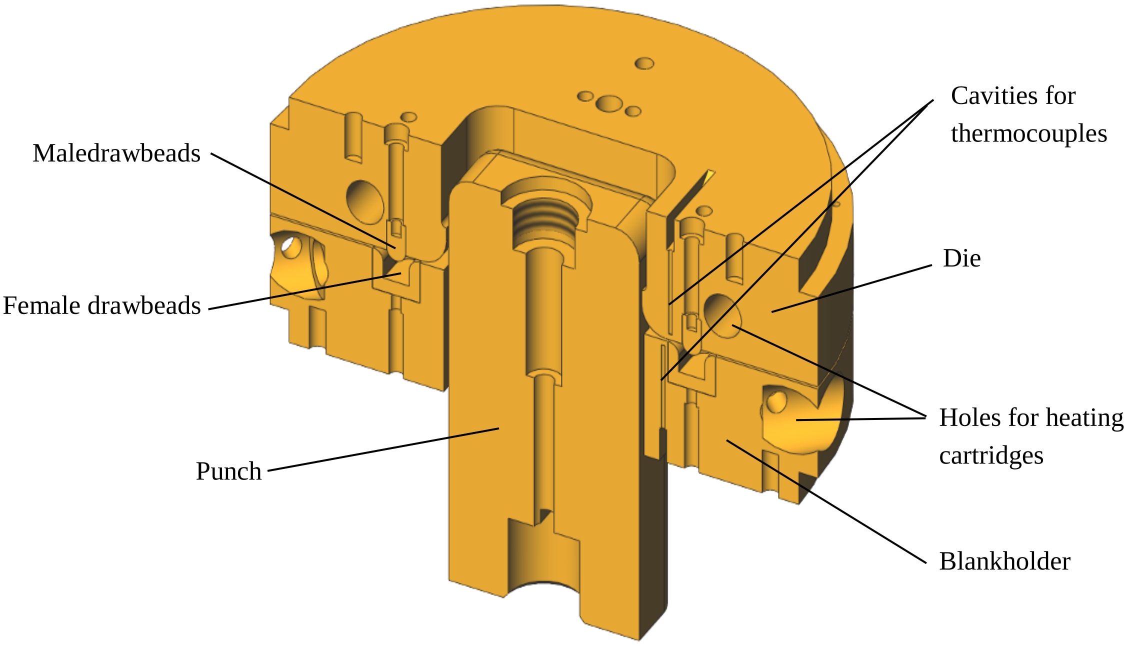
Cavities for thermocouples
Maledrawbeads
Die
Female drawbeads
Holes for heating cartridges
Punch
Blankholder

Figure 55. Assembly of the heated deep-drawing tool with drawbeads

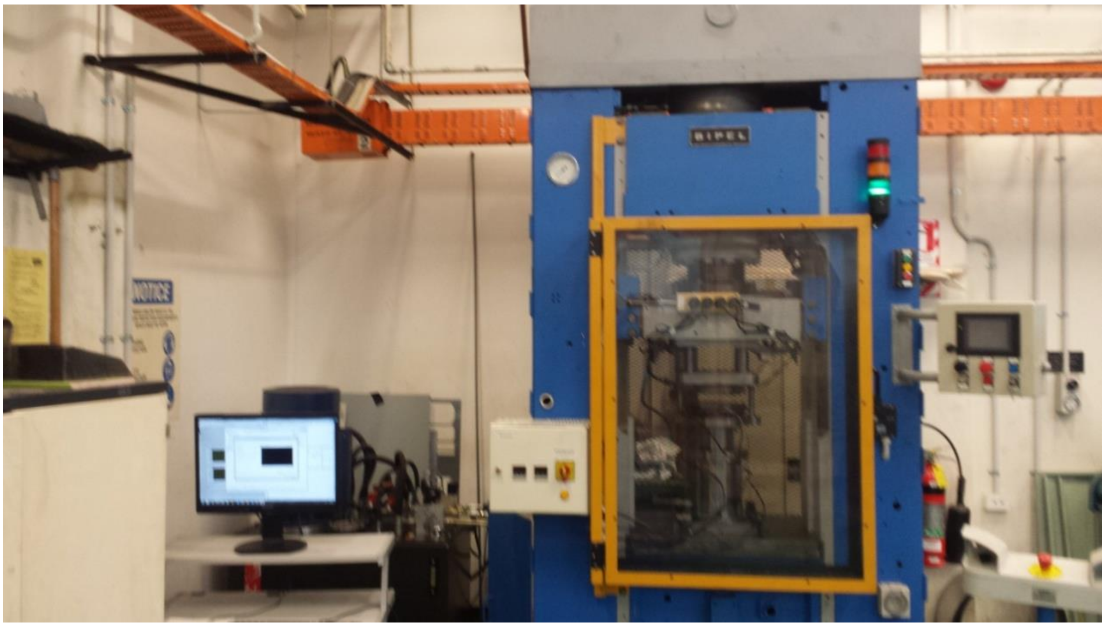

Figure 56. Assembly of the heated deep-drawing tool

The temperature in the die and blankholder can be measured with thermocouples close to the surfaces contacting the blank, where the temperature can be controlled.

The cavities for the chosen K-type thermocouples with a diameter of 1.5 mm are cut as shown in Figure 55, so that they can be inserted from the other side of the contact surfaces.

To insulate the die and blankholder from the adjoining tool parts, insulation plates were used, with a thickness of 3 mm and a thermal conductivity of 0.42 W/mK.

The complete setup of the assembly tooling inside the hydraulic press is shown in Figure 56. A schematic representation of the test setup for Marciniak tests is shown in Figure 57.

Drawbeads are used in sheet-metal forming tools to control the flow of sheet metal materials into a die. The shape of the chosen drawbeads is shown in Figure 55. The radii of the male and female draw beads were both set to 4 mm and the clearance between them was 1.5 mm.

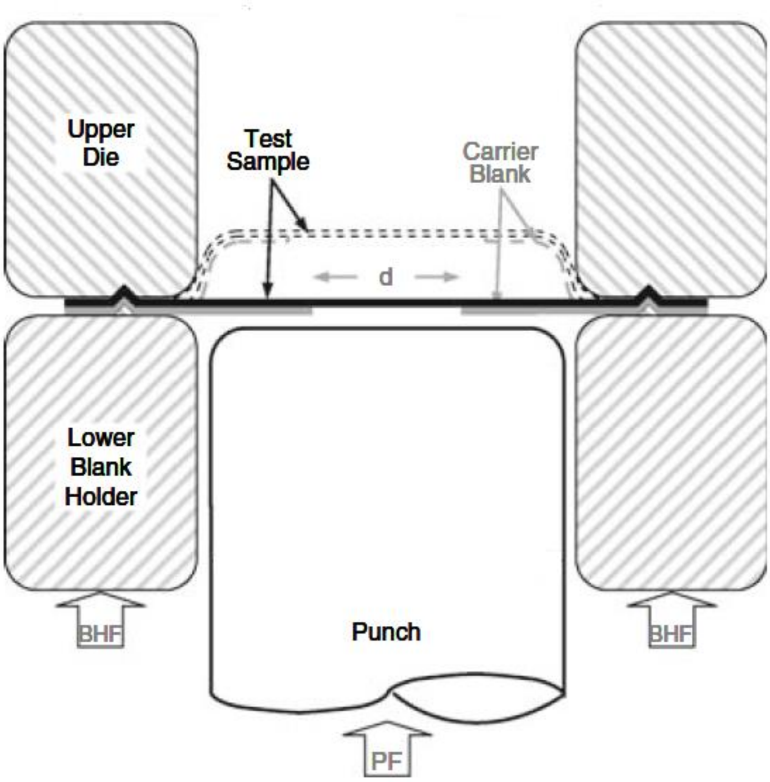
Upper Die
Test Sample
Carrier Blank
d
Lower Blank Holder
BHF
Punch
BHF
PF

Figure 57. Schematic deep-drawing setup of Marciniak test

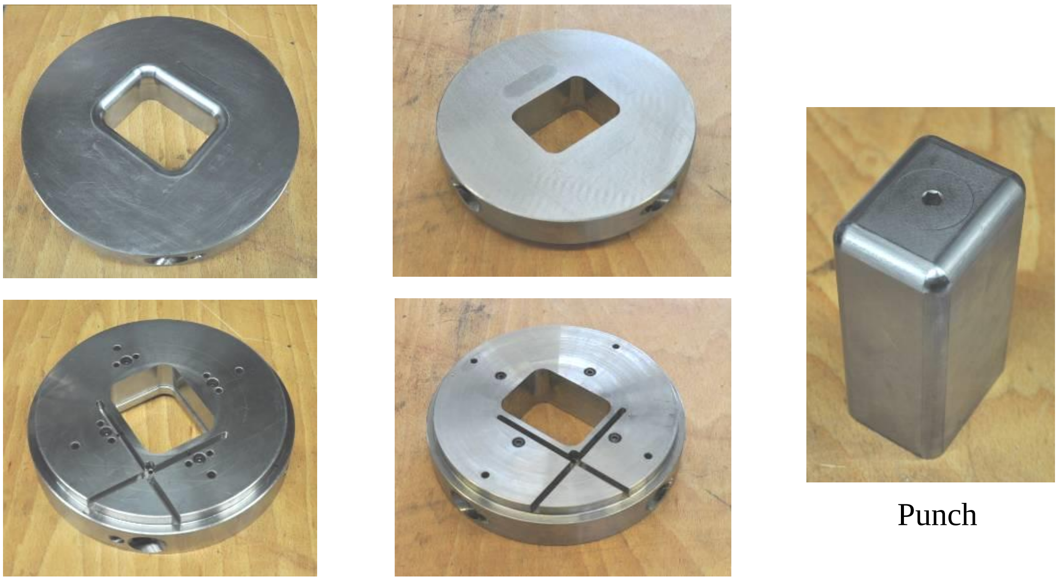

Punch

Die

Blankholder

Figure 58. Manufactured tool parts

These radii are larger than the minimal bending radii for magnesium sheets recommended inISO 12004 – 2 [342]. The recommended radii decreased with increasing temperatures and depend also on the magnesium alloy used.

Figure 58 shows the manufactured punch, die and blankholder with inserts and ground surfaces in contact with the blank during the forming process. The holes for the heating cartridges have a transition fit, so that they can be inserted and removed easily, while still providing heat flow from the cartridges into the tool.

Holes at the straight edges and the corner close to the ground surfaces, as well as grooves, are required for the thermocouples that provide the current temperature readings to the controllers. The punch is screwed onto the lower adjoining part and the screw hole can be closed with a lid.

5.2.2.2 Assembling and checking of heating and measurement equipment

To heat the tool and control temperature during the tests, an electrical circuit with devices such as temperature controllers, solid state relays and circuit breakers was designed and assembled.

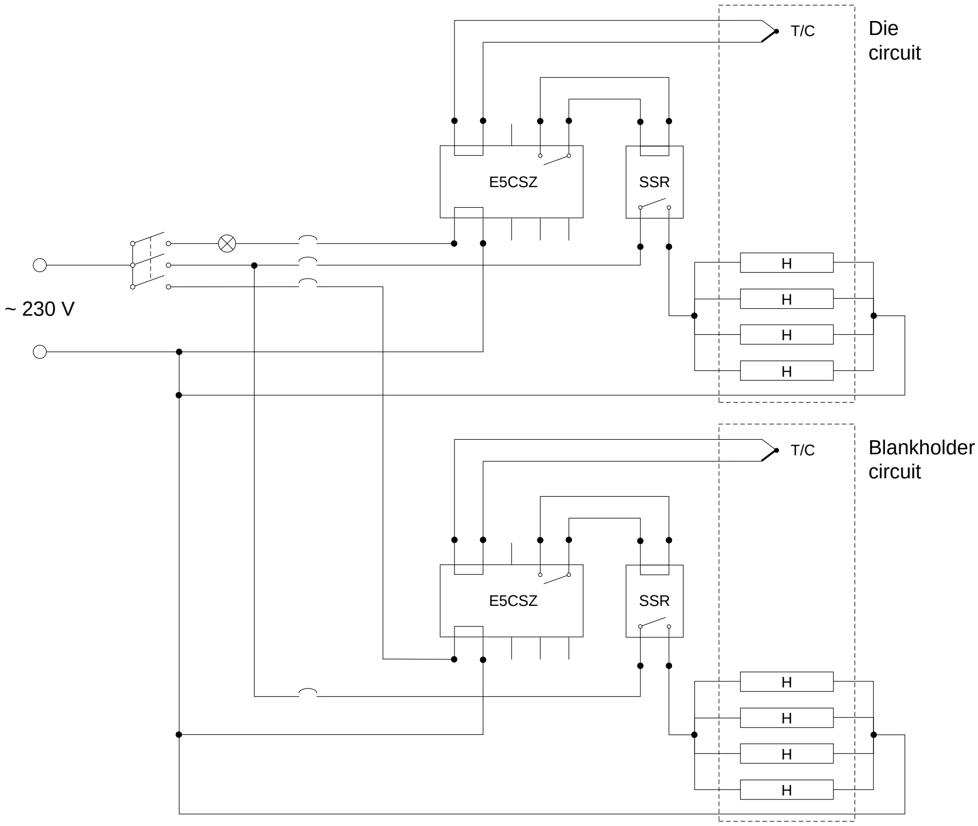

Figure 59. Circuit diagram of heating and controlling equipment

The devices were connected to each other according to the circuit diagram in Figure 59.The temperature controllers have one input for the thermocouples and one output signal, which controls solid state relays to switch on and off the power supply of the heating cartridges.

For protection overload, circuit breakers were connected between the power support and the temperature controllers and solid state relays.

A functional check of these devices was carried out with the set-up as shown in Figure 60.

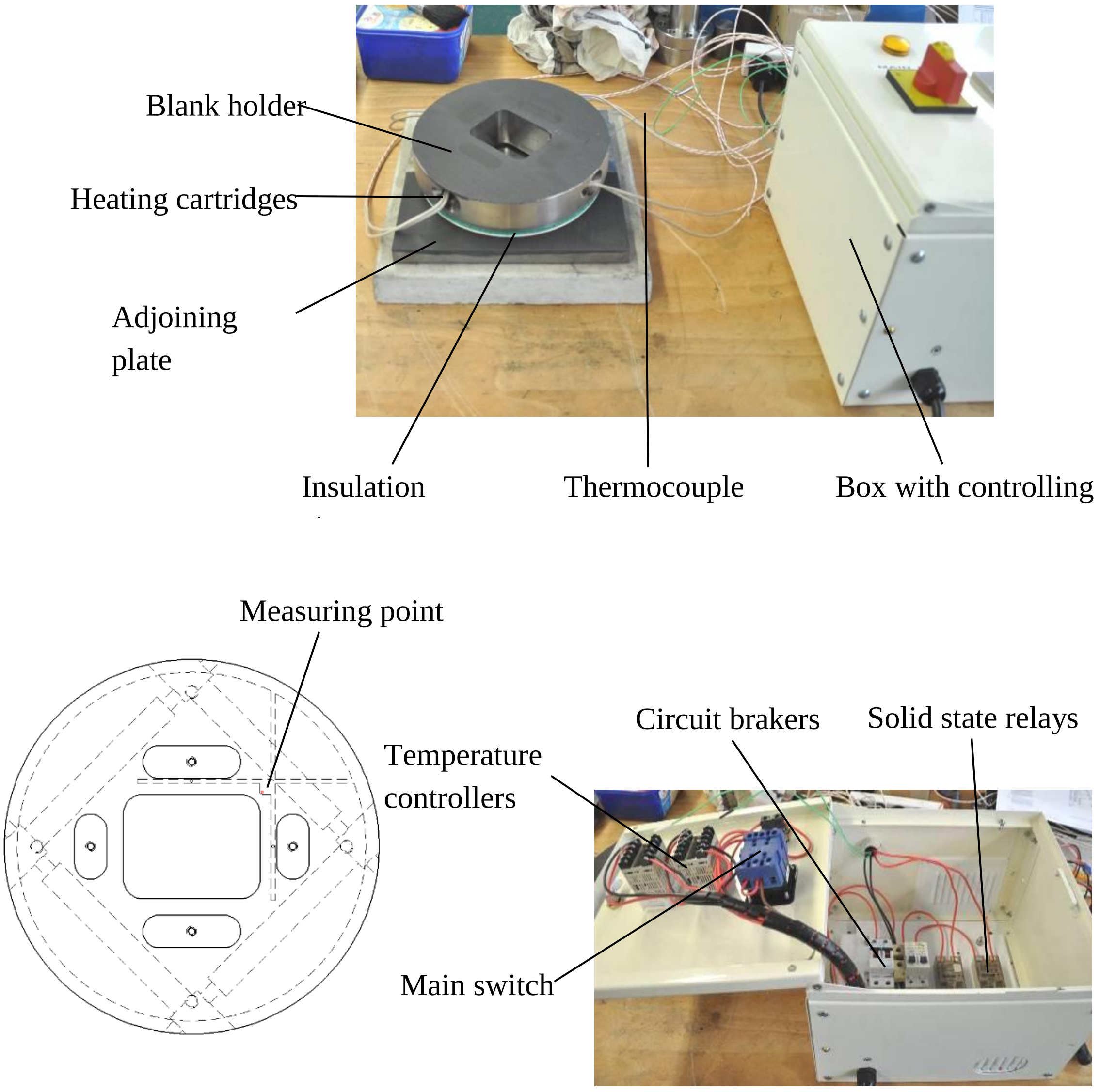
Blank holder
Heating cartridges
Adjoining plate
Insulation
Thermocouple
Box with controlling
Measuring point
Temperature controllers
Circuit brakers
Solid state relays
Main switch

Figure 60. Set-up for heating and controlling

During the heating process, the four sections above the heating cartridges as expected were warmer than the rest of the surface, as shown on the thermal images in Figure 61.

After 16 minutes and at a set temperature of 100 °C, an almost even distribution of the temperature was achieved, with an average value of around 96 °C and a variation of ± 5 °C.

This temperature difference between the surface sections decreased just slightly during a constantly measured and controlled temperature of 100 °C. The heating cartridges of the die were orientated 45 ° to the cartridges of the blankholder. The heating in the press took place while the tool was closed. Therefore it could be expected that the temperature distribution would be more even and any variation would decrease. Further simulations were carried out, with a set temperature of 200 °C, of which the results can be seen in Figure 62.

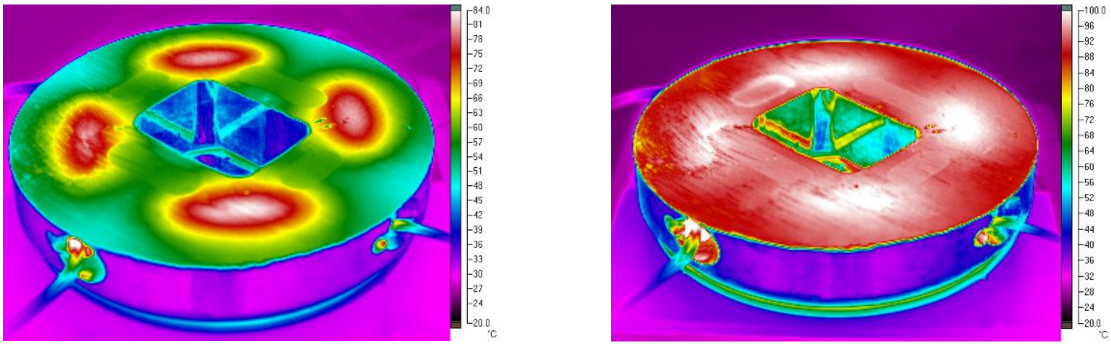
84.0
81
78
75
72
69
66
63
60
57
54
51
48
45
42
39
36
33
30
27
24
20.0
°C
100.0
96
92
88
84
80
76
72
68
64
60
56
52
48
44
40
36
32
28
24
20.0
°C

4 minutes

10 minutes

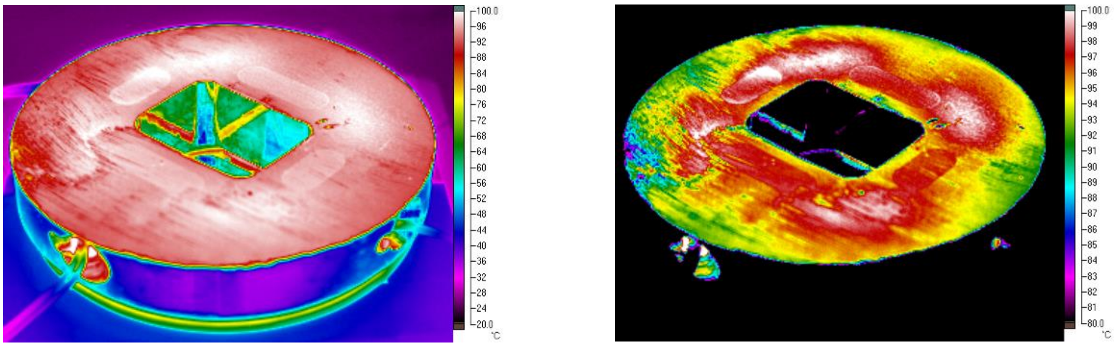
100.0
96
92
88
84
80
76
72
68
64
60
56
52
48
44
40
36
32
28
24
20.0
°C
100.0
99
98
97
96
95
94
93
92
91
90
89
88
87
86
85
84
83
82
81
80.0
°C

16 minutes

Figure 61. Temperature distribution on the surface after 4, 10 and 16 minutes, at a set temperature of 100 °C

Additionally, the surface temperature at the point marked in Figure 63 directly above the cartridge was measured.

The set temperature of 200 °C was achieved directly above the heating cartridges after 20 minutes, while other outer sections had a temperature of around 160 to 170 °C. After a further 16 minutes, the distribution was more even and the average temperature was 185 °C on the whole surface.

The maximum surface temperature of the adjoining plate after 36 minutes of heating was around 100 °C, and it could be assumed that this value was even higher in the sections below the heating cartridges, and after a longer heating period. That is why further insulation plates per tool part had to be applied. The temperature rise at the surface temperature measuring point is shown in Figure 62.

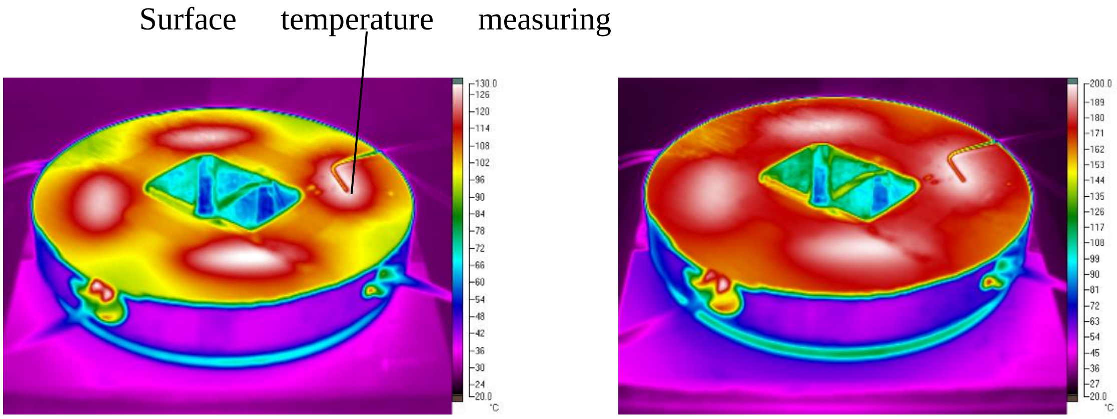
Surface temperature measuring
130.0
126
120
114
108
102
96
90
84
78
72
66
60
54
48
42
36
30
24
20.0
°C
200.0
189
180
171
162
153
144
135
126
117
108
99
90
81
72
63
54
45
36
27
20.0
°C

10 minutes

20 minutes

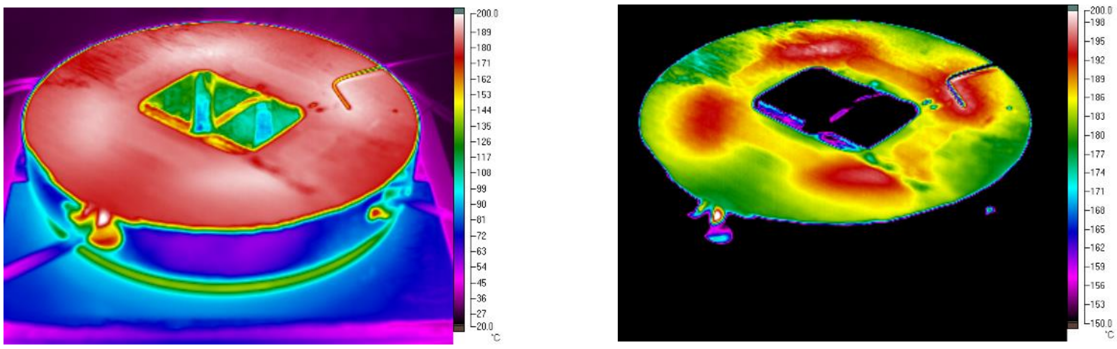
200.0
189
180
171
162
153
144
135
126
117
108
99
90
81
72
63
54
45
36
27
20.0
°C
200.0
198
195
192
189
186
183
180
177
174
171
168
165
162
159
156
153
150.0
°C

36 minutes

Figure 62. Temperature distribution on the surface after 10, 20 and 36 minutes at a set temperature of 200 °C

The approximately linear increase stopped at 200 °C after 20 minutes, and an almost constant temperature run followed, which means the temperature control worked accurately.

A further preparation for the experiments was the measurement of the punch force and stroke. For that, a LabVIEW program, or virtual instrument, was written to acquire, display and save the measured values of the punch force and stroke versus time taken during the tests.

The load cell located under the punch gave an analogue voltage input signal, which was converted to the correlating force value. The signal of an incremental encoder provided the displacement of the punch as a counter-input. Both values could be saved in a worksheet file at a frequency of 100 Hz.

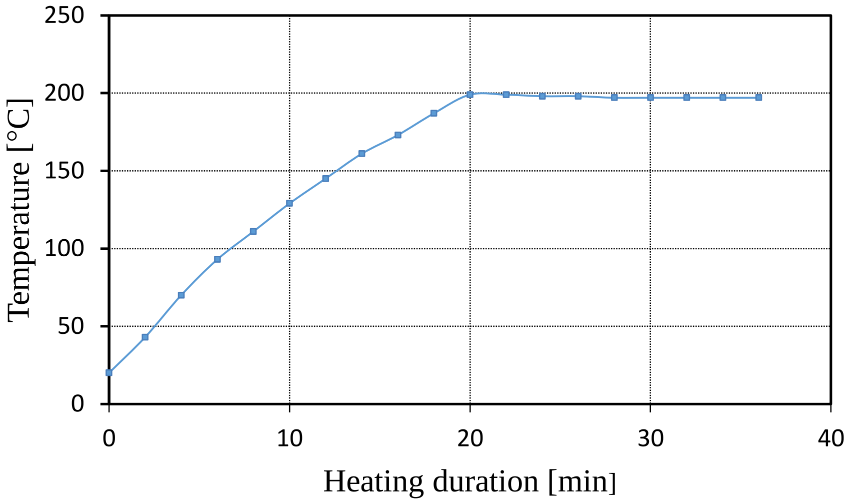

Figure 63. Temperature rise at the surface temperature measuring point at a set temperature of 200 °C

5.3 Strain Measurement

Deep-drawing results cannot be analysed without measuring of the surface strains. There are several available methods for strain measurements, but an extensometer is the most commonly used device in a tensile testing machine for recording two-dimensional strain in width and thickness direction. Another method is grid deformation, in which a specific grid is painted on samples and later any distortion is observed manually with the help of a ruler and Vernier calliper. The strain-measurement setup was installed for the Nakazima tests at the Institute of Frontier Materials (IFM) at Deakin University.

The latest addition to strain-measurement systems is the use of a digital image correlation system (DIC). In a DIC system four-charge-coupled device (CCD) cameras are used in different orientations. Each camera captures an image from a specific position, and later all four images are synchronised to capture a volume of 400 x 300 x 150 mm^3, as shown in Figure 64. Pictures are captured from the start of loading until the deformation of the surface. Images are recorded at a rate of 30 x 4 images per second. Later all images are collected to generate a single image including the mesh. The installation of four CCD cameras is shown in Figure 65 above the Erichsen formability tester.

In addition, four ultra-high beam LED lights were also installed on top of the tooling so that the CCD cameras could clearly focus on the blank and capture any deformation with the application of load. This was also aided by an alignment process with a calibrated wooden sheet.

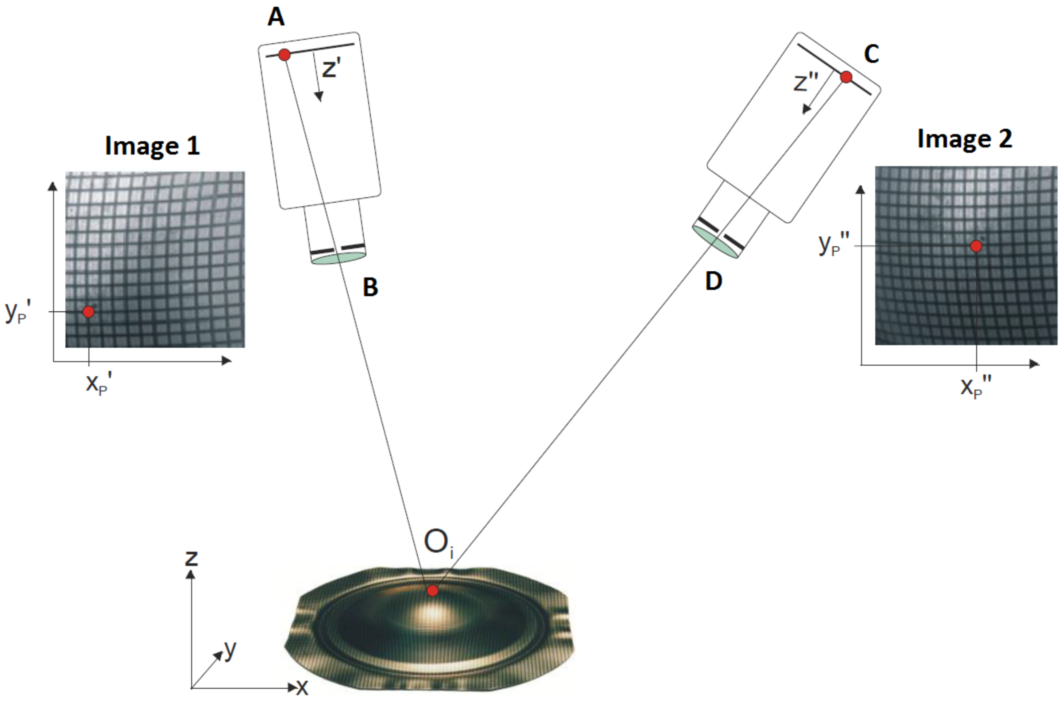

Figure 64. CCD camera image capturing methodology

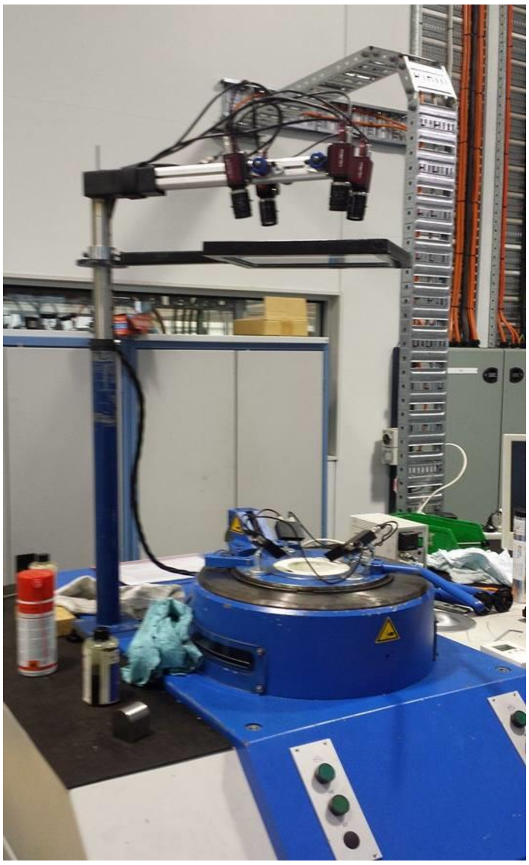

Figure 65. Installation setup of CCD cameras above the tooling, along with 4 ultra-high beam LED lights.

Calibration is the most important step in strain measurement. Initially a dummy wooden sheet with a circular grid pattern was placed to calibrate all four cameras.

The wooden sheet was elevated from all sides, one by one, with a metallic wedge so that its calibration could be precisely made. This also ensured that the CCD cameras correctly captured the dome shape generated with the application of load. Later meshes were generated through computer software, to ensure the cameras were focussed on the middle portion of the sheet. Then the calibration sheet was replaced with the original thin magnesium sheet.

Meshes were generated to calculate the strains on the surface of a formed shape. Autogrid (special software for the Erichsen formability tester) was used to calculate strains and generate FLDs for formed material before and after it cracked. Strains were calculated on the assumption of non-compressibility, that is, the volume of material remains the same before and after the deformation.

In-plane strain components in x and y direction were measured to calculate strain in the z direction. Finally, the contours of the strain distributions were plotted on the formed shape of the magnesium sheet.

5.4 Problems during warm deep-drawing

Deep-drawing of magnesium is quite complex compared with other metals, related to the use of elevated temperatures and heating equipment. As discussed earlier, due to the HCP crystal structure of magnesium alloys, elevated temperature processing is necessary to activate additional slip systems for homogenous deformation. Problems during deep-drawing are mostly associated with temperature control, calibration of the test setup for every test and the amount of lubrication film required for an even distribution of load.

Control of temperature during a test is one of the great challenges that were faced. Heating of the components can be performed in two ways: the external and the internal heating method. In this research, both procedures were adopted due to restrictions in the test setup. External heating was used in the Nakazima tests, while internal heating was adopted in the Marciniak tests.

During internal heating, control and distribution of temperature in the die and the blank holder was a major challenge. In the internal heating setup, as discussed earlier, separate heating elements of 280W were used, inserted into the die and the blank holder.

The punch was also heated externally by a heating element. In contrast to this, for the Nakazima tests punch, blankholder and die assembly were heated externally and after achieving the required temperature, the whole assembly was shifted to the press. Careful examination of the temperature was required so that during transfer of the die and the blank holder assembly, temperature loss could be compensated.

Another problem was related to the type and thickness of the lubrication film. Lubrication plays a vital role in deep-drawing to provide a homogeneous distribution of load on the blank at elevated temperatures. Various types of lubrication are available for deep-drawing, so a careful selection of a specific lubricant was required to sustain a high temperature and extensive load. Constant observation was essential so that during deformation it would not slip but remain in the middle of the blank and punch. Misplacement of the lubricant from its position causes divergence of the crack from the middle position, which results in inaccurate distributions of strain measurements. The thickness of the lubricant film should be applied properly. Consistency of film thickness is also required during repetition of any tests at similar parameters.

To generate accurate FLCs, control of the strain rate is required to avoid cracks in samples. It is also a trial-and-error method initially, in which several samples are tested at each temperature to measure depth before cracking.

All these problems are reasons for variations of results in FLDs. Due to the unavailability of these issues in forming standards, different researchers have adopted different procedures for the generation of results.

5.5 Sample sizes and standards

Hemispherical punch and rectangular punch deep-drawing tests were performed to measure the influence of punch force, blank holder force, strain rate and lubrication on both magnesium AZ80 – O and AZ80 – F. Samples were machined according to ISO 12004 – 2, as shown in Figure 66. Samples were machined by a CNC machine so that changes in microstructure could be avoided.

As it was mentioned earlier both hemispherical and rectangular shape tests were performed to measure strains and drawability. To produce FLDs, six strain paths were required [343], which were obtained with six varying geometries according to the ISO 12004 – 2 standard [342] as shown in Figure 66(a) for hemispherical punch tests. Figure 66(b) is showing the geometry of the specimen used for rectangular punch tests.

To produce FLDs at each RT, 100^{0}C and 200^{0}C, three sets of specimen were used for both alloys, each containing six dog bone specimens.

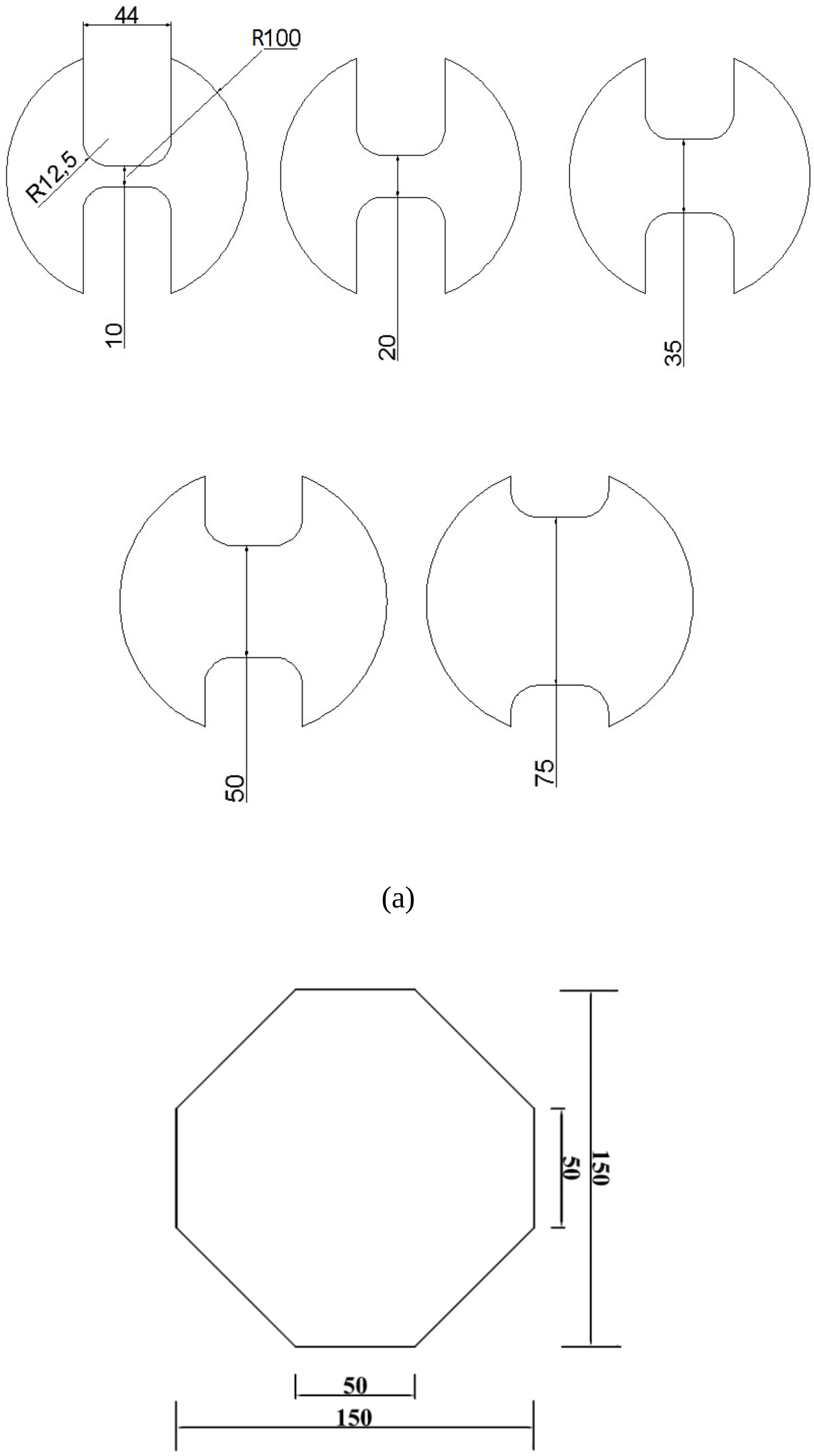
44
R100
R12,5
10
20
35
50
75
50
150
50
150

(a)

(b)

Figure 66. Standard sample sizes that were used for deep-drawing of AZ80,

(a) Hemispherical punch (Nakazima) tests blanks, (b) Rectangular punch (Marciniak) tests blanks

In addition, specimens were machined in such a way that the 0^0 RD axis of the samples became parallel to the notch's longitudinal axis in the dog bone shapes to avoid effects of varying anisotropy. As these tests were conducted at room temperature to warm temperature (that is up to 200^0C) it is quite important to note that anisotropy affects material at this temperature range. Additional samples were used to investigate the effect of variation in blank holder force, punch velocity and blank width.

5.6 Grid printing

Grid printing on thin sheets of magnesium has to be done accurately. Grids are printed on the sheets so that strains can be calculated in specific grid regions. Grids were selected and etched according to the methodology given in ASTM E 2218 – 02 [344].

Initially, all the CNC-machined specimen edges were manually ground with fine 500µm grinding paper to remove any sharp or bent edges. These sharp edges had to be removed because they could tear the grid sheet during ink polishing. Later, all samples were washed with ethanol to clean any granules of residual dirt and the material itself after grinding.

Black polishing ink was made by mixing a hardener, softener, thinner and retarder together. At first, 40 g of black ink was poured into a cup, then 3g of the hardener and 3g of the thinner were mixed into it.

Rectangular grids of 2 x 2 mm^2 were printed manually on magnesium sheets with a mesh grid sheet as shown in Figure 67 (a).

Hardener was added to the paint to solidify it immediately after masking. However, thinner was added to reduce the viscosity of the paint so it could easily be spread on the sheets.

This also helped in covering the potential area of the meshed sheet by providing less resistance to the flow of ink. In the final stage, softener (0.04 g) and retarder (2.5 g) were also added to remove any markings produced during pasting. All the chemicals were measured using a digital weight balance and mixed with the ink thoroughly to make it a compound ink.

After the compound ink was prepared, specimens were laid on the table under a mesh grid sheet, as shown in Figure 67 (b). Ink was spread on the whole area of the specimen and allowed to dry for a few seconds. After each cycle of grid-marking, the mesh grid sheet was washed thoroughly with ethanol and acid to make it ready for new specimens.

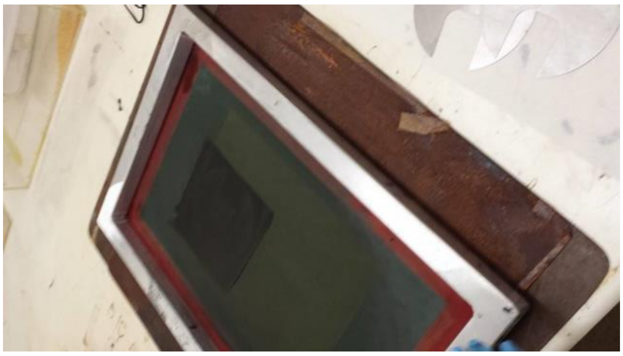

(a)

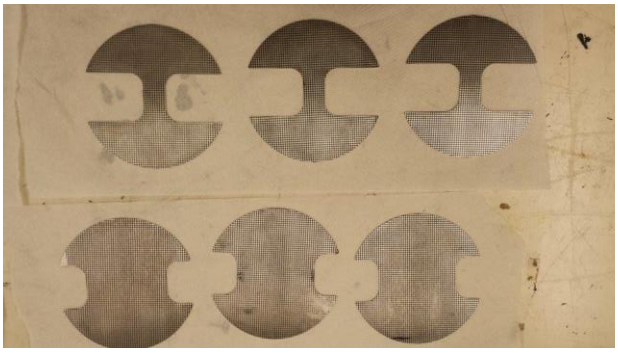

(b)

Figure 67. Grid painting, (a) Grid painting setup, (b) Specimens after grid painting

5.7 Test procedure

It was mentioned that hemispherical and rectangular punch tests were performed at Deakin University and AUT University, respectively. All the samples were machined at AUT University and later manually ground. Etching of samples was conducted to paint the rectangular grids. Samples were washed with ethanol to clean them exhaustively. Specimens were placed under mesh grid sheets and painted carefully and allowed to dry for a few minutes. Six specimen sets of AZ80 – O and AZ80 – F were used to draw a single FLD diagram. Additional full circle samples were also used to investigate the influence of variations in pre-processing parameters.

Hemispherical punch tests were conducted on the Erichsen formability tester. The blank holder and die were fixed on top. The blank was locked between both the die and blankholder, however, the punch was allowed to move vertically. Before conducting tests, two furnaces were used to heat the die and blankholder assembly in a small round furnace, as shown in Figure 53 (a). Two lever rods with a round plastic holder were used to clamp the assembly from the top to transfer it from the Erichsen formability tester to the round furnace. The punch was heated separately in the vertical furnace. Both furnaces were operated by digital temperature controllers and after achieving the required temperature samples were immediately transferred to the formability testing machine.

Lubrication is also an essential part of the deep-drawing tests. Lubrication film usually helps to distribute load evenly on blanks and also assists in the prevention of the development of cracks in the centre of specimens. Displacement of insufficient lubrication film will decrease the formability of magnesium sheets. In the case of magnesium alloys, selection of the lubricant is not trivial because it has to bear excessive loading under high temperature. In this case, high temperature sulphuric grease was selected. Another problem in high temperature deep-drawing tests is that the grease itself cannot maintain its presence between the punch and blank for a long enough time or we cannot directly apply grease on top of the punch, otherwise it would slip during the application of a heavy load.

Therefore, Polytetrafluoroethylene (PTFE) sheets were used as a sandwich and a thick high temperature grease (i.e. sulphuric grease) layer was applied on it. These sheets are commercially called Teflon sheets. These were selected according to ASTM D3418 [345], due to their low coefficient of friction which ranges from 0.05 to 0.1, as mentioned in ASTM D1894 [346].

Round circles of the Teflon sheets were cut to fit the punch diameter. This sandwich of a Teflon sheet and sulphuric grease was placed between the punch and blank carefully, so that a homogeneous load could be distributed onto the surface of the blank. Both provided an adequate amount of lubrication to conduct the high temperature trials.

CCD cameras were hooked on top of the Erichsen formability tester by a vertical rod. Their calibration was performed by a dummy wooden grid sheet before the start of the deep-drawing trials. Meshes were generated to ensure that the whole blank forming area could be covered. CCD camera lenses are quite sensitive to heat, therefore a glass shield was fabricated at the machine shop to protect them from heat generated during the process, as shown in Figure 68.

Operating the cameras was essential during the heating trials, because FLCs recorded after fracture always show a decline in FLC curves compared with FLCs that are captured just before necking. Therefore a tailor-made heat shield with dimensions 14 x 15 cm was welded to cover all four CCD cameras, and transparent glass was affixed in it.

Four LED lights were also installed on top of the blank to assist to produce high quality pictures, as shown in Figure 68. After performing safety precautions, the punch was allowed to move and various sheets were tested at varying pre-processing parameters. CCD cameras captured the pictures from the start of forming until a crack occurred in the part.

Rectangular punch trials were also performed in a similar way. A custom-made program of LabVIEW was generated which recorded the load-displacement data on the press machine. MTS servo controllers were used to control the machine’s displacement, force and blankholder force.

Different to the hemispherical punch tests, internal heating cartridges of 280W were used, which were placed inside the die and blank holder. The blank was allowed to acquire temperature gradually by making contact with the blank holder.

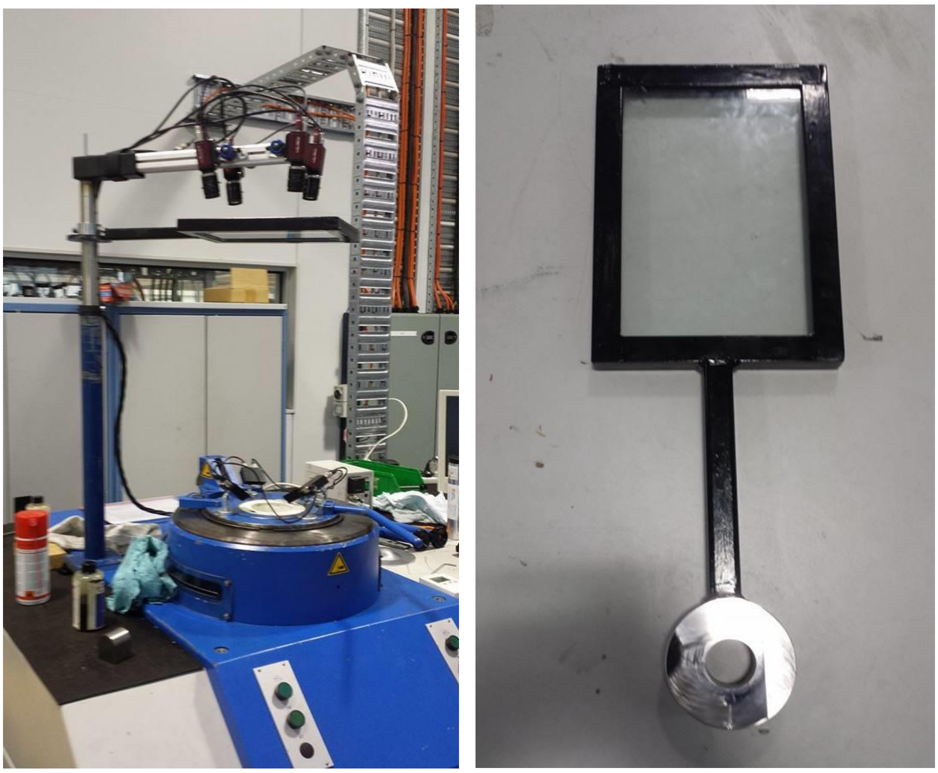

Figure 68. A view of the heat shield used to protect cameras from heat.

Thermocouples were installed inside the die and the blank holder to monitor and control the temperature of the toolset; however, the temperature of the blank was measured manually with a digital thermometer, along with a K - type thermocouple.

Lubrication was also considered an essential step for the deep-drawing trials. Ordinary machine oil was initially sprayed on the toolset and a similar sandwich of the Teflon sheet and sulphide grease was placed between the contact zone of punch and blank. Finally, the punch was allowed to move at a constant speed to form the magnesium AZ80 alloys. Tests were conducted by varying pre-processing parameters such as blank holder force, punch velocity and blank width. Load displacement data for all tests are discussed in the next section.

5.8 Results and discussion

5.8.1 Forming limit curves

Stretch-forming Nakazima tests were conducted for identification of the forming limit curves of AZ80 – O and AZ80 – F. A smaller punch of 45mm was used, due to the limited availability of the material. Forming-limit curves were drawn, as shown in Figure 69. With the help of Autogrid software, forming-limit curves were generated and the distribution of the strain was plotted as a function of major and minor strains on the formed shape for both AZ80 – O and AZ80 – F. As mentioned, AZ80 – O exhibits more formability than AZ80 – F, due to additional heat treatment and fine grain size, so similar results were also experienced here. Major and minor strains were recorded at the onset of necking, and forming limit curves were generated as shown in Figure 69. Specimens of various widths formed at room temperature for round punch tests are also shown in Figure 70.

FLCs are drawn in Figures 71 and 72 for both magnesium AZ80 – F and AZ80 – O. Each point on the FLCs indicates a specific blank width from left to right. Blank widths vary from left to right from 10mm to 100mm. It is quite clear that formability increases drastically at elevated temperatures compared with room temperature for both AZ80 – O and AZ80 – F. However, AZ80 – F shows less formability than AZ80 – O because of its coarse grain size.

This exactly portrays a similar trend that developed during the tensile tests. Variations in major and minor strains of strain paths are also indicating this.

The reason is similar, as discussed earlier, because for a fine-grain size strain rate sensitivity is more than 0.3, which allows grains to recrystallise and form new shapes, which increases drawn depth, and the materials exhibit superplasticity.

In addition, the influence of the punch velocity was also examined on FLCs at 200^0C, as shown in Figure 73.

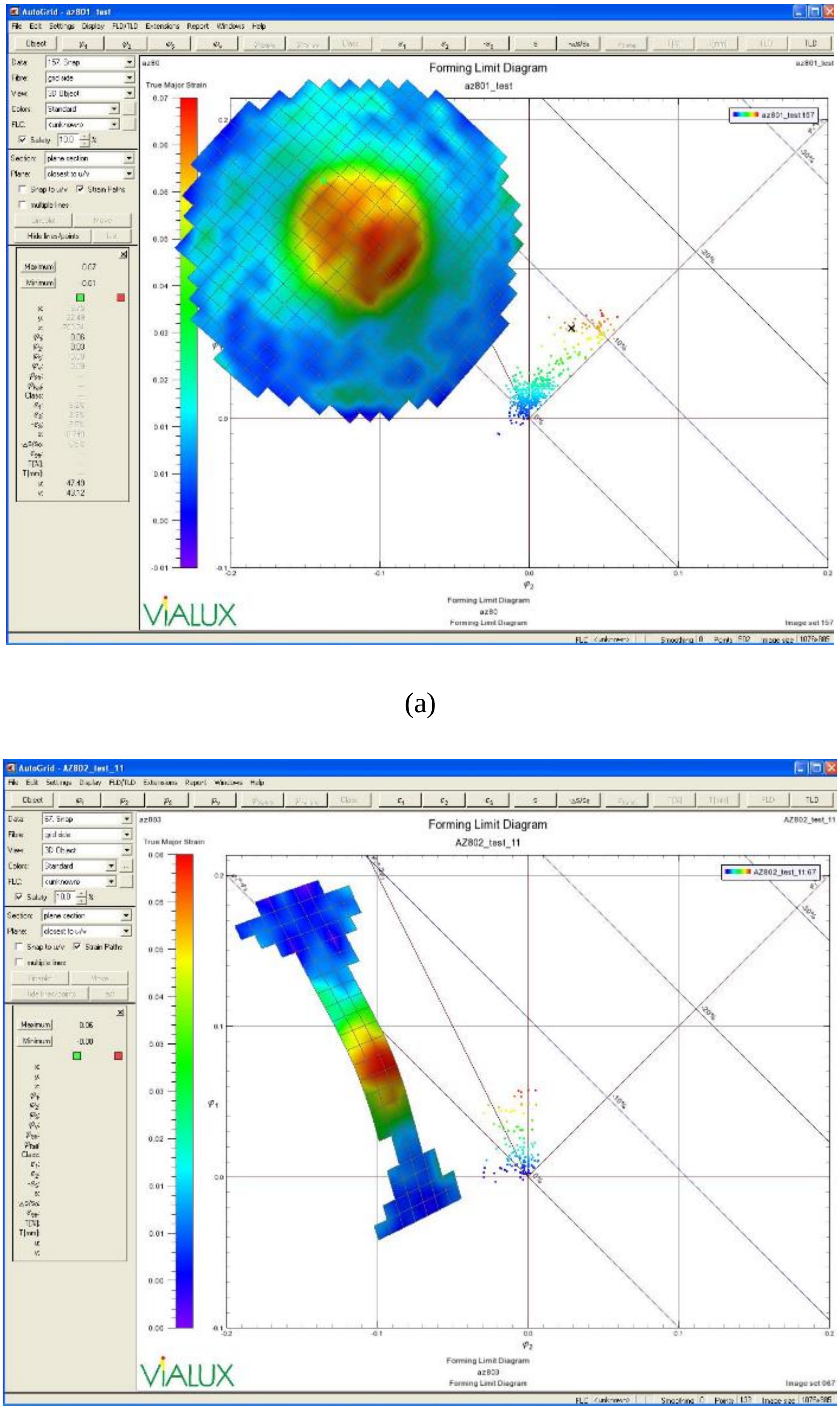
AutoGrid - az801_test
Forming Limit Diagram
az801_test
True Major Strain
az801_test 157
VIALUX
Image set 157
AutoGrid - AZ802_test_11
Forming Limit Diagram
AZ802_test_11
True Major Strain
AZ802_test_11 67
VIALUX
Image set 067
φ1
φ2
10%
20%
30%

(a)

(b)

Figure 69. View of strain paths generated by Autogrid software for various blank widths at RT and 1mm/min (Nakazima tests), (a)15mm, (b) 100mm

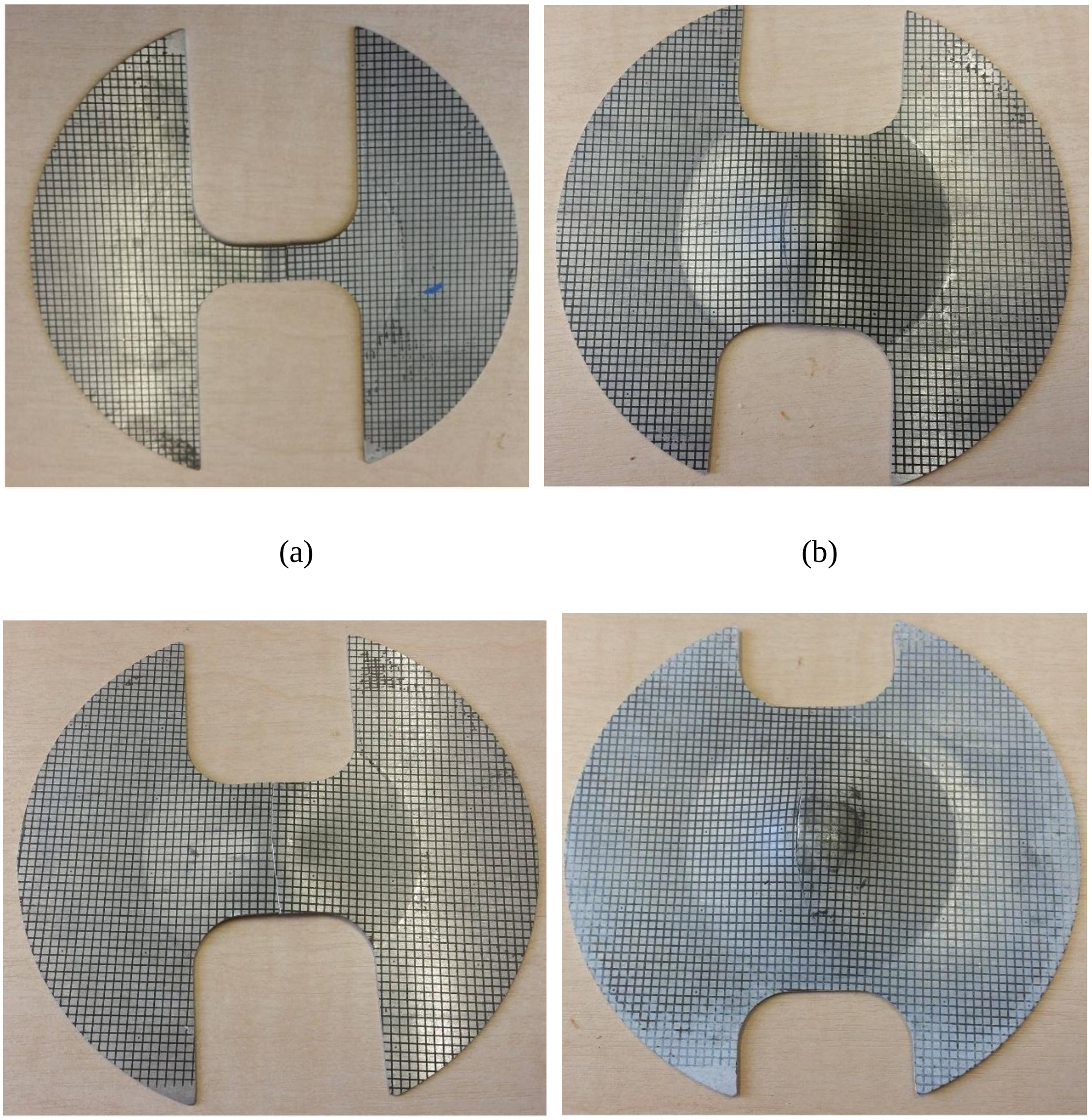

(a) (b)

(c) (d)

Figure 70. Round Punch samples of various widths (Nakazima tests) (a)10mm (b)20mm (c)35mm (d)50mm at RT and 1mm/min speed

Two punch velocities were used: 1 mm/min and 10 mm/min. Due to limited availability of material, tests were only conducted with AZ80 – O. As similar trends were followed in the tensile tests and deep-drawing tests, it can be concluded that AZ80 – F would also follow similar trends in deep-drawing tests. It is quite clear from Figure 72 that the FLC shifted upwards by about 33 percent, especially on the left side with increase in temperature.

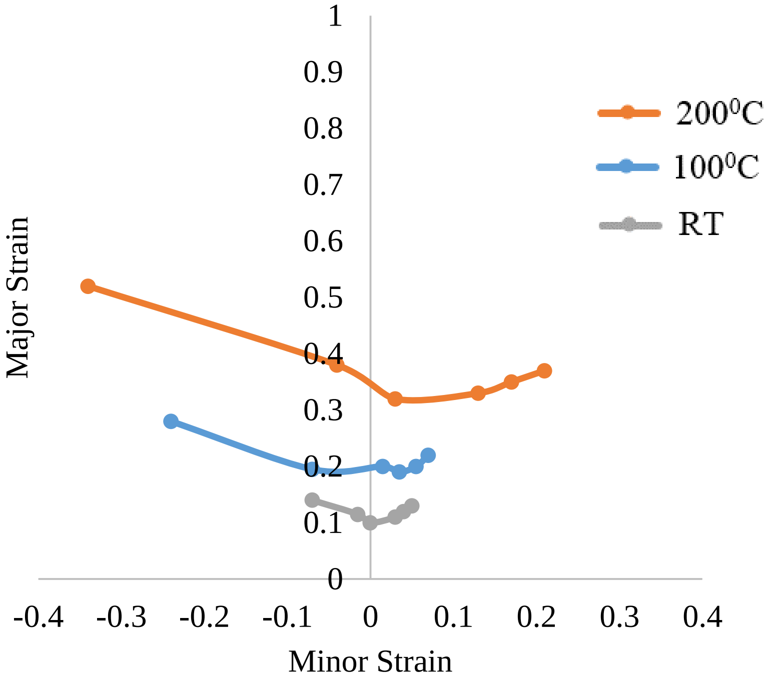

Figure 71. Forming limit curves of AZ80 – F at various temperatures (Nakazima tests)

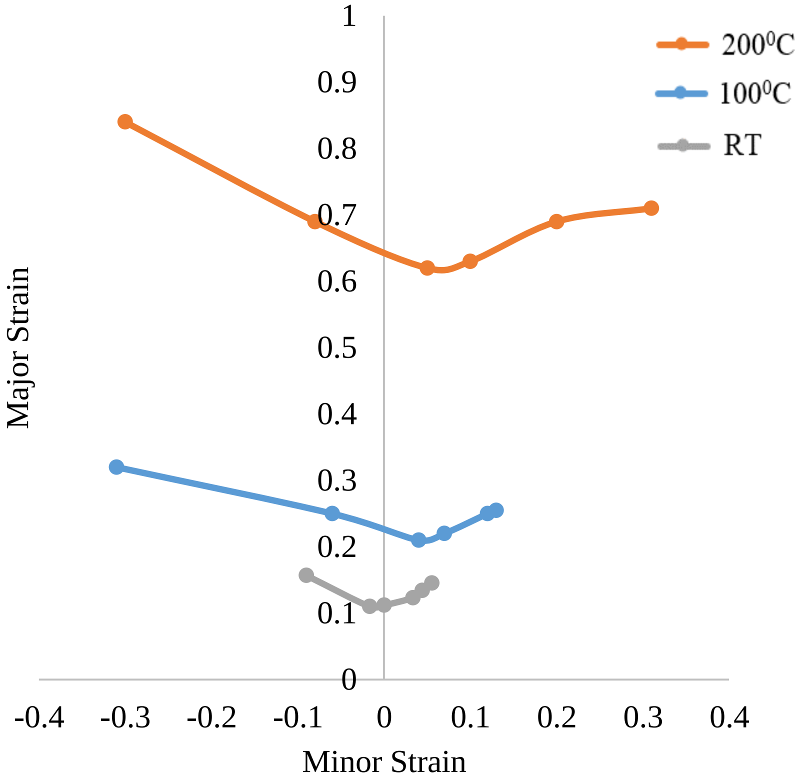

Figure 72. Forming limit curves of AZ80 – O at various temperaturestemperatures (Nakazima tests)

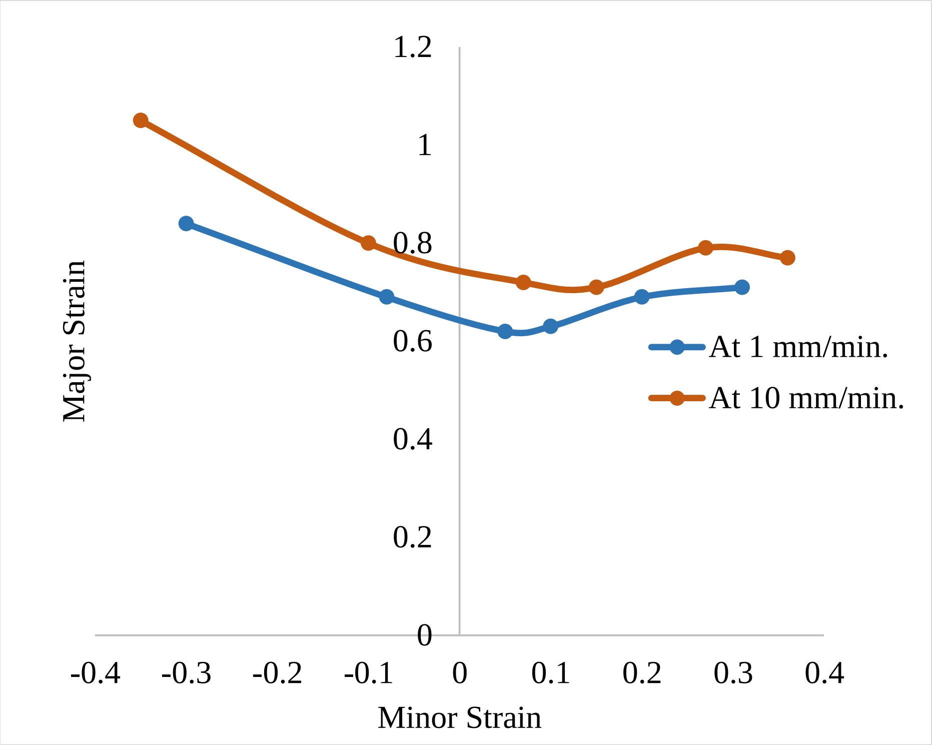

Figure 73. Effect of punch velocity on forming limit curves of AZ80 – O at 200^{0}C (Nakazima tests)

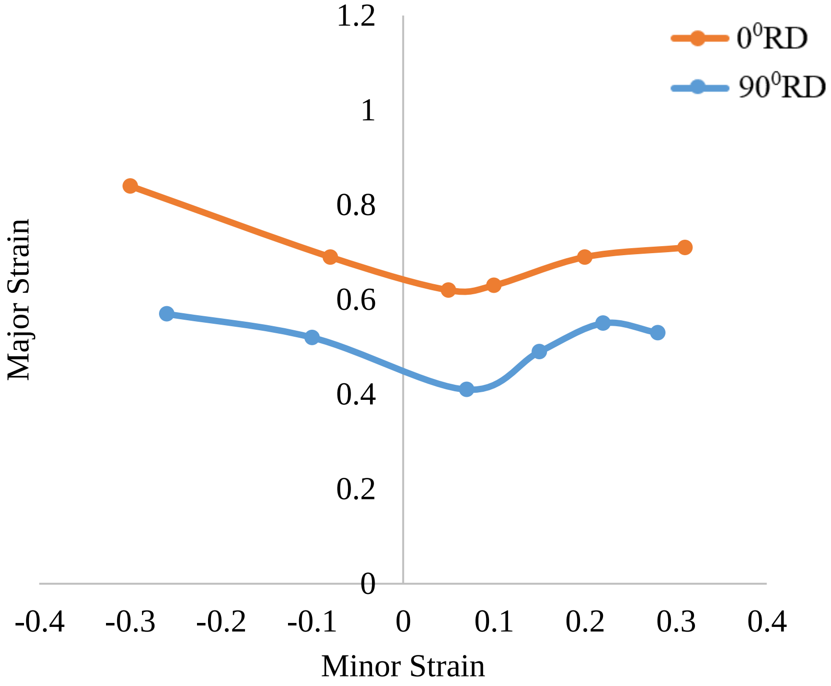

Figure 74. Anisotropy effects on forming limit curves of AZ80 – O at 200^{0}C (Nakazima tests)

The influence of anisotropy was investigated at 200^0C, as shown in Figure 74. Two sheets were examined along rolling direction (0^0RD) and in transverse direction (90^0RD). As limited material was available, this influence was only investigated on AZ80 – O. The influence is quite visible in the 0^0RD sheet showing more formability than the 90^0RD sheet. This exactly confirms the results of tensile testing, where a similar behaviour was witnessed.

5.8.2 Pre-processing parameter characteristics

5.8.2.1 Influence of temperature

Temperature is the pre-processing parameter with the most influence on magnesium alloys, due to their HCP structure, as previously mentioned. Due to the additional heat, slip systems are activated and provide more homogeneous deformation. In the deep-drawing process, the influence of temperature is visible in the FLD diagrams for both AZ80 – O and AZ80 – F, as limits of strain increase and the curve moves upwards from room temperature to 200^0C, as shown in Figure 71 and 72. Formed cups of magnesium AZ80 – O at various temperatures are shown in Figure 75. To investigate the effect of temperature, rectangular punch tests were undertaken at the ERI Institute of AUT University, Auckland.

Load displacement curves are given in Figure 76. AZ80 – O shows a strong sensitivity to temperature, which also confirms its behaviour during tensile testing. The reduction in load and a drastic increase in displacement is due to the activation of additional slip systems, as discussed in section 2.5.

Deep-drawing tests with the AZ80 magnesium sheets were carried out between room temperature and 250 °C to find out the limit drawing ratio at different temperatures. The punch velocity and blankholder force were chosen between 1 and 10 mm/min and in a range of 0.5 to 70 kN, respectively. The used blank shape is shown in Figure 66(b) and the corresponding limit drawing ratio for rectangular parts can be calculated as follows:

$$LDR = \frac{Maximum\_Blank\_Diameter}{Punch\_Diameter} = \frac{\sqrt{4\frac{A_{blank}}{\pi}}}{\sqrt{4\frac{A_{punch}}{\pi}}} = \sqrt{\frac{A_{blank}}{A_{punch}}} \tag{25}$$

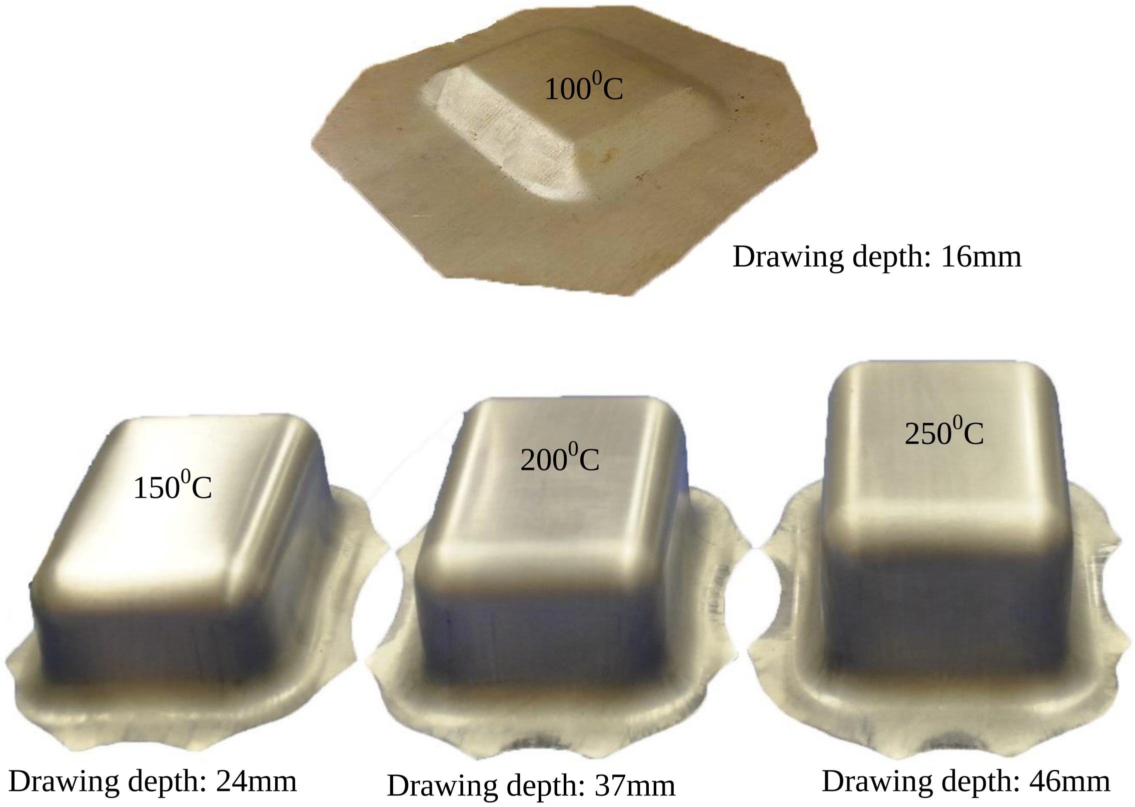
100^0C
Drawing depth: 16mm
150^0C
200^0C
250^0C
Drawing depth: 24mm
Drawing depth: 37mm
Drawing depth: 46mm

Figure 75. Formed cups at various temperature and at speed of 1mm/min (Marciniak tests).

The limit drawing ratio (LDR) is an indicator for the formability of the material and describes the maximum possible drawing ratio between the size of the blank which can be safely drawn, and the punch cross-section. It is a ratio of square root of blank area to punch area. It was tried to achieve this limit drawing ratio at 100, 150, 175, 200 and 250 °C by varying the blankholder force. Results of various trials at different temperatures in form of load displacement curves are given in Figure 76 and also in the next sections.

As expected it was not possible to draw good parts at room temperature and also at 50 °C the parts have fractures in the edges where a high formability is required.

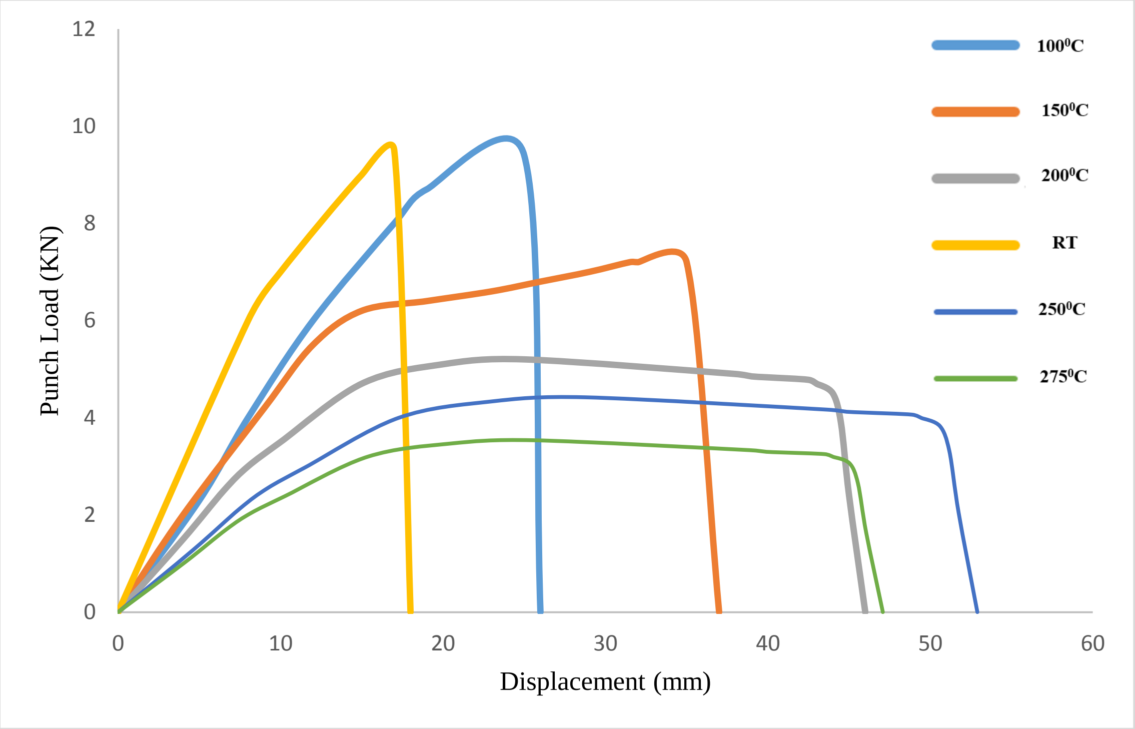

Figure 76. Load displacement curves for deep-drawing tests for magnesium AZ80 – O at various temperatures (Marciniak tests)

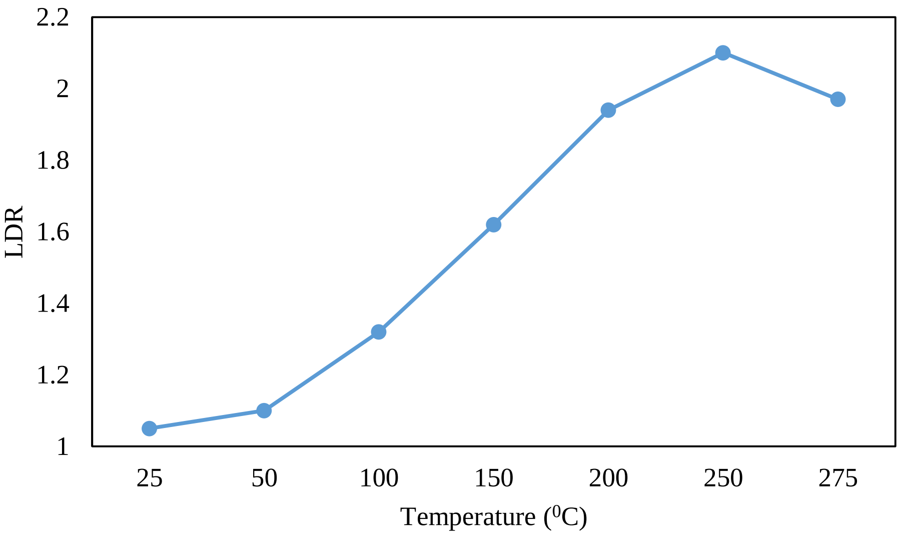

Figure 77. Variation in Limit Drawing Ratio (LDR) with temperature at punch speed of 1mm/min for magnesium AZ80 – O (Marciniak tests).

The first good part could be drawn at 100 °C, a LDR of 1.32 and a blankholder force of 0.5 kN as shown in Figure 75. LDR values are highly influenced with temperature as shown in Figure 77.

It is visible in Figure 77 that LDR values increase with an increase in temperature. A maximum LDR value of 2.1 was achieved at 250^0C, however after which the curve indicates a decline in values at a temperature of 275^0C. This decline in LDR is an indication of a decrease in the strain hardening exponent. This also indicates that maximum drawability can only be achieved up to a temperature of 250^0C and there is no need to increase temperature beyond this point.

At 150 °C a LDR of 1.62 and drawing depth of 24 mm was achieved in a large range of the blankholder force.

At 200 and 250 °C a LDR of 1.94 and 2.1 as well as a drawing depth of 37 and 46 mm, respectively were achieved. Good parts with a lower drawing ratio could be drawn in a wide range of the blankholder force. With an increasing drawing ratio more material remains in the flange at the short side of the part whereas at the long side more material flows into the cavity. As a result wrinkling starts earlier and fractures occur always at the shorter side of the parts because the blank is longer clamped in this section where the whole blankholder force is applied after the blank at the long side is completely drawn into the cavity. The range of the possible blankholder force to draw good parts is very large at a drawing ratio of 1.94 and decreases dramatically at a drawing ratio of 2.1.

This is a result of the limited formability at that temperature and is additionally supported by the abovementioned behaviour.

Trials at 250 °C and a LDR of 2.1 show fractures very early in the forming process even at a lower blankholder force. It can be assumed that this drawing ratio is also not achievable at higher temperatures. On the contrary the LDR becomes lower above 250 °C due to the further softening of the magnesium with which the required force cannot be transmitted any longer at higher drawing ratios.

In conclusion of the deep-drawing tests it can be said that the LDR increases continuously from lower temperatures up to 250 °C as seen in Figure 77. The first good part could be drawn with a LDR of 1.62 and a drawing depth of 24 mm at 150 °C and the deepest drawn part at 250 °C with a LDR of 2.1 and a depth of 46 mm. A recommendation for deep-drawing of AZ80 – O magnesium sheet with an even distributed surface temperature is that a temperature rise above 250 °C is not practical for the investigated cup geometry because of a decrease of the drawing ratio and also with regards to the required energy. However the formability of the AZ80 – O magnesium is even better at 250 °C than at lower temperatures, which confirms the activating of additional deformation mechanisms of the hexagonal closed packed crystal structure as mentioned in section 2.4.1.

5.8.2.2 Influence of blankholder force

The influence of the blank holder force was examined, with three blank holder forces: 50kN, 75kN and 100kN, as shown in Figure 78 for magnesium AZ80 – O.

This investigation was necessary to avoid wrinkles at the flange area of deep-drawn cups, which ultimately lead to defects. At 75kN and 100kN the material failed in the flange area, due to a too tight grip, however, at 50kN a properly formed shape was achieved. The blank holder force will also influence the strain distribution on walls of formed cups that results in rupture on top of the wall as shown in Figure 78(e). The rupture was observed at 200^{0}C at a constant punch speed of 1 mm/min and a blank holder force of 100kN. These type of ruptures are also termed as ductile ruptures that occur in cup walls due to low ductility in magnesium AZ80 – O under these conditions as shown in Figure 79.

5.8.2.3 Influence of blank notch width

The influence of the blank notch width was investigated by considering various notch widths of 100mm, 75mm, 50mm, and 35mm and 20mm, as shown in Figure 80 for magnesium AZ80 – O. Notch widths exhibit an inversely proportional relationship with the amount of displacement, while the load proportionally increased with each increase in notch width as shown in Figure 80.

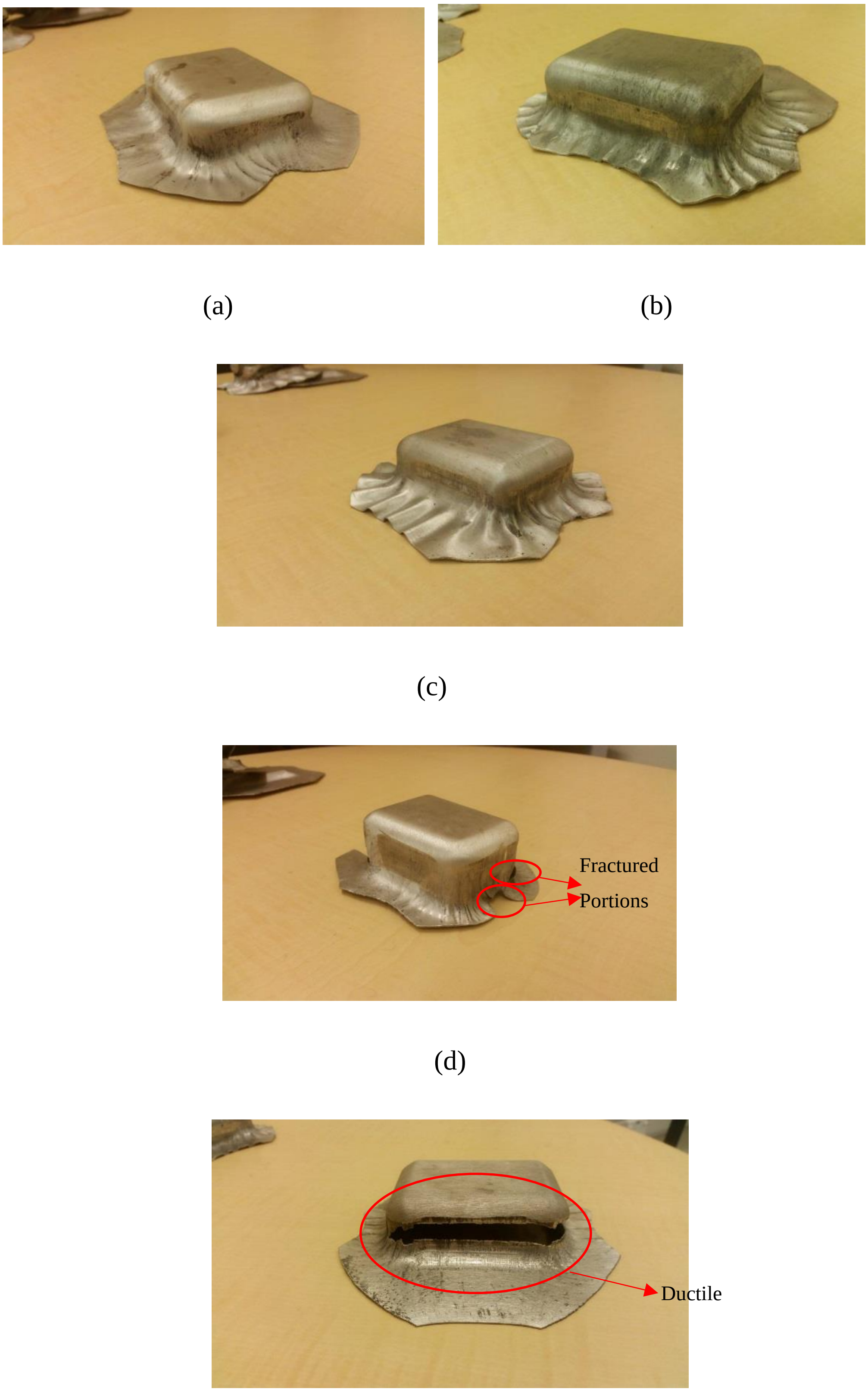

Fractured
Portions
Ductile

(a) (b)

(c)

(d)

(e)

Figure 78. Effect of Blank holder force at 150^{0}C and 1mm/min. (a) 50 kN, (b) 75kN, (c) 100kN, (d) 75kN and 200^{0}C, (e) 100kN and 200^{0}C (Marciniak tests)

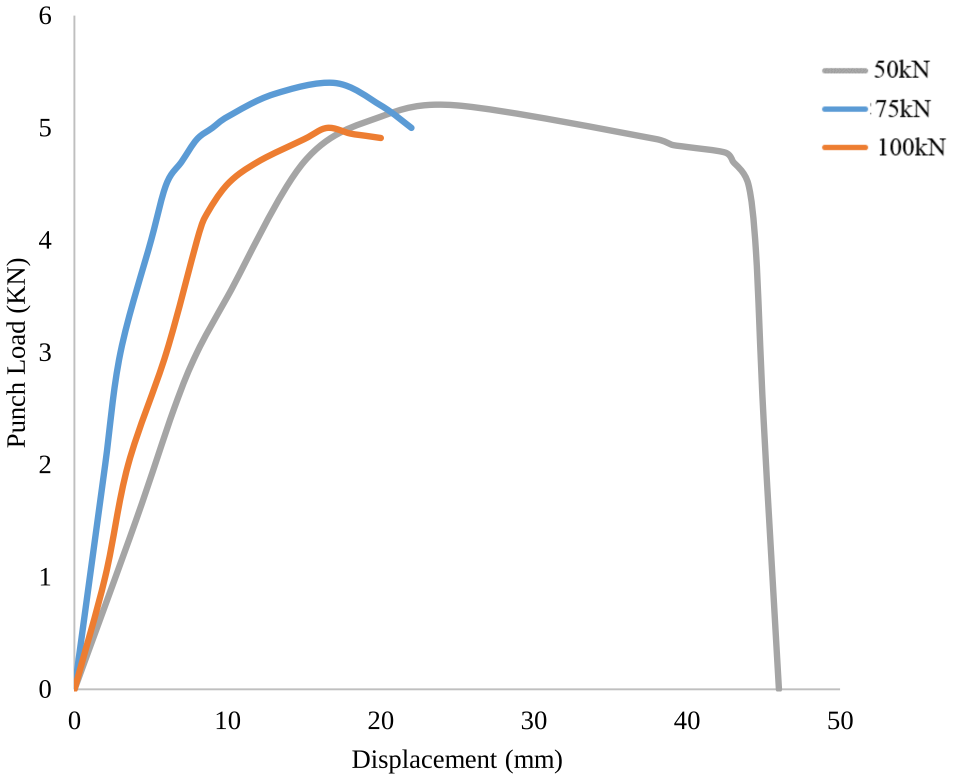

Figure 79. Load displacement curves for deep-drawing tests for magnesium AZ80 – O at various blank holder forces (Marciniak tests)

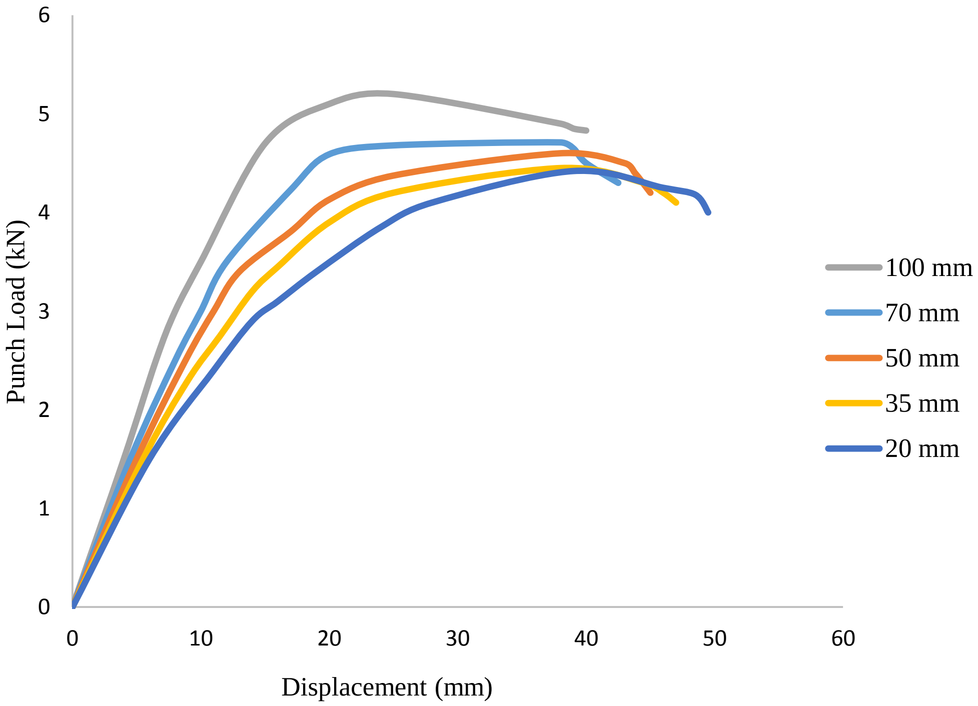

Figure 80. Load displacement curves for deep-drawing tests of magnesium AZ80 – O for various blank notch widths (Marciniak tests)

5.8.2.4 Influence of punch velocity

Punch velocity has a major influence on the forming properties of magnesium AZ80. Due to variations in punch velocity, processing time varied, which resulted in variations in temperature distribution on blanks. This allowed more grain refinement with the application of load, however, increasing the load beyond 300^0C reduced formability instead of increasing it, due to the effect of cavitation. A comparison of FLCs for two punch speeds is shown in Figure 73.

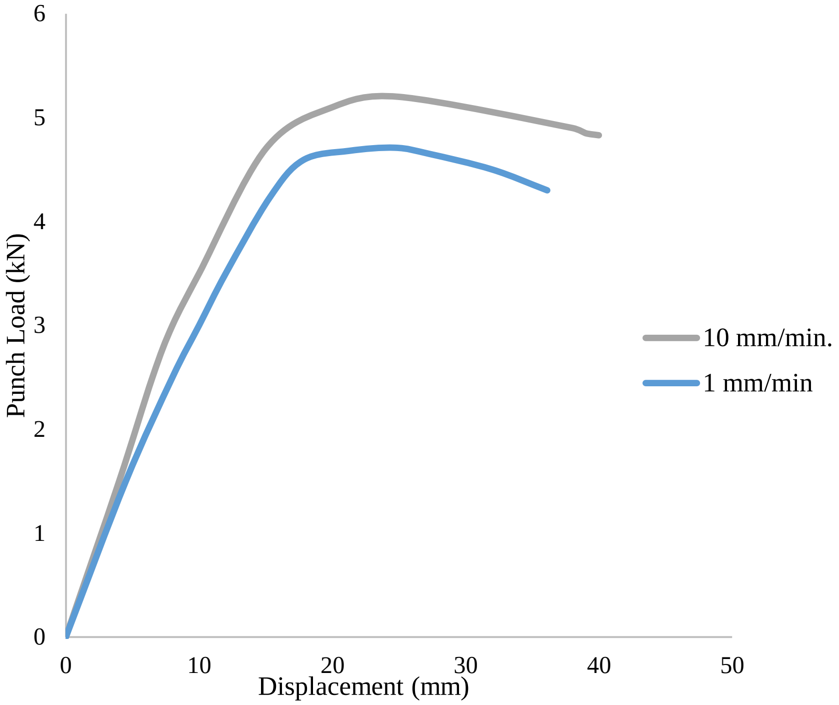

Figure 81. Load displacement curves for deep-drawing tests for magnesium AZ80 – O for various punch velocities (Marciniak tests)

Load displacement curves for AZ80 – O with varying velocities are shown in Figure 81. It is quite clear that with decreasing punch velocity, load decreases, but this will increase production time.

5.9 Conclusions

In this chapter, the formability of the magnesium alloy AZ80 was thoroughly investigated. Magnesium AZ80 was investigated with two grain sizes, AZ80 – O and AZ80 – F. Two types of test setups were used; the

Nakazima and Marciniak tests. These tests were arranged at two different locations. The Nakazima tests were performed at the Institute of Frontier Materials (IFM) at Deakin University, Geelong, Australia, while the Marciniak tests were performed at the Institute for Engineering research (IRF) at AUT University Auckland, New Zealand. Both internal and external heating procedures were adopted, due to the limitations in the test bed setups for the Marciniak and Nakazima tests. Strain measurements were done by a DIC system that was equipped with four CCD cameras. To distribute load evenly on the magnesium sheet, a sandwich of a Teflon sheet and high temperature sulphide grease were used for both magnesium AZ80 – O and AZ80 – F.

Forming limit diagrams (FLDs) were plotted with the help of the Autogrid software that provided strain path distributions on various widths of blanks. The influence of various pre-processing parameters temperature, blank holder force, punch velocity and blank notch width, were measured. The main findings are:

1. It is quite clear that formability increases drastically at elevated temperatures compared with room temperature for both AZ80 – O and AZ80 – F. However AZ80 – F shows less formability thanAZ80 – O, due to its coarse grain-size, as shown in Figures71 and 72.
2. Effects of the punch velocities were examined and data were plotted as FLDs and load displacement curves, as shown in Figures73 and 81 respectively. It can be concluded that punch load reduces with a decrease in punch velocity, however, process time increases with lower punch velocity, which reduces the scope for commercial applications of magnesium AZ80 – O.
3. The influence of the blank holder force was investigated, as shown in Figure 79 for magnesium AZ80 – O. At 50kN of blankholder force, good parts were drawn, however, with increasing blankholder forces of 75kN and 100kN the material failed in the flange region due to a too tight grip.

4. The width of the blank notch also played a role in the load displacement curves. The notch widths exhibit an inversely proportional relationship with the amount of displacement, while the load proportionally increased with an increase in notch width, as shown in Figure 80 for magnesium AZ80 – O.
5. LDR increases continuously from lower temperatures up to 250 °C as seen in Figure 77. The first good part could be drawn with a LDR of 1.62 and a drawing depth of 24 mm at 150 °C and the deepest drawn part at 250 °C with a LDR of 2.1 and a depth of 46 mm.

Chapter 6

Microstructure analysis

6.1 Introduction

Variations in mechanical and forming characteristics are entirely dependent on microstructure changes in materials [347]. Magnesium alloys, due to their HCP crystal structure, exhibit poor formability at room temperature due to the limited availability of independent slip systems [46]. However, these characteristics improve dramatically at elevated temperatures, as discussed in chapters 4 and 5. The obvious reason is activation of additional slip systems that boost mechanical and forming capabilities to compete with extant commercial aluminium and steel alloys [63]. It was therefore necessary to investigate microstructure characteristics to understand the behaviour of magnesium alloys.

Microscopy slides also clarify the effect of fine and coarse grain sizes on mechanical and forming characteristics. As discussed, the fine alloy exhibits more ductility than the coarse-grain alloy, so the behaviour of both alloys is investigated here. From the literature [85] - [90] it is quite clear that the deformation behaviour of these magnesium alloys varies according to the range of temperatures at which they are processed. The effects of twinning, grain boundary sliding, cavitation and the generation of filaments at higher temperatures are thoroughly reported here.

Heat treatment and additional hot rolling also affects the microstructure of magnesium alloys and makes them more suitable for producing long elongations before failures, and finally leads to superplasticity. An explanation of these processes will help to understand the behaviour of magnesium alloys so that its use in the sheet metal industry can be increased according to commercial requirements.

In this chapter, micrographs from a scanning electron microscope and an optical microscope are analysed in order to understand variations in behaviour of the material at elevated temperatures. In addition, energy dispersive X – ray spectroscopy (EDS) tests were also performed to examine the orientation of grains and variations in percentage of constituents under different loading conditions.

6.2 Methodology

6.2.1 Sample preparation

Sample preparation is an important metallographic process. To investigate magnesium AZ80’s properties, tensile specimens and deep-drawn specimens were cut with a grinder cutter at a distance of 2 mm from the fractured surface, so that the influence of fractured material could be avoided. Later the specimens were held in circular rings and mounted in phenolic hot mounting resin at 150^0C by a Struers mounting machine. After the hot mounting, specimens were ground with 180, 500, 800 and 1200-grit silicon carbide papers to produce mirror-like surfaces. In a subsequent step, the samples were polished in a Struers Tegra Pol-25 automatic polishing machine. Various grades of grinding paper with roughness values of 6μm, 3μm and 1μm were used in stages to polish the specimens. Samples were polished with these cloths for one minute each.

The next step after grinding and polishing was etching of samples. The etchant recommended by the ASM standard for magnesium alloys is Acetic-Picral [348]. An accurate amount was measured with a digital balance. Acetic-Picral was made with 5 g of picric – acid, 6 g of acetic acid, 10 ml of water and 100 ml of ethanol. Samples were etched in Acetic-Picral for 3 to 5 seconds until the colour started changing. Later, the samples were washed carefully with ethanol and dried. Etching and washing of the samples was performed underneath a fume collector chimney so that the effects of acids on skin could be avoided.

6.2.2 Optical and electron microscopes

An Olympus stereo microscope (SZX9 series) was used for low-magnification microscopy analysis. It had a zoom ratio of 9 with a maximum resolution of 600 lines per minute. For high magnification slides, a Hitachi SU-70 scanning electron microscope (SEM) was used, as shown in Figure 82. The microscope was capable of increasing magnification to 800,000 times with a 1nm resolution at 4mm distance. It was equipped with an electron lithography system (NPGS) for producing a focused beam. An Omniprobe gas injection system was also employed to produce high precision images. A quasor detector and nano trace Si (Li) detector were also installed for both EBSD and EDS testing.

Grain sizes were measured with average grain intercept method (AGI). In this method a random line was drawn on micrograph and then number of grains were counted wherever the line intersects the grain boundary.

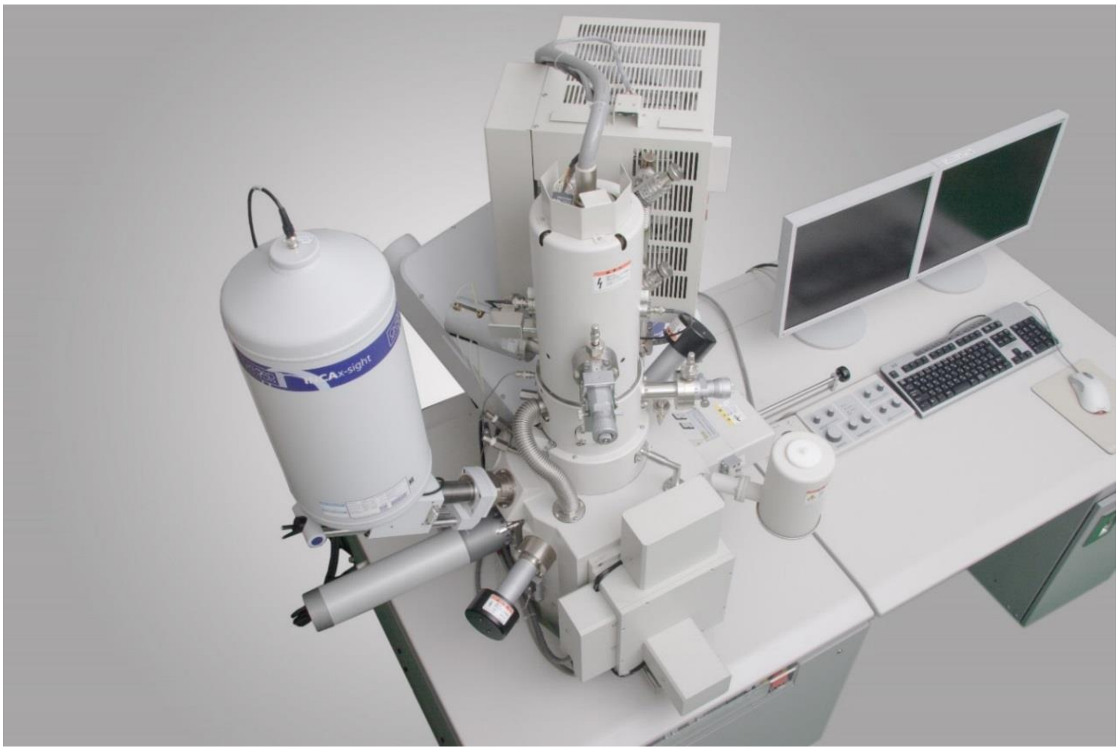

Figure 82. Hitachi SU – 70 scanning electron microscope

6.3 Results and discussion

6.3.1 Surface morphology

The fractured surface morphology of the specimens at various temperatures and strain rates are shown in Figure 83 for both magnesium AZ80 – O and AZ80 – F. Figure 84 shows the surface morphology of both alloys at various temperatures and strain rates. In Figure 83 there are no voids and nucleated grains on the deformed surface and the fracture is seen to be the result of pure necking. However, in Figure 84 as temperature increased from room temperature to 200^0C and later was raised to 300^0C and 400^0C, various voids and nucleated grains were visible as marked. A cone-shaped macroscopic surface is visible in Figure 84 at the necking area, with evident micro voids scattered along the fractured surface.

A large number of dimples of cavities and highly dense tearing edges are visible in the higher resolution micrographs, as shown in Figures 85 and 86 respectively, which is a clear indication of a ductile fracture. These figures also show that with an increase in temperature, these nucleated voids are the dominating fracture mechanism, and the decreasing effect of pure necking at the instantaneous deformation zone. At the higher temperature of 400^0C, the material exhibited a higher shrinkage rate due to localised necking.

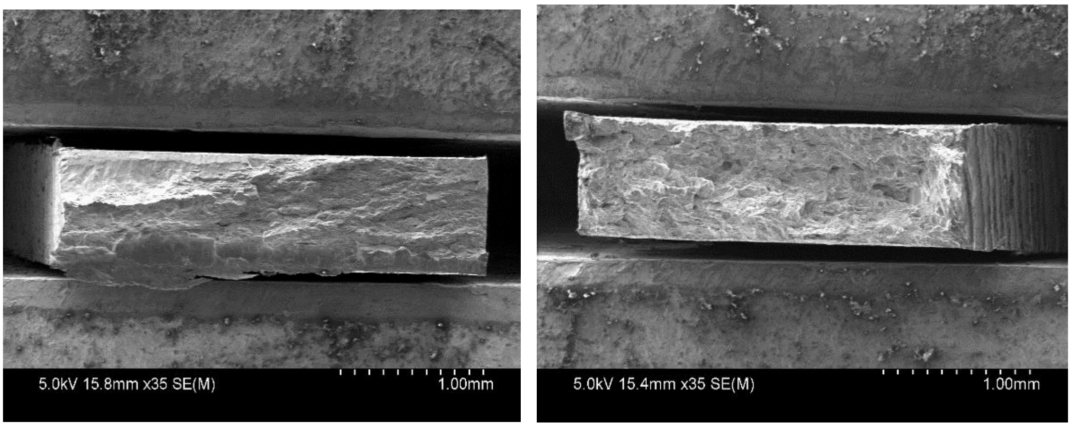

(a) (b)

Figure 83. Surface morphology of (a) AZ80 – O and (b) AZ80 – F at room temperature at 1 x 10^{-3} sec^{-1}

At 400^{0}C, the fractured surface shows two types of fracture morphology, one with cavitation and the other with intergranular fractures as shown in Figures 84(e) and 84(f) for both alloys. Cavities with voids can be noted in both figures. When these cavities grow, they generate stress concentration regions in nearby grains, which leads to premature fractures of material.

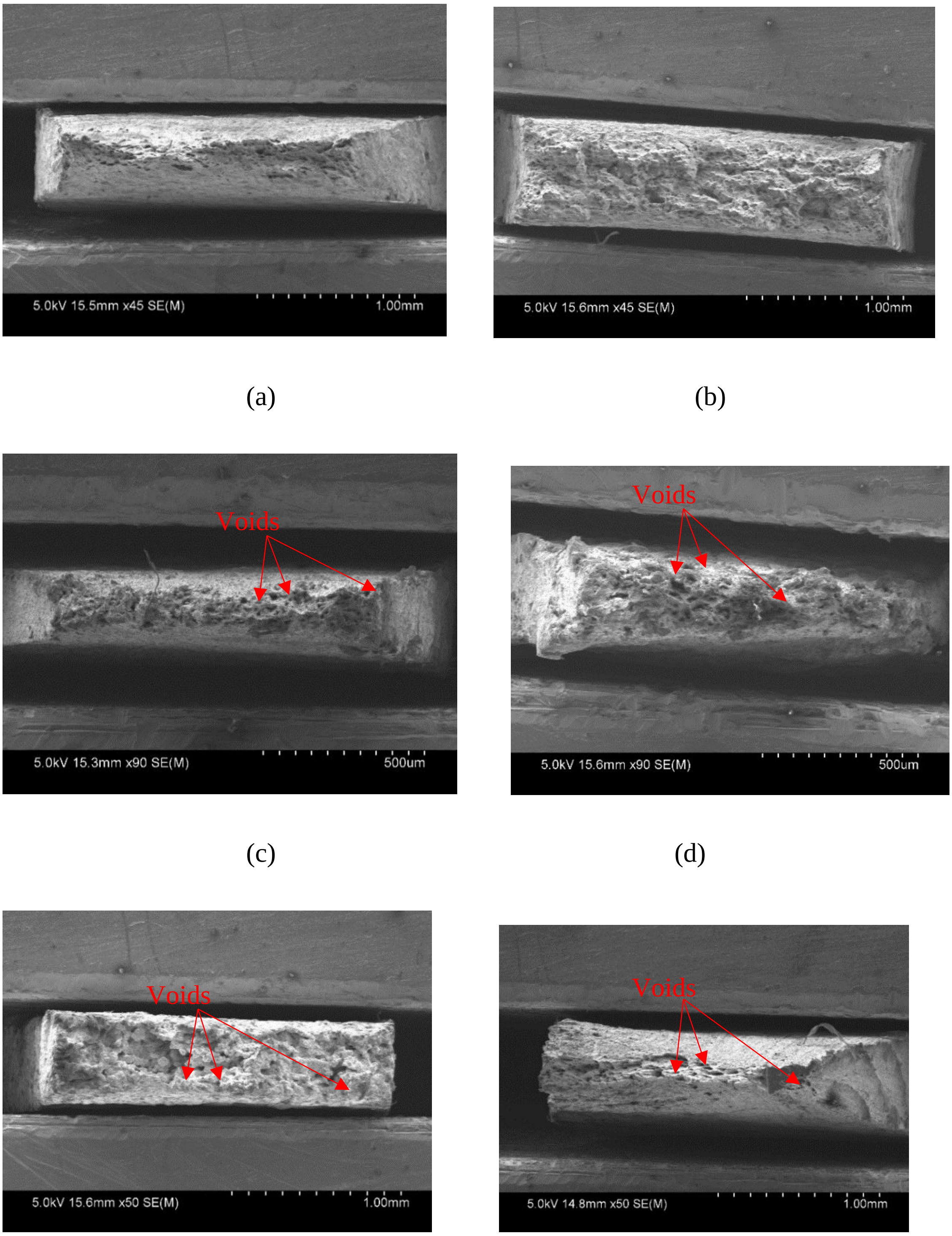
5.0kV 15.5mm x45 SE(M)
1.00mm
5.0kV 15.6mm x45 SE(M)
1.00mm
Voids
5.0kV 15.3mm x90 SE(M)
500um
Voids
5.0kV 15.6mm x90 SE(M)
500um
Voids
5.0kV 15.6mm x50 SE(M)
1.00mm
Voids
5.0kV 14.8mm x50 SE(M)
1.00mm

(a) (b)

(c) (d)

(e) (f)

Figure 84. Surface morphology of (a) AZ80 – O at 200^{0}C, (b) AZ80 – F at 200^{0}C, (c) AZ80 – O at 300^{0}C, (d) AZ80 – F at 300^{0}C, (e) AZ80 – O at 400^{0}C and (f) AZ80 – F at 400^{0}C at 1 x 10^{-3} sec^{-1}

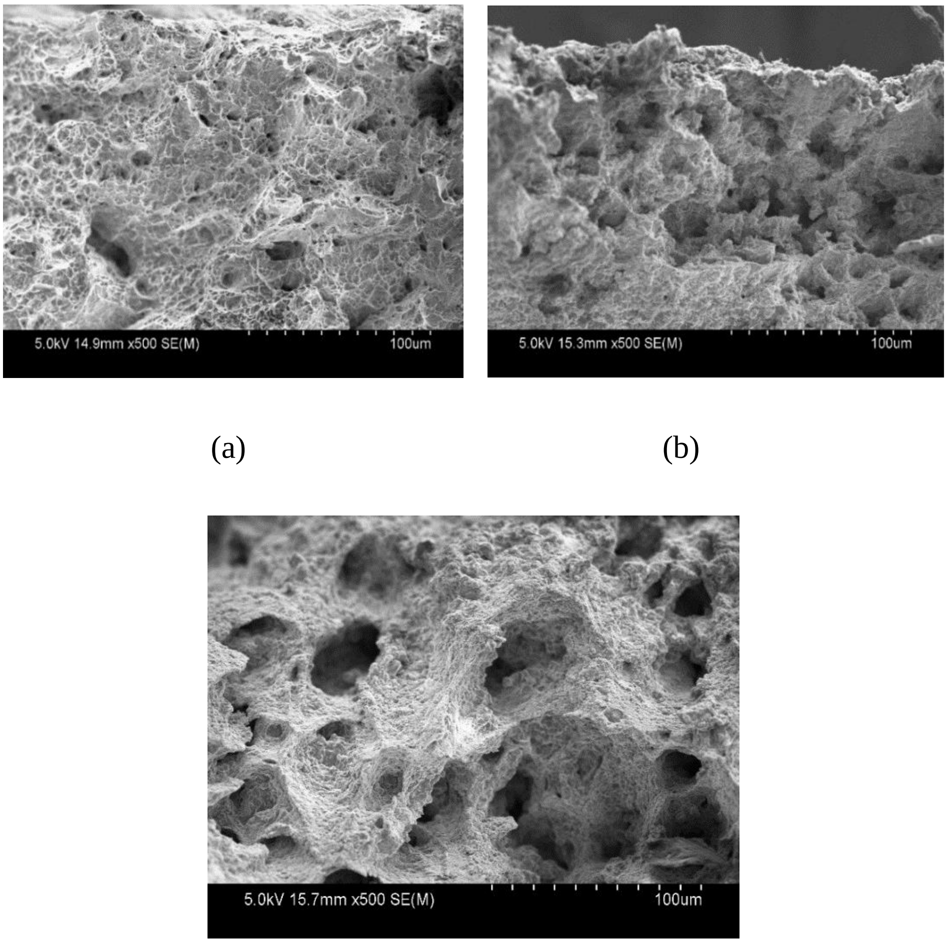
5.0kV 14.9mm x500 SE(M)
100um
5.0kV 15.3mm x500 SE(M)
100um
5.0kV 15.7mm x500 SE(M)
100um

(a) (b)

(c)

Figure 85. Surface morphology of AZ80 – O at (a) 200^{0}C and (b) 300^{0}C (c) 400^{0}C at 1 x 10^{-3} sec^{-1} showing dense dimples

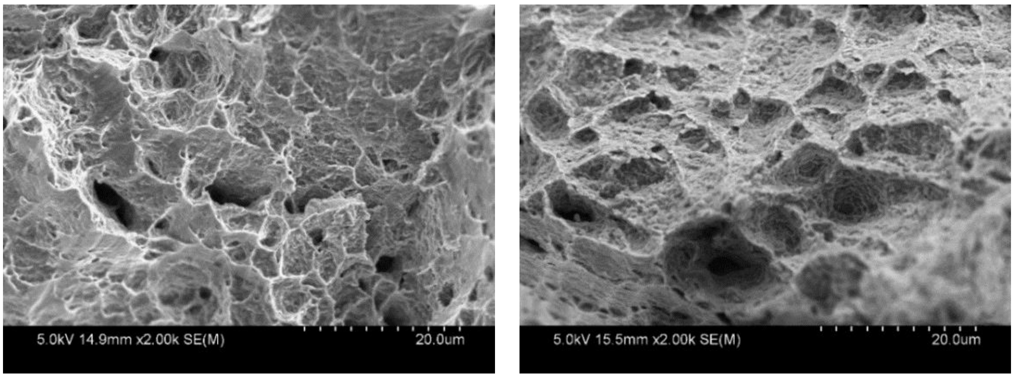

(a) (b)

Figure 86. Surface morphology of AZ80 – O at (a) 200^0C and (b) 300^0C showing dense dimples

6.3.2 Twinning

Under the application of load at various strain rates, numerous twins are seen to emerge on the surface of magnesium AZ80 – O and AZ80 – F at room temperature. However, their influence reduced considerably when both alloys were loaded at elevated temperatures. Twin marks are visible on both AZ80 – F and AZ80 – O. The original magnesium structure was inspected under the optical microscope.

A micrograph outlining the two fundamental twin types discussed in section 2.4.2, and the double twin they created, are clearly shown in Figure 87, which demonstrates a behaviour of rolled specimens of magnesium AZ80 – O and AZ80 – F in different rolling directions.

In micrographs, shapes like lenticular clouds refer to 1012 tensile twins, however, compressive twins 1011 are also visible. The twins at the upper right of the grain have experienced significant thickening and result from rolling.

Double twins are also visible in various locations, as marked in Figure 87. These twins mostly nucleate at grain boundaries and areas that face high stress concentrations. This is because along the high stress regions, grain boundaries support imperfection locations, which allows all these twins to nucleate.

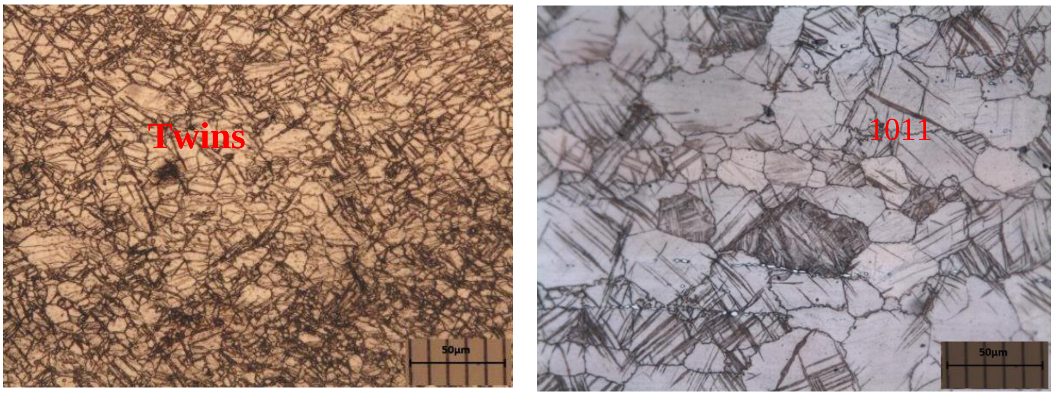
Twins
50µm
1011
50µm

(a) (b)

Figure 87. Effect of twinning on both magnesium (a) AZ80 – O and (b) AZ80 – F at room temperature and 1 x 10^{-3} sec^{-1}

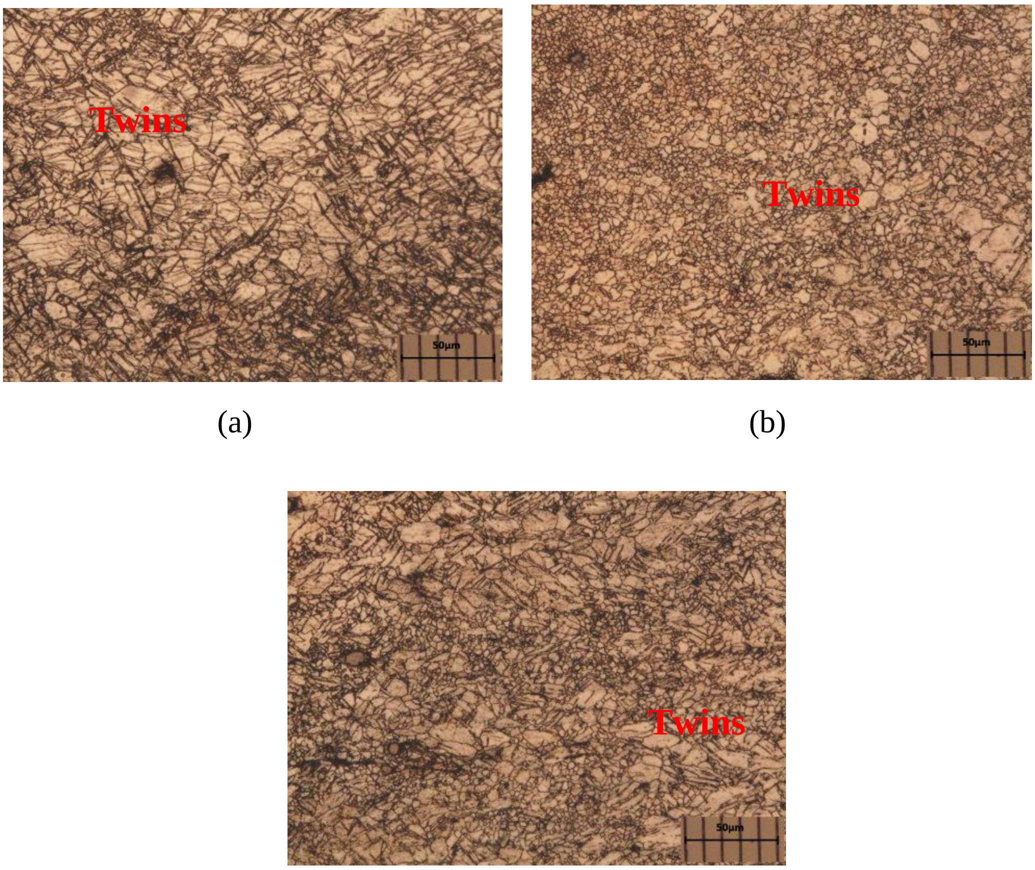
Twins
50µm
Twins
50µm
Twins
50µm

(a) (b)

(c)

Figure 88. Effect of variation in strain rate on twinning in AZ80 – O (a) $10^{-2}sec^{-1}$, (b) $10^{-3}sec^{-1}$, (c) $10^{-4}sec^{-1}$

Twinning affects several other characteristics during tensile loading. These characteristics include yielding, work hardening, ductility, fatigue and fracture toughness. Asymmetry in yield tension and compression behaviour mostly occurs due to 1012 twins [101]. This asymmetry in yielding also restricts magnesium alloys in the sheet metal industry, as the compressive face of sheets will exhibit long deformation compared with the tension face in the deep-drawing process.

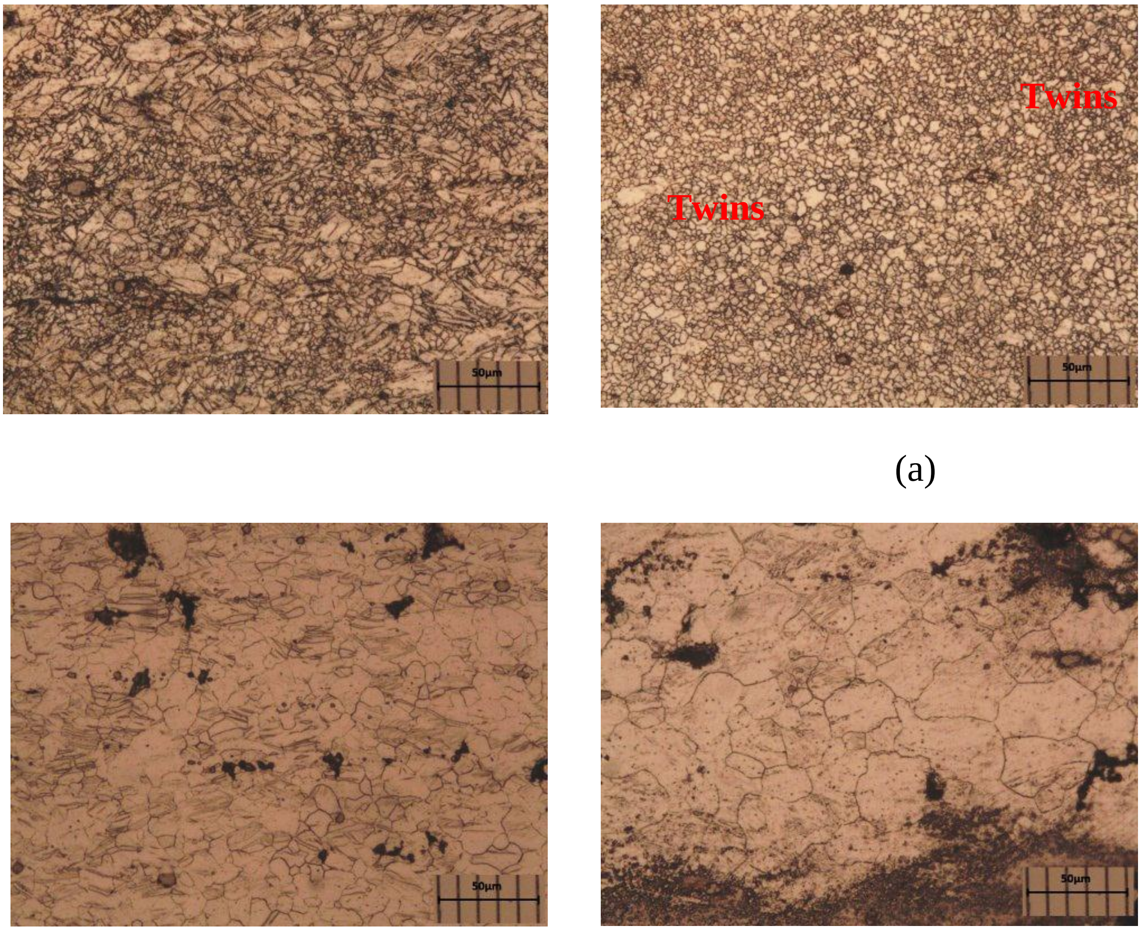

(a)

(c) (d)

Figure 89. Effect of variation in temperature on twinning in AZ80 – O (a) room temperature, (b) 200^0C, (c) 300^0C and (d) 400^0C at $10^{-4}$$sec^{-1}$

. In addition, Somekawa et al. [349] have reported that twins also affect the fracture toughness of materials.

Processing parameters also affect twinning behaviour in magnesium alloys. Three parameters observed here are strain rate, temperature and grain size. Tensile specimens were tested under all these conditions, and later their microstructures were observed with an optical microscope. Strain rate marginally affects twinning behaviour in both alloys, as shown in Figure 88. It was also observed that magnesium AZ80 – F and AZ80 – O behave very similarly for various strain rates at room temperature. Therefore, in this chapter the focus is more on AZ80 – O than AZ80 – F, due to its fine-grain structure and increased probability of showing superplasticity. This was validated by observing stress strain curves at room temperature for both alloys at three different strain rates.

The second parameter observed was temperature. Twinning was heavily influenced by temperature, as twining dominates only at room temperature, as shown in Figure 89 for AZ80 – O. At elevated temperatures, other mechanisms such as grain boundary sliding and cavitation take over.

Twinning is reduced by refinement of grains during rolling. Twinning can likewise maintain its level in high temperature deformations, if the grain sizes are sufficiently coarse, that is much greater than 60µm [106].More numerous twins were seen in AZ80 – F than AZ80 – O, as shown in Figure 87. This pattern is in concurrence with Lahaie et al. [350], that twin development is increased in magnesium with larger grain sizes. A twin basically behaves as a deterrent for movement of the dislocations on grain boundaries. Hence, when twins appeared during a deformation process, the number of dislocations heaped up at twins increase with straining, which enhances the work hardening behaviour. Stress concentrations accumulate around dislocations, which leads to premature failure. Consequently, large twin formations decrease ductility and suppress long elongations before failure, at room and warm temperatures.

The phenomenological explanation is that with the refinement of grains, twins being heavily suppressed which ultimately results in enhanced elongations in magnesium alloys at warm temperatures. Another effect of the influence of twinning in coarse-grained AZ80 – F compared with fine-grained AZ80 – O is twin nucleation. As discussed, these twins mostly nucleate at grain boundaries and areas that face high stress concentrations, so in fine grains, grain boundaries are quite weak and cannot hold these twins for longer times, which means fine-grain AZ80 – O shows larger elongations before failure than does AZ80 – F.

6.3.3 Grain growth

Grain growth is another significant phenomenon that results in the enlargement and reshaping of grains at higher temperatures.

Grain growth due to temperature can occur through any heat treatment process which is static growth, and it can also be influenced by strain at a higher temperature, which is called dynamic grain growth.

To investigate whether grain growth is merely due to strain at higher temperatures that is dynamic grain growth in magnesium AZ80 – O and AZ80 – F, samples were initially strained at various temperatures and strain rates, and later, sections were ground from the gauge sections a few millimetres away from the fractured area. Then, to observe static grain growth, more sections were taken from the grip section of specimens that experienced growth only through time and temperature. The heating time varied between 25 to 50 minutes at a 10^{-3} sec^{-1} strain rate.

The reason for selecting the lowest strain rate was that at extremely slow strain rates, both the static and dynamic changes in microstructure can be compared, with sufficient time available, and meaningful conclusions can be drawn. In order to check variations in microstructure with respect to rolling directions, samples were also investigated in both rolling direction (0^0RD) and transverse direction (90^0RD).

In addition, to investigate grain growth at various levels of strain, different samples were strained at 25%, 50% and 75% of total strain, so that grain growth could be researched with respect to load and temperature at progressive loading levels.

Optical and SEM micrographs indicate that for both AZ80 – O and AZ80 – F the grain size increases more in the gauge section than the grip section, which results from dynamic grain growth as the dominating phenomenon, as compared with static grain growth, shown in Figures 90 - 91. Additional SEM micrographs are also shown in Appendix 2.

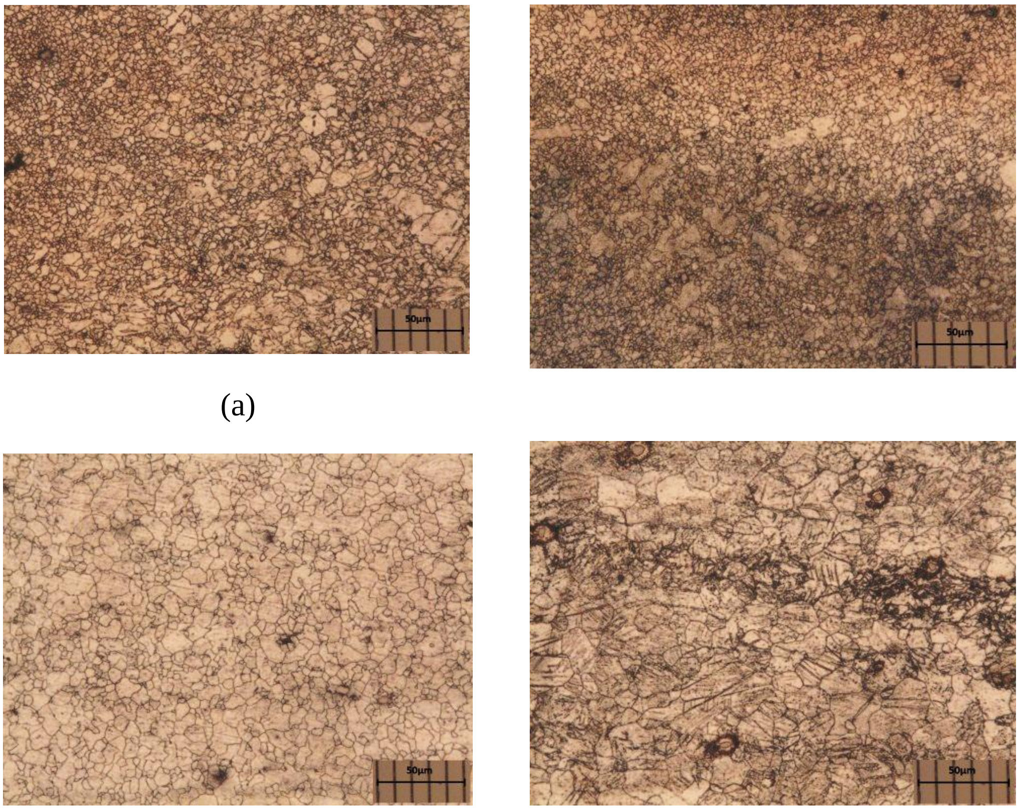
50µm
50µm
50µm
50µm

(a)

(b)

(c)

(d)

Figure 90. Grain size increments with varying temperature in AZ80 – O at gauge (a) room temperature (b) 200^0C (c) 300^0C and (d) 400^0C at 10^{-3}sec^{-1}

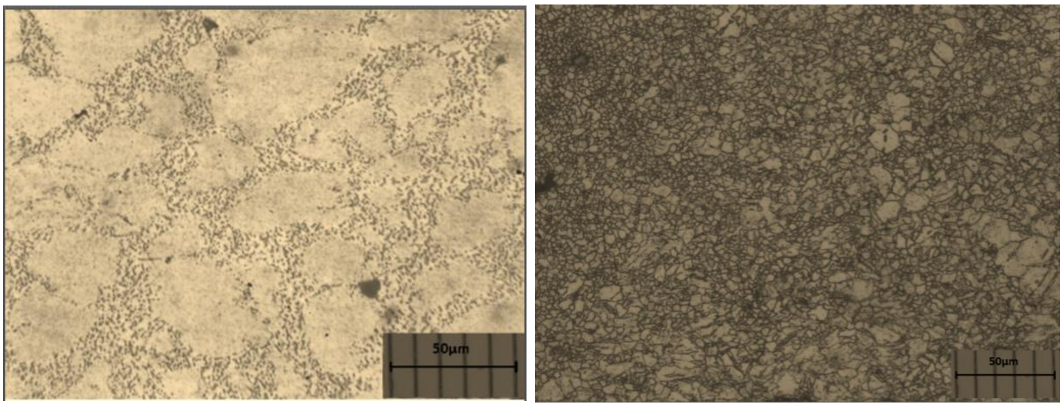

(a)

(b)

Figure 91. Microstructure of magnesium AZ80 – O at 300^{0}C and 10^{-3}sec^{-1} (a) gauge section (b) grip

In Figure 92, grain growth as a function of temperature is plotted at a strain rate of 10^{-4} sec^{-1}. It is quite evident that in AZ80 – O, grain size increases approximately four times, that is, from 10µm to 42µm. However, in AZ80 – F with a coarse grain-size, the increment is less; up to 1.5 times. It was also observed that grain growth shows an inversely proportional relation with loading time or straining time. A comparison of average grain sizes growth with respect to temperature is given in Figure 93 for both magnesium AZ80 - O and AZ80 - F. It is quite visible that grain growth is more significant in AZ80- O as compared to AZ80 - F, due to smaller initial grain size. Grains increase at the initial stage of the deformation, and then become steady at 70% - 80% of strain.

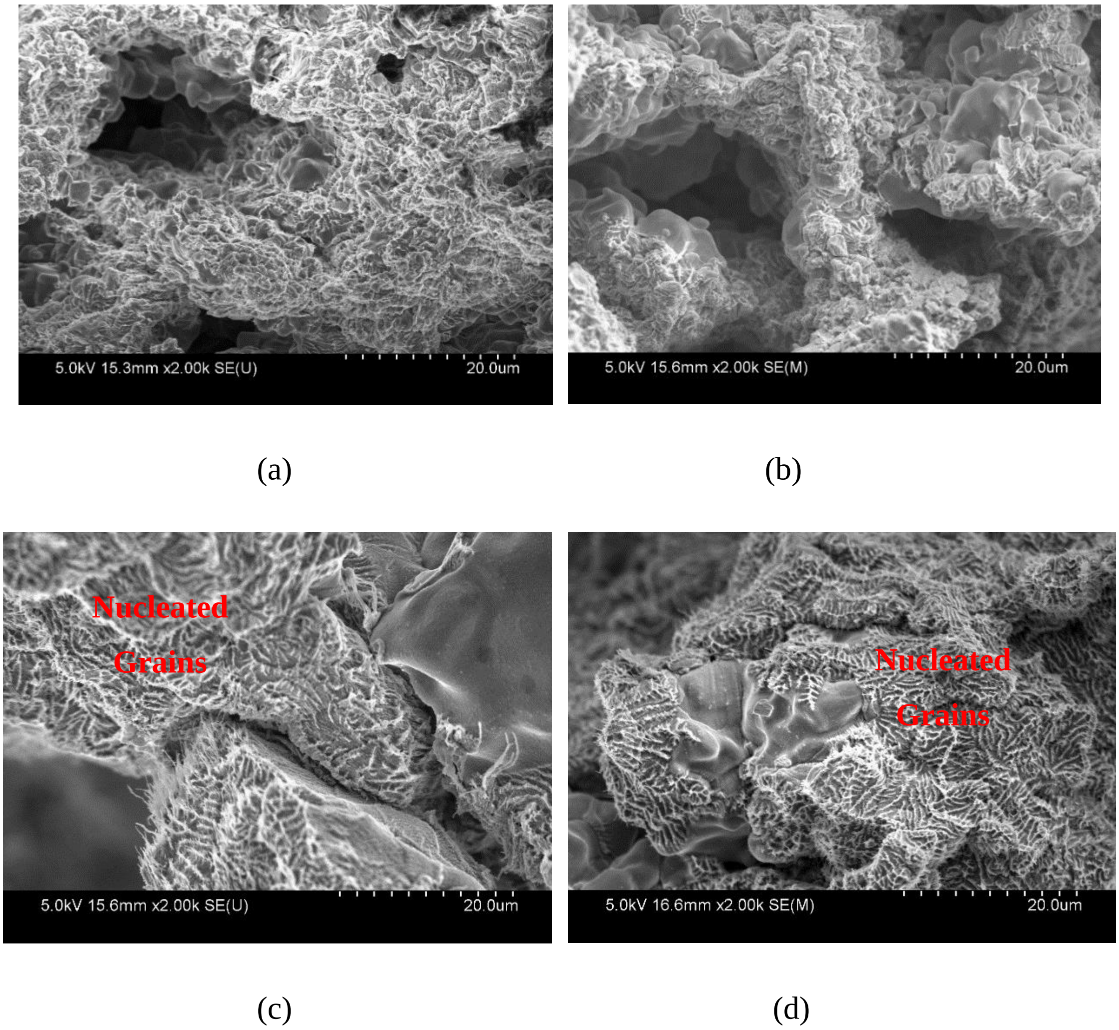
5.0kV 15.3mm x2.00k SE(U) 20.0um
5.0kV 15.6mm x2.00k SE(M) 20.0um
(a)
(b)
Nucleated Grains
5.0kV 15.6mm x2.00k SE(U) 20.0um
Nucleated Grains
5.0kV 16.6mm x2.00k SE(M) 20.0um
(c)
(d)

Figure 92. SEM micrographs of nucleated grains at 10^{-4}sec^{-1} (a) AZ80 – O at 300^0C (b) AZ80 – F at 300^0C (c) AZ80 – O at 400^0C AZ80 – F at 400^0C

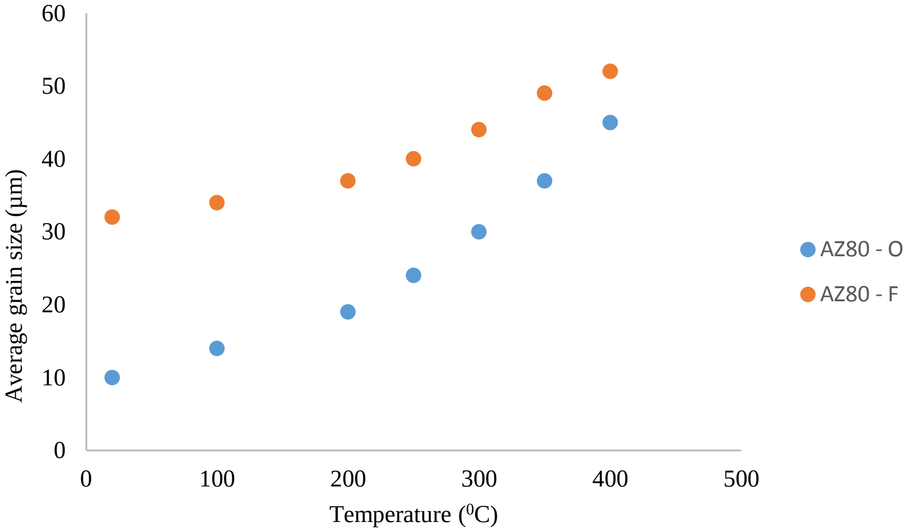

Figure 93. SEM micrographs of nucleated grains at 10^{-4}sec^{-1} (a) AZ80 – O at 300^0C (b) AZ80 – F at 300^0C (c) AZ80 – O at 400^0C AZ80 – F at 400^0C

Moreover, the grain-aspect ratio was also calculated for AZ80 – O and AZ80 – F at the grip and gauge sections. The grain-aspect ratio is the ratio of grain diameters in both rolling and transverse directions. Additional SEM micrographs are also shown in Appendix 2.

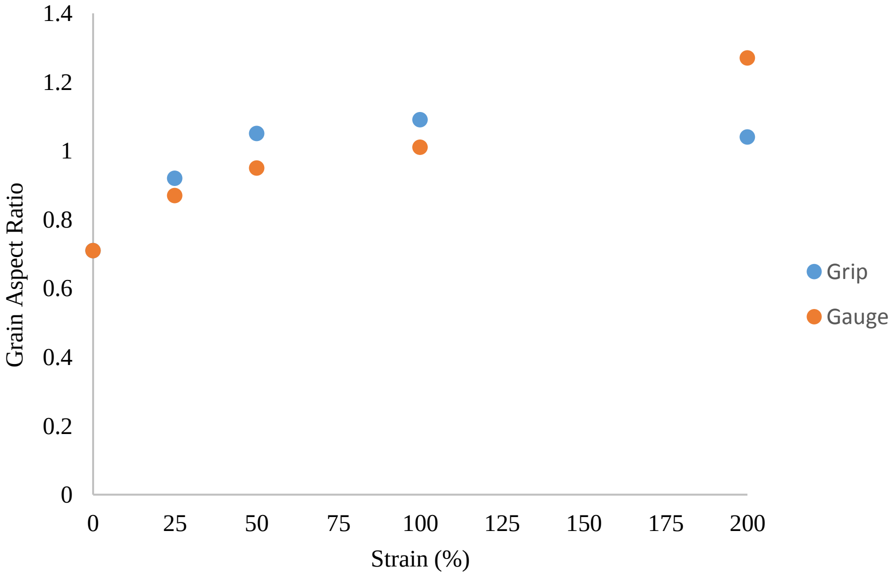

Figure 94. Grain aspect ratio of AZ80 – O as function of strain

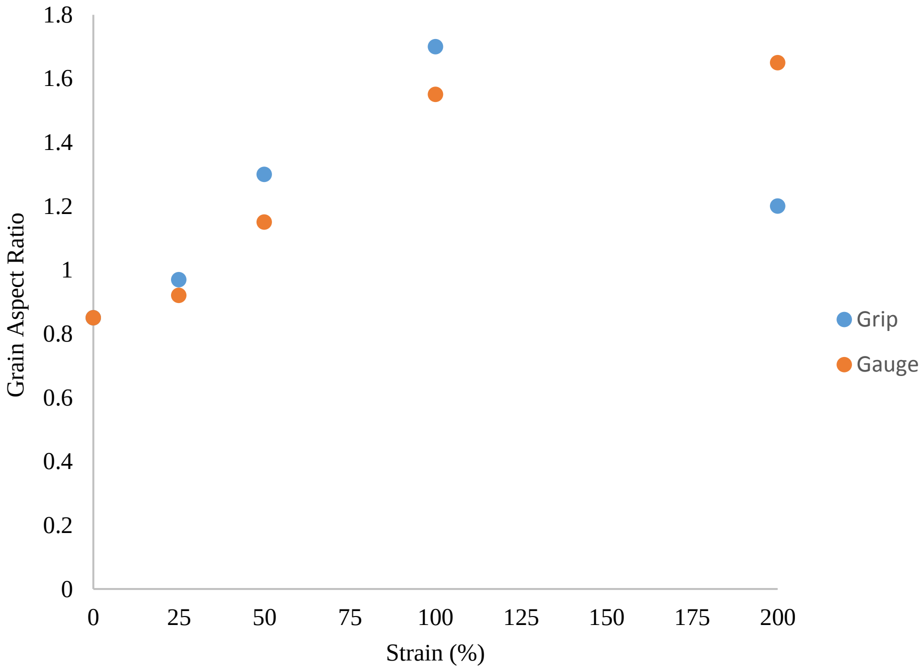

Figure 95. Grain aspect ratio of AZ80 – F as function of strain

Aspect ratios were measured experimentally and compared with the Bae et al. [351] model at various strain levels:

$$d_{0^{0}RD} = d_i \exp \varepsilon \tag{26}$$

$$d_{90^{0}RD} = d_i \exp \varepsilon \tag{27}$$

$$x = \frac{d_{0^{0}RD}}{d_{90^{0}RD}} \tag{28}$$

Where x is grain-aspect ratio, ε is applied strain, d_i is initial grain size, $d_{0^{0}RD}$ is grain size in 0^0RD and $d_{90^{0}RD}$ is grain size in 90^0RD.

A comparison of grain-aspect ratios in grip and gauge sections is given in Figures 94 and 95 for magnesium AZ80 – O and AZ80 – F respectively. Both alloys are following similar trends, however, the difference in aspect ratios with increasing strain is greater in AZ80 – F than AZ80 – O, due to having a coarser grain size. This confirms the anisotropy results presented in chapter 4, that anisotropy dominates AZ80 – F more than AZ80 – O.

Interesting results can be drawn from both Figures 94 and 95. It is quite evident that the grain aspect ratio for the grip section decreased from 100% to 200% strain within the strain region, however, while for the gauge section it continously increased in both AZ80 – O and AZ80 – F. This is because the difference in pattern of grain growth in both sections. Static grain growth was observed in the grip section while the gauge section has to go through dynamic gowth due to continous application of load, as it is shown in Figure 90. During dynamic grain growth, initialy grain boundary sliding dominated the deformation process and later, at elevated temperatures, diffusion of grains along grain boundaries continued this growth. Another interesting fact can be concluded: after 50 percent strain, grains mostly grow in the longitudinal direction not the transverse direction. These results concur with J.A. Dell et al. [352], who explained the difference between coarse and fine grains and predicted that grain boundary sliding is the dominating mechanism in fine-grain magnesium, while coarse-grain is controlled by viscous glide, due to large grain-sizes where grains cannot be easily reoriented.

Therefore, it can be concluded that the grip section is purely dominated by static grain growth, while the gauge section is predominantly controlled by dynamic grain growth, which results in continuous increments of the aspect ratio.

6.3.4 Dynamic recrystallisation and gliding

Dynamic recrystallisation is a process of grain growth that results from contributions of temperature and strain rate. Static and dynamic grain growth has already been discussed in the previous section in detail, for both magnesium AZ80 – O and AZ80 – F. Dynamic recrystallization can be classified into two types: continuous and discontinuous recrystallisation. Continuous recrystallisation is a type of dynamic recrystallisation in which dislocations are restricted within newly recrystallised grains however, in discontinuous recrystallisation these dislocations will travel within grain boundaries during transformation of the low angle boundaries into high angle boundaries, as described in the literature section 2.8 [353].

Dynamic recrystallization is mostly found in fine grains with grain sizes lower than 10 – 15µm. In this study, dynamic recrystallisation was studied in both AZ80 – O, which is a fine-grain material and AZ80 – F, holding a coarse-grain microstructure [354]. Dynamic recrystallisation nucleates around 300^{0}C and 400^{0}C for AZ80 – O and AZ80 – F, respectively. To confirm this, microstructures were observed for both grip and gauge sections. As discussed in the literature review, dynamic recrystallisation will only occur with loading together with temperature. In Figure 91 micrographs for both grip and gauge sections are shown, which clearly indicate the effect of loading at 300^{0}C for AZ80 – O.

In AZ80 – O, recrystallisation frequently occurs, due to the fine-grain size, and new grains mostly grow on grain boundaries, as shown in Figure 96 and 97, with the help of SEM micrographs.

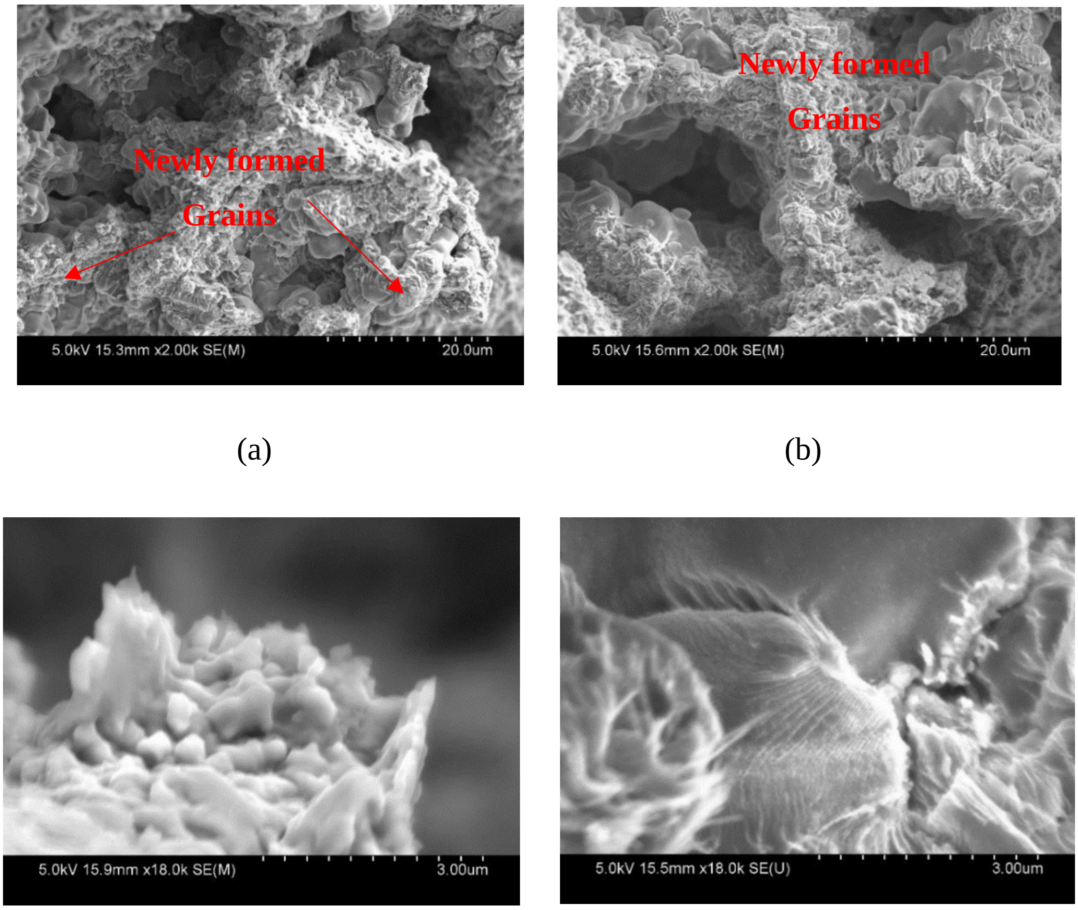
Newly formed
Grains
5.0kV 15.3mm x2.00k SE(M)
20.0um
Newly formed
Grains
5.0kV 15.6mm x2.00k SE(M)
20.0um
5.0kV 15.9mm x18.0k SE(M)
3.00um
5.0kV 15.5mm x18.0k SE(U)
3.00um

(a) (b)

(c) (d)

Figure 96. Dynamic grain growth at 300^{0}C and $1x10^{-3}$ sec^{-1} (a,c) AZ80 - O (d,e) AZ80 - F

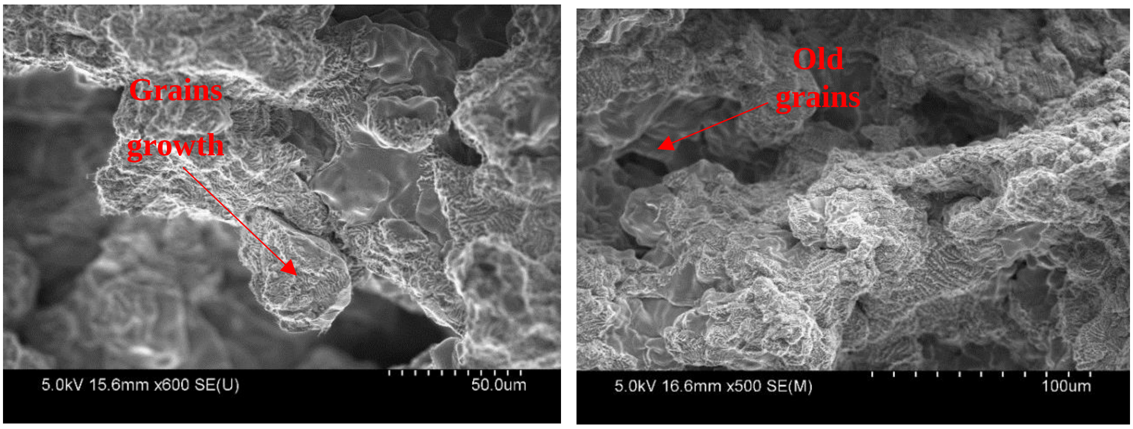

(a) (b)

Figure 97. Dynamic grain growth at 400^{0}C and $1x10^{-3}$ sec^{-1} (a) AZ80 – O, (b) AZ80 – F

At 300^{0}C in magnesium AZ80 – O partial recrystallization starts, as the microstructure shows a combination of old and new grains, as demonstrated in figure 96(a). This grain growth is a result of an increase in the processing temperature and a slowing strain rate. These newly crystallised grains grow rapidly at temperatures between 350^{0}C to 400^{0}C, and their sizes will increase from 7 – 9μm to 25 - 32μm.

This rapid increase in grains then further deforms under load. The deformation mechanism that is suggested by Watanabe et al. [355] and Vespa et al. [356] after rapid grain growth is the viscous glide mechanism, rather than grain boundary sliding.

To further investigate the effect of processing parameters, specimens were tested at various temperatures and strain rates, and it was observed that a maximum number of recrystallised grains were attainable at 300^{0}C - 400^{0}C, for AZ80 – O and AZ80 – F respectively, at the slowest strain rate of 10^{-3} sec^{-1}, as shown in Figures 96 and 97. At the lower temperatures of 200^{0}C – 325^{0}C, and high strain rates, dynamic recrystallisation become less effective, as it was interrupted by low elongations to failure. Additional SEM micrographs for dynamic grain growth are also shown in Appendix 2 at various temperatures and strain rates.

6.3.5 Cavitation and filaments

Cavitation is a process that occurs in magnesium alloys at high temperatures and leads to premature failure of magnesium alloys in a forming process. Cavitation starts at various temperatures, depending on grain size and strain rate. In magnesium AZ80 - O and AZ80 – F, it starts after 300^0C, as shown in Figures 92(a) and 92(b). After 350^0C, cavitation was the dominant mechanism along with grain growth as shown in Figures 98 and 99. However, only a few authors have doubted that these cavities may pre-exist in alloys during hot rolling [357] - [358].

Mukherjee et al. [359] also mentioned that cavity sizes may be quite small (less than 1µm), so they can be ignored at room and warm temperatures. Therefore, a detailed observation was made on cavitation influence at elevated temperatures and with varying strain rates. It is also quite interesting to note that cavitation influence and volume is much greater in magnesium alloys than aluminium and steel alloys at high temperature, as mentioned in section 2.11. It is therefore necessary to investigate cavitation sites and parameters at which these cavities mostly form, so that they can be minimised in order to enhance the formability of magnesium alloys.

Samples were examined with a scanning electron microscope and an optical microscope. In addition, energy-dispersive X-ray spectroscopy (EDS) analysis was performed to ascertain the constituting elements at various loading levels with varying temperatures and strain rates.

Micrographs of SEM AZ80 – O and AZ80 – F are given in Figure 98 for AZ80 – O and AZ80 – F. Similarly, Figures 99 and 100 show optical microscopy (OP) micrographs of cavities at various locations in coarse-and fine-grain magnesium alloys.

Figure 98 shows cavity proportions at 60% of strain, while Figure 99 indicates material behaviours right at the fractured edge. Samples were initially strained at temperatures ranging from 250^{0}C to 450^{0}C, at strain rates of 10^{-3} and 10^{-4} sec^{-1}.

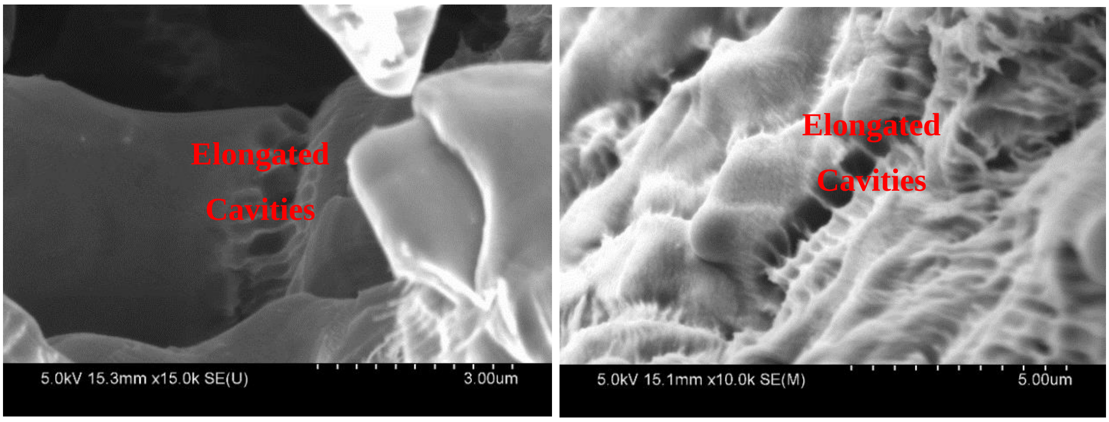
Elongated
Cavities
5.0kV 15.3mm x15.0k SE(U)
3.00um
Elongated
Cavities
5.0kV 15.1mm x10.0k SE(M)
5.00um

(a) (b)

Figure 98. Various cavities shown at 300^{0}C and 10^{-4} sec^{-1} at 60% of strain (a) AZ80 – O and (b) AZ80 – F

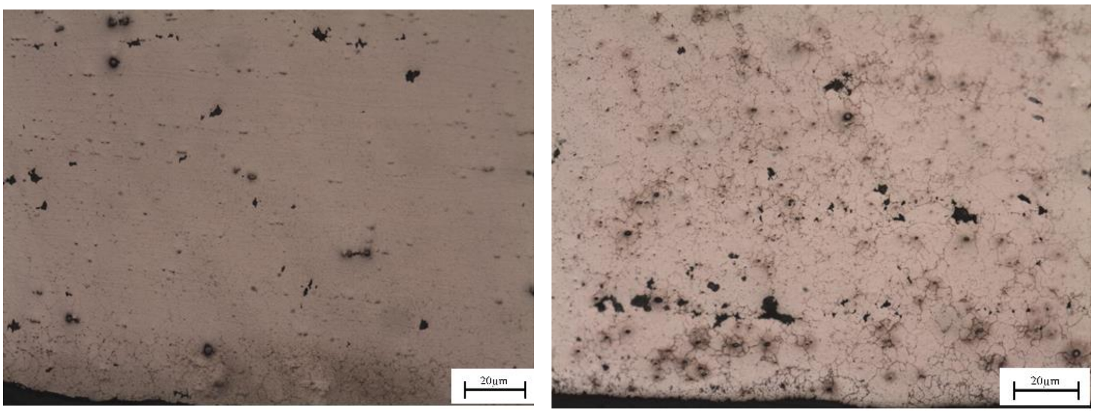

(a) (b)

Figure 99. OP micrographs showing cavities at 300^{0}C and 10^{-4} sec^{-1} at 60% of strain (a) AZ80 – O and (b) AZ80 – F

To observe the influence of loading on the volume of cavities, various tests were also conducted at different strain values before failure. Samples were immediately removed from the grips and quenched to preserve their microstructure, and later were examined in the SEM.

The reason for doing so was that nucleation of cavitation can be observed under the influence of strain. It was observed that both materials behaved similarly at elevated temperatures and the volume of cavities grew with increased strain and near failure of the specimen. It was also found that large elongations before failure can only be obtained by a reduction in cavity volume.

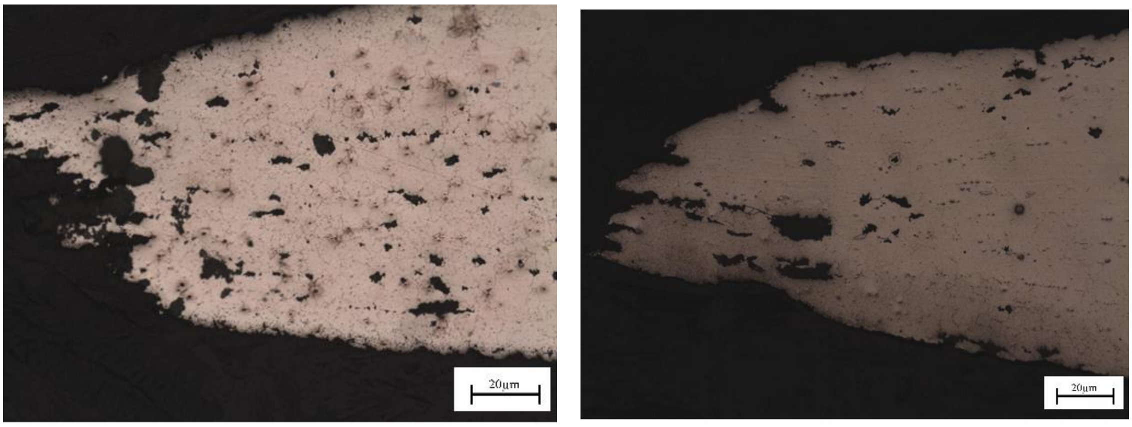

(a) (b)

Figure 100. OP micrographs showing cavities at 300^0C and 10^{-4} sec^{-1} at 60% of strain (a) AZ80 – O and (b) AZ80 – F

Several cavities were observed at the grain boundaries, along with long hair like filaments attached to them. Most cavities were elongated elliptical shapes, a few were approximate circles and a few were irregular shapes as shown in Figures 98 – 100. By observing the microstructure through SEM and OP, it can be claimed that cavities were mostly elongated in the tensile direction and approximately 75 percent of these cavities formed at temperatures above 300^0C, at strain rates of 10^{-4} sec^{-1} for both AZ80 – O and AZ80 – F. Optical microscope results are showing similar results to the SEM results. In addition, several long hair-like filaments occurred that were attached to most of these cavities with diameters of 1μm or less, however cavity sizes varied from 1.5μm to 25μm, as shown in Figures 98 - 100. To investigate the filaments further, EDS analysis was used to answer whether these filaments were formed in a liquid phase or were generated by local stress concentrations of grains at grain boundaries.

Cavitation is a unique process, as compared with other deformation processes. It has not been widely investigated in magnesium alloy formability research. Only a few researchers have reported it as an ordinary phase, which starts from the separation of second-phase particles.

However, it needs to be stressed that AZ80 is a single-phase alloy, so there should be no contribution from second-phase particles to the generation of cavities within grain boundaries. Therefore, local stress concentration influences the generation of these cavities and filaments at grain boundaries.

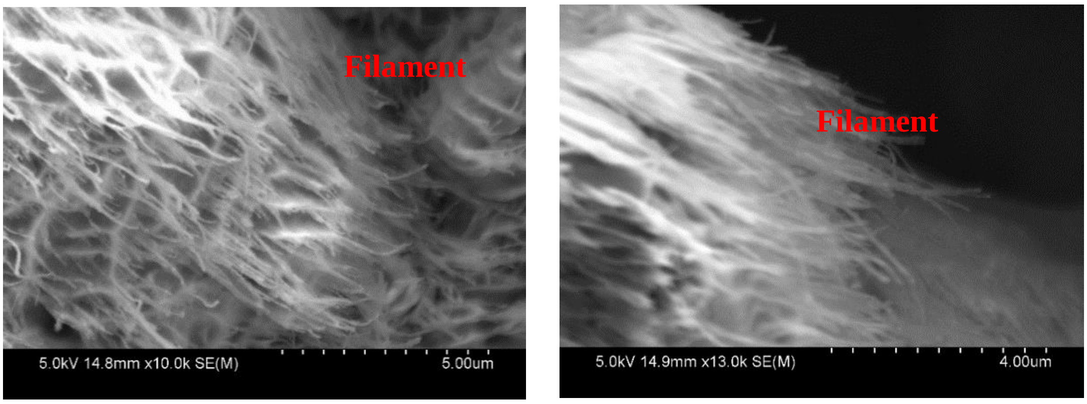
Filament
5.0kV 14.8mm x10.0k SE(M)
5.00um
Filament
5.0kV 14.9mm x13.0k SE(M)
4.00um

(a) (b)

Figure 1011. SEM micrographs showing cavities at 300^{0}C and 10^{-4} sec^{-1} at 60% of strain (a) AZ80 – O and (b) AZ80 – F

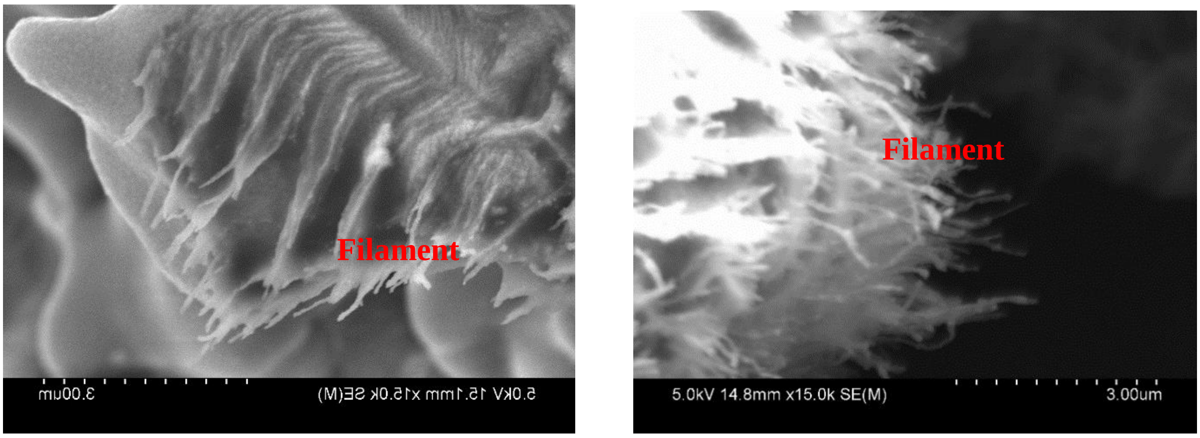
3.00um
5.0kV 15.1mm x15.0k SE(M)
Filament
Filament
5.0kV 14.8mm x15.0k SE(M)
3.00um

(a) (b)

Figure 102. SEM micrographs showing filaments at 3500C and 10-4 sec-1 at 60% of strain (a) AZ80 – O and (b) AZ80 – F

In addition, grain boundaries are dominated by a pure plasticity phenomenon, due to the absence of any second-phase particles.

For most cast alloys it has been reported that at temperatures above 400^0C, these cavities mostly originate near second-phase particles. In contrast, in this investigation of magnesium AZ80 – O and AZ80 – F, these cavities appear at 300^0C, which is far less than the melting temperature of the magnesium, and negates that claim. It means these cavities are not originating due to second phase particles. Based on these observations, it can also be said that the tearing of grain boundaries also occurs due to the pure plastic behaviour of the material, instead of the influence of second-phase particles.

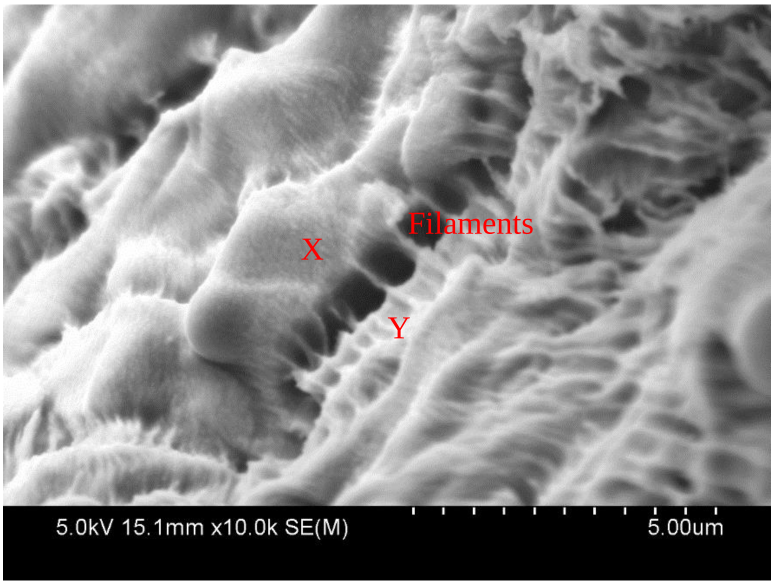

Figure 103. SEM micrograph showing locations for EDS analysis on AZ80 – O

Filaments are mostly found in the direction along the loading axis; these filaments varied from 1µm to 3µm and are mostly attached to grains along the grain boundaries. Chen et al. [360] reported the generation of these filaments in aluminium 7475 as a result of a liquid phase, however, here it has been already noted that in magnesium AZ80 – O and AZ80 – F, these filaments appear at 350^0C, which is far from magnesium's melting point of 650^0C.

Therefore it is impossible that there would be a liquid phase at this temperature in magnesium AZ80 – O and AZ80 – F.

A further investigation of these filaments was performed by EDS analysis, in which a percentage weight of alloying constituents was measured on the grains middle portions, grains located along grain boundaries, and filaments.

The EDS analysis results are shown in Figures 103 and 104 along with SEM micrographs that indicate the locations of these tests. Position X is marked as a location far from a grain boundary and position Y is marked as a location near grain boundaries where most of cavities and filaments nucleate. The observations were focused on the variation of aluminium and zinc content in both AZ80 – O and AZ80 – F. Some additional EDS results are also mentioned in Appendix B.

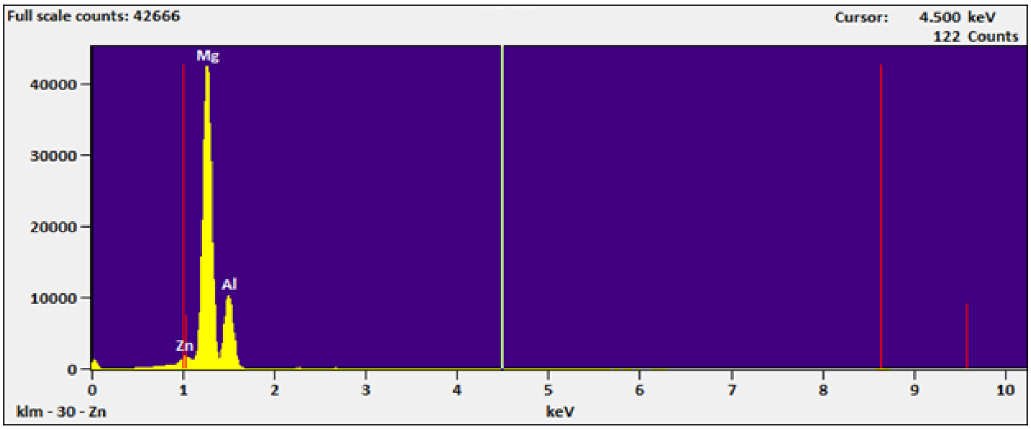

(a)

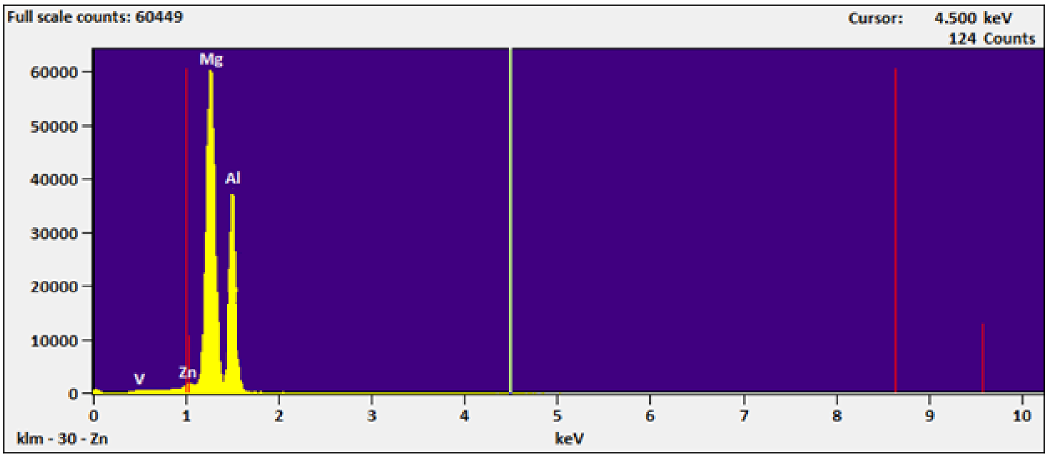

(b)

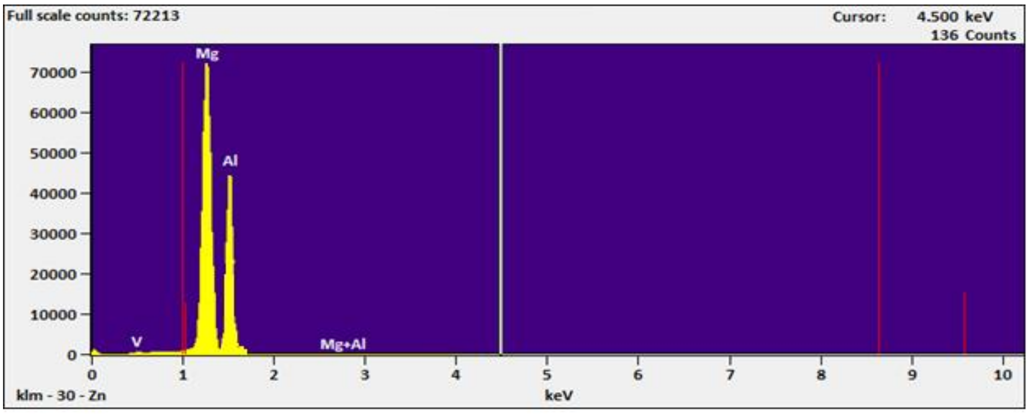

(c)

Figure 104. EDS analysis showing position at 60% of strain (a) X, (b) Y, and (c) filaments

The aluminium content reduced significantly from 8% to 1.3 % at grain boundaries, compared with the middle of a grain, which maintained it at 3.8 percent. The zinc content also reduced from 0.8 to 0.5 percent from position X to position Y. The EDS analysis indicates that in the filaments, aluminium content remains the same as at position Y, however, the zinc percentage reduced to approximately 0.1 percent. This indicates that these filaments are generated solely due to the diffusion of zinc atoms, as reported in section 2.11, though aluminium atoms were also present in large quantities, but unable to diffuse due to their larger atomic radius. These facts also confirm for AZ80 the research findings of J.C. Tan et al. [361] who suggested a similar behaviour for magnesium AZ31.

Nucleation sites of cavities are also very important to locate. The nucleation of cavities mostly occurs at grain boundaries due to the inadequate capability of grains to accommodate irregularities developed during high temperatures and loading. These irregularities create local stresses at grain boundaries, which is a major factor in the nucleation of cavities. Moreover, grain growth is also involved in developing local stress at grain boundaries.

As mentioned, these cavities may pre-exist in alloys during hot rolling, but this is still doubtful according to the literature reported in section 2.11. After thoroughly investigating the material in the SEM at high magnification, at 200^0C 10^{-4} sec^{-1} a few cavities were found in AZ80 – O, near grain boundaries, but their size was less than 1μm (approximately equal to 0.1 - 0.3μm) as shown in Figure 105. At lower temperatures, grain-boundary sliding was accommodated by the diffusion process to reduce local stresses generated at grain boundaries. This resulted in a reduction in the formation of cavities at grain boundaries, however, at temperatures above 300^0C and at strain rates of 10^{-4}, it was quite difficult to relax the local stresses generated within grains with a diffusion process.

Watanabe et al. [361] also demonstrated this behaviour in magnesium AZ31 and defined it as a grain boundary diffusion-controlled deformation mechanism.

A comparison of the variation in grain structure is shown in SEM micrographs in Figure 106 and 107 for both AZ80 – O and AZ80 – F.

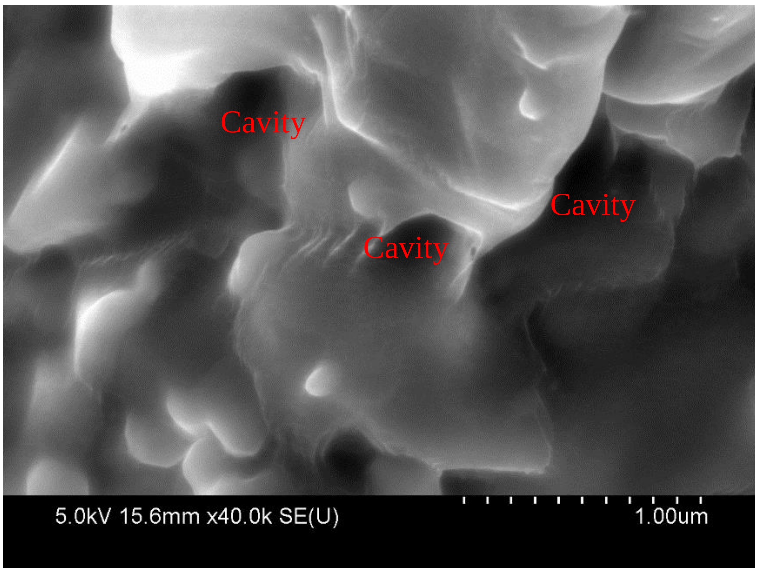

Figure 105. Evidence of pre-existing cavities at grain boundaries with size 0.1 - 0.3μm at 200^0C and 10^{-4} $\sec^{-1}$

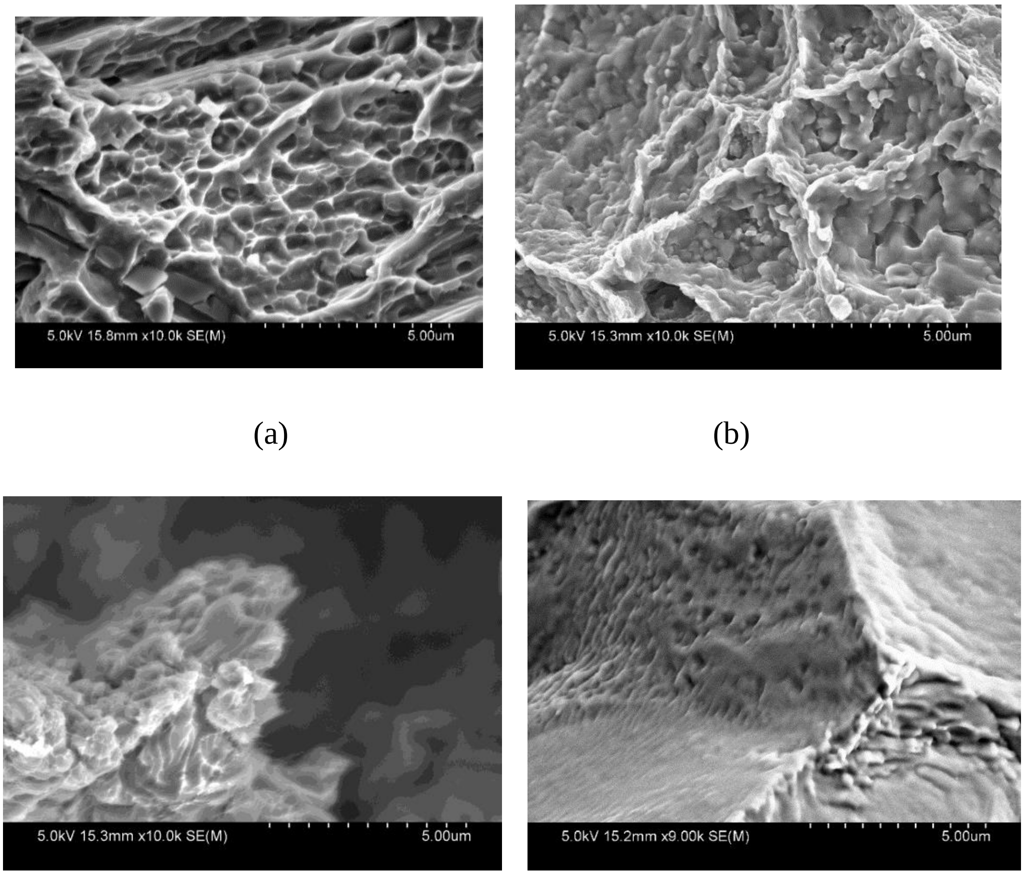
5.0kV 15.8mm x10.0k SE(M) 5.00um
5.0kV 15.3mm x10.0k SE(M) 5.00um
5.0kV 15.3mm x10.0k SE(M) 5.00um
5.0kV 15.2mm x9.00k SE(M) 5.00um

(a) (b)

(c) (d)

Figure 106. SEM micrographs of AZ80 – F at 60% strain (a) room temperature, (b) 200^0C, (c) 300^0C (d) 400^0C

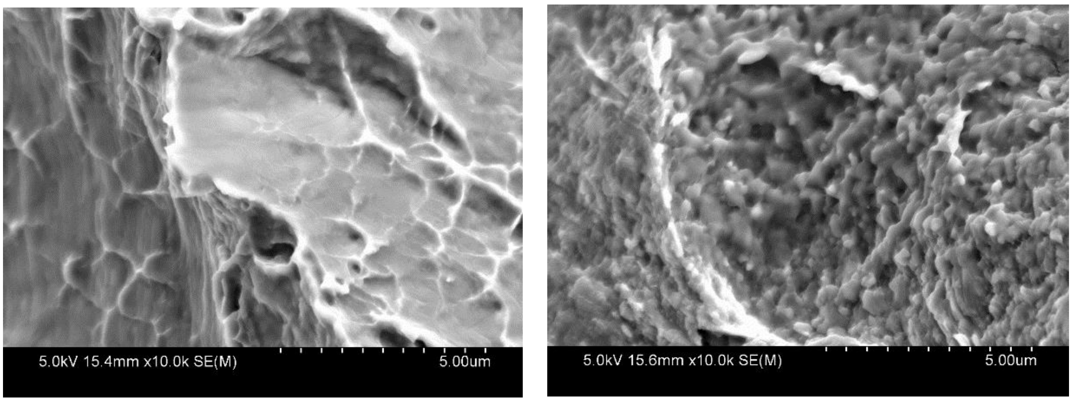
5.0kV 15.4mm x10.0k SE(M) 5.00um
5.0kV 15.6mm x10.0k SE(M) 5.00um

(a) (b)

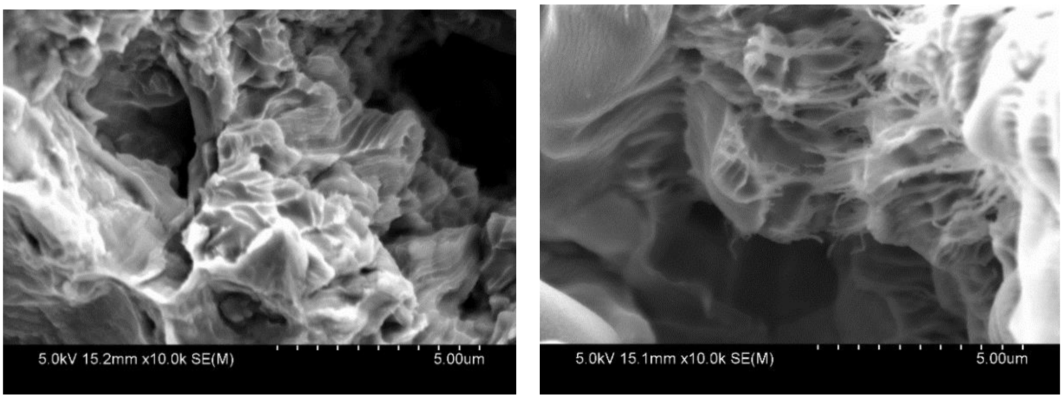

(c) (d)

Figure 107. SEM micrographs of AZ80 – F at 60% strain (a) room temperature (b) 200^0C (c) 300^0C(d) 400^0C

It is quite visible, that grains are experiencing recrystallization with an increase in temperature, however at room temperature twinning is the major deformation mechanism. Cavities start appearing at temperatures around 300^0C and further elongation of these cavities results in thin filaments which lead to premature failure of the material.

In addition, sizes of cavities were also observed to vary from 1.5µm to 25µm with varying loading and strain rates. Amongst these cavities, approximately 65 to 70 percent of cavities were less than 8µm at all strains, in both AZ80 – O and AZ80 – F. Only a few cavities were observed (mostly less than 5 percent) with sizes greater than 20µm at long strains and near the necking region. To summarise results, a plot of the number of cavities for both magnesium AZ80 – O and AZ80 – F is given in Figures 108 and 109.

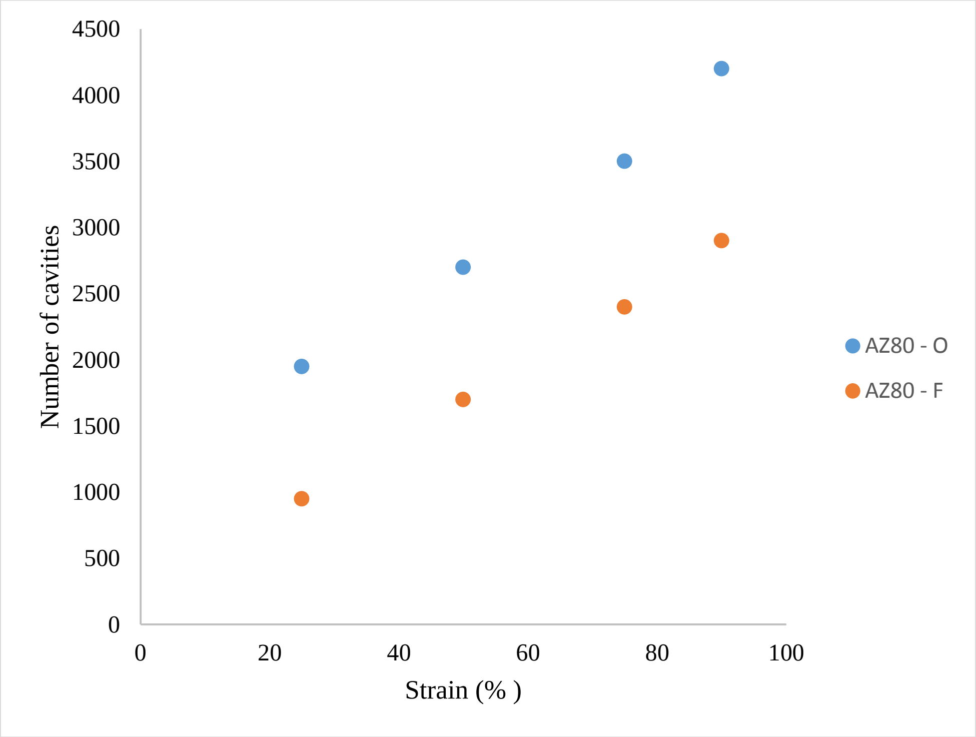

Figure 108. Comparison of the number of cavities as a function of percentage of strain at 400^{0}C and 10^{-4} sec^{-1} for both magnesium materials

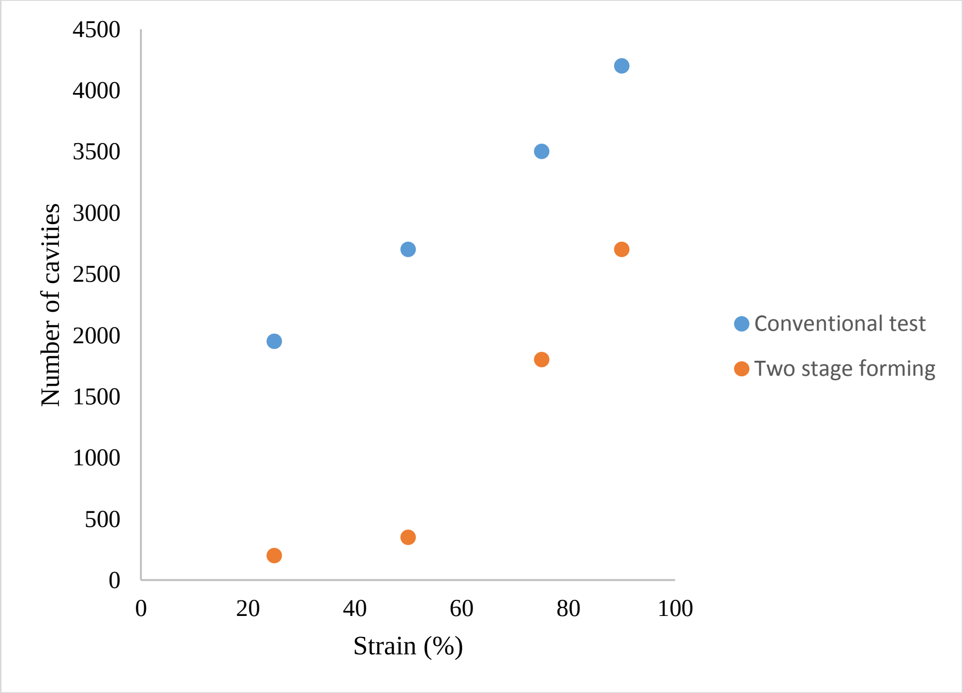

Figure 109. Comparison of the number of cavities as a function of percentage of strain at 400^{0}C and 10^{-4} sec^{-1} for AZ80 – O for conventional and two-stage forming.

It is quite clear from that these figures the number of cavities in AZ80 – O is significantly higher than in AZ80 – F, due to fine-grain sizes.

To increase elongation before failure, these cavities need to be minimised. Therefore, a novel method of two-stage forming was introduced in section 4.6 to avoid premature failing.

In two-stage deformation, samples were initially strained under warm conditions with a constant strain rate, and later the temperature was raised to a maximum value to achieve pure plastic deformation through necking instead of cavitation. Two values of temperatures of 200^0C and 400^0C were chosen for two-stage tensile testing.

In Figures 108 and 109 number of cavities are plotted against strain at 400^0C and 10^{-4} sec^{-1} for both alloys at a sampling area of 100 mm^2.

The main advantage of this process is that initially specimens are stretched at 200^0C for a strain of 1.5, which allows material to deform under pure grain-boundary sliding, as mentioned in section 6.3.2. These grains are also refined for approximately half an hour. The deformation was also supported by various slip systems and diffusion across grains near the grain boundary. After that, further heating and loading of the material would nucleate cavities within the grain boundaries. To avoid this, the loading was interrupted and the temperature was increased to the highest level, of 400^0C, and the load test was then restarted.

Due to this technique, nucleation of cavities was avoided, which would otherwise start at temperatures of about 250^0C and 300^0C within grain boundaries.

A plot of the reduction in numbers of cavities, compared with a conventional test, is given in Figure 109 for AZ80 – O at 400^0C and 10^{-4} sec^{-1}. The material continues to deform by pure necking and small sized cavities were observed, with a size of 0.7µm - 3µm.

This also provided pre-refined grains at the initial stage, which further assisted deformation by pure necking.

These pre-refined grains also help in forming uniform nucleation of grain growth in stage two, which reduces stress concentration inside grain boundaries and thus chances of nucleation of cavities are further reduced. There were also fewer of them, compared with the conventional tensile-testing method.

This effect of cavitation was further minimised by reducing the strain rate in two-stage deformation, as shown in Figures 49 and 50 in section 4.12. This gives an additional elongation of 10 and 15 percent before failure in magnesium AZ80 – O and AZ80 – F, respectively. These facts are also supported by Mandal et al. [362], Jarrrar [363] and Wei et al. [364], who claimed in their publications that with an increase of temperature and strain rate, dynamic recrystallisation also increases significantly and leads to the accumulation of dislocations on grain boundaries.

It can be concluded from the above that a two-stage deformation mechanism is very suitable for reducing cavitation inside magnesium alloys, however, a disadvantage of this method is that it is quite slow and time-consuming, which may reduce its adoption at a commercial level in the sheet metal-forming industry. This could also be the reason that it has been neglected in the literature thus far.

6.4 Deep-drawn cups microstructure

Deep-drawn cups microstructure was examined in detail in context with previous findings. Various sections of a deep-drawn cup are marked as shown in Figure 110. SEM micrographs of deep-drawn cups at 100^0C and 200^0C are shown in Figures 111 and 112 respectively. It is quite visible in both Figures 111 and 112 that the bottom area of cups experiences negligible deformation as compared to wall and flange. It was mentioned earlier that the punch was driven cold while dies, blank-holder and blank itself were heated at appropriate temperatures. As a result of this, the bottom face of a drawn cup was in contact with the punch face only and deformed under the influence of a twinning mechanism. These twins indicate that the bottom face of a deep-drawn cup is not experiencing high temperature deformation, and we can observe a large number of deformation twins on the whole surface. In contrast to this, these twins are not observed in other areas of the drawn cups at both 100^0C and 200^0C.

In the flange and wall regions few fine recrystallized grains can be observed in Figures 111 and 112. The reason for variations in these recrystallized grains is the amount of strain that is generated in these deep-drawn cups at 100^0C and 200^0C. Both cups are not showing any voids or cavities which is indicating that cavitation is not contributing to the forming at these warm temperatures.

It can be concluded that deep-drawn cups at warm temperatures are experiencing negligible deformation at the bottom face as large number of twins were observed there. Wall and flange are mostly experiencing the grain boundary sliding mechanism and some newly formed grains can also be observed due to the variation in strains at both regions.

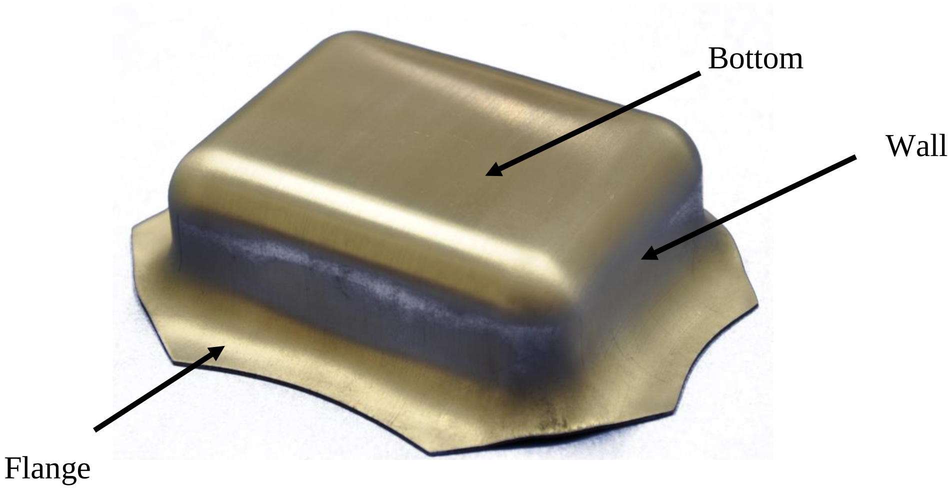

Figure 110. Measured areas in deep-drawn cup

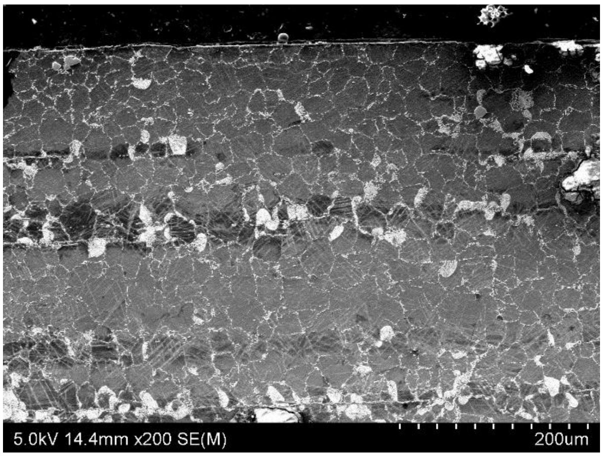
5.0kV 14.4mm x200 SE(M)
200um

(a)

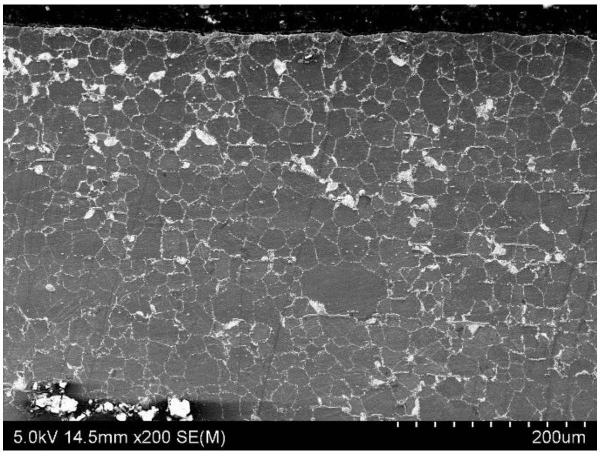
5.0kV 14.5mm x200 SE(M)
200um

(b)

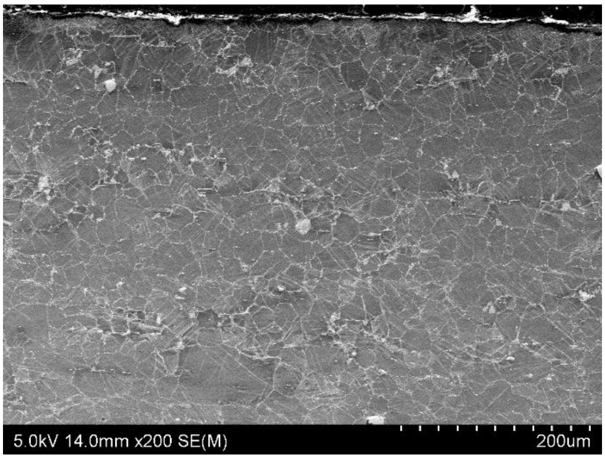
5.0kV 14.0mm x200 SE(M)
200um

(c)

Figure 111. SEM micrographs of deep-drawn cup at 100^0C for magnesium AZ80 – O
(a) Flange (b) Wall (c) Bottom

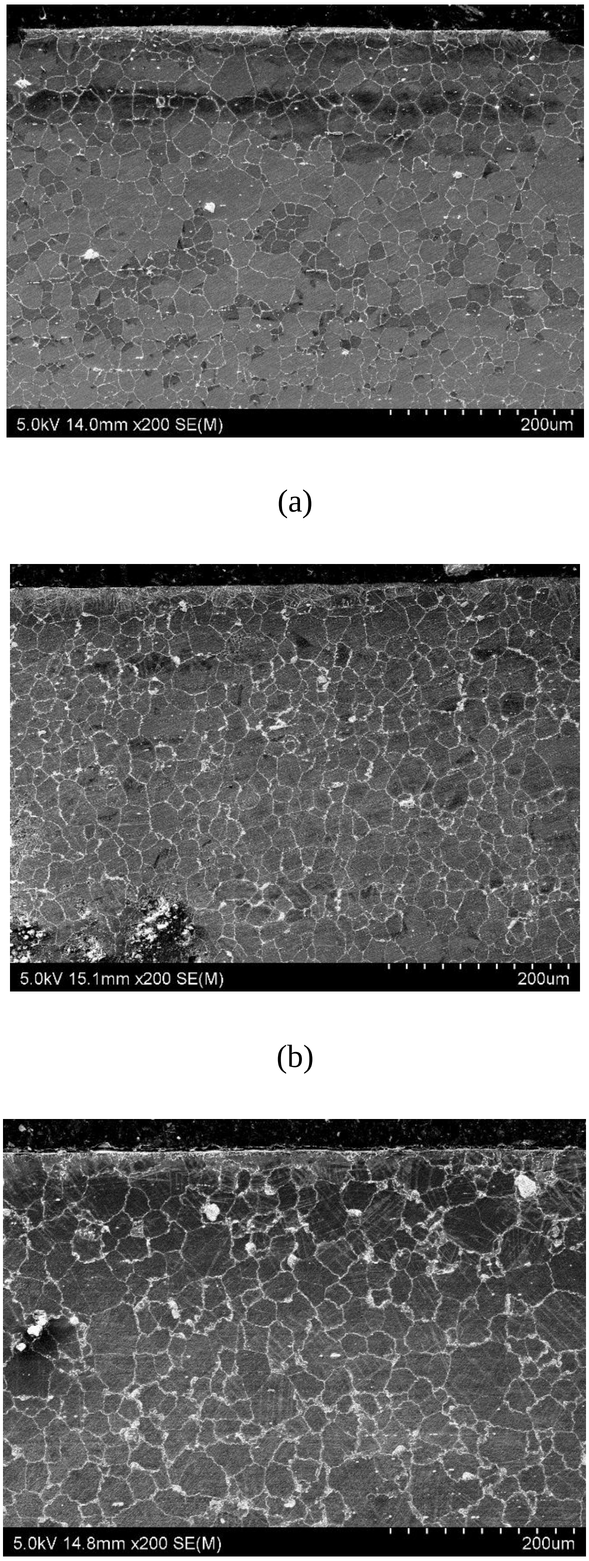
5.0kV 14.0mm x200 SE(M)
200um
5.0kV 15.1mm x200 SE(M)
200um
5.0kV 14.8mm x200 SE(M)
200um

(a)

(b)

(c)

Figure 112. SEM micrographs of deep-drawn cup at 200^{0}Cfor magnesium AZ80 – O(a) Flange (b) Wall (c) Bottom

6.5 Conclusions

In this chapter, the microstructures of magnesium AZ80 – O and AZ80 – F were discussed in detail. Various characteristics involved in their deformation processes were investigated through SEM and OP micrographs. The influence of parameters such as temperature, strain rate and grain size was observed. In summary, several conclusions can be drawn:

1. Twinning mostly occurs at room temperature. However, its influence reduces considerable when both materials are loaded at elevated temperatures.
2. Both compression and tension twins were observed in specimens at room temperature.
3. Twin nucleation is mostly visible at high stress-concentration areas such as grain boundaries.
4. Static and dynamic grain growth is observed at grip and gauge sections respectively.
5. The grain-aspect ratio for the grip section decreases with a rise of strain from 100 to 200 percent, however, for the gauge section it increases continously for both AZ80 – O and AZ80 – F.
6. The grain-aspect ratio also indicates that after 50 percent strain, grains in the tensile loading direction are bigger than in the perpendicular direction, that is, the aspect ratio is greater than 1.
7. After 50 percent of strain, grains have mostly enlarged in the longitudinal direction, compared with the transverse direction.
8. Dynamic recrystallisation is mostly seen in fine grains with grain sizes smaller than 10 – 15µm.
9. Dynamic recrystallisation nucleates around 300^0C and 400^0C for AZ80 – O and AZ80 – F, respectively.
10. After 350^0C, cavitation was the dominant mechanism along with grain growth.
11. Several cavities were observed at grain boundaries, with long thread hair type filaments attached to them. Most of these cavities were an

elongated elliptical shape, a few were approximate circles and a few were irregular-shaped.

12. These cavities were mostly elongated along the tensile direction, and approximately 75% of these cavities form at temperatures above 300^0C and at strain rates of 10^{-4} sec^{-1}, for both AZ80 – O and AZ80 – F.
13. At 200^0C and 10^{-4} sec^{-1} only a few cavities were found in AZ80 – O near grain boundaries and they were approximately equal to 0.1 - 0.3µm.
14. Several long thread-like filaments were found, attached to most of these cavities with diameters of 1µm or less, however, the cavity sizes varied from 10µm to 25µm.
15. Filaments are generated purely due to diffusion of zinc atoms, though aluminium atoms were also present in large quantities but were unable to diffuse, due to their larger atomic radius, as shown by EDS analysis.
16. Two-stage deformation reduced the number of cavities significantly.
17. Deep-drawn cups at warm temperatures are experiencing negligible deformation at the bottom face as shown in Figures 111(c) and 112(c) .
18. Wall and flange are mostly experiencing a grain boundary sliding mechanism and some newly formed grains can also be observed due to the variation in strains at both regions.

Chapter 7

Simulation and Modelling

7.1 Introduction

Magnesium alloys have been extensively discussed in the previous chapters in regard to their mechanical, forming and microstructure characteristics. It was shown that magnesium alloys’ mechanical and forming characteristics can have advantages over other sheet metal alloys. They are lighter in specific weight, easily formable at warm temperatures and also provide the strength required for more sustainable sheet metal components in numerous applications. Various experimental results were represented in the form of stress/strain diagrams, elongation before failure, fracture strength, deep-drawing load displacement curves, forming limit curves, twinning, grain growth, dynamic recrystallisation and cavitation. These results show the substantial capabilities of magnesium alloys as an alternative to aluminium and steel in the sheet metal industry.

In this chapter, the mechanical and forming characteristics of magnesium alloys are mathematically modelled with the help of various constitutive mathematical models and computer finite element analysis (FEA) simulations. These constitutive and simulation results provide verification of the experimental results reported in previous chapters.

To predict the stress strain characteristics of magnesium alloys, two well-known constitutive models are used: that are the Johnson and Cook model and the Arrhenius type constitutive equations [365]. Both models are used for predicting material behaviour in tensile testing (stretch forming) and are widely used in several FEA codes and software for predicting material flow behaviour at room temperature, as well as at elevated temperatures with varying strain rates and other processing parameters [366].

For computer simulations of deep-drawing in both magnesium AZ80 – O and AZ80 – F, computer aided engineering (CAE) technology is an innovative and important tool that is mostly used in industry and academia. Several FEA software codes such as Abaqus, ANSYS and ALGOR, are commercially available with various tools for simulations [367]. For this research Abaqus v 6.14 was used because of its extensive tools for sheet deformation processes. Finite element analysis is the most widely used simulation tool in the design industry, through which tool geometries, pre-processing parameters and post-processing parameters of deep-drawing processes can be utilised to predict the flow behaviour of materials [368]. It is also useful in predicting variations in sheet thickness in the walls, flange and bottom of sheets after pressing by a punch. In this chapter, load displacement data from experimental results is used to perform accurate FEA simulations, to demonstrate that such material behaviour can be predicted at different temperatures and strain rates without lengthy experiments.

7.2 Constitutive analysis

Material-flow prediction during hot tests is a topic of interest here. Unlike at room temperature, the effect of elevated temperature enables material to exhibit long elongation before failure. These elongations are heavily dependent on the processing parameters like strain rate, grain size and temperature. Prediction of these elongations will help to modify the process parameters and improve the material flow [369]. Variations in the thermomechanical parameters will not only affect the mechanical properties but also influence the kinetics of metallurgical characteristics. Constitutive modelling is considered effective in predicting the flow behaviour of materials through using mathematical formulations [370]. Numerical simulations also rely on these constitutive models. A comparison of all these formulations leads to an effective prediction.

In ideal conditions, it is usually expected that any constitutive model should consider the effects of variations in strain rate, temperature, grain size, work hardening behaviour etc., and based on these, it will calculate the instantaneous flow stresses. However, practically it is impossible to accommodate all these parameters in a single equation [371]. Several constitutive equations are presented by researchers for stretch forming behaviour, which can be categorised in three ways.

7.3 Phenomenological models

These are the most widely used constitutive equations or models. Phenomenological models are mostly used to predict flow stress by considering the effects of temperature and strain rate. They are easy to use, as they do not consider the physical history of a material's behaviour and material's characteristics. Therefore fewer constants are employed in these models. Some of the frequently used models are: the Johnson and Cook (JC) model [276], the Khan, Liang and Farrokh (KLF) model [276], an Arrhenius equation [276]-[279], the Molinari and Ravichandran (MR) model [280], the Khan and Huang (KH) model [281], the Fields and Backofen (FB) model [282], the Khan, Huang and Liang (KHL) model [283–285], the Voce and Kocks (VK) model [285 – 286], and a few others [287].

Of all these physical models, the Johnson and Cook (J – C) model and the Arrhenius models are most widely used, due to their limited number of constants and adequate flow behaviour predictions [276].

7.3.1 Johnson and Cook (J – C) model

The Johnson and Cook (J – C) model-presented in 1983, is the strain-and strain-rate-dependent phenomenological formula for the prediction of the flow stress of material in stretch forming. The Johnson and Cook model is widely used for aluminium and steel, but there are very few studies available where it has been applied to magnesium alloys [372] - [376]. Several modifications were suggested by researchers of the J – C model, according to their own requirements for the material and processing conditions. Zang et al. [377] introduced the effects of forming temperature, Vural and Caro [378] suggested a modification of the strain-hardening coefficient, Shin and Kim [379] suggested modifications for strain-rate hardening and thermal softening, Lin and Chen

[380] presented a combined Johnson – Cook and Zerilli – Armstrong formula that includes constants of both equations to cover the combined effects of materials and processing parameters for 42CrMo alloy steel. However, their combined equations show significant deviations at various loading conditions at high temperatures. Hou and Wang [381] developed a modified J – C model for body-centred cubic (BCC) materials.

Johnson and Cook suggested an empirical formula, in which they divided an equation into three parts: strain, strain rate and temperature terms. It can be represented as:

$$\sigma = f(\varepsilon)\ f(\acute{\varepsilon})\ f(T) \tag{29}$$

Where σ is flow stress, ε represents strain and $\acute{\varepsilon}$ strain rate and T stands for temperature. It was further expanded as:

$$\sigma = (Y+H\varepsilon^{n})\ (1+S\ \ln\frac{\acute{\varepsilon}}{\acute{\varepsilon}_{r}})\ [(1-(T''){}^{m}] \tag{30}$$

Where $\acute{\varepsilon}_r$ is referred to strain rate, and Y, H, S, n and m are material constants. Y is referred to as the yield stress at a certain reference temperature (T_r), H indicates the coefficient of strain hardening, n is the strain hardening exponent, S and m indicate strain-rate hardening and thermal-softening exponents respectively. T'' representing the homologous temperature, which can be represented as:

$$T'' = \frac{T - T_r}{T_m - T_r} \tag{31}$$

Where T indicates absolute temperature, T_m is melting temperature and T_r is reference temperature.

For magnesium AZ80 – O and AZ80 – F, the melting temperature is considered to be 650^0C and the reference temperature is 250^0C, while the experimental temperature varies in this study from 200^0C to 400^0C. Strain rate varies from 10^{-2} sec^{-1} to 10^{-4} sec^{-1}. To calculate individual terms, one should initially consider the first bracket of equation (29) which includes terms of yield stress, that is 'Y', and strain-hardening coefficient 'H', and can be written as:

$$Y+H\varepsilon^{n}$$

These values will be calculated at a strain value (ε) of 0.002, which is the yield zone normally described by the 0.2% offset method [276]. To calculate 'n', which is the strain-hardening exponent, a plot is shown in Fig. 113 of ln (σ – Y) over ln (ε). To accommodate a range of temperatures which vary from room temperature to warm temperatures, it was necessary to select a range of strain values that covers every category of stress/strain values at various temperatures and strain rates, so that homogeneity could be maintained. Based on the stress/strain curve observations, a range of 0.02 to 0.2 strain (ε) was selected for both AZ80 – O and AZ80 – F. Flow stress and yield stress values were recorded from a stress/strain curve and a plot of ln (σ – A) over ln (ε) was generated. A best fit straight line was then created for that curve whose intercept with the original curve results in 'H', and the slope of the line provides the strain hardening exponent 'n'. To calculate the next constant, that is 'S', which represents the strain-rate hardening coefficient, equation (30) can be simplified by assuming T* equal to zero (i.e. $T = T_r$). This will reduce equation (30) as follows:

$$\sigma = (Y+H\varepsilon^{n})\,(1+S\,\ln\frac{\dot{\varepsilon}}{\dot{\varepsilon}_r}) \tag{32}$$

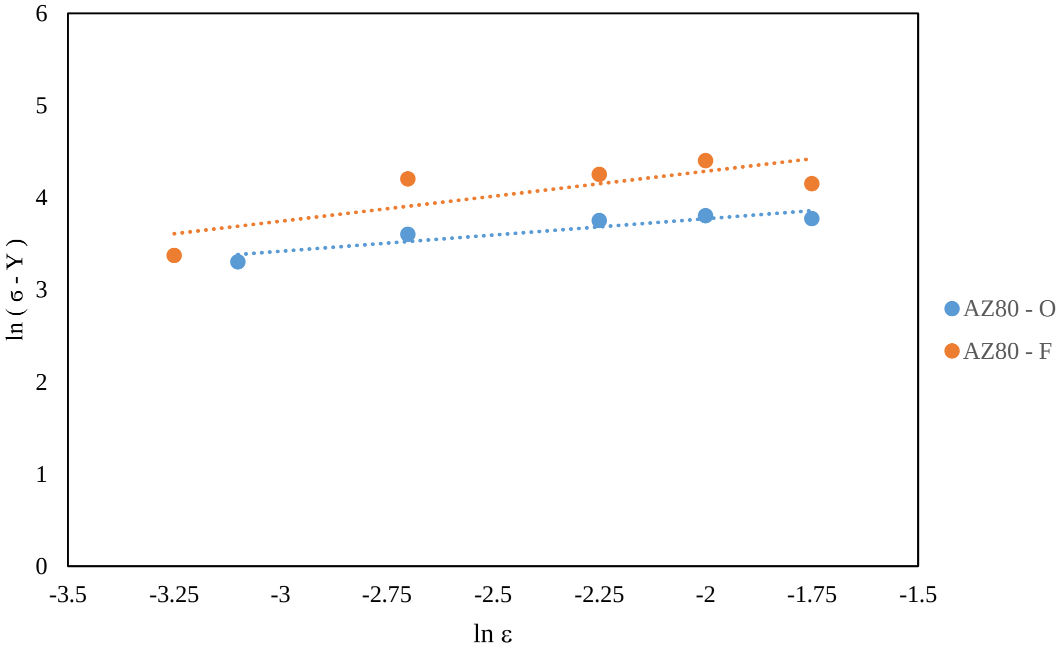

Figure 113. Plot of ln (σ – Y) vs ln ε at 200^0C and 10^{-4} sec^{-1} for both magnesium materials

S can be calculated by a plot of σ / (Y + Hε^n) over $ln\frac{\dot{\varepsilon}}{\dot{\varepsilon}_r}$, as shown in Figure 114. Two strain rate values, 10^{-3} sec^{-1} and 10^{-2} sec^{-1}, were selected as applied strain rates, while 10^{-4} sec^{-1} was fixed as the reference strain rate ($\dot{\varepsilon}_r$). These are the same strain rates used in the tensile test experiments reported in previous chapters. Yield value ‘Y’ was selected at 200^0C, while ‘H’ and ‘n’ were obtained from Figure 113. Then the natural log of both strain rate and reference strain-rate values were plotted against σ / (Y + Hε^n), as shown in Figure 114. The value of strain was fixed at 0.002, while the values of stress varied with different strain rates for both magnesium AZ80 – O and AZ80 – F. ‘S’ can be evaluated by the slope of the line that is drawn in Figure 114.

In the same way, ‘m’ refers to the thermal softening exponent, independent of strain rate and its coefficient ‘S’. To calculate this another assumption was made, that $\dot{\varepsilon} = \dot{\varepsilon}_r$. This makes the second bracket in equation (30) disappear and it is modified as follows:

$$\sigma = (Y+H\varepsilon^n)\ [(1 - (T^*)^{\,m}] \qquad (33)$$

A plot of ln [1 – σ /(Y+H ε^n)] vs. ln (T*) is given in Figure 115. To calculate T*, the melting temperature (T_m) of 650^0C was used and the reference temperature was selected as 200^0C, while other values for T were taken as 300^0C and 400^0C. Later, the natural log of T* was taken and the graph was plotted as ln [1 – σ /(Y+H ε^n)] and ln (T*) for both magnesium materials. A line was plotted between given points to reveal the value of ‘m’.

All material constant values of equation (30) are summarised in Table 18 for both magnesium AZ80 – O and AZ80 – F. Based on these constants, equation (30) can be simplified for both materials as follows, in Eq. (34) and (35).

$$\sigma = (125.2+326.2\ \varepsilon^{0.353})\ (1+0.013\ \ln\frac{\dot{\varepsilon}}{\dot{\varepsilon}_r})\ [(1 - (T^*)^{\,0.451}] \qquad (34)$$

$$\sigma = (143.4+271.5\ \varepsilon^{0.524})\ (1+0.011\ \ln\frac{\acute{\varepsilon}}{\acute{\varepsilon}_r})\ [(1-(T^*)^{0.28}] \qquad (35)$$

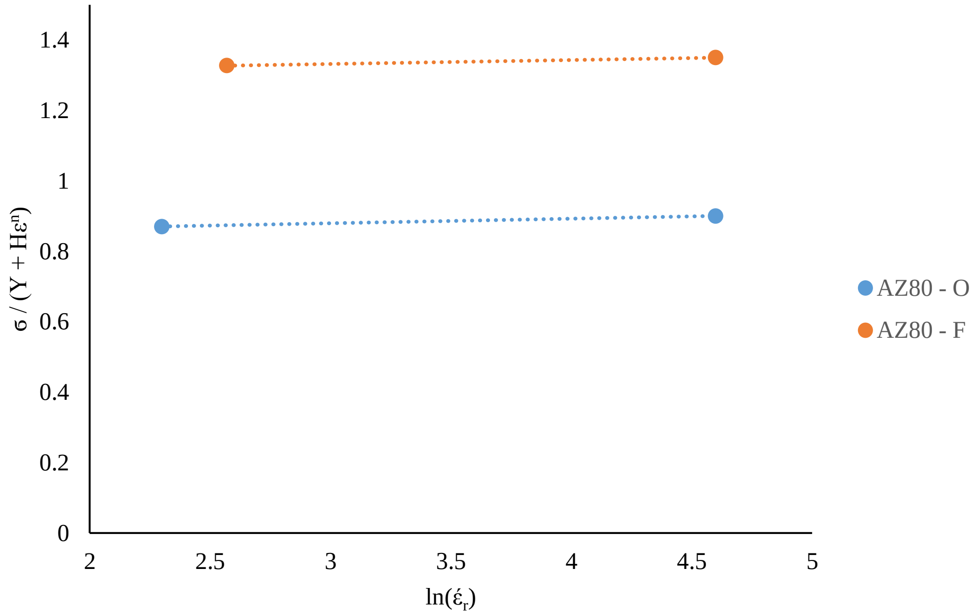

Figure 114. Plot of $\sigma / (Y + H\varepsilon^n)$ vs ln $\acute{\varepsilon}_r$ at 200^0C and 10^{-4} sec^{-1} for both magnesium materials

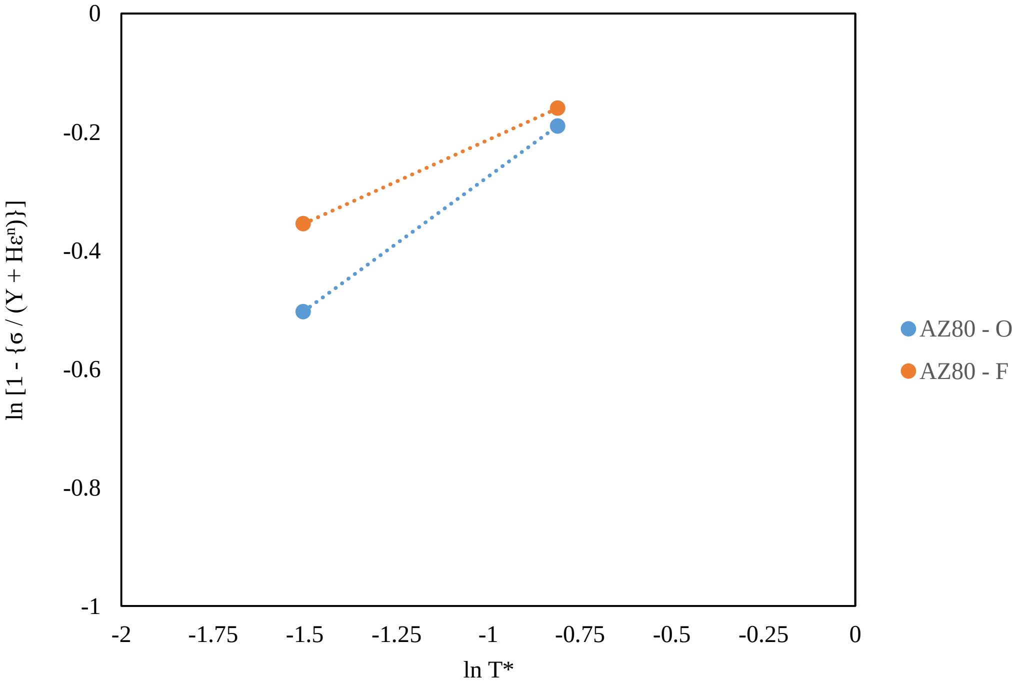

Figure 115. Plot of ln [1-{σ / (Y + Hε^{n})}] vs ln T* at 300^{0}C and 400^{0}C and 10^{-4} sec^{-1} for both magnesium alloys

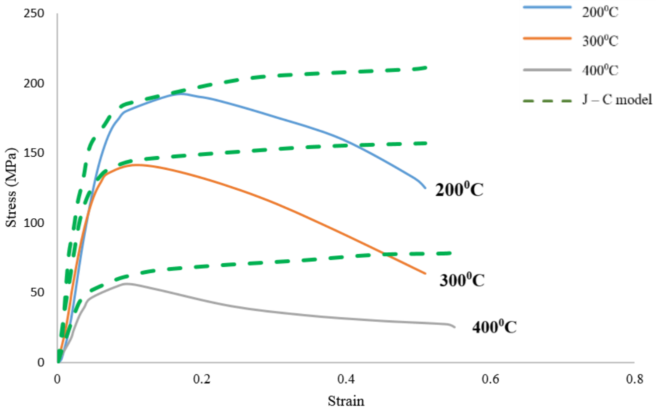

(a)

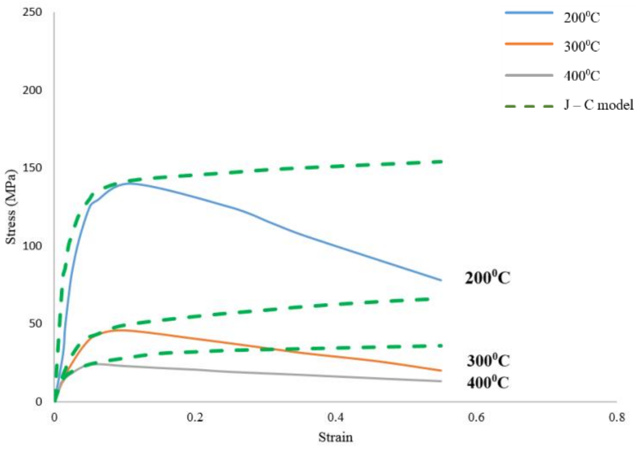

(b)

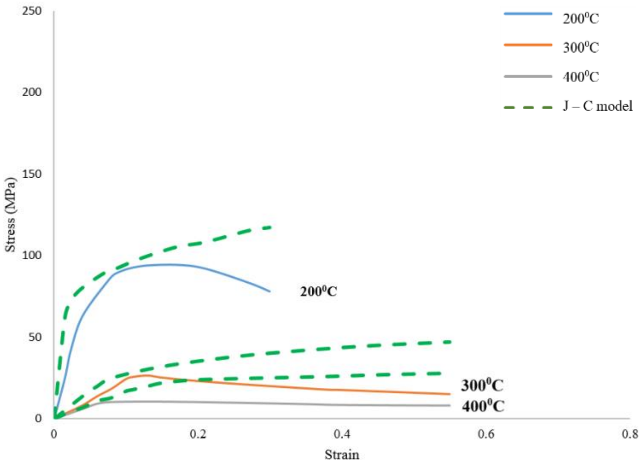

(c)

Figure 116. Stress strain diagrams for magnesium AZ80 – O, predicted vs experimental results (a) 0.1 sec^{-1}, (b) 0.01 sec^{-1}, (c) 0.001 sec^{-1}

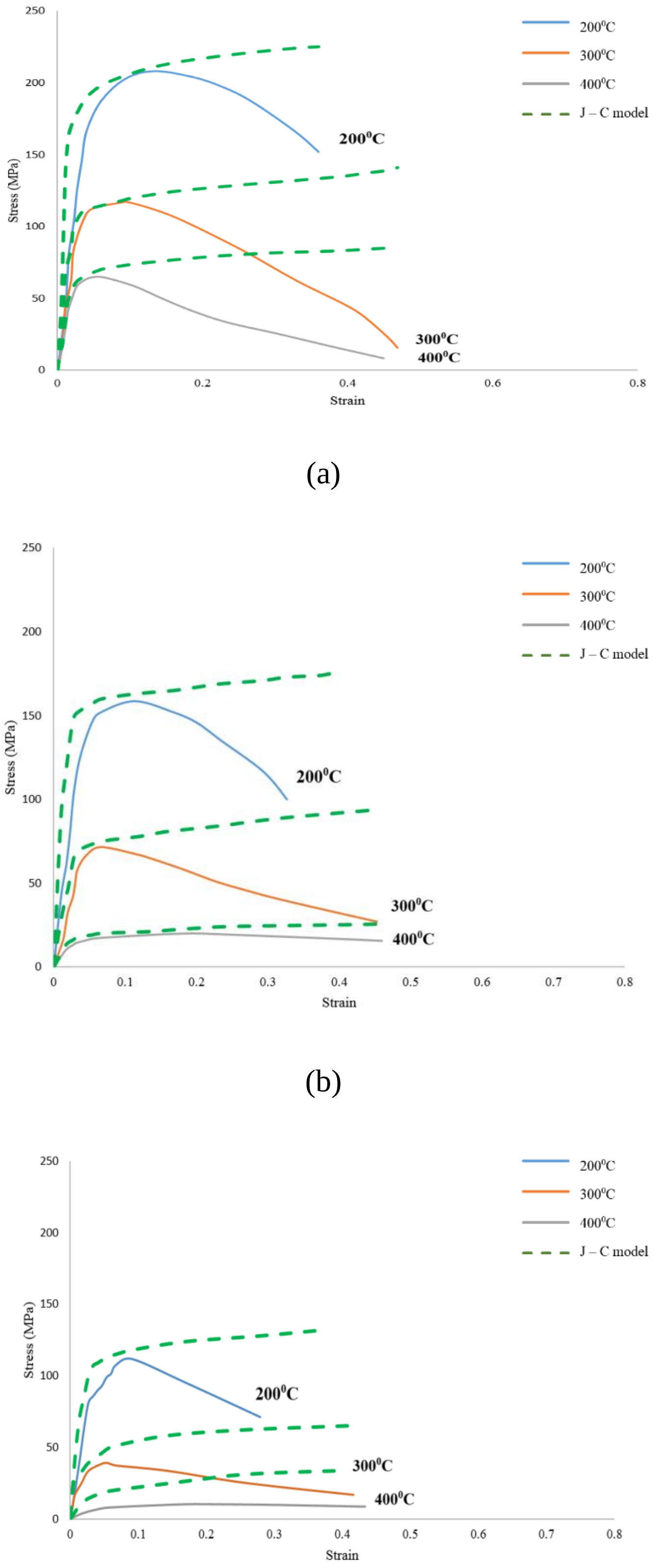

(a)

(b)

(c)

Figure 117. Stress strain diagrams for magnesium AZ80 – F, predicted vs experimental results (a) 0.1 sec^{-1}, (b) 0.01 sec^{-1}, (c) 0.001 sec^{-1}

Table 18. Various material constants in Johnson – Cook model for magnesium AZ80 – O and AZ80 – F

	Material constants				
	Y	***H***	***S***	***n***	***m***
AZ80 – O	*125.2*	*326.2*	*0.013*	*0.353*	*0.451*
AZ80 – F	*143.4*	*271.5*	*0.011*	*0.524*	*0.28*

Stress-strain diagrams with experimental and predicted values were plotted in Figures 116and 117 for both magnesium AZ80 – O and AZ80 – F, respectively. It is quite clear that the J – C model provides reasonable adequate results for material behaviour at varying strain rates and temperatures. The work-hardening region of the diagrams are mainly important in the practical applications before failure, which are quite correctly plotted by the J – C model, however, at large strains, the model’s accuracy is not as good as can be seen from Figures 117. Apart from this, it can be concluded this model is quite simple to use, through having fewer constants than other constitutive models.

7.3.2 Arrhenius model

The Arrhenius equation is the second-most widely applied model to predict material behaviour, after the J – C model. It is widely used by researchers for predicting material’s behaviour at various strain rates and temperatures. The Zener-Holloman parameters were used to represent strain rate and temperature parameters, as described in Eq. (36).

$$Z = \acute{\varepsilon} \exp(-Q / RT) \qquad (36)$$

Where Q is activation energy at deformation, R is universal gas constant (8.31kJ/mol), T is absolute temperature and $\acute{\varepsilon}$ is strain rate for the process.

A hyperbolic law is used for a more precise approximation of flow behaviour using Zener-Holloman equation parameters and flow stress. A hyperbolic law combines an exponential and a power law to predict behaviour at high temperatures and stresses.

Frost and Ashby [382] used a power law for pure magnesium at 300^0C and up to 80MPa stress, but report that it is quite inaccurate for higher stresses at warm temperatures. The equation for a power law is given in Eq. 37.

$$\acute{\varepsilon} = \sigma_s^{n} \exp(-Q/RT) \tag{37}$$

Where σ_s is flow stress and n is material stress index constant.

Similarly, Sloof et al. [383] used an exponential law, as given in equation (38), but again found it is not useful for slow strain rates and high temperatures over 300^0C.

$$\acute{\varepsilon} = A\sigma_s^{\,n} \exp(\beta\sigma) \exp(-Q/RT) \tag{38}$$

Where β is material constant equal to αn^*. Again α and n^* are material constants and can be determined from experiments. A is frequency factor while ln A is an intercept of the plot ln [sinh ($\alpha\sigma_s$)] - ln Z. Where Z is Zenor Hollman parameter.

A hyperbolic law combines exponential and power laws to predict behaviour at high temperatures and stresses, as given mathematically in Eq. (39).

$$\acute{\varepsilon} = A\,[\sinh(\alpha\sigma_s)]^{n} \exp(-Q/RT) \tag{39}$$

Where α is the ratio of two material constants β/n^*.

Hagdadi et al. [384] explained a detailed procedure describing material constants that are involved in a sine-hyperbolic law for their aluminium A356 alloy investigation. After simplification, they suggested the following equations for calculating constants B and C.

$$\acute{\varepsilon} = B\sigma_s^{n*} \tag{40}$$

$$\acute{\varepsilon} = C \exp(\beta\sigma_s) \tag{41}$$

By taking a logarithm of both sides, Eq. (40) and (41) can be represented as follows:

$$\ln(\sigma_s) = [(1/n*) \ln(\acute{\varepsilon})] - [(1/n*) \ln(B)] \tag{42}$$

$$\sigma_s = [(1/\beta) \ln(\acute{\varepsilon})] - [(1/\beta) \ln(C)] \tag{43}$$

For calculating ‘β’, σ_s is plotted vs. ln ($\acute{\varepsilon}$) and for ‘n*’ ln (σ_s) is plotted vs. ln ($\acute{\varepsilon}$). The slope of both lines delivers β and n* respectively, as shown in Figure 118.

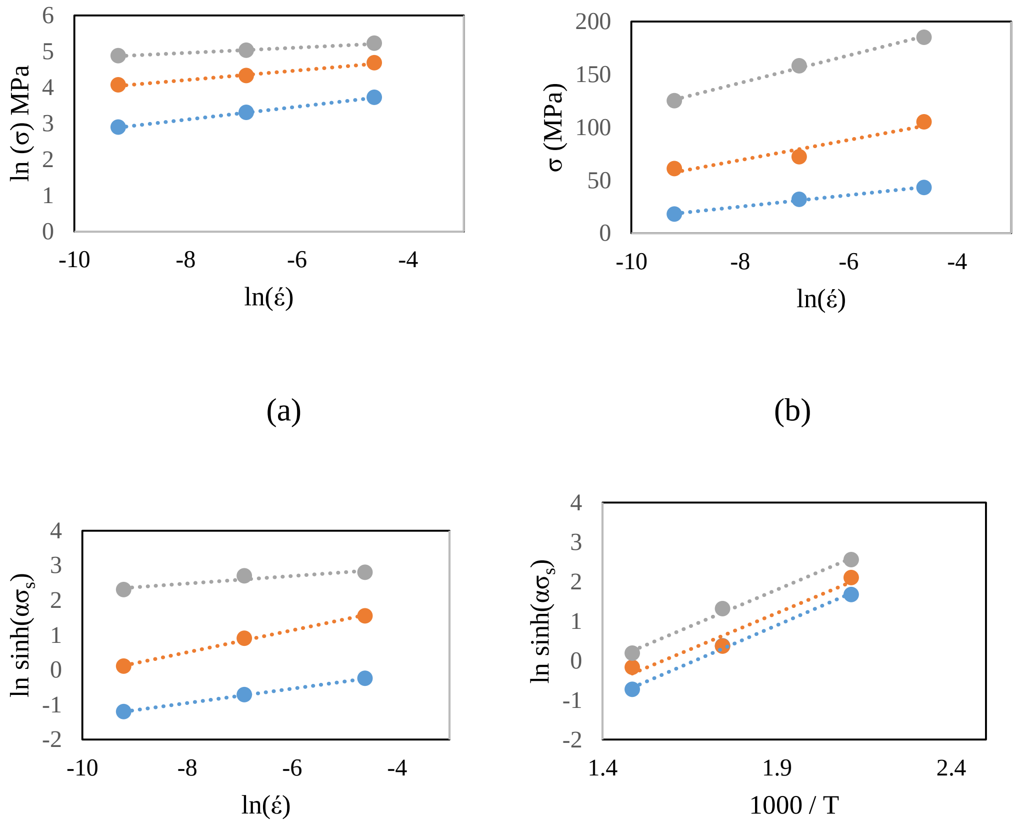

(a) (b)

(c) (d)

Figure 118. Plot for evaluation of material constants (a) $\ln(\sigma)$ vs $\ln(\dot{\varepsilon})$ yields ‘n*’, (b) σ vs $\ln(\dot{\varepsilon})$ results β, (c) ln sinh ($\alpha\sigma s$) vs $\ln(\dot{\varepsilon})$ provides n and (d) ln sinh ($\alpha\sigma_s$) vs 1000 / T results Q for AZ80 – O

To calculate the value of activation energy Q, one takes the logarithm of both sides of Eq. (39), which results in Eq. (44), and after differentiating Eq. (45) we have activation energy as a function of material constants, temperature and flow stress.

$$\ln\,[\sinh(\alpha\sigma_s) = \frac{ln\dot{\varepsilon}}{n} + \frac{Q}{nRT} - \frac{\ln A}{n} \tag{44}$$

$$Q = Rn\left\{\frac{\partial \ln \sinh(\alpha\sigma_s)}{\partial\,(\frac{1}{T})}\right\} \tag{45}$$

The slope of the lines of a plot of ln (sinh $\alpha\sigma_s$) vs. 1000/T provides values for Q at various strain rates.

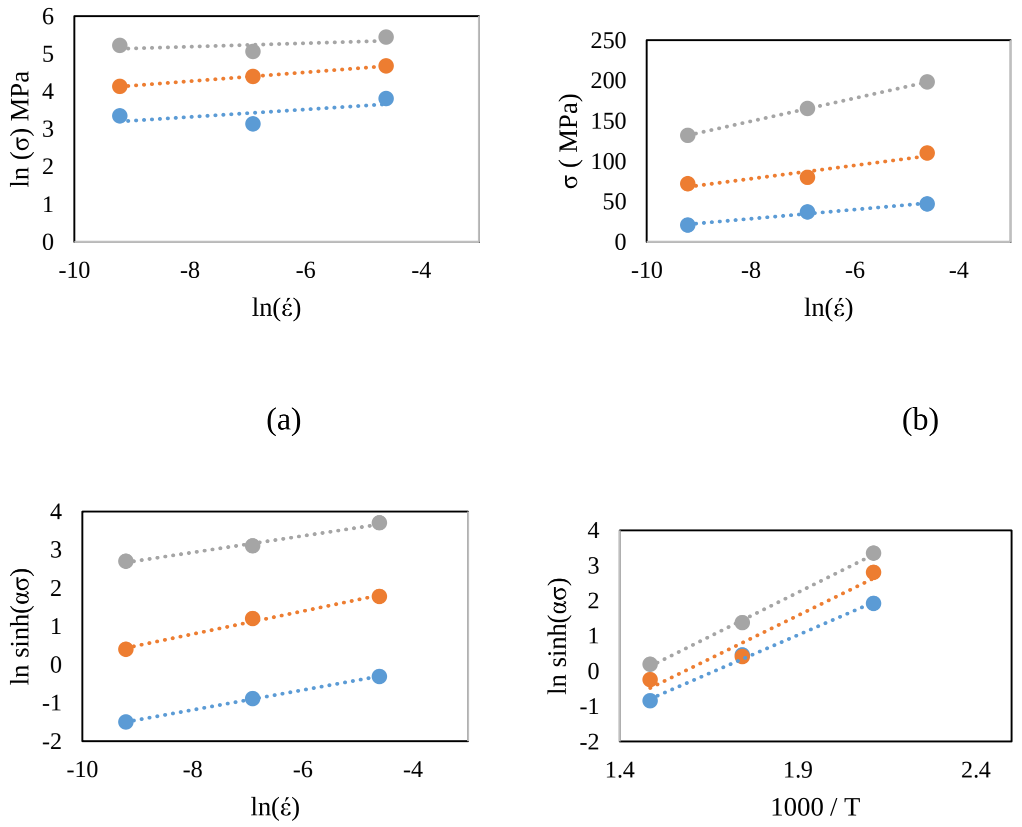

(c) (d)

Figure 119. Plot for evaluation of material constants (a) ln(σ) vs. ln(έ) yields 'n*', (b) σ vs. ln(έ) results β, (c) ln sinh (ασs) vs. ln(έ) provides n and (d) ln sinh ($\alpha\sigma_s$) vs. 1000 / T results Q for AZ80 – F

Similarly, another plot of ln (sinh $\alpha\sigma_s$) vs. ln (έ) results in 1/n at various temperatures for both magnesium AZ80 – O and AZ80 – F, as shown in Figure 119.

All values of material constants and activation energy are summarised in Table 20 and 21 for both magnesium AZ80 – O and AZ80 – F at a strain value of 0.2.

After evaluating these constants, the flow stress equation finally can be described using the Zener-Holloman parameter as follows:

$$\sigma_s = \frac{1}{\alpha}\, ln\left\{(\frac{Z}{A})^{\frac{1}{n}} + \left[(\frac{Z}{A})^{\frac{1}{n}} + 1\right]\right\} \quad (46)$$

The activation energy for magnesium AZ31 reported by various researchers varies from 160 – 164 kJ/mol. Similarly activation energy is calculated here from tensile test data. The amount of activation energy increases up to 310 – 313 kJ/mol for magnesium AZ80 – O and AZ80 – F respectively, as shown in Table 19,caused by the increased aluminium content. This increase could be due to the atomic size of aluminium, as its density in a unit volume of magnesium AZ80 increases and provides an additional hindrance to moving dislocations near the grain boundaries as noted in section 6.4. In addition, the activation energy also increases for coarse grain AZ80 – F compared with AZ80 – O, which again shows that in AZ80 – O deformation is slightly easier than in AZ80 – F. Negative activation energy indicates

After obtaining all material constants at a given strain, strain rate and temperatures, stress/strain curves for both magnesium AZ80 – O and AZ80 – F were plotted as shown in Figure 120 and 121. It is clear that the Arrhenius model predicts material behaviour quite well. In addition, as opposed to the J – C model that did not predict the work hardening regions accurately, the Arrhenius model shows curves closely fitting the experimental data in the work-hardening region, which strongly suggests that the Arrhenius model is more accurate than the J – C model for magnesium alloys.

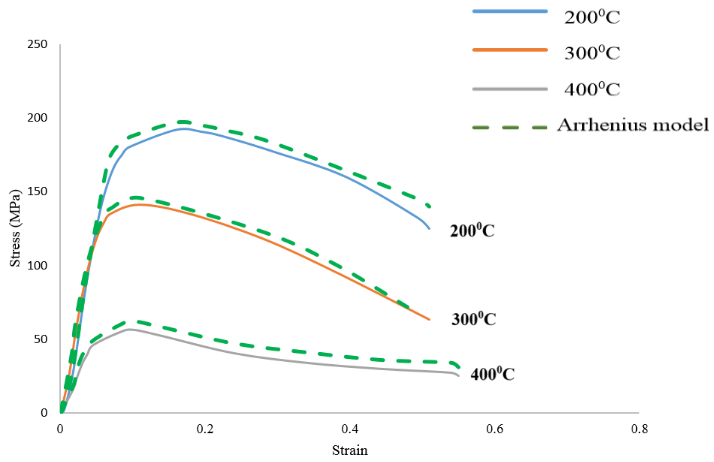

(a)

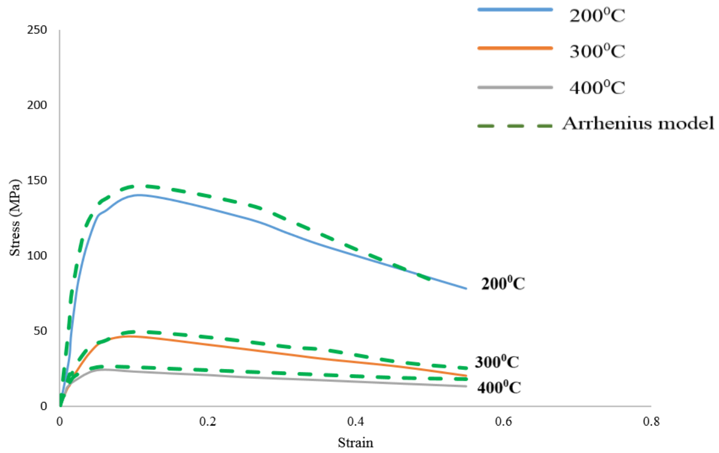

(b)

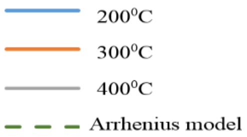

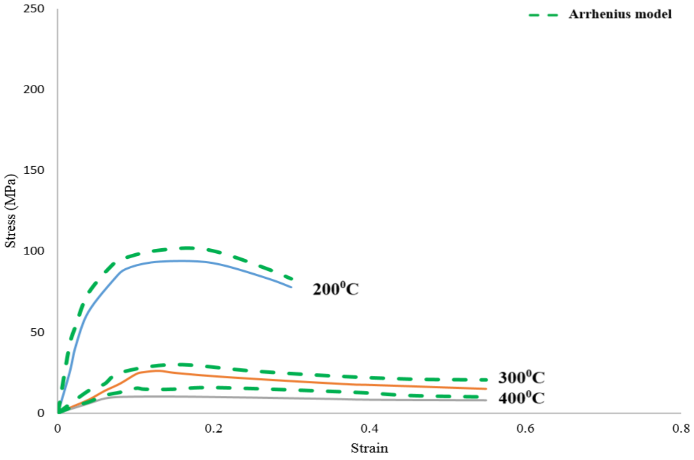

(c)

Figure 120. Stress strain diagrams for magnesium AZ80 – O, predicted vs. experimental results (a) 0.1 sec^{-1}, (b) 0.01 sec^{-1}, (c) 0.001 sec^{-1}

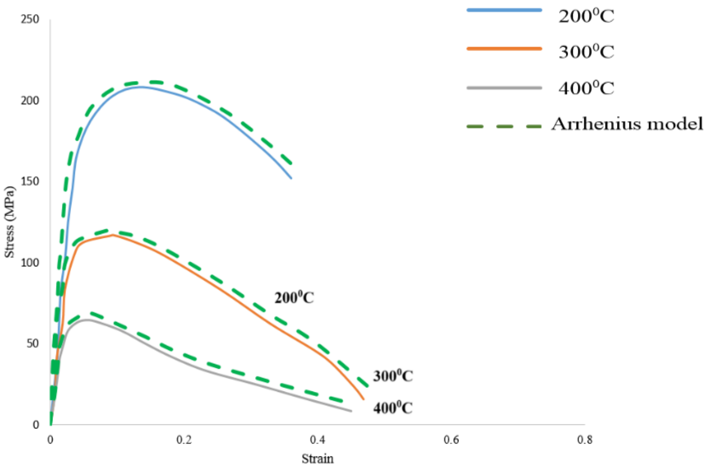

(a)

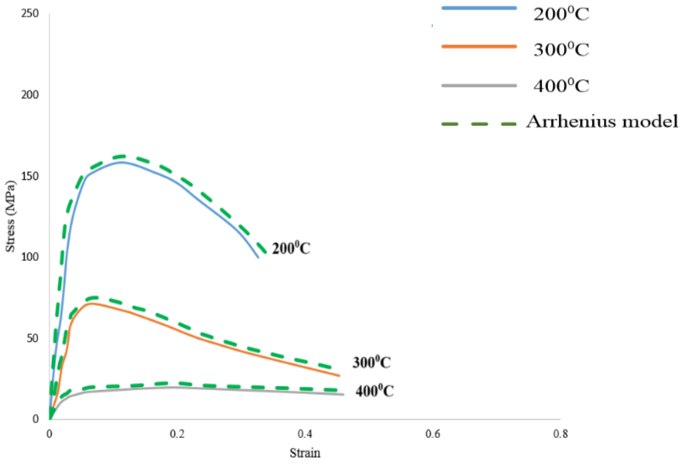

(b)

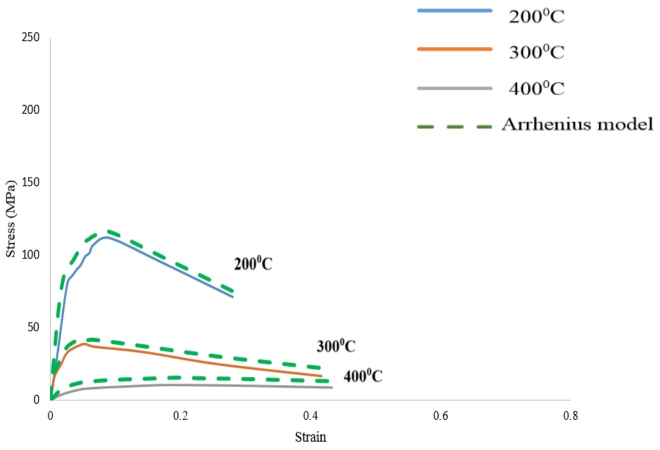

(c)

Figure 121. Stress strain diagrams for magnesium AZ80 – F, predicted vs. experimental results (a) 0.1 sec^{-1}, (b) 0.01 sec^{-1}, (c) 0.001 sec^{-1}

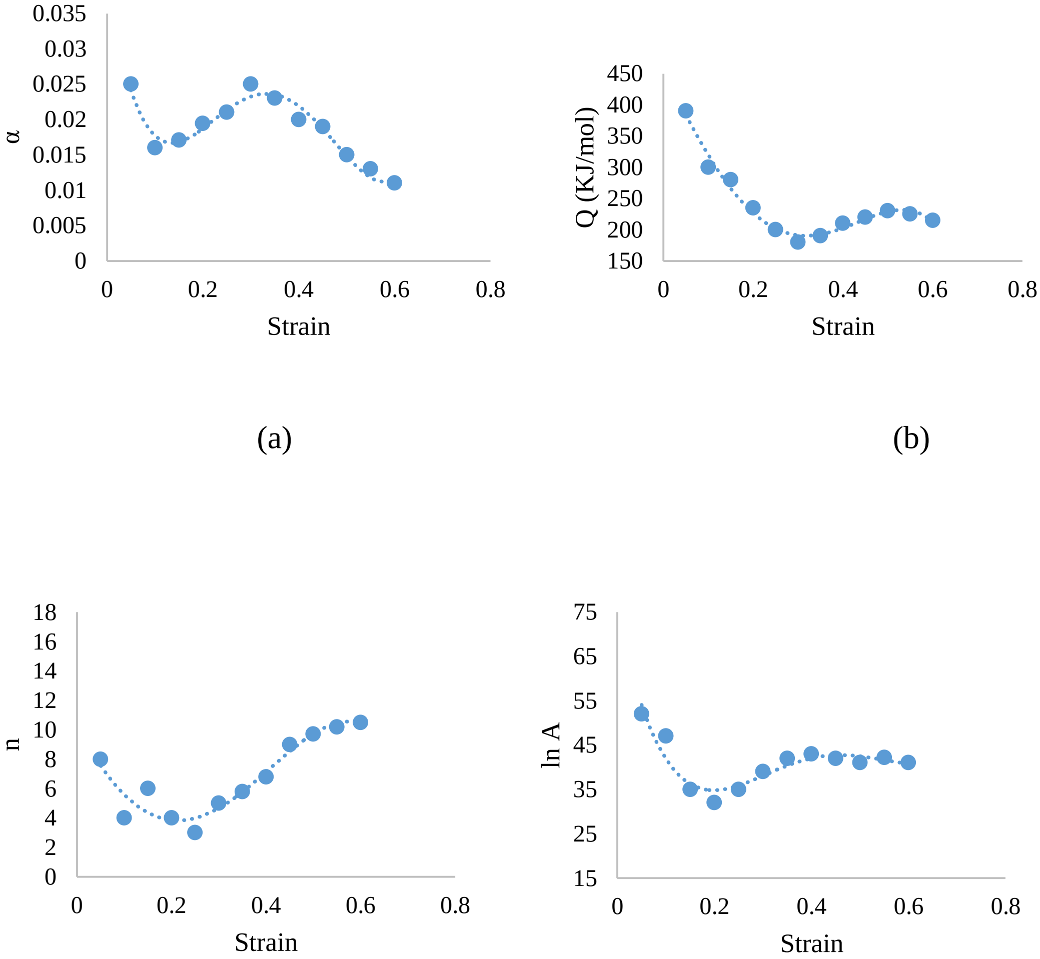

(a)

(b)

(c) (d)

Figure 122. Sensitiveness of material constants towards strain (a) α, (b) Q, (c) n, (d) ln A for AZ80 – O

This has been also reported in the literature by Pilehva et al., Marandi et al. and Lin et al. [385]-[387]. To investigate this further, all material constants were plotted against strain values to observe their sensitivity to strain, as shown in Figures 122 – 123. To evaluate this, all constants used in the Arrhenius model are rewritten in Eqs. (46) – (49) in the form of fourth-order polynomials. Curves were fitted in Matlab across the plotted points and their equations were generated by plotting fourth-order polynomial curves across the points. These constants are shown in Tables 20 and 21.

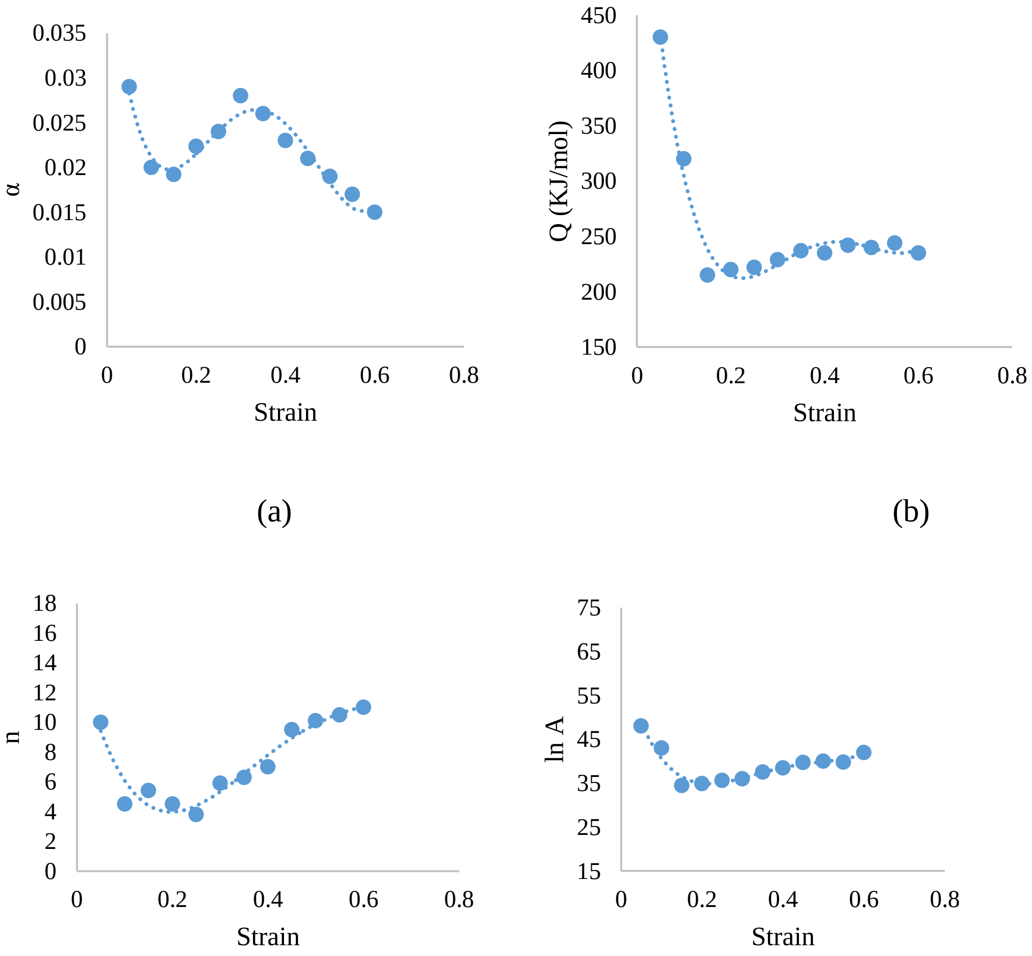

(a) (b)

(c) (d)

Figure 123. Sensitivity of material constants to strain (a) α, (b) Q, (c) n, (d) ln A for AZ80 – F

Table 19. Various material constants in Arrhenius model for magnesium AZ80 – O and AZ80 – F.

	Material Constants			
	Q	***ln A***	***n***	***α***
AZ80 – O	*216.38*	*35.586*	*4.3*	*0.0065*
AZ80 – F	*181.533*	*33.873*	*2.7*	*0.00*

$$\alpha = \alpha_0 + \alpha_1\varepsilon + \alpha_2\varepsilon^2 + \alpha_3\varepsilon^3 + \alpha_4\varepsilon^4 \quad (47)$$

$$Q = Q_0 + Q_1\varepsilon + Q_2\varepsilon^2 + Q_3\varepsilon^3 + Q_4\varepsilon^4 \quad (48)$$

$$n = n_0 + n_1\varepsilon + n_2\varepsilon^2 + n_3\varepsilon^3 + n_4\varepsilon^4 \quad (49)$$

$$\ln A = A_0 + A_1\varepsilon + A_2\varepsilon^2 + A_3\varepsilon^3 + A_4\varepsilon^4 \quad (50)$$

Table 20. Various polynomial curve fitting material constants in the Arrhenius model for magnesium AZ80 – O.

Q	***ln A***	***n***	***α***
Q_0 = 9761.1	A_0 = 2299.5	n_0 = -233.1	α_0= 3.97
Q_1= 8146.5	A_1 = - 3919.3	n_1 = 78.632	α_1 = - 5.5433
Q_2= 405.62	A_2 = 2298.4	n_2 = 138.95	α_2 = 2.51
Q_3= 1472.2	A_3 = -521.57	n_3 = - 61.068	α_3 = -0.41
Q_4= 455.47	A_4 = 74.871	n_4 = 10.252	α_4= 0.0393

Table 21. Various polynomial curve fitting material constants in the Arrhenius model for magnesium AZ80 – F

Q	**ln A**	**n**	**α**
Q_0 = 24639	A_0 = 1476.1	n_0 = 382.87	α_0= 4.107
Q_1= - 39888	A_1 = - 2426.1	n_1 = - 779.83	α_1 = - 5.735
Q_2= 22803	A_2 = 1429.9	n_2 = 545.72	α_2 = 2.611
Q_3= - 5322.6	A_3 = - 337.94	n_3 = - 135.9	α_3 = - 0.4228
Q_4= 646.56	A_4 = 62.407	n_4 = 14.95	α_4= 0.0446

As temperature increases, carriers with higher momentum have lower probability to be captured in a potential well. Thus the conductivity decreases as temperature increases, resulting in Arrhenius equation with negative activation energy. It can be concluded that the material constants are more sensitive to strain and the activation energy increases with increasing aluminium content.

7.4 Finite Element Simulations

For this research Abaqus was used because of its extensive tools for sheet deformation processes.

In finite element analysis there are usually five steps in the analysis of any problem: discretisation, boundary conditions, finite element formulations, solution phase and post-processing. In FEA analysis, various components are modelled as an assembly of finite elements interconnected with nodes and element boundaries. In this chapter, nonlinear analysis was performed to accommodate variations of large displacements and forces in regard to time. To accommodate this, a nonlinear solution was performed with incremental analysis, that is, a solution with respect to discrete time intervals.

7.5 Formulations Algorithms

There are mainly two formulation algorithms in nonlinear FEA, the implicit method and the dynamic explicit method. Implicit analysis consumes a large amount of time with an increase in problem size, which is why the preferred method to solve nonlinear problems is the explicit methodology.

7.6 FEA formulations

7.6.1 Discretisation

The model was created initially with the help of the parametric modelling package within Abaqus. A quarter model of the die blank holder and punch was created, as shown in Figure 124. Key points, lines, arcs, circles were created and trimmed in a 2D model and then revolved and extruded to convert them into 3-D geometry. Material properties were assigned, such as density (1668kg/m^3), Poisson's ratio (0.27) and Young's modulus (32GPa) from suppliers literature and tensile test data.

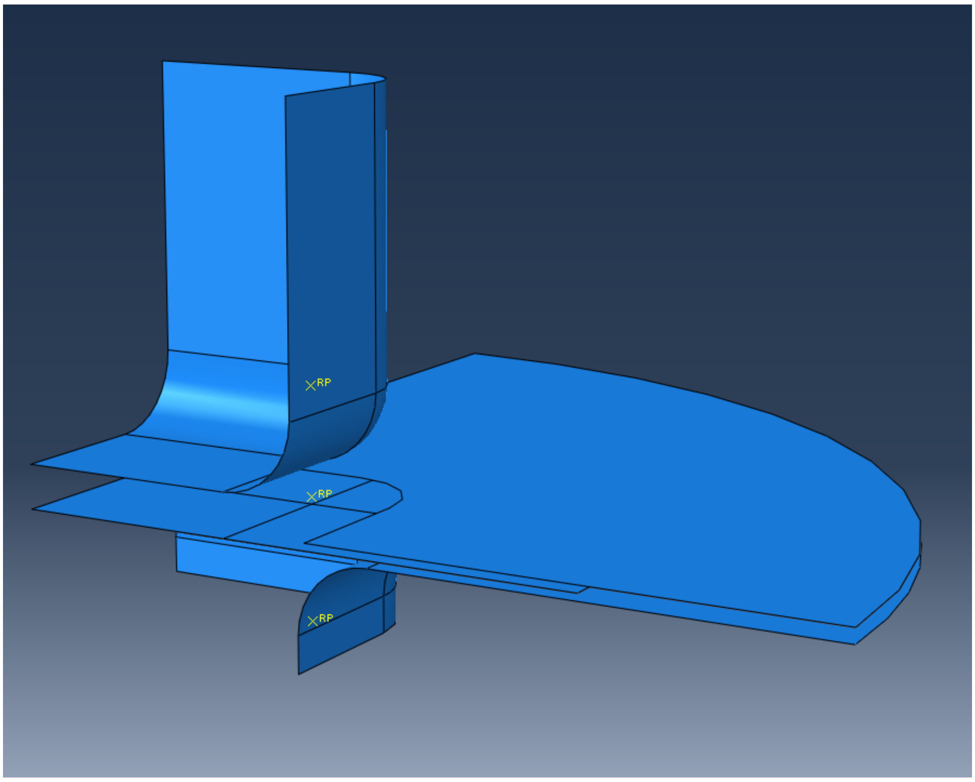

Figure 124. FEA model of deep-drawing setup

The selection of the structural element is an important step in FE simulations. The blank-shell element 163 was used with 12 degrees of freedom at each node. Shell elements are the obvious choice in finite simulation processes for sheet metals rather than solid elements. Thin-shell elements were also used for tooling, with fewer nodes than the blank. Contact points were also generated between punch, blank and dies.

7.6.2 Meshing

Meshing was generated with the Abaqus mesh tool, which generates meshes easily and accurately. Meshing of die, blank, punch and blankholder is shown in Figure 125 and 126. Coulomb friction model was adopted with a friction factor of 0.1 between tool and blank.

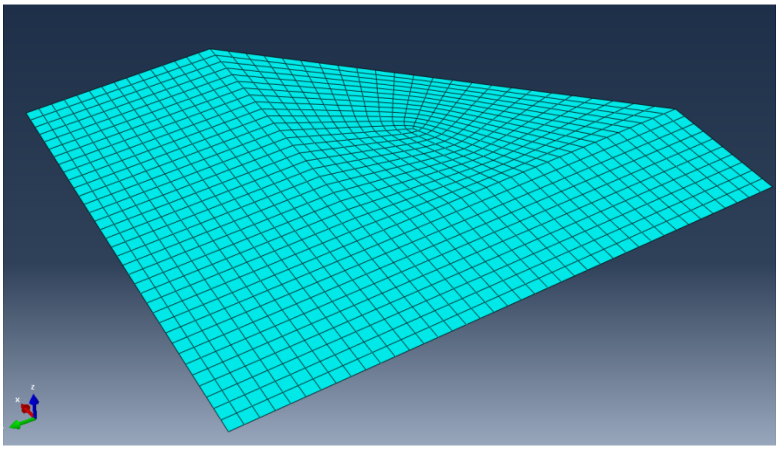

Figure 125. FEA quarter model of deep-drawing setup with mesh of blank

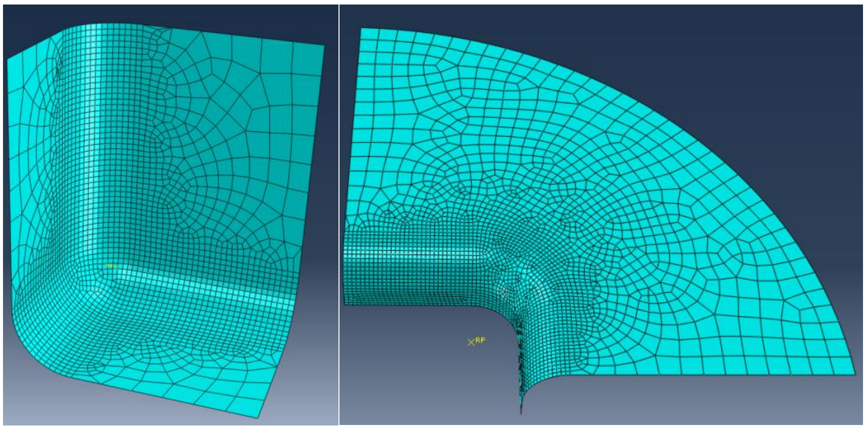

(a) (b)

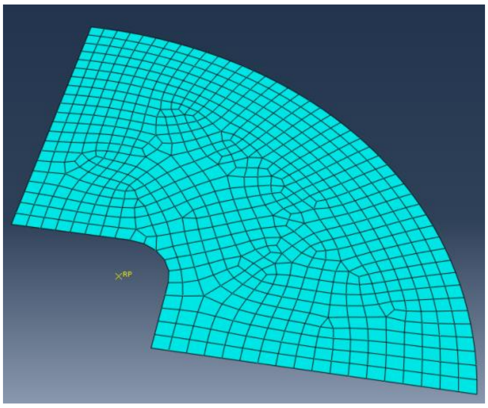

(c)

Figure 126. Quarter model of deep-drawing tools with meshes (a)punch, (b)die and (c) blank holder

7.7 Results and discussion

The analysis results are shown in Figures 127 and 128. Thickness and temperature distributions are displayed in Figures 129 and 130. A comparison of experimental and simulation results is shown in Figure 129. A thickening effect is visible at the flange, while a thinning effect is observed at the walls. It is also noticeable that the part of the blank that comes in contact with the die corner shows maximum thinning, however, in the experimental results the blank portion in contact with the punch radius shows thinning. The reason for this variation in behaviour is the existence of variability in the strength of the cup walls during deep-drawing process. In addition to that temperature drop during deep drawing process along walls cannot be measured during experiments. The absence of these temperature distribution data generates inaccuracy in simulation results. This variation is also explained by Hariharasudhan et al., [254] from his experiments on AZ31 and AZ31B.

This strength variation in the cup wall was caused by variation in temperature distribution in the cup wall, as explained in section 3.3.2.6. As noted the temperature increased more at the die corner than the punch corner, which resulted in a lower yield strength at the cup wall than in the material portion in contact with the punch corner, which ultimately is the reason for thinning of the wall material. The amount of thinning observed is 17, 21 and 25 percent with forming temperatures of 150, 200 and 250^{0}C, respectively.

Understanding temperature distribution is important for the forming process, to predict the thinning and thickening of the sheet during forming. In the warm forming process, when the punch travels towards the cavity in the die, contact of the blank with the punch increases, while contact with the die decreases, as explained in section 3.3.2.6. Therefore the blank loses some of its heat energy to the punch, which has a lower temperature at the shoulder radius and increases temperature at the shoulder radius of the die. This also affects the yield strength of the material near the die corner, which is lower than that of the material in contact with the punch corner. Another reason for this is the low specific heat capacity and high thermal conductivity value of magnesium.

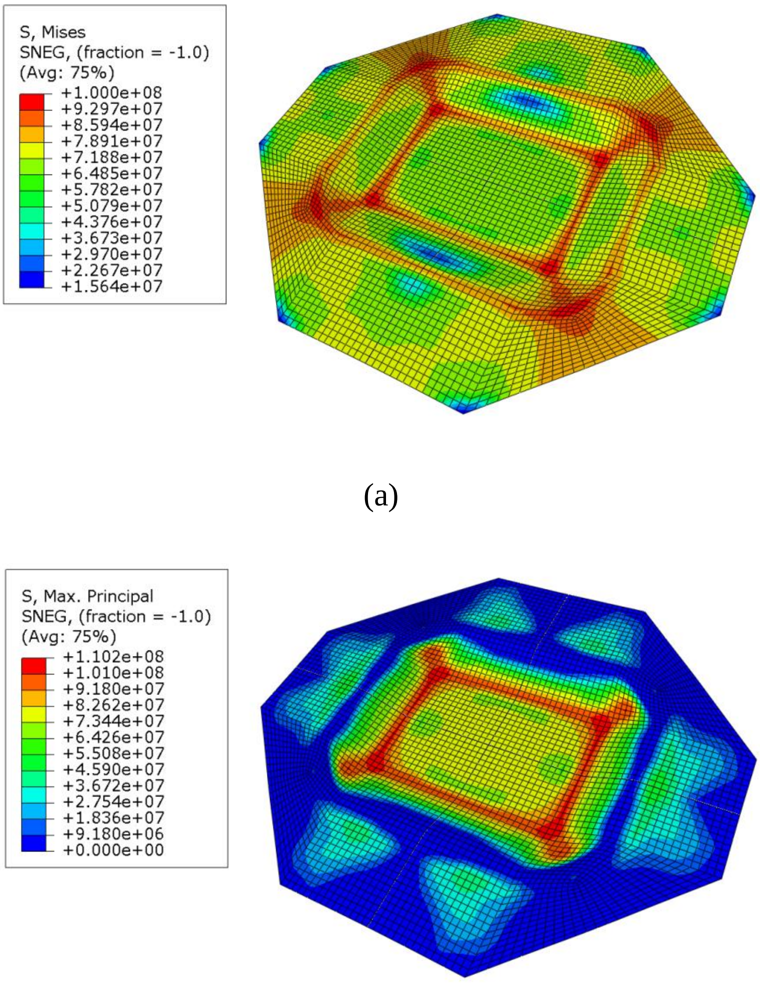

(a)

(b)

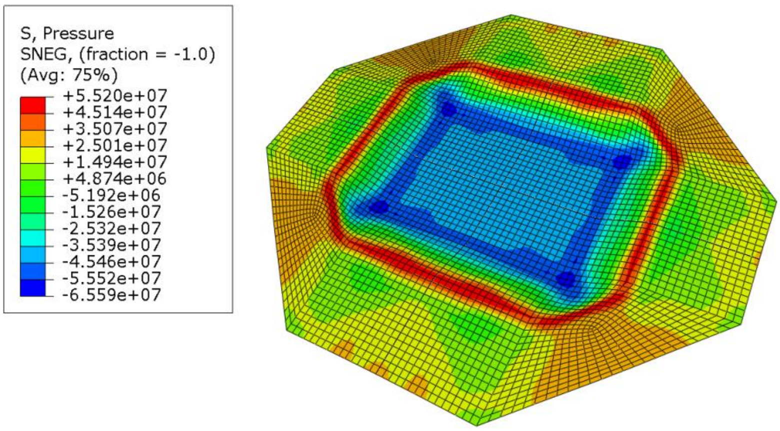

(c)

Figure 127. FEA analysis of deep-drawn cup at 100^{0}C with 10kN force for magnesium AZ80 – O (a) Von Mises stress distribution, (b) Principal stress distributions, (c) Pressure distributions

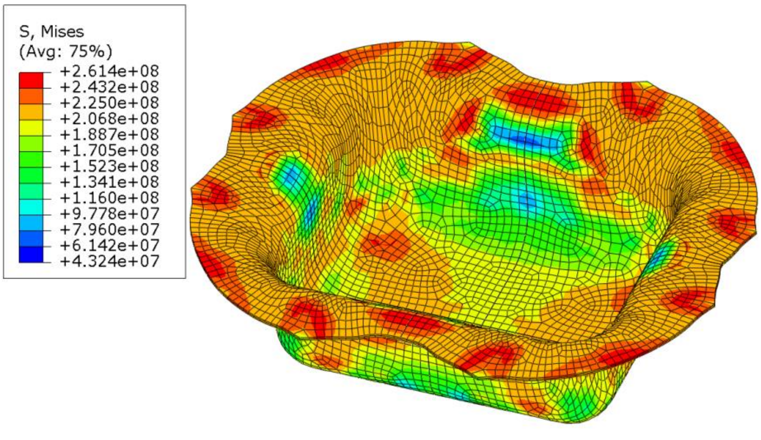

(a)

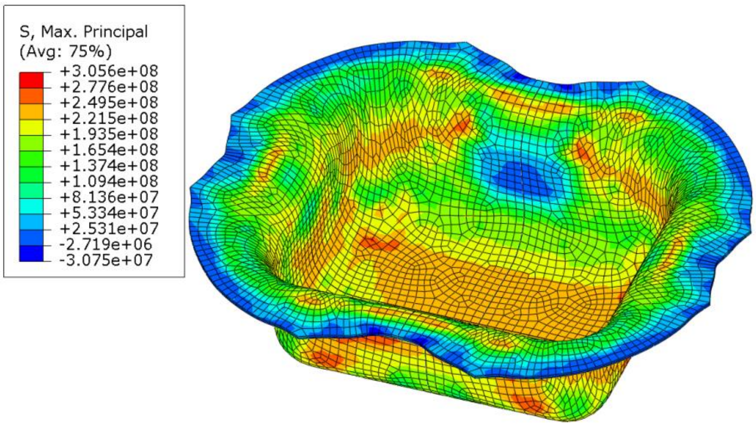

(b)

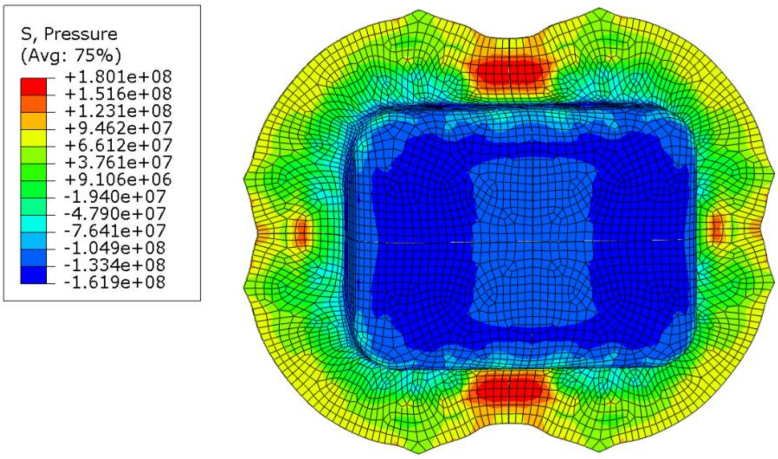
S, Pressure
(Avg: 75%)
+1.801e+08
+1.516e+08
+1.231e+08
+9.462e+07
+6.612e+07
+3.761e+07
+9.106e+06
-1.940e+07
-4.790e+07
-7.641e+07
-1.049e+08
-1.334e+08
-1.619e+08

(c)

Figure 128. FEA analysis of deep-drawn cup at 250^{0}C with 10kN force for magnesium AZ80 – O (a) Von Mises stress distribution, (b) Principal stress distributions, (c) Pressure distributions

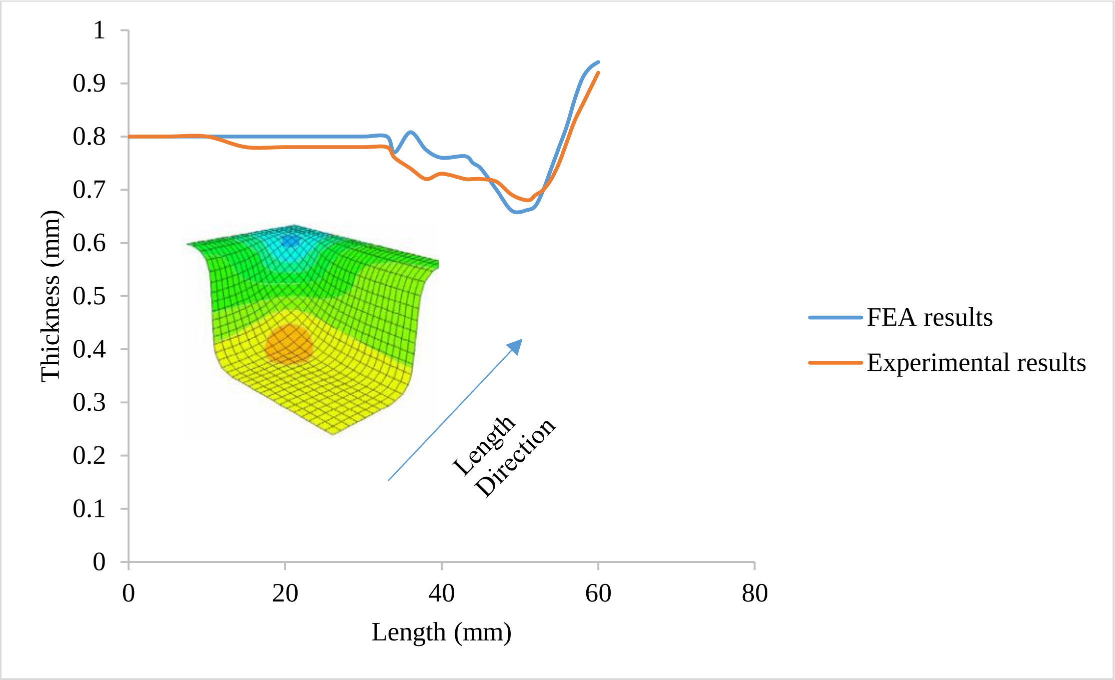

Figure 129. Thickness distribution of specimen with a blankholder force of 10 kN at 250^{0}C for magnesium AZ80 – O

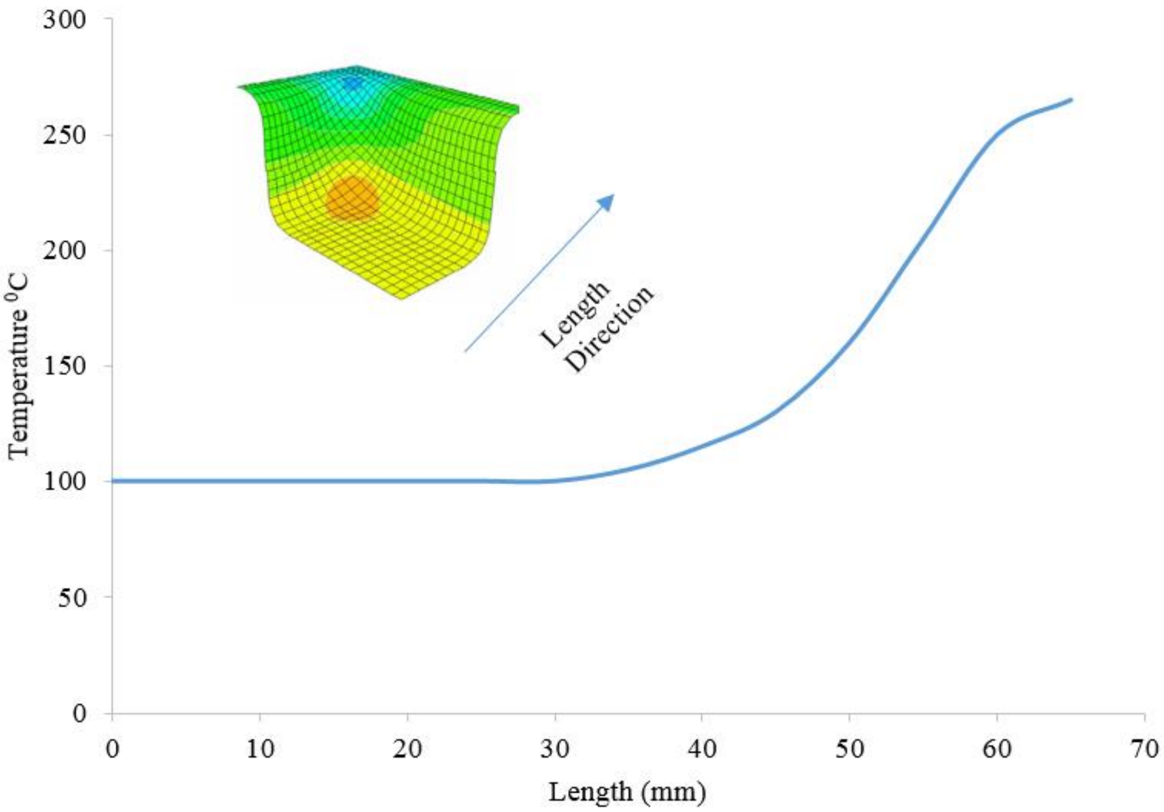

Figure 130. Temperature distribution of specimen with a blankholder force of 10 kN and at 250^{0}C for magnesium AZ80 – O (Simulation results)

Droder and Doege [250] and Yoshihara [251] also state that because of low temperatures in the wall, flow stress increases, which makes temperature controls an important parameter in the formability of magnesium alloys. A similar temperature distribution was investigated by Hariharasudhan et al. [252] when they conducted forming tests of round shapes of magnesium AZ31B at 200^{0}C. They observed an additional increase in the temperature of the flange, which was set to 200^{0}C. The reason stated for this increase was the amount of heat generated during plastic work. They also support the above reasoning, that high flange temperature and low temperature in the wall are necessary for proper drawing of magnesium alloys, as this increases the flow stress and enables the cup wall to bear more stress at the punch corner. This strategy also avoids localised necking in the material. They also explained the punch should be always kept at a lower temperature than the blank, because the punch temperature will automatically increases during the forming operation.

It is also necessary to note here that the blank temperature is always greatest at the corners, because there is less available area for convection than along its bottom area, where the lowest temperature is observed, because of losses due to a large convection area and contact with the punch [253]. This also aids the forming operation. As explained earlier, flow stress always increases with a decrease in temperature, while increased temperatures at the corners avoid fractures and large drawn-depth can be achieved.

7.8 Conclusions

1) Arrhenius equations predict magnesium's behaviour more accurately than the J – C model does.
2) The J – C model did not predict the work-hardening region accurately.
3) It can be concluded that material constants are sensitive to strain and activation energy increases with an increase in aluminium content, which increases the atomic density per unit volume of magnesium alloys.
4) A deep-drawing setup was modelled in FEA using Abaqus. Drawing simulation of a cup was achieved at various temperatures and contours were plotted.
5) Thickness and temperature distributions are also successfully modelled. A thickening effect is visible at the flange, while a thinning effect is observed at the walls.
6) The blank that comes in contact with the die corner shows greatest thinning, however in the experimental results, the blank portion contacted by the punch radius shows greatest thinning.
7) Temperature distribution simulations show the blank has the lowest temperature at the shoulder radius of the punch, and an increased temperature at the shoulder radius of the die.
8) It is concluded that the blank temperature is always greatest at its corners, since a smaller area is available for convection than the surface area where the lowest temperature is observed, because of losses due to a large convection area and contact with the punch.

Chapter 8

Conclusion and Future Work

8.1 Conclusion

This chapter concludes the investigations of magnesium AZ80 forming characteristics, by reviewing their experimental and simulation results. The forming characteristic examinations were divided into four categories:

i. Tensile (stretch forming) behaviour investigations
ii. Deep-drawing behaviour investigations
iii. Microstructure investigations
iv. Finite element simulations

8.1.1 Tensile behaviour investigations

1) Anisotropy plays a major role at room temperature, however 45^0RD samples showed more elongation than the other two.

2) Percent elongation at a strain rate of 1 x 10^{-2} sec^{-1} at room temperature was 13% which increases to 57% at a temperature of 400^0C for magnesium AZ80 - F. A similarly percent elongation of magnesium AZ80 - O is observed with an increase from 17 percent (at room temperature) to 73% (at temperature of 400^0C) at a constant strain rate of 1 x 10^{-2} sec^{-1} . Maximum elongations achieved were 153 percent and 140 percent for magnesium AZ80 – O and AZ80 – F respectively at a temperature of 300^0C and a strain rate of 1 x 10^{-4} sec^{-1}.

3) Fine grain-size magnesium shows more ductility due to the easy movement of grains during deformations and recrystallisation that occurs at higher temperatures.

4) Yield stresses and ultimate tensile stresses are higher in coarse grain compared to fine grain at 200^0C to 400^0C. The amount of elongation of fine grain is about 153 percent compared with 140 percent in coarse grain.

5) To increase elongations, a technique was adopted, that is two-stage forming. In two-stage deformation, elongation at a constant strain-rate before failure reaches 195 percent, compared with 153 percent at 400^0C and $2x10^{-4}$ sec^{-1}. Similarly for AZ80 – F, fracture strain increased by 11% while elongation before failure was raised to 186% compared with 140 percent at 400^0C and $2x10^{-4}$ sec^{-1}.

6) In two-stage deformation at a varying strain-rate an additional elongation of 7% was achieved for AZ80 – O, and elongation before failure reached 205 percent. AZ80 – F touched a maximum value of 189 percent. The maximum or ultimate load also reduced by up to 8 percent and 6 percent for AZ80 – O and AZ80 – F respectively.

8.1.2 Deep-drawing behaviour investigations

1) It is quite clear that formability increases drastically at elevated temperatures compared with room temperature for both AZ80 – O and AZ80 – F. However, AZ80 – F shows less formability than AZ80 – O, due to its coarse grain-size, as shown in Figures 71 and 72.

2) LDR increases continuously from lower temperatures up to 250 °C as seen in Figure 77. The first good part could be drawn with a LDR of 1.62 and a drawing depth of 24 mm at 150 °C and the deepest drawn part was achieved at 250 °C with a LDR of 2.1 and a depth of 46 mm.

3) A recommendation for deep-drawing of AZ80 – O magnesium sheet with an even distributed surface temperature is that a temperature rise

above 250 °C is not practical because of a decrease of the drawing ratio and also with regards to the required energy.

4) Effects of the punch velocities were examined and data were plotted as FLDs and load displacement curves, as shown in Figure 73 and 81 respectively. It can be concluded that punch load reduces with a decrease in punch velocity, however, process time increases with lower punch velocity, which reduces the scope for commercial applications of magnesium AZ80 – O.

5) The influence of the blank holder force was investigated, as shown in Figure 78 for magnesium AZ80 – O. At 50 kN of blank holder force, good parts were drawn, however, with increasing blank holder forces of 75 kN and 100 kN the material failed in the flange region, due to a too tight grip for magnesium AZ80 – O.

6) The width of the blank notch also played a role in the load displacement curves. The notch widths exhibit an inversely proportional relationship with the amount of displacement, while the load proportionally increased with an increase in notch width, as shown in Figure 80 for magnesium AZ80 – O.

8.1.3 Microstructure investigations

7) Twinning mostly occurs at room temperature. However, its influence reduces considerable when both alloys are loaded at elevated temperatures.

8) Static and dynamic grain growth is observed at grip and gauge sections respectively in both materials.

9) Dynamic recrystallisation is mostly seen in fine grains with grain sizes smaller than 10 – 15µm.

10) Dynamic recrystallisation nucleates around 300^0C and 400^0C for AZ80 – O and AZ80 – F, respectively.

11) After 350^{0}C, cavitation was the dominant mechanism, along with grain growth.

12) Several cavities were observed at grain boundaries, with long threaded hair type filaments attached to them. Most of these cavities were elongated elliptical in shape, a few were approximate circles and a few were irregular-shaped at 300^{0}C and 1 x 10^{-4} sec^{-1} for magnesium AZ80 - O.

13) These cavities were mostly elongated along the tensile direction, and approximately 75% of these cavities form at temperatures above 300^{0}C and at strain rates of 10^{-4} sec^{-1}, for both AZ80 – O and AZ80 – F.

14) At 200^{0}C 10^{-4} sec^{-1} only a few cavities were found in AZ80 – O near grain boundaries and they were approximately 0.1 - 0.3µm in size.

15) Several long thread like filaments were found, attached to most of these cavities with diameters of 1µm or less, however, the cavity sizes varied from 1.5µm to 25µm at 300^{0}C and 1 x 10^{-4} sec^{-1} for magnesium AZ80 - O.

16) Filaments are generated purely due to diffusion of zinc atoms, though aluminium atoms were also present in large quantities but were unable to diffuse, due to their larger atomic radius, as shown by EDS analysis.

17) Two-stage deformation reduces the number of cavities significantly and enhances the formability of magnesium.

8.1.4 Mathematical modelling and finite element simulations

18) Arrhenius equations predict magnesium's behaviour more accurately than the J – C model does. Predictions by the Arrhenius model are shown in Figures 116 – 117 and 120 – 121.

19) The J – C model did not predict the work-hardening region accurately.

20) It can be concluded that material constants are sensitive to strain and activation energy increases with an increase in aluminium content, which increases the atomic density per unit volume of magnesium alloys.

21) Thickness and temperature distributions are displayed. A thickening effect is visible at the flange, while a thinning effect is observed at the walls.

22) The blank that comes in contact with the die corner shows greatest thinning, however in the experimental results, the blank portion contacted by the punch radius shows greatest thinning.

8.2 Future Work

This thesis covered many aspects of the forming behaviour of magnesium alloys, but still many research opportunities remain that need investigation. An in-depth study of variations in tool geometric parameters could be performed to improve formability, which will make this alloy comparable to other sheet metal materials. Furthermore the chemical composition of materials could be optimised to achieve additional formability at lower temperatures and higher ram speeds. Various thermomechanical processes could also be adopted to vary grain size of a material at specific locations, so that large elongations before failure can be achieved.

Strain measurement methods needs to be improved for higher temperature tests, as it is difficult to measure strains accurately from certain temperatures onwards due to heat. Spring-back characteristics also need to be investigated to analyse post processing characteristics. Furthermore accurate mathematical models for predicting deep-drawing behaviour need to be developed to accommodate microstructure changes occurring in materials, due to variations in temperature and strain rate.

In finite element analysis, further investigation is required to simulate two stage deformation, temperature distribution on sheets, temperature drops inside tooling, optimal blank size that will accurately predict deep-drawing behaviour. Convergence analysis can also be performed to calculate accurate mesh size.

List of Publications from this Project

1. **Muhammad Waseem Soomro** and Thomas Neitzert, “Effects of temperature, strain rate and grain size on superplastic behaviour of magnesium,” *Advanced Materials Research Journal*, vol. 488 – 489, pp. 27 – 34, 2012.

2. **Muhammad Waseem Soomro** and Thomas Neitzert, “Effects of temperature, strain rate and grain size on superplastic behaviour of magnesium,” *Advanced Materials Research Journal*, vol. 488 – 489, pp. 27 – 34, 2012.

3. **Muhammad Waseem Soomro** and Thomas Neitzert, “Effects of pre-process and post-process parameters on formability of magnesium alloys,” *Journal of Achievements in Materials and Manufacturing Engineering*, vol. 55(2), pp. 799 – 809, 2013.

4. T. Pasang, V. Satanin, M. Ramezani, **Muhammad Waseem**, T. Neitzert, O. Kamiya, “Formability of magnesium alloys AZ80 and ZE10,” *Key Engineering Materials*, vol. 622 - 623, pp. 284-291, 2014.

5. **Muhammad Waseem Soomro** and Thomas Neitzert, “Investigation of variations in tensile anisotropy properties of magnesium alloys due to temperature,” *The International Deep Drawing Research Group Conference (IDDRG 2012)*, **INDIA,** Nov 25th – 29th, 2012.

6. Holger Heinzel, Thomas Neitzert**, Muhammad Waseem Soomro,** M Weiss, “Investigation of the performance of pre-painted sheet metal material during press forming,” *The International Deep Drawing Research Group Conference (IDDRG 2012)*, **INDIA,** Nov 25th – 29th, 2012.

7. **Muhammad Waseem Soomro** and Thomas Neitzert, (2012), “Recent developments and trends in metal forming of magnesium alloys”, *11th Global congress on manufacturing and management (GCMM)*, **NEW ZEALAND**, Nov. 28th - 30th, 2012.

References

[1] E. Aghion, B. Bronfin and D. Eliezer, “The role of magnesium in protecting environment,” *Journal of Materials Processing Technology*, vol. 117, p. 381, 2001.

[2] G. Ingarao, R. Di Lorenzo and F. Micari, “Sustainability issues in sheet metal forming process: an overview,” *Journal of cleaner Productions*, vol. 19, p. 337, 2011.

[3] J. Kaneko, M. Sugamata, M. Numa, Y. Nishikawa and H. Takada, “Effect of texture on the mechanical properties and formability of magnesium wrought materials,” *Journal of Japan Institute of Metals*, vol. 64, p. 141, 2000.

[4] J. Wu, X. Lu, H. Xu and N. Nakagoshi, “Application of energy-saving magnesium alloy in automotive industry,” *Journal of Advanced Materials Research*, vol. 734, p. 2244, 2013.

[5] A. A. Luo, “Magnesium casting technology for structural applications,” *Journal of Magnesium and Alloys*, vol. 1, p. 2, 2013.

[6] S. R. Agnew and O. Duygulu, “A Mechanistic understanding of the formability of magnesium: Examining the role of temperature on the deformation mechanisms,” *Material Science Forum*, vol. 419 - 422, p. 177, 2003.

[7] E. Aghion, B. Bronfin and D. Eliezer, “The Role of Magnesium industry in protecting the environment,” *Material Processes and Technology*, vol. 117, p. 381, 2001.

[8] H. Friedrich and S. Schumann, “Research for a new age of magnesium in the automotive industry,” *Material Processes and Technology*, Vol. 117, p. 276, 2001.

[9] B. L. Mordike and T. Ebert, “Magnesium: Properties — applications — potential,” *Materials Science and Engineering*, vol. A302, p. 37, 2001.

[10] F. Abu-Farha and M. Khraisheh, “Deformation characteristics of AZ31 magnesium alloy under various forming temperatures and strain rates,”

Proceedings of the 8th ESAFORM Conference on Material Forming, Cluj-Napoca, Romania, p. 627, April 27-29, 2005.

[11] P. Cavaliere and P.P. De Marco, “Effect of friction stir processing on mechanical and microstructural properties of AM60B Magnesium alloy,” *Material Science*, vol. 41, p. 3459, 2006.

[12] F. K. Abu-Farha, “Integrated approach to the superplastic forming of magnesium alloys”, Ph.D. dissertation, University of Kentucky, 2007.

[13] F. Abu-Farha, N. Rawashdeh and M. Khraisheh, “Superplastic Deformation of magnesium alloy AZ31 under biaxial loading condition,” *Material Science Forum*, vol. 551-552, p. 219, 2007.

[14] C. Chang, C. Lee and J. Huang, “Cavitation characteristics in AZ31 magnesium alloys during LTSP or HSRSP,” *Scripta Materialia*, vol. 51, p. 509, 2004.

[15] A. Mwembela, E.B. Konopleva and H.J. McQueen, “Microstructural development in Magnesium alloy AZ31 during hot working,” *Scripta Materialia*, vol. 37, p. 1789, 1997.

[16] W. Zhongjun, W. Zhaojing and Z. Jing, “Superplastic deformation of a relatively coarse grained AZ80 magnesium alloy,” *Advanced Material Letters*, vol. 2, p. 113, 2011.

[17] W.J.Kim and W.G. Lee, “Enhanced superplasticity of 1 wt.%Ca-AZ80 Mg alloy with ultrafine grains,” *Material Letters*, vol. 64, p. 1759, 2010.

[18] F. Abu-Farha and M. Khraisheh, “Analysis of superplastic deformation of AZ31 magnesium alloy,” *Journal of Advanced Engineering*, vol. 9, p. 777, 2007.

[19] M. Mabuchi, H. Iwasaki, K. Yanase and K. Higashi, “Low temperature superplasticity in an AZ91 magnesium alloy processed by ECAE,” *Scripta Materialia*, vol. 36, p. 681, 1997.

[20] H. Watanabe, T. Mukai, K. Ishikawa, Y. Okanda and K. Higashi, “Superplastic characteristics in an extruded AZ31 magnesium alloy,” *Journal of Japan Institute of Light Metals*, vol. 49, p. 401, 1999.

[21] T. C. Changa, J. Y. Wang, C. M. Ob and S. Lee, “Grain refining of magnesium alloy AZ31 by rolling,” *Journal of Material Processes and Technology*, vol. 140, p.588, 2003.

[22] A. Bussiba, A.B. Artzy, A. Shtechman, S. Iftergan and M. Kupiec, “Grain Refinement of AZ31 and AZ60 Mg Alloys – Towards Superplasticity Studies,” *Material Science Engineering*, vol. 302, p .56, 2001.

[23] H. Watanabe, H.Tsutsui, T.Mukai, K. Ishikawa, Y. Okanda, M. Kohzu and K. Higashi, “Superplastic behavior in commercial wrought magnesium alloys,” *Mater. Sci. Forum*, vol. 350 - 35, p. 171, 2000.

[24] N. V. Thuramalla and M. K. Khraisheh, “Effects of microstructural evolution on the stability of superplastic deformation,” *Proceedings of the Second MIT Conference on Computational Fluid and Solid Mechanics, Elsevier*, vol. 1, p. 683, 2003.

[25] Y. Xue, Z. Min Zhang and Yao Jin Wu, “A study on processing map and flow stress model of AZ80 magnesium alloy forming at elevated temperature,” *Applied Mechanics and Materials*, vol. 121-126, p. 3, 2011.

[26] L. Yan, Z. Zhi-min and X. Yong, “Influence of aging on microstructure and mechanical properties of AZ80 and ZK60 magnesium alloys,” *Transactions of Non Ferrous Metals*, vol. 21, p. 739, 2011.

[27] G. Zhi-hong, H. Hua, Z. Yu-hong and Q. Shu-wei, “Optimization of AZ80 magnesium alloy squeeze cast process parameters using morphological matrix,” *Transactions of Non Ferrous Metals*, vol. 22, p. 411, 2012.

[28] N. Kashefi and R. Mahmudi, “The microstructure and Impression creep behaviour of cast AZ80 magnesium alloy with Yttrium additions,” *Materials and Design*, vol. 39, p. 200, 2012.

[29] B.Q. Shia, R.S. Chena and W. Kea, “Effects of forging processing on the texture and tensile properties of ECAE AZ80 magnesium alloy,” *Materials Science and Engineering A*, vol. 546, p. 323, 2012.

[30] C. Lv, T. Liu, D. Liu, S. Jiang and W. Zeng, “Effect of heat treatment on tension–compression yield asymmetry of AZ80 magnesium alloy,” *Materials and Design*, vol. 33, p. 529, 2012.

[31] Z. J. Wang, “Influence of heat treatment condition on low cycle fatigue life of a rolled AZ80 magnesium alloy sheet,” *Advanced Materials Research,* vol. 239 - 242, p. 1309, 2011.

[32] G. Z. Quan, T. W. Ku, W. J. Song and B. S. Kang, “The workability evaluation of wrought AZ80 magnesium alloy in hot compression,” *Materials and Design*, vol. 32, p. 2462, 2011.

[33] E. Doege and K. Droder, “Sheet metal forming of wrought magnesium alloys – formability and process technology,” *Journal of Material Process and Technology*, vol. 115, p. 14, 2001.

[34] S. Yoshihara, H. Nishimura, H. Yamamoto and K. Manabe, “Formability enhancement in magnesium alloy stamping using a local heating and cooling technique: circular cup deep drawing process,” *Journal of Materials Processing Technology*, vol. 146, p. 52, 2004.

[35] F. Chen, T. Huang and C. Kun Chang, “Deep drawing of square cups with magnesium alloy AZ31 sheets,” *International Journal of Machine Tools and Manufacturing*, vol. 43, p. 1553, 2003.

[36] K. Droder and E. Doege, “Processing of magnesium sheet metals by deep drawing and stretch forming,” *Material Technology,* vol. 78, p. 19, 1997.

[37] T.B. Huang, Y.A. Tsai and F.K. Chen, “Finite element analysis and formability of non-isothermal deep drawing of AZ31B sheets,” *Journal of Material Process and Technology*, vol. 177, p. 142, 2006.

[38] S. Yoshihara, K. Manabe and H. Nishimura, "Effect of blank holder force control in deep drawing process of magnesium alloy sheet," *Journal of Material Process Technology*, vol. 170, p. 579, 2005.

[39] L.F. Yuang, K.I. Mori and H. Tsuji, "Deformation behaviours of magnesium alloy AZ31 in cold deep drawing," *Transactions Non Ferrous Metallurgical Society China*, vol. 18, p. 86, 2008.

[40] S.P. Keeler and W.A. Backofen, "Plastic instability and fracture in sheets stretched over rigid punches," *ASM Trans. Quart.*, vol. 56, p. 25-48, 1963.

[41] E. Hsu, J. E. Carsley, and R. Verma, "Development of forming limit diagrams of aluminium and magnesium sheet alloys at elevated temperatures," *Journal of Material Engineering and Performance*, vol. 17, p. 288, 2008.

[42] Z. Gronostajski. "The constitutive equations for FEM analysis," *J. Mat. Processing Technology*, vol. 106, p. 40, 2000.

[43] A. Gavrus, E. Massoni and J. L. Cheno, "An inverse analysis using a finite element model for identification of rheological parameters," *Journal of Materials Processing Technology*, vol. 60, p. 447, 1996.

[44] A. Prakash, S.M. Weygand and H. Riedel, "Modelling the evolution of texture and grain shape in Mg alloy AZ31 using the crystal plasticity finite element method," *Computational Materials Science*, vol. 45, p. 744, 2009.

[45] S. Gall, S. Müller and W. Reimers, "Microstructure and mechanical properties of magnesium AZ31 sheets produced by extrusion," *International Journal of Materials Form*, vol. 6, p. 187, 2013.

[46] A.C.S. Reddy, S. Rajesham and P.R. Reddy, "Experimental and simulation study on the warm deep drawing of AZ31 alloy," *Advances in Production Engineering & Management*, vol. 10(3), p. 153, 2015.

[47] D.L. Atwell, M.R. Barnett and W.B. Hutchinson, "The effect of initial grain size and temperature on the tensile properties of magnesium alloy AZ31 sheet," *Materials Science and Engineering: A*, vol. 549, p. 1, 2012.

[48] W. Tang, S. Huang, D. Li and Y. Peng, “Mechanical anisotropy and deep drawing behaviours of AZ31 magnesium alloy sheets produced by unidirectional and cross rolling,” *Journal of Materials Processing Technology*, vol. 215, p. 320, 2015.

[49] S. Galla, , R.S. Coelhoc, S. Müllera, and W. Reimersb, “Mechanical properties and forming behavior of extruded AZ31 and ME21 magnesium alloy sheets,” *Materials Science and Engineering: A*, vol. 579, p. 180, 2013.

[50] X. W. Ma, F. Wang and G. Q. Zhao, “The limiting dome height tests and formability of magnesium alloy sheet AZ31B,” *Applied Mechanics and Materials* vol. 302, p. 140, 2013.

[51] Q. Yang, B. Jiang, J. Li, H. Dong, W. Liu, S. Luo and F. Pan, “Modified texture and room temperature formability of magnesium alloy sheet by Li addition,” *International Journal of Material Form*, vol. 8, p. 1, 2015.

[52] H. Zhang, W. Chenga, J. F. Fana, B. Xua and H. Dong, “Improved mechanical properties of AZ31 magnesium alloy sheets by repeated cold rolling and annealing using a small pass reduction,” *Materials Science and Engineering: A*, vol. 637, p. 243, 2015.

[53] L. Wang, G. Huang, Q. Quana, P. Bassani, E. Mostaed, M. Vedani and F. Pan, “The effect of twinning and detwinning on the mechanical property of AZ31 extruded magnesium alloy during strain-path changes,” *Materials and Design*, vol. 63, p. 177, 2014.

[54] Y. Meng, S. Fukushima, S. Sugiyama and J. Yanagimoto, “Cold formability of AZ31 wrought magnesium alloy undergoing semisolid spheroidization treatment,” *Materials Science and Engineering: A*, vol. 624, p. 148, 2015.

[55] S. Fida Hassan, M. Paramsothy, Z.M. Gasem, F. Patel, and M. Gupta, “Effect of carbon nanotube on high-temperature formability of AZ31 magnesium alloy,” *Journal of Materials Engineering and Performance*, vol. 23(8), p. 2984, 2014.

[56] M. Gupta and N. M. L. Sharon, “Magnesium, Magnesium Alloys, and Magnesium Composites,” *John Wiley & Sons Publications*, 2011.

[57] B. C. Suh, M. S. Shim, K.S. Shin and N. J. Kim, “Current issues in magnesium sheet alloys” *Scripta Materialia*, vol. 84 - 85, p. 1, 2014.

[58] D. Wu, R.S. Chena and E.H. Han, “Excellent room-temperature ductility and formability of rolled Mg–Gd–Zn alloy sheets,” *Journal of Alloys and Compounds*, vol. 509(6), p. 2856, 2011.

[59] Y. Han, Q. Zhang and B. Jiang, “Effect of additional shear stress on microstructure evolution of AZ31 sheet by differential speed rolling,” *Materials Science Forum*, vol. 816, p. 433, 2015.

[60] J. G. Kaufman, “Introduction to Aluminium Alloys and Tempers,” *ASM International publisher*, 2000.

[61] M. A. García-Bernal, R.S. Mishra, R. Verma and D. Hernández-Silva, “High strain rate superplasticity in continuous cast Al–Mg alloys prepared via friction stir processing”, *Scripta Materialia*, vol. 60, p. 580, 2009.

[62] P. Cavaliere and P. P. De. Marco, “Superplastic behaviour of friction stir processed AZ91 magnesium alloy produced by high pressure die cast,” *Material Process Technology*, vol. 184, p. 77, 2007.

[63] F. Abu-Farha and M. Khraisheh, “Modelling of Anisotropic Deformation in Superplastic Sheet Metal Stretching,” *Journal of Engineering Materials and Technology*, vol. 127(1), p. 159, 2005.

[64] H. Watari, R. Paisarn, T. Haga, K. Noda, K. Davey and N. Koga, “Development of manufacturing of wrought magnesium alloy sheets by twin roll casting,” *Journal of Achieves In Material and Manufacturing Engineering*, vol. 20(1 - 2), p. 515, 2007.

[65] F. K. Abu-Farha and M. K. Khraisheh, “On the Superplastic Forming of the AZ31 Magnesium Alloy,” *Proceedings of the 7th International Conference on*

Magnesium Alloys and their Applications, Dresden, Germany, p. 399, November 6-9, 2006.

[66] S. H. Zhang, Y. C. Xu, G. Palumbo, S. Pinto, L. Tricarico, Z. T. Wang and Q. L. Zhang, “Formability and Process Conditions of Magnesium Alloy Sheets,” *Materials Science Forum*, vol. 488 - 489, p. 453, 2005.

[67] J. She, F. S. Pan , H. H. Hu, A. T. Tang, Z. W. Yu and K. Song “Effect of Mg_2Sn intermetallic on the grain refinement in as-cast AM series alloy,” *Journal of Materials Engineering and Performance*, vol. 24(8), p. 2937, 2015.

[68] K. Suresh, K. P. Rao, Y. V. R. K. Prasad, N. Hort and K. U. Kainer, “Microstructure and mechanical properties of as-cast Mg–Sn–Ca alloys and effect of alloying elements,” *Transactions of Nonferrous Metals Society of China*, vol. 23(12), p. 3604, 2013.

[69] J. Geng and J. F. Nie, “Unloading yield effect in a twin-roll-cast Mg–3Al–1Zn alloy,” *Scripta Materialia*, vol. 100, p. 78, 2015.

[70] S. M. Zhua, M. A. Easton, M. A. Gibson, M. S. Dargusch and J. F. Nie, “Analysis of the creep behaviour of die-cast Mg–3Al–1Si alloy,” *Materials Science and Engineering: A*, vol. 578, p. 377, 2013.

[71] D. Liu, Y. Ding, T. Guo, X. Qin, C. Guo, S. Yu and S. Lin, “Influence of fine-grain and solid-solution strengthening on mechanical properties and in vitro degradation of WE43 alloy,” *Biomedical Materials*, vol. 9(1), p. 13, 2014.

[72] M. Lentz , S. Gall, F. Schmack, H. M. Mayer and W. Reimers, “Hot working behaviour of a WE54 magnesium alloy,” *Journal of Materials Science*, vol. 49(3), p. 1121, 2014.

[73] N. Tahreen, D.L. Chen, M. Nouri and D.Y. Li, “Effects of aluminium content and strain rate on strain hardening behaviour of cast magnesium alloys during compression,” *Materials Science and Engineering: A*, vol. 594, p. 235, 2014.

[74] Q. Zhang, M. Masoumi and H. Hu, “Influence of Applied Pressure on Tensile behaviour and microstructure of squeeze cast Mg alloy AM50 with Ca

addition," *Journal of Materials Engineering and Performance*, vol. 21(1), p. 38, 2015.

[75] M. Liu, D. S. Shih, C. Parish and A. Atrens, "The ignition temperature of Mg alloys WE43, AZ31 and AZ91," *Corrosion Science*, vol. 54, p. 139, 2012.

[76] A. Hadadzadeh and M. A. Wells, "Mathematical modelling of thermo-mechanical behavior of strip during twin roll casting of an AZ31 magnesium alloy," *Journal of Magnesium and Alloys*, vol. 1(2), p. 101, 2013.

[77] C. Bettles and M. Barnett, "Advances in Wrought Magnesium Alloys: Fundamentals of Processing, Properties and Applications," *Elsevier publisher*, 2012.

[78] Z. J. Yu and J. H. Li, "Temperature controlling system design of non-isothermal deep drawing mould for magnesium alloy sheet," *Advanced Materials Research*, vols. 887-888, p. 1129, 2014.

[79] M. Masoumi, F. Zarandi and M. Pekguleryuz, "Microstructure and texture studies on twin-roll cast AZ31 (Mg–3 wt.%Al–1 wt.%Zn) alloy and the effect of thermomechanical processing," *Materials Science and Engineering: A*, vol. 528(3), p. 1268, 2011.

[80] Y. Chu , J. Chen, X. Li, S. Wu and Z. Yang, "Effects of thermomechanical treatments on the microstructures and mechanical properties of GTA-welded AZ31B magnesium alloy," *International Journal of Minerals, Metallurgy, and Materials*, vol. 19(10), p. 945, 2012.

[81] K. H. Jung, Y. B. Kim, G. A. Lee, S. Lee, E. Z. Kim and D. S. Choi, "Formability of ZK60A magnesium alloy determined by compression and backward extrusion," *Materials and Manufacturing Processes*, vol. 29(2), p. 115, 2014.

[82] T. Al-Samman and X. Li, "Sheet texture modification in magnesium-based alloys by selective rare earth alloying," *Materials Science and Engineering: A*, vol. 528(10 - 11), p. 3809, 2011.

[83] H. Harada, S. I. Nishida, M. Suzuki, H. Watari and T. Haga, “Direct cladding from molten metals of aluminium and magnesium alloys using a tandem horizontal twin roll caster,” *Applied Mechanics and Materials*, vol. 772, p. 250, 2015.

[84] T. Chandra, M. Ionescu and D. Mantovani, “Formability of magnesium-lithium alloy sheet by multi-stage deep drawing,” *Materials Science Forum*, vol. 706 - 709, p. 1164, 2012.

[85]. A. Albert, W. G. Drossel, W. Zorn, W. Nendel and D. Raithel, “Process combination of hydroforming and injection moulding for the in situ manufacturing of metal and plastic composite structures,” *Materials Science Forum*, vols. 825 - 26, p. 522, 2015.

[86] G. Gottstein, “Physical Foundations of Materials Science,” *Springer Science and Business Media publisher*, 2013.

[87] J. G. Tweeddale, “The nature of materials: Materials technology,” *Elsevier*, 2013.

[88] B. Song, N. Guo, T. Liu and Q. Yang, “Improvement of formability and mechanical properties of magnesium alloys via pre-twinning: A review,” *Materials and Design*, vol. 62, p. 352, 2014.

[89] J. W. Martin, “Precipitation hardening: Theory and Applications,” *Butterworth-Heinemann*, 2012.

[90] M. Mezbahul-Islam, A. O. Mostafa, and M. Medraj, “Essential magnesium alloys binary phase diagrams and their thermochemical data,” *Journal of Materials*, vol. 14, p. 33, 2014.

[91] J. Bohlen, J. Wendt, M. Nienaber, K. U. Kainer, L. Stutz and D. Letzig, “Calcium and zirconium as texture modifiers during rolling and annealing of magnesium–zinc alloys,” *Materials Characterization*, vol. 101, p. 144, 2015.

[92] X. Wan, H. Ni, M. Huang, Y. Zhu and X. Wang, “Improvements of elevated temperature strength and creep resistance of Mg-12Zn-4Al based alloy with

calcium addition," *Journal of Shanghai Jiaotong University (Science)*, vol. 17(3), p. 273, 2012.

[93] X. Huang, K. Suzuki, Y. Chino and M. Mabuchi, "Influence of aluminium content on the texture and sheet formability of AM series magnesium alloys," *Materials Science and Engineering: A*, vol. 633(1), p. 144, 2015.

[94] J. Liao, M. Hotta, S. Motoda and T. Shinohara, "Atmospheric corrosion of two field-exposed AZ31B magnesium alloys with different grain size," *Corrosion Science*, vol. 71, p. 53, 2013.

[95] K. Illkova, P. Dobroň, F. Chmelík, K. U. Kainer, J. Balík, S. Yi, D. Letzig and J. Bohlen, "Effect of aluminium and calcium on the microstructure, texture, plastic deformation and related acoustic emission of extruded magnesium–manganese alloys," *Journal of Alloys and Compounds*, vol. 617, p. 253, 2014.

[96] J. Liao, M. Hotta and N. Yamamoto, "Corrosion behaviour of fine-grained AZ31B magnesium alloy," *Corrosion Science*, vol. 61, p. 208, 2012.

[97] S. H. Park, S. Hong, C. S. Lee, "Enhanced stretch formability of rolled Mg–3Al–1Zn alloy at room temperature by initial {10–12} twins," *Materials Science and Engineering: A*, vol. 578, p. 271, 2013.

[98] T. Matsunaga, H. Somekawa, H. Hongo and M. Tabuchi, "Deformation mechanism transition with strain rate in Mg–3Al–1Zn alloy at room temperature," *Materials Science and Engineering: A*, vol. 647, p. 212, 2015.

[99] S. Gall , M. Huppmann, H. M. Mayer, S. Müller and W. Reimers, "Hot working behavior of AZ31 and ME21 magnesium alloys," *Journal of Materials Science*, vol. 48(1), p. 473, 2013.

[100] J. Suh, J. Victoria-Hernandez, D. Letzig, R. Golle, S. Yi, J. Bohlen and W. Volk, "Improvement in cold formability of AZ31 magnesium alloy sheets processed by equal channel angular pressing, Journal of Materials Processing Technology," vol. 217, p. 286, 2015.

[101] M. Habibnejad-Korayem, M. K. Jain and R. K. Mishr, “Surface microstructure modification by wire-brushing and annealing and its effect on tensile ductility and bendability of Mg sheet,” *Materials Science Forum*, vols. 828 - 829, p. 340, Aug. 2015

[102] A. Khosravani, J. Scott, M. P. Miles, D. Fullwood, B. L. Adams and R. K. Mishra, “Twinning in magnesium alloy AZ31B under different strain paths at moderately elevated temperatures,” *International Journal of Plasticity*, vol. 45, p. 160 , 2013.

[103] X. Huang, K. Suzuki, Y. Chino and M. Mabuchi, “Texture and stretch formability of AZ61 and AM60 magnesium alloy sheets processed by high-temperature rolling,” *Journal of Alloys and Compounds*, vol. 632, p. 94 , 2015.

[104] H. L. Kim, W. K. Bang, Y. W. Chang, “Effect of initial texture on deformation behaviour of AZ31 magnesium alloy sheets under biaxial loading,” *Materials Science and Engineering: A*, vol. 552, p. 245, 2015.

[105] P. A. Juan, S. Berbenni, M. R. Barnett, C. N. Tomé and L. Capolungo, “A double inclusion homogenization scheme for poly-crystals with hierarchal topologies: application to twinning in Mg alloys,” *International Journal of Plasticity*, vol. 60, p. 182 , 2014.

[106] R. Xin, Y. Liang, C. Ding, C. Guo, B. Wang and Q. Liu, “Geometrical compatibility factor analysis of paired extension twins in extruded Mg–3Al–1Zn alloys,” *Materials and Design*, vol. 86, p. 656, 2015.

[107] S. Kim, D. Kim, K. Lee, H. Cho and H. N. Han, “Residual-stress-induced grain growth of twinned grains and its effect on formability of magnesium alloy sheet at room temperature,” *Materials Characterization*, vol. 109, p. 88 , 2015.

[108] S. M. Fatemi-Varzaneh, A. Zarei-Hanzaki, J. M. Cabrera and P. R. Calvillo, “EBSD characterization of repetitive grain refinement in AZ31 magnesium alloy,” *Materials Chemistry and Physics*, vol. 149 - 150, p. 339 , 2015.

[109] M. S. Kaiser, S. Datta, A. Roychowdhury and M. K. Banerjee, "Effect of prior cold work on tensile properties of Al–6Mg alloy with minor scandium additions," *Canadian Metallurgical Quarterly*, vol. 53(4), p. 486 , 2014.

[110] J. Scott, M. Miles, D. Fullwood, B. Adams, A. Khosravani and R. K. Mishra, "Room temperature shear band development in highly twinned wrought magnesium AZ31B Sheet," *Metallurgical and Materials Transactions A*, vol. 4(1), p. 512, 2013.

[111] Q. Yang, B. Jiang, Y. Tian, W. Liu, F. Pan, "A tilted weak texture processed by an asymmetric extrusion for magnesium alloy sheets," *Materials Letters*, vol. 100, p. 29, 2013.

[112] T. Al-Samman, "Modification of texture and microstructure of magnesium alloy extrusions by particle-stimulated recrystallization," *Materials Science and Engineering: A*, vol. 560, p. 561, 2013.

[113] G. Huang, L. Wang, H. Zhang, Y. Wang, Z. Shi, F. Pan, "Evolution of neutral layer and microstructure of AZ31B magnesium alloy sheet during bending," *Materials Letters*, vol. 98, p. 47, 2013.

[114] R. D. Kamachali, S. Kim, I. Steinbach, "Texture evolution in deformed AZ31 magnesium sheets: Experiments and phase-field study," *Computational Materials Science*, vol. 104, p. 193, 2015.

[115] D. Kim, K. Lee, J. Lee, Y. Yoon and H. Son, "Evolution of microstructures and textures in magnesium AZ31 alloys deformed by normal and cross-roll rolling," *Materials Letters*, vol. 75, p. 122, 2012.

[116] M. Pekguleryuz, M. Celikin, M. Hoseini, A. Becerra and L. Mackenzie, "Study on edge cracking and texture evolution during 150 °C rolling of magnesium alloys: The effects of axial ratio and grain size," *Journal of Alloys and Compounds*, vol. 510(1), p. 15, 2012.

[117] M. O. Pekguleryuz, K. Kainer and A. Kaya, "Fundamentals of Magnesium Alloy Metallurgy," *Elsevier publisher*, 2013.

[118] Y. Chino, X. Huang, K. Suzuki, M. Yuasa and M. Mabuchi, "Texture formation and room-temperature formability of rolled Mg–Zn–Ce alloys, Material Transactions, vol. 55(8), p. 1190, 2014.

[119] N. Stanford, M.D. Callaghan, B.de Jong, "The effect of rare earth elements on the behaviour of magnesium-based alloys: Part 1—Hot deformation behaviour," *Materials Science and Engineering: A*, vol. 565, p. 459, 2013.

[120] I. Basu and T. Al-Samman, "Triggering rare earth texture modification in magnesium alloys by addition of zinc and zirconium," *Acta Materialia*, vol. 67, p. 116, 2014.

[121] J. Xua, M. Shirooyeh, J. Wongsa-Ngam, D. Shan, B. Guo and T. G. Langdon, "Hardness homogeneity and micro-tensile behavior in a magnesium AZ31 alloy processed by equal-channel angular pressing," *Materials Science and Engineering: A*, vol. 586, p. 108, 2013.

[122] R. B. Figueiredo and T. G. Langdon, "Evaluating the Superplastic Flow of a Magnesium AZ31 Alloy Processed by Equal-Channel Angular Pressing," *Metallurgical and Materials Transactions A*, vol. 45(8), p. 3197, 2014.

[123] R. B. Figueiredo, M. Teresa, P. Aguilar, P. R. Cetlin and T. G Langdon, "Processing magnesium alloys by severe plastic deformation," *IOP Conference Series: Materials Science and Engineering*, vol. 63, p. 1, 2014.

[124] D. Zhang, F. Xiong, W. Zhang, C. Qiu, W. Zhang, "Superplasticity of AZ31 magnesium alloy prepared by friction stir processing," *Transactions of Nonferrous Metals Society of China*, vol. 21(9), p. 1911, 2011.

[125] R. B. Figueiredo and T. G. Langdon, "Influence of rolling direction on flow and cavitation in a superplastic magnesium alloy processed by equal-channel angular pressing," *Materials Science and Engineering: A*, vol. 556, p. 211, 2012.

[126] L. Raquel C. Malheiros, R. B. Figueiredo and T. G. Langdon, "Grain size and micro-hardness evolution during annealing of a magnesium alloy processed by

high-pressure torsion," *Journal of Materials Research and Technology*, vol. 4(1), p. 14, 2015.

[127] F. Berge, L. Kruger, H. Ouaziz and C. Ullrich, "Influence of temperature and strain rate on flow stress behaviour of twin-roll cast, rolled and heat-treated AZ31 magnesium alloys," *Transactions of Nonferrous Metals Society of China*, vol. 25(1), p. 1, 2015.

[128] T. J. Lee, Y. B. Park and W. J. Kim, "Importance of diffusional creep in fine grained Mg–3Al–1Zn alloys," *Materials Science and Engineering: A*, vol. 580, p. 133, 2013.

[129] Y. Chino, R. Kishihara, K. Shimojima, H. Hosokawa, Y. Yamada, C. Wen, H. Iwasaki and M. Mubuchi, "Superplasticity and cavitation of recycled AZ31 magnesium alloy fabricated by solid recycling process," *Material Transactions*, vol. 43, p. 2437, 2002.

[130] C. Chang, C. Lee and J. Huang, "Cavitation Characteristics in AZ31 Mg Alloys During LTSP or HSRSP," *Scripta Materialia*, vol. 51 p. 509, 2004.

[131] M. A. Wen-yu, B. Wang, L. Fu, J. Zhou, M. Huang, "Effect of friction coefficient in deep drawing of AA6111 sheet at elevated temperatures," *Transactions of Nonferrous Metals Society of China*, vol. 25(7), p. 2342, 2015.

[132] E. C. Ashby and R. D. Schwartz, "Reactions of lithium, sodium, and potassium hydrides with magnesium halides in ether solvents. Convenient and economic route to reactive magnesium hydride," *ACS Publications*, vol. 10(2), p. 355, 1971.

[133] K. Matsubara, Y. Miyahara, Z. Horita and T.G. Langdon, "Developing superplasticity in a magnesium alloy through a combination of extrusion and ECAP," *Acta Materialia*, vol. 51(27), p. 3073, 2003.

[134] M. Merklein, A. Maier, D. Kinnstätter, C. Jaremenko and E. Affronti, "A new approach to the evaluation of forming limits in sheet metal forming," *Key Engineering Materials*, vol. 639, p. 333, 2015.

[135] K. Wu, S. Chang and J. Yeh, “Optimizing superplasticity of AZ91−xSn magnesium alloys with competitive grain growth and boundary sliding,” *Materials Science and Engineering: A*, vol. 646, p. 201, 2015.

[136] T.J. Lee and W.J. Kim, “The significant effect of adding trace amounts of Ti on the high-temperature deformation behaviour of fine-grained Mg–6Al–1Zn magnesium alloys,” *Journal of Alloys and Compounds*, vol. 617, p. 352, 2014.

[137] Y. H. Kim and W. J. Kim, “Flame-resistant Ca-containing AZ31 magnesium alloy sheets with good mechanical properties fabricated by a combination of strip casting and high-ratio differential speed rolling methods,” *Metals and Materials International*, vol. 21(2), p. 374, 2015.

[138] H. Somekawa, K. Hirai, H. Watanabe, Y. Takigawa and K. Higashi, “Dislocation creep behavior in Mg–Al–Zn alloys,” *Materials Science and Engineering: A*, vol. 407(1 - 2), p. 53, 2005.

[139] F.R. Cao, H. Ding, Y.L. Li, G. Zhou and J.Z. Cui, “Superplasticity, dynamic grain growth and deformation mechanism in ultra-light two-phase magnesium–lithium alloys,” *Materials Science and Engineering: A*, vol. 527(9), p. 2335, 2010.

[140] V. Srivastava, K. R. McNee, G. W. Greenwood and H. Jones, “Creep behaviour of AZ61 magnesium alloy at low stresses and intermediate temperatures,” *Materials Science and Technology*, vol. 20(1), p. 42, 2004.

[141] H. Watanabe, H. Tsutsui, T. Mukai, M. Kohzu, S. Tanabe and K. Higashi “Deformation mechanism in a coarse-grained Mg–Al–Zn alloy at elevated temperatures,” *International Journal of Plasticity*, vol. 17(3), p. 387, 2001.

[142] W.J. Kim, S.W. Chung, C.S. Chung and D. Kum, “Superplasticity in thin magnesium alloy sheets and deformation mechanism maps for magnesium alloys at elevated temperatures,” *Acta Materialia*, vol. 49(16), p. 3337, 2001.

[143] P. S. Roodposhti, A. Sarkar and K. L. Murty, “Microstructural development of high temperature deformed AZ31 magnesium alloys,” *Materials Science and Engineering: A*, vol. 626, p. 195, 2015.

[144] P. Nautiyal, J. Jain and A. Agarwal, “A comparative study of indentation induced creep in pure magnesium and AZ61 alloy,” *Materials Science and Engineering: A*, vol. 630, p. 131, 2015.

[145] T. G. Langdon, D. Simpson and R. C. Gifkins, “Grain boundary sliding at high temperatures in torsional fatigue,” *Journal of Materials Science Letters*, vol. 2(1), p. 25, 1983.

[146] C. Poletti, M. Rodriguez-Hortalá, M. Hauser and C. Sommitsch, “Microstructure development in hot deformed AA6082,” *Materials Science and Engineering: A*, vol. 528(6), p. 2423, 2011.

[147] A. Ball and M.M. Hutchison, “Superplasticity in the Aluminium-Zinc Eutectoid,” *Journal of Material Science*, vol. 3, p. 1, 1969.

[148] T. G. Langdon, “Grain boundary sliding as a deformation mechanism during creep,” *Philosophical Magazine*, vol. 22(178), p. 18, 1970.

[149] A. K. Mukherjee, “The rate controlling mechanism in superplasticity,” *Materials Science and Engineering*, vol. 8(2), p. 83, 1971.

[150] R. C. Gifkins, “Grain-boundary sliding and its accommodation during creep and superplasticity,” *Metallurgical Transactions A*, vol. 7(8), p. 1225, 1976.

[151] H. W. Hayden, S. Floreen, and P.D. Goodall, “The deformation mechanisms of superplasticity,” *Metallurgical Transactions*, vol. 3(4), p. 833, 1972.

[152] J. H. Gittus, “Theory of superplastic flow in two-phase materials: Roles of interphase boundary dislocations, ledges, and diffusion,” *Trans. ASME- Journal of Engineering Materials and Technology*, vol. 99, p. 244, 1977.

[153] A. Arieli and A. K. Mukherjee, “A model for the rate-controlling mechanism in superplasticity,” *Materials Science and Engineering*, vol. 45(1), p. 61, 1980.

[154] O. D. Sherby and J. Wadsworth, “Development and characterization of fine grain superplastic materials, in deformation processing and structure,” *ASM, Metal Park, Ohio,* p. 355, 1984.

[155] O. A. Kaibyshev, R. Z. Valiev, and A. K. Emaletdinov, “Deformation mechanisms and the theory of structural superplasticity of metals,” *Physica Status Solidi*, vol. 90, p. 197, 1985.

[156] H. Fukuyo, H. C. Tsai, T. Oyama, and O. D. Sherby, “Superplasticity and Newtonian-viscous flow in fine-grained class I solid solution alloys,” *ISIJ International*, vol. 31, p.76, 1991.

[157] H. Zhanga, G. Huang, J. Fan, H. J. Roven, F. Pan and B. Xu, “Deep drawability and deformation behaviour of AZ31 magnesium alloy sheets at 473 K,” *Materials Science and Engineering: A*, vol. 608, p. 234, 2014.

[158] P. Hildenbrand, T. Schneider and M. Merklein, “Flexible rolling of process adapted semi-finished parts and its application in a sheet-bulk metal forming process,” *Key Engineering Materials*, vol. 639, p. 259, Mar. 2015.

[159] P. S. Bate, K.B. Hyde, S.A. Court and J. F. Humphreys, “Dynamic grain growth in superplastic and non-superplastic aluminium alloys,” *Materials Science Forum*, vol. 447 - 448, p. 61, 2004.

[160] H. G. Tattersall and F. J. P. Clarke, “Slip distribution and fracture in magnesium oxide,” *Philosophical Magazine*, vol. 7(84), 1962.

[161] S. Song, X. Zhou, L. Li, W. Ma, “Numerical simulation and experimental validation of SiC nanoparticle distribution in magnesium melts during ultrasonic cavitation based processing of magnesium matrix nanocomposites,” *Ultrasonics Sonochemistry*, vol. 24, p. 43, 2015.

[162] P. P. Bhingole, V. Tomer and U. N. Sharma, “An Investigation on the tribological behaviour of ultrasonically processed carbon black inoculated AZ31 magnesium alloys,” *Materials Today: Proceedings*, vol. 2(4 - 5), p. 1487, 2015.

[163] X. J. Wang, N. Z. Wang, L. Y. Wang, X. S. Hu, K. Wu, Y. Q. Wang and Y. D. Huang, "Processing, microstructure and mechanical properties of micro-SiC particles reinforced magnesium matrix composites fabricated by stir casting assisted by ultrasonic treatment processing," *Materials and Design*, vol. 57, p. 638, 2014.

[164] C. Fang, L. Wang, H. Hao and X. Zhang, "Distribution of TiB2 reinforcements in magnesium matrix composites by a multi-physical coupling field," *Journal of Materials Processing Technology*, vol. 214(3), p. 551, 2014.

[165] N. Horiike, S. Yoshihara, Y. Tsuji and Y. Okude, "Effect of blank holder force with low frequency vibration technique in circular-cup deep-drawing using AZ31 magnesium alloy sheet," *Advanced Materials Research*, vols. 383 - 390, p. 2785, 2011.

[166] S. X. Lin, J. Gao, J. H. Gong and C. L. Zhang, "Drawing behaviours of ME20 and ZE10 sheets under mechanical press," *Applied Mechanics and Materials*, vols. 229-231, p. 2497, 2012.

[167] A. Jambor and M. Beyer, "New cars – new materials," *Materials & Design*, vol. 18(4 - 6), p. 203, 1997.

[168] S. Schumann and F. Friedrich, "The use of magnesium in cars - Today and in the Future," *Magnesium Alloys and their Applications, Wolfsburg Germany*, p. 28, 1998.

[169] T. Burk and W. Vogel, "Lightweight materials for automotive structures," *Materials Week 2002, International Congress Centre, Munich, Germany*, September 30th - October 02nd, 2002.

[170] T. Katahira, T. Naka, M. Kohzu and F. Yoshida, "Forming limit of AZ31 magnesium alloy sheet under non-proportional deformation at elevated temperature," *Key Engineering Materials*, vols. 535-536, p. 292, 2013.

[171] H. Zhang, G. S. Huang, J. H. Lin and L. F. Wang, "Influence of annealing temperature on microstructure and properties of warm-rolled AZ31 magnesium alloy sheets," *Materials Science Forum*, vols. 747-748, p. 352, 2013.

[172] T. C. Lowe and R. Z. Valiev, "Producing nanoscale microstructures through severe plastic deformation," *Journal of Materials*, vol. 52(4), p. 27, 2000.

[173] K. Nakashima, Z. Horita, M. Nemoto and T.G. Langdon, "Development of a multi-pass facility for equal-channel angular pressing to high total strains," *Mater. Sci. Eng.*, vol. 281, p. 82, 2000.

[174] Y. Saito, H. Utsunomiya, N. Tsuji and T. Sakai, "Novel ultra-high straining process for bulk materials—development of the accumulative roll-bonding (ARB) process," *Acta Materialia*, vol. 47, p. 579, 1999.

[175] J. A. del Valle, F. Carreno and O. A. Ruano, "Influence of texture and grain size on work hardening and ductility in magnesium-based alloys processed by ECAP and rolling," *Acta Materialia*, vol. 54, p. 4247, 2006.

[176] Y. Kwon, N. Saito and I. Shigematsu, "Friction stir process as a new manufacturing technique of ultrafine grained aluminum alloy," *Journal of Material Science Letters*, vol. 21, p. 1473, 2001.

[177] R. Zettler, A. Blanco J. Santos and S. Marya, "Study on dissimilar friction stir welds between Al and Mg alloys," *Magnesium Technology TMS.*, p. 409, 2005.

[178] P. Kaldunski and L. Kukielka, "Numerical analysis and simulation of drawpiece forming process by finite element method," *Applied Mechanics and Materials*, vol. 474, p. 153, 2014.

[179] X. Wu and Y. Liu, "Superplasticity of coarse-grained magnesium alloy," *Scripta Materialia*, vol. 46 p. 269, 2002.

[180] H. Q. Liu, Z. L. Mi, S. P. Hu and Z. Wang, "The study on the thermal formability of AZ31 magnesium alloy sheets," *Advanced Materials Research*, vols. 476-478, p. 592, 2012.

[181] R. Z. Valiev, N. A. Krasilnikov and N. K. Tsenev, “Plastic deformation of alloys with submicron-grained structure,” *Material Science Engineering,* vol. 137, p. 35, 1991.

[182] R. D. Doherty, D. A. Hughes, F. J. Humphreys, J. J. Jonas, D. Juul Jensen, M. E. Kassner, W. E. King, T. R. McNelley, H. J. McQueen and A. D. Rollett, “Current issues in recrystallization: a review,” *Materials Science and Engineering: A*, vol. 238, p. 219, 1997.

[183] R. Z. Valiev and T. G. Langdon, “Principles of equal-channel angular pressing as a processing tool for grain refinement,” *Progress in Materials Science*, vol. 51(7), p. 881, 2006.

[184] H.P. Pu, F.C. Liu and C. Huang, “Characterization and analysis of low temperature in 8090 Al-Li Alloys,” *Metal and Materials Transactions*, vol. 26, p. 1153, 1995.

[185] H.P. Pu and J.C. Huang, “Low temperature superplasticity in 8090 Al-Li alloys,” *Scripta Metallurgica et Materialia*, vol. 28, p.1125, 1993.

[186] M. Mabuchi, K. Kubota and K. Higashi, “New recycling process by extrusion for mechanical chips of AZ91 magnesium and mechanical properties of extruded bars,” *Material Transactions,* vol. 36, p. 1249, 1995.

[187] M. Mabuchi, M. Asahina, T. Iwasaki and H. Higashi, “Experimental investigation of superplastic behaviour in magnesium alloys,” *Material Science and Technology*, vol. 13, p. 825, 1997.

[188] J. Qiao, Y. Wang, G. D. Shi, B. X. Nie, "Enhanced tensile ductility of AZ80 magnesium alloy," *Advanced Materials Research*, vol. 284 - 286, p. 1635, 2011.

[189] T. Pasang, V. Satanin, M. Ramezani, M. Waseem, T. Neitzert, “Formability of magnesium alloys AZ80 and ZE10,” *Key Engineering Materials*, vol. 622 - 623, p. 284, 2014.

[190] J. K. Solberg, J. Torklep, O. Bauger and H. Gjestland, "Superplasticity in magnesium alloy AZ91," *Material Science Engineering*, vol. A134, p. 1201, 1991.

[191] Y. Chino, J. Lee, K. Sassa, A. Kamiya and M. Mabuchi, "Press formability of a rolled AZ31 Mg alloy sheet with controlled texture," *Materials Letters*, vol. 60(2), p. 173, 2006.

[192] Y. Chino, M. Mabuchi, R. Kishihara, H. Hosokawa, Y. Yamada, C. Wen, K. Shimojima and H. Iwasaki, "Mechanical Properties and Press Formability at Room Temperature of AZ31 Mg Alloy Processed by Single Roller Drive Rolling," *Materials Transactions*, vol. 43(10), p. 2554, 2002.

[193] M. Mabuchi, K. Kubota and K. Higashi, "New recycling process by extrusion for machined chips of AZ91 magnesium and mechanical properties of extruded bars," *Journal of Inorganic Materials*, vol. 36, p. 1249, 1995.

[194] H. K. Lin and J. C. Huang, "High strain rate and / or low temperature superplasticity in AZ31 Mg alloys processed by simple high-ratio extrusion methods," *Materials Transactions*, vol. 43(10), p. 2424, 2002.

[195] R. G. Chang, "Application of Expert System in axis-symmetric stamping process design, Master Thesis, Tsing Hua University, 2000.

[196] J. Kaneko, M. Sugamata and N. Hisata, "Superplastic properties of rapidly solidified Mg-Al-Zn alloys," *Materials Science Forum*, vols. 304 - 306, p. 85, 1999.

[197] H. Watanabe, T. Mukai, K. Ishikawa, Y. Okanda and K. Higashi, "Grain size control of commercial wrought Mg-Al-Zn alloys utilizing dynamic recrystallization," *Journal of Japan Institute of Light Metals*, vol. 49, p. 401, 1999.

[198] A. Bussiba, A. B. Artzy, A. Shtechman, S. Ifergan and M. Kupiec, "Grain refinement of AZ31 and ZK60 Mg alloys — towards superplasticity studies," *Material Science Engineering*, vol. A302, p. 56, 2001.

[199] J. Koike, T. Kobayashi, T. Mukai, H. Watanabe, M. Suzuki, K. Maruyamaa, K. Higashic, “The activity of non-basal slip systems and dynamic recovery at room temperature in fine-grained AZ31B magnesium alloys,” *Acta Materialia*, vol. 51(7), p. 2055, 2003.

[200] H.Watanabe, T. Mukai, M. Kohzu, S. Tanabe and K. Higashi, “Effect of temperature and grain size on the dominant diffusion process for superplastic flow in an AZ61 magnesium alloy,” *Acta Materialia*, vol. 47(14), p. 3753, 1999.

[201] M. Mabuchi, H. Jeong, K. Hiraga and K. Higashi, “Partial melting at interfaces and grain boundaries for high-strain-rate superplastic materials,” *Interface Science*, vol. 4, p. 357, 1997.

[202] H. Watanabe, T. Mukai and K. Higashi, “Superplasticity in a ZK60 magnesium alloy at low temperatures,” *Scripta Materialia*, vol. 40(4), p. 477, 1999.

[203] H. Watanabe, T. Mukai and K. Ishikawa, “Differential speed rolling of an AZ31 magnesium alloy and the resulting mechanical properties,” *Journal of Material Science*, vol. 39, p. 1477, 2004.

[204] H. Watanabe, T. Mukai, K. Ishikawaa and K. Higashi, “Low temperature superplasticity of a fine-grained ZK60 magnesium alloy processed by equal-channel-angular extrusion,” *Scripta Materialia*, vol. 46(12), p. 851, 2002.

[205] H. Watanabe, T. Mukai, M. Mabuchi and K. Higashi, “High-strain-rate superplasticity at low temperature in a ZK61 magnesium alloy produced by powder metallurgy,” *Scripta Materialia*, vol. 41(2), p. 209, 1999.

[206] L. C. Chan and X. Z. Lu, “Material sensitivity and formability prediction of warm-forming magnesium alloy sheets with experimental verification,” *The International Journal of Advanced Manufacturing Technology*, vol. 71(1), p. 253, 2014.

[207] W. C. Kim, J. G. Kim, J. Y. Lee and H. K. Seok, “Influence of Ca on the corrosion properties of magnesium for biomaterials,” *Materials Letters*, vol. 62(25), p. 4146, 2008.

[208] M. G. Lee, R. H. Wagoner, J. K. Lee, K. Chung and H. Y. Kim, “Constitutive modelling for anisotropic/asymmetric hardening behaviour of magnesium alloy sheets,” *International Journal of Plasticity*, vol. 24(4), p. 545, 2008.

[209] H. Fuji, H. Iwasaki and J. K. Araki, “Press forming technology using superplastic deformation for Mg alloy sheet,” *Materials Science Forum*, vol. 488 - 489, p. 571, 2005.

[210] J. M. P. Martins, J. L. Alves, D. M. Neto, M. C. Oliveira and L. F. Menezes, “Numerical analysis of different heating systems for warm sheet metal forming,” *The International Journal of Advanced Manufacturing Technology*, vol. 1, p. 1, 2015.

[211] T. Naka, T. Uemori, R. Hino, M. Kohzu, K. Higashi and F. Yoshida, “Effects of strain rate, temperature and sheet thickness on yield locus of AZ31 magnesium alloy sheet,” *Journal of Materials Processing Technology,* vol. 201(1 - 3), p. 395, 2008.

[212] E. Doege and K. Droder, “Sheet metal forming of magnesium wrought alloys formability and process technology,” *J. Mater. Process. Technol.*, vol. 115, p. 14, 2001.

[213] D. Letzig, J. Suh, J. Bohlen, S. Yi, G. Kurz, R. Golle, W. Volk and J. Victoria-Hernandez, “On the development of Mg sheets with improved formability by applying additional shear strain during processing,” *Materials Science Forum*, vol. 828 - 829, p. 395, 2015.

[214] K. Manabe, H. Koyama, S. Yoshihara and T. Yagami, “Development of a combination punch speed and blank-holder fuzzy control system for the deep-drawing process,” *Journal of Materials Processing Technology,* vol. 125 - 127, p. 440, 2002.

[215] S. Lee, Y. H. Chen and J. Y. Wang, “Isothermal sheet formability of magnesium alloy AZ31 and AZ61,” *Journal of Materials Processing Technology*, vol. 124(1 - 2), p. 19, 2002.

[216] K. Manabe, M. Yang and S. Yoshihara, "Artificial intelligence identification of process parameters and adaptive control system for deep-drawing process," *Journal of Materials Processing Technology*, vol. 80 - 81, p. 421, 1998.

[217] E. Doege and K. Droder, "Sheet metal forming of wrought magnesium alloys-formability and process technology," *Journal of Materials Processing Technology*, vol. 115(1), p. 14, 2001.

[218] M. Sellars and J. Whiteman, "Recrystallization and grain growth in hot rolling," *Material Science*, vol. 13, p. 187, 1979.

[219] K. F. Zhang, D. L. Yin and D. N. Wu, "Formability of AZ31 magnesium alloy sheets at warm working conditions," *International Journal of Machine Tools and Manufacture*, vol. 46(11), p. 1276, 2006.

[220] K. Dröder and S. Janssen, "Forming of magnesium alloys - A solution for light weight construction," *SAE International*, vol. 10, p. 4271, 1999.

[221] S. Yoshihara, H. Nishimura, H. Yamamoto and K. Manabe, "Formability enhancement in magnesium alloy stamping using a local heating and cooling technique, circular cup deep drawing process," *Journal of Materials Processing Technology*, vol. 142(3), p. 609, 2003.

[222] H. Somekawa, M. Kohzu, S. Tanabe and K. Higashi, "The press formability in magnesium alloy AZ31," *Materials Science Forum*, vol. 350 - 351, p. 177, 2000.

[223] Y. Chino, M. Mabuchi, K. Shimojima, Y. Yamada, C. Wen, K. Miwa, M. Nakamura, T. Asahina, K. Higashi and T. Aizawa, "Forging Characteristics of AZ31 Mg Alloy," *Material Transactions*, vol. 42, p. 414, 2001.

[224] Y. C. Shao, T. Tang, D. Y. Li, Y. H. Peng, "Simulation of the extrusion texture of magnesium alloy AZ31 using crystal plasticity finite element method," *Materials Science Forum*, vol. 817, p. 538, Apr. 2015.

[225] G. Palumbo, D. Sorgente, L. Tricarico , S. H. Zhang and W. T. Zheng, "Numerical and experimental investigations on the effect of the heating strategy

and the punch speed on the warm deep drawing of magnesium alloy AZ31," *Journal of Materials Processing Technology*, vol. 191, p. 342, 2007.

[226] Y. Tsuji, S. Yoshihara, S. Tsuda, Y. Iriyama and Y. Nakano, "Effect of DLC coating on Limiting drawing ratio of AZ31 magnesium alloy sheet," *Design and Manufacturing*, vol. 4, p. 313, 2009.

[227] S. Tsuda, S. Yoshihara and S. Kataoka, "Formability of AZ31 Magnesium Alloy Sheet in Dry Press Forming Using Diamond-Coated Dies," *Design and Manufacturing,* vol. 4, p. 15, 2009.

[228] M. Kohzu, T. Hironaka, S. Nakatsuka, N. Saito, F. Yoshida, T. Naka, H. Okahara and K. Higashi, "Effect of texture of AZ31 magnesium alloy sheet on mechanical properties and formability at high strain rate," *Materials transactions*, vol. 48(4), p. 764, 2007.

[229] J. P. Nobre, U. Noster, M. Kornmeier, A. M. Dias and B. Scholtes, "Deformation asymmetry of AZ31 wrought magnesium alloy," *Key Engineering Materials*, vols. 230 - 232, p. 267, Oct. 2002.

[230] Z. Hua, H. G. Sheng, S. Bo, Z. Lei and K. D. Qiang, "Influence of initial texture on formability of AZ31B magnesium alloy sheets at different temperatures," *Journal of Materials Processing Technology*, vol. 211(10), p. 1575, 2011.

[231] F. Chen and T. Huang, "Formability of stamping magnesium-alloy AZ31 sheets," *Journal of Materials Processing Technology*, vol. 142(3), p. 643, 2003.

[232] M. Jain, J. Allin and M. J. Bull, "Deep drawing characteristics of automotive aluminium alloys," *Materials Science and Engineering A,* vol. 256(1 - 2), p. 69, 1998.

[233] Q. F. Chang, D. Y. Li, Y. H. Peng and X. Q. Zeng, "Experimental and numerical study of warm deep drawing of AZ31 magnesium alloy sheet," *International Journal of Machine Tools and Manufacture*, vol. 47(3 - 4), p. 436, 2007.

[234] S. Yoshihara, “Corrosion behaviour of AZ31 magnesium alloy sheet in flow field of 0.9wt% NaCl sodium chloride solution,” *16th International conference on advances in material processing technologies*, 2013.

[235] L.M. Ren, S.H. Zhang, G. Palumbo, D. Sorgente and L. Tricarico, “Numerical simulation on warm deep drawing of magnesium alloy AZ31 sheets,” *Materials Science and Engineering: A*, vol. 15, p. 40, 2009.

[236] H. Watanabe, T. Mukai and K. Ishikawa, “Effect of temperature of differential speed rolling on room temperature mechanical properties and texture in an AZ31 magnesium alloy,” *Journal of Materials Processing Technology*, vol. 182(1 - 3), p. 644, 2007.

[237] X. S. Huang, K. Suzuki, A. Watazu, I. Shigematsu and N. Saito, “Improvement of formability of Mg-Al-Zn alloy sheet at low temperature using differential speed rolling,” *Journal of Alloys and Compounds*, vol. 470(1 - 2), p. 263, 2009.

[238] K. Iwanaga, H. Tashiro, H. Okamoto and K. Shimizu, “Improvement of formability from room temperature to warm temperature in AZ31 magnesium alloy,” *Journal of Materials Processing Technology*, vol. 155 - 156, p. 1313, 2004.

[239] Y. Q. Cheng, Z. Hua, W. J. Xia and T. Zhou, “Effect of channel clearance on crystal orientation development in AZ31 magnesium alloy sheet produced by equal channel angular rolling,” *Journal of Materials Processing Technology*, vol. 184(1 - 4), p. 97, 2007.

[240] Y. S. Bohlen, J. Bohlen, F. Heinemann and F. Letzig, “Mechanical anisotropy and deep drawing behaviour of AZ31 and ZE10 magnesium alloy sheets,” *Acta Materialia*, vol. 58(2), p. 592, 2010.

[241] S. B. Yi, D. Letzig, K. Hantzsche, R. G. Martinez, J. Bohlen, I. Schestakow and S. Zaefferer, “Improvement of Magnesium Sheet Formability by Alloying Addition of Rare Earth Elements,” *Materials Science Forum*, vol. 638 - 642, p. 1506, 2010.

[242] U. F. Kocks, C. N. Tomé and H. R. Wenk, “Texture and anisotropy,” *Cambridge University Press*, Cambridge, 1998.

[243] M. J. Philippe, “Texture formation in hexagonal materials,” *Materials Science Forum*, vol. 157 - 162, p. 1337, 1994.

[244] F. Kaiser, D. Letzig, J. Bohlen, A. Styczynski, C. Hartig and K. U. Kainer, “Anisotropic Properties of Magnesium Sheet AZ31,” *Materials Science Forum*, vol. 419 - 422, p. 315, 2003.

[245] A. Styczynski, C. Hartig, J. Bohlen and D. Letzig, “Cold rolling textures in AZ31 wrought magnesium alloy,” *Scripta Materialia*, vol. 50(7), p. 943, 2004.

[246] L. M. Ren, S. H. Zhang, G. Palumbo and L. Tricarico, “Warm deep drawing of magnesium alloy sheets-formability and process conditions,” *Journal of Engineering Manufacture*, vol. 222(11), p. 1347, 2008.

[247] R. C. Zeng, W. Dietzel, J. Chen, W. J. Huang and J. Wang, “Corrosion behaviour of TiO2 coating on magnesium alloy AM60 in Hank’s solution,” *Key Engineering Materials*, Vols. 373 - 374, p. 609, 2008.

[248] D. V. Hai, S. Itoh, T. Sakai, S. Kamado and Y. Kojima, “Experimentally and numerical study on deep drawing process for magnesium alloy sheet at elevated temperatures,” *Materials Transactions*, vol. 49(5), p. 1101, 2008.

[249] A. C. S. Reddy, S. Rajesham and P. R. Reddy, “Experimental and simulation study on the warm deep drawing of AZ31 alloy,” *Advances in Production Engineering & Management*, vol. 10(3), p. 153, 2015.

[250] J. Bohlen, D. Letzig and K. U. Kainer, “New perspectives for wrought magnesium alloys,” *Materials Science Forum*, vols. 546 - 549, p. 1, 2007.

[251] S. Yoshihara, B. J. MacDonald, H. Nishimura, H. Yamamoto and K. Manabe, “Optimisation of magnesium alloy stamping with local heating and cooling using the finite element method,” *Journal of Materials Processing Technology*, vol. 153 - 154, p. 319, 2004.

[252] H. Palaniswamy, G. Ngaile and T. Altan, “Finite element simulations of magnesium alloy sheet forming at elevated temperatures,” *Journal of Materials Processing Technology*, vol. 146(1), p. 52, 2004.

[253] Y. T. Gu, “An adaptive local meshfree updated lagrangian approach for large deformation analysis of metal forming,” *Advanced Materials Research*, vols. 97-101, p. 2664, 2010.

[254] H. Palaniswamy, G. Ngaile and T. Altan, “Finite element simulation of magnesium alloy sheet forming at elevated temperatures,” *Journal of Materials Processing Technology*, vol. 146(1), p. 52, 2004.

[255] D. B. Zhu, “Newest progress on the spring-back’s study of plate forming,” *Journal Plastics Engineering 1*, p. 11, 2000.

[256] Y. H. Moon, S. S. Kang, J. R. Cho and T. G. Kim, “Effect of tool temperature on the reduction of the spring-back of aluminium sheets,” *Journal of Materials Processing Technology*, vol. 132(1 - 3), p. 365, 2003.

[257] L. Marretta and R. D. Lorenzo, “Influence of material properties variability on spring-back and thinning in sheet stamping processes: A stochastic analysis,” *The International Journal of Advanced Manufacturing Technology*, vol. 51(1 - 4), p. 117, 2010.

[258] X. Li, Y. Yang, Y. Wang, J. Bao and S. Li, “Effect of the material hardening mode on the spring-back simulation accuracy of V-free bending,” *Journal of Materials Processing Technology*, vol. 123(2), p. 209, 2002.

[259] T. J. Gau and L. G. Kinzel, “A new model for spring-back prediction in which the bauschinger effect is considered,” *International Journal of Mechanical Sciences*, vol. 43(8), p. 1813, 2001.

[260] H. Y. Yu, “Variation of elastic modulus during plastic deformation and its influence on spring-back,” *Materials and Design*, vol. 30(3), p. 846, 2009.

[261] L. Geng and R. H. Wagoner, “Role of plastic anisotropy and its evolution on spring-back,” *International Journal of Mechanical Sciences*, vol. 44(1), p. 123, 2002.

[262] I. Ragai, D. Lazim and J. A. Nemes, “Anisotropy and spring-back in draw-bending of stainless steel 410, experimental and numerical study,” *Journal of Materials Processing Technology*, vol. 166(1), p. 116, 2005.

[263] T. Hama, Y. Kariyazaki, K. Ochi, H. Fujimoto and H. Takuda, “Spring-back characteristics of magnesium alloy sheet AZ31B in draw-bending,” *Materials Transactions*, vol. 51(4), p. 685, 2009.

[264] H. J. Kim, S. C. Choi, K. T. Lee and H. Y. Kim, “Experimental determination of forming limit diagram and spring-back characteristics of AZ31B Mg alloy sheets at elevated temperatures,” *Materials Transactions*, vol. 49(5), p. 1112, 2008.

[265] R. K. Verma and A. Haldar, “Effect of normal anisotropy on spring-back,” *Journal of Materials Processing Technology*, vol. 190(1 - 3), p. 300, 2007.

[266] S. L. Zang, “A new model to describe effect of plastic deformation on elastic modulus of aluminium alloy,” *Transactions of Nonferrous Metals Society of China*, vol. 16, p. 1314, 2006.

[267] S. K. Paul, “Theoretical analysis of strain- and stress-based forming limit diagrams,” *Journal of strain analysis*, vol. 48(3), p. 177, 2013.

[268] G. Palumbo, D. Sorgente and L. Tricarico, “A numerical and experimental investigation of AZ31 Formability at elevated temperature using a constant strain rate test,” *Materials and Design*, vol. 31(3), p. 1308, 2010.

[269] ASTM E 2218-02, “Standard test method for determining forming limit curves,” p. 151, 2013.

[270] E. Hsu, J. E. Carsley and R. Verma, “Development of forming limit diagrams of aluminium and magnesium sheet alloys at elevated temperatures,” *Journal of materials engineering and performance*, vol. 17(3), p. 288, 2008.

[271] K. S. Raghavan and Jr W. M. Garrison, "An investigation of the relative effects of thickness and strength on the formability of steel sheet," *Material Science and Engineering: A*, vol. 527, p. 5565, 2010.

[272] A. R. Ragab, "Prediction of fracture limit curves in sheet metals using a void growth and coalescence model," *Journal of Material Processes and Technology*, vol. 199, p. 206, 2008.

[273] E. Hsu, J. Szpunar and R. Verma, "Effect of Temperature and Strain Rate on Formability of AZ31 Magnesium Sheet Alloy," *SAE Technical Paper 2006-01-0258*, 2006.

[274] W. T. Zheng, S. H. Zhang, D. Sorgente, L. Tricarico and G. Palumbo, "Approach of using a ductile fracture criterion in deep drawing of magnesium alloy cylindrical cups under non-isothermal condition," *Journal of engineering manufacture*, vol. 221(6), p. 981, 2007.

[275] W. Wang, L. Huang, K. Tao, S. Chen and X. Wei, "Formability and numerical simulation of AZ31B magnesium alloy sheet in warm stamping process," *Materials and Design*, vol. 87, p. 835, 2015.

[276] G. R. Johnson and W. H. Cook, "A constitutive model and data for metals subjected to large strains, high strain rates and high temperatures," *Proceedings of the 7th International Symposium on Ballistics*. *Den Haag, The Netherlands*, p. 541, 1983.

[277] B. Farrokh and A. S. Khan, "Grain size, strain rate, and temperature dependence of flow stress in ultra-fine grained and nano-crystalline Cu and Al: synthesis, experiment, and constitutive modelling," *International Journal of Plasticity.*, vol. 25, p. 715, 2009.

[278] C. Zener and H. Hollomon, "Effect of strain rate upon plastic flow of steel," *J. of Applied Physics*, vol. 15, p. 22, 1944.

[279] J. Jonas, C. M. Sellars and W. J. Tegart, "Strength and structure under hot-working conditions," *International Metal Reviews*, vol. 14, p. 1, 1969.

[280] A. Molinari and G. Ravichandran, “Constitutive modelling of high-strain-rate deformation in metals based on the evolution of an effective microstructural length,” *Mechanical Materials*, vol. 37, p.737, 2005.

[281] A. S. Khan, H. Y. Zhang and L. Takacs, “Mechanical response and modelling of fully compacted nano-crystalline iron and copper,” *International Journal of Plasticity*, vol. 16, p. 1459, 2000.

[282] D. S. Fields and W. A. Bachofen, “Determination of strain hardening characteristics by torsion testing,” *ASTM, Proceedings of American Society of Test Materials*, vol. 57, p. 1259, 1957.

[283] A. S. Khan and S. Huang, “Experimental and theoretical study of mechanical behaviour of 1100 aluminium in the strain rate range 105—104 s1,” *International Journal of Plasticity*, vol. 8, p. 397, 1992.

[284] R. Q. Liang and A. S. Khan, “A critical review of experimental results and constitutive models for BCC and FCC metals over a wide range of strain rates and temperatures,” *International Journal of Plasticity*, vol. 15, p. 963, 1999.

[285] S. Y. Chen, C. G. Huang, C. K. Wang and Z. P. Duan, “Mechanical properties and constitutive relationships of 30CrMnSiA steel heated at high rate,” *Material Science Engineering: A*, vol. 483 - 484, p. 105, 2008.

[286] E. Voce, “The relationship between stress and strain for homogeneous deformation,” *Journal of the Japan Institute of Metals and Materials*, vol. 74, p. 537, 1948.

[287] U. F. Kocks, “Laws for work-hardening and low-temperature creep,” *Journal of Engineering Material Technology*, vol. 98, p. 76, 1976.

[288] Y. C. Lin and X. M. Chen, “A combined Johnson–Cook and Zerilli–Armstrong model for hot compressed typical high-strength alloy steel,” *Computational Material Science*, vol. 49, p. 628, 2010.

[289] D. L. Preston, D. L. Tonks and D. C. Wallace, “Model of plastic deformation for extreme loading conditions,” *Journal of Applied Physics*, vol. 93, p. 211, 2003.

[290] Y. C. Lin, M. S. Chen and J. Zhang, “Prediction of 42CrMo steel flow stress at high temperature and strain rate,” *Mechanics Research Communications*, vol. 35, p. 142, 2008.

[291] G. Z. Voyiadjis and A. H. Almasri, “A physically based constitutive model for fcc metals with applications to dynamic hardness,” *Mechanical Materials*, vol. 40, p. 549, 2008.

[292] S. R. Bodner and Y. Partom, “Constitutive equations for elastic–viscoplastic strainhardening materials,” *Journal of Applied Mechanics*, vol. 42, p. 385, 1975.

[293] A. Rusinek and Jr. Klepaczko, “Shear testing of a sheet steel at wide range of strain rates and a constitutive relation with strain-rate and temperature dependence of the flow stress,” *International Journal of Plasticity*, vol. 17, p. 87, 2001.

[294] R. L. Goetz and V. Seetharaman, “Modeling dynamic recrystallization using cellular automaton,” *Scripta Materiala*, vol. 38, vol. 405 - 13, 1998.

[295] M. C. Cai, L. S. Niu, X. F. Ma and H. J. Shi, “A constitutive description of the strain rate and temperature effects on the mechanical behaviour of materials,” *Mechanical Materials*, vol. 42, p. 774, 2010.

[296] Y. C. Lin, J. Zhang and J. Zhong, “Application of neural networks to predict the elevated temperature flow behaviour of a low alloy steel,” *Computational Material Science*, vol. 43, p. 752, 2008.

[297] P. F. Bariani, S. Bruschi and T. D. Negro, “Prediction of nickel-base super-alloys rheological behaviour under hot forging conditions using artificial neural networks,” *Journal of Materials Processing Technology*, vol. 152(3), p. 395, 2004.

[298] A. Z. Al-Garni and A. Jamal, “Artificial neural network application of modelling failure rate for Boeing 737 tires,” *Quality and Reliability Engineering International*, vol. 27(2), p. 209, 2011.

[299] F. P. Beer, E. R. Johnston and J. T. Dewolf, “Mechanics of Materials (3rd ed.), *McGraw- Hill*, 2001.

[300] J. Cao, H. Yao, A. Karafillis and M. C. Boyce, “Prediction of localized thinning in sheet metal using a general anisotropic yield criterion,” *International Journal of Plasticity*, vol. 16(9), p. 1105, 2000.

[301] H. Tresca, “Mémoire sur l'écoulement des corps solides soumis à de fortes pressions,” *C.R. Acad. Sci. Paris*, vol. 59, p. 754, 1864.

[302] R. Von Mises, “Mechanik der festen Körper im plastisch deformablen Zustand. Göttin. Nachr,” *Math. Phys.*, vol. 1, p. 582, 1913.

[303] A. Nadai, “Theory of flow and fracture of solids,” vol. 2, *McGraw-Hill*, 1963.

[304] W. F. Hosford, “Comments on anisotropic yield criteria,” *International Journal of Mechanical Sciences*, vol. 27(7/8), p. 423, 1985.

[305] R. Hill, “The mathematical theory of plasticity,” *Oxford, Clarendon Press*, 1950.

[306] R. Hill, “On discontinuous plastic states, with special reference to localized necking in thin sheets,” *Journal of the Mechanics and Physics of Solids*, vol. 1, p. 19, 1952.

[307] F. Barlat and J. Lian, “Plastic behaviour and stretch ability of sheet metals, Part I: A Yield function for orthotropic sheets under plane stress conditions,” *International Journal of Plasticity*, vol. 5, p. 51, 1989.

[308] F. Barlat, D. J. Lege and J. C. Brem, “A six-component yield functions for anisotropic materials,” *International Journal of Plasticity*, vol. 7, p. 693, 1991.

[309] F. Barlat and R. C. Becker, “Yielding description for solution strengthened aluminium alloys,” *International Journal of Plasticity*, vol. 13, p. 385, 1997.

[310] F. Barlat, Y. Maeda and K. Chung, “Yield function development for aluminium alloy sheets,” *Journal of the Mechanics and Physics of Solids*, vol. 45(11 - 12), p. 1727, 1997.

[311] J. W. Yoon, F. Barlat and J. J. Gracio, "Anisotropic strain hardening behaviour in simple shear for cube textured aluminium alloy sheets," *International Journal of Plasticity*, vol. 21, p. 2426, 2005.

[312] F. Barlat, H. Aretz and J. W. Yoon, "Linear transformation-based anisotropic yield functions," *International Journal of Plasticity*, vol. 21, p. 1009, 2005.

[313] J. Yoon, F. Barlat, R. E. Dick, K. Chung and T. J. Kang, "Plane stress yield function for aluminium alloy sheets—part II: FE formulation and its implementation, *International Journal of Plasticity*," vol. 20(3), p. 495, 2004.

[314] K. Ghavam, R. Naghdabadi, "Constitutive modelling of temperature and strain rate dependent elastoplastic hardening materials using a co-rotational rate associated with the plastic deformation," *International Journal of Plasticity*, vol. 27(9), p. 1445, 2011.

[315] R. Bagheriasl, K. Ghavam and M. J. Worswick, "Formability analysis of aluminum alloy sheets at elevated temperatures with numerical simulation based on the M-K method," *Proc. of ESAFORM*, Belfast, Ireland, 2011.

[316] R. Desmorat and R. Marull, "Non-quadratic Kelvin modes based plasticity criteria for anisotropic materials," *International Journal of Plasticity*, vol. 27(3), p. 328, 2011.

[317] P. Hidalgo-Manrique, V. Herrera-Solaz, J. Segurado, J. Llorca, F. Gálvez, O.A. Ruano, S.B. Yi and M.T. Pérez-Prado, "Origin of the reversed yield asymmetry in Mg-rare earth alloys at high temperature," *Acta Materialia*, vol. 92, p. 265, 2015.

[318] N. Abedrabbo, M. A. Zampaloni and F. Pourboghrat, "Wrinkling control in aluminum sheet hydroforming," *International Journal of Mechanical Sciences*, vol. 47(3), p. 333, 2005.

[319] Z. Marciniak, J. L. Duncan and J. Hu, "Mechanics of sheet metal forming," *Butterworth- Heinemann*, 2002.

[320] Z. Marciniak, K. Kuczynski and T. Pokora, “Influence of the plastic properties of a material on the forming limit diagram for sheet metal in tension,” *International Journal of Mechanical Sciences*, vol. 15, p.789, 1973.

[321] H. W. Swift, “Plastic instability under plane stress,” *Journal of the Mechanics and Physics of Solids*, vol. 1, p. 1, 1952.

[322] Z. Marciniak and K. Kuczynski, “Limit strain in the processes of stretch-forming sheet metal,” *International Journal of Mechanical Sciences*, vol. 9, p. 609, 1967.

[324] D. Banabic and E. Dannenmann, “Prediction of the influence of yield locus on the limit strains in sheet metals,” *Journal of Materials Processing Technology*, vol. 109(1 - 2), p. 9, 2001.

[325] D. Kuc and E. Hadasik, “Model of microstructure development in hot deformed magnesium alloy AZ31 type,” *Solid State Phenomena*, vol. 197, p. 232, 2013.

[326] S. Stören and J. R. Rice, “Localized necking in thin sheets,” *Journal of the Mechanics and Physics of Solids*, vol. 23(6), p. 421, 1975.

[327] X. Zhu, K. Weinmann, and A. Chandra, “Unified bifurcation analysis of sheet metal forming limits,” *Journal of Engineering Materials and Technology*, vol. 123(3), p. 329, 2001.

[328] JIS H 7501, “Method for evaluation of tensile properties of metallic superplastic materials”, *Japanese industrial standard*, 2013.

[329] ASTM E21, “Standard test methods for elevated temperature testing tests for metallic materials”, *American Society for Testing and Materials*, p. 139, 2013.

[330] ISO 783:1999, Metallic materials - Tensile testing at elevated temperature, International standard organization, 2013.

[331] ASM Specialty Handbook, “Magnesium and magnesium alloys”, *Editors M. Avedesian and H. Baker*, 1st print, 1999.

[332] ASM Specialty Handbook, “Tensile testing handbook”, *Editors J. R. Davis and Davis & Associates*, 2nd Edition, 2004.

[333] S. Bruschi, , T. Altan, D. Banabic, P. F. Bariani, A. Brosius, J. Cao, A. Ghiotti, M. Khraisheh, M. Merklein and A.E. Tekkaya, “Testing and modelling of material behaviour and formability in sheet metal forming,” *CIRP Annals - Manufacturing Technology*, vol. 63(2), p. 727, 2014.

[334] D. Yin, K. Zhang, G. Wang and W. Han, “Superplasticity of fine grained AZ31 Mg alloy sheets,” *Transactions of Nonferrous Metals Society of China*, vol. 14(6), p. 1100, 2004.

[335] M. Suresh and S. Suwas, “Modification in texture of magnesium by the addition of rare earth elements and its influence on mechanical properties,” *Materials Science Forum*, vol. 736, p. 307, 2012.

[336] L. Guo and F. Fujita, “Influence of rolling parameters on dynamically recrystallized microstructures in AZ31 magnesium alloy sheets,” *Journal of Magnesium and Alloys*, vol. 3(2), p. 95, 2015.

[337] S. Kaya, “Improving the formability limits lightweight metal alloy Sheet using advanced processes - finite element modelling and experiment validation,” PhD dissertation, *The Ohio State University*, 2008.

[338] R. Neugebauer, T. Altan, M. Geiger, M. Kleiner and A. Sterzing, “Sheet metal forming at elevated temperatures,” *CIRP Annals - Manufacturing Technology*, vol. 55(2), p.793, 2006.

[339] K. Droder, “Analysis on forming of thin magnesium sheets,” Ph.D. dissertation, *IFUM, University of Hanover*, 1999.

[340] ISO 1204-2:2008, Metallic materials – sheet and strip – Determination of forming limit curves, *International standard organization*, 2013.

[341] S. Toros, F. Ozturk and I. Kacar, “Review of warm forming of aluminium–magnesium alloys,” *Journal of Materials Processing Technology*, vol. 207(1 - 3), p. 1, 2008.

[342] L. L. Hütsch, J. Hütsch, K. Herzberg, J.F. dos Santos and N. Huber, “Increased room temperature formability of Mg AZ31 by high speed, friction stir processing,” *Materials and Design*, vol. 54, p. 980, 2014.

[343] A. Barata, D. Rocha and J. M. Jalinier, “Plastic instability of sheet metals under simple and complex strain paths,” *Trans. Iron Steel Inst. Jpn.*, vol. 24(2), p. 132, 1984.

[344] ASTM E2218, “Standard test methods for determining forming limit curves”, *American Society for Testing and Materials*, 2010.

[345] ASTM D3418, “Standard test method for transition temperatures and enthalpies of fusion and crystallization of polymers by differential scanning calorimetry”, *American Society for Testing and Materials*, 2010.

[346] ASTM D1894, “Standard test method for static and kinetic coefficients of friction of plastic film and sheeting”, *American Society for Testing and Materials*, 2010.

[347] J. G. Liu and W. Liu, “Evaluation of seven ductile fracture criteria for failure prediction of AZ31 sheet in warm forming,” *Advanced Materials Research*, vols. 482 - 484, p. 1947, 2012.

[348] D. Letzig, L. Stutz, J. Bohlen and K. U. Kainer, “Effects of processing, texture and temperature on the formability of AZ31 and ZE10 sheets,” *Materials Science Forum*, vol. 690, p. 298, 2011.

[349] H. Somekawa, T. Inoue and K. Tsuzaki, “Effect of deformation twin on toughness in magnesium binary alloys,” *Philosophical Magazine*, vol. 95(23), p. 2513, 2015.

[350] D. Lahaie, J. D. Embury, M. M. Chadwick and G. T. Gray, “A note on the deformation of fine grained magnesium alloys,” *Scripta Metallurgica et Materialia*, vol. 27(2), p. 139, 1992.

[351] H. J. Choi, G. B. Kwon, G. Y. Lee and D. H. Bae, “Reinforcement with carbon nanotubes in aluminium matrix composites,” *Scripta Materialia*, vol. 59(3), p. 360, 2008.

[352] J. A. del Valle, M. T. Pérez-Prado and O. A. Ruano, “Deformation mechanisms responsible for the high ductility in a Mg AZ31 alloy analysed by electron backscattered diffraction,” *Metallurgical and Materials Transactions A*, vol. 36(6), p. 1427, 2005.

[353] W. Jin, J. Fan, H. Zhang, Y. Liu, H. Dong, B. Xu, “Microstructure, mechanical properties and static recrystallization behaviour of the rolled ZK60 magnesium alloy sheets processed by electro-pulsing treatment,” *Journal of Alloys and Compounds*, vol. 646, p. 1, 2015.

[354] X. H. Deng, D. Y. Ju, X. D. Hu and H. Y. Zhao, “Modelling of dynamic recrystallization process in AZ31 magnesium alloy using cellular automaton method,” *Materials Science Forum*, vol. 833, p. 19, 2015.

[355] H. Watanabe, T. Mukai, M. Kohzu, S. Tanabe and K. Higashi, “Low temperature superplasticity in a ZK60 magnesium alloy,” *Materials Transactions*, vol. 40(8), p. 809, 1999.

[356] G. Vespa, L. W. F. Mackenzie, R. Verma, F. Zarandi, E. Essadiqi and S. Yue, “The influence of the as-hot rolled microstructure on the elevated temperature mechanical properties of magnesium AZ31 sheet,” *Material Science Engineering A*, vol. 487, p. 243, 2007.

[357] A. S. J. Al-Zubaydi, A. P. Zhilyaev, S. C. Wang and P. A. S. Reed, “Superplastic behaviour of AZ91 magnesium alloy processed by high-pressure torsion,” *Materials Science and Engineering: A*, vol. 637, p. 1, 2015.

[358] C. Furong, L. Zhuoliang, Z. Nianxian, D. Hua, Y. Fuxiao and Z. Liang, “Superplasticity, flow and fracture mechanism in an Al–12.7Si–0.7Mg alloy,” *Materials Science and Engineering: A*, vol. 571, p. 167, 2013.

[359] N. Ridley, D. W. Livesey and A. K. Mukherjee, “Effect of cavitation on post-deformation tensile properties of a superplastic copper-base alloy,” *Metallurgical Transactions A*, vol. 15(7), p. 1443, 1984.

[360] C. L. Chen and M. J Tan, “Cavity growth and filament formation of superplastically deformed Al 7475 Alloy,” *Materials Science and Engineering: A*, vol. 298(1 - 2), p. 235, 2001.

[361] J. C Tan and M. J Tan, “Superplasticity and grain boundary sliding characteristics in two stage deformation of Mg–3Al–1Zn alloy sheet,” *Materials Science and Engineering: A*, vol. 339(1 - 2), p. 81, 2003.

[362] S. Mandal, P. V. Sivaprasad, R. K. Dube and B. Raj, “Kinetics, mechanism and modelling of microstructural evolution during dynamic recrystallization in a 15Cr-15Ni-2.2Mo-Ti modified austenitic stainless steel,” *Material Science Forum*, vol. 550, p. 601, 2007.

[363] F. S. Jarrar, L. G. Hector Jr., M. K. Khraisheh and K. Deshpande, “Gas Pressure Profile Prediction from Variable Strain Rate Deformation Paths in AA5083 Bulge Forming,” *Journal of Materials Engineering and Performance*, vol. 21(11), p. 2263, 2012.

[364] Y. Wang, M. Wei, J. Gao, J. Hu and Y. Zhang, “Corrosion process of pure magnesium in simulated body fluid,” *Materials Letters*, vol. 62, p. 2181, 2008.

[365] J. Cai, F. Li, T. Liu, B. Chen and M. He, “Constitutive equations for elevated temperature flow stress of Ti–6Al–4V alloy considering the effect of strain,” *Material Design*, vol. 32, p. 1144, 2011.

[366] T. Shih-Tsung and H. Hsuan-Teh, “Finite element verification on constitutive law of AZ31 magnesium alloy at 400°C,” *The Chinese Journal of Nonferrous Metals*, vol. 23(11), p. 203, 2013.

[367] W. L. Xu, C. H. Ma, C. H. Li and W. J. Feng, “Sensitive factors in spring-back simulation for sheet metal forming,” *Journal of Materials Processing Technology*, vol. 151, p. 217, 2004.

[368] P. Xiongqi, S. Shaoqing and H. Kangkang, “Comparison of Material Models for Spring Back Prediction in an Automotive Panel Using Finite Element Method,” *Journal of Materials Engineering and Performance,* vol. 22, p. 2990, 2013.

[369] H. R. Abedi, A. Zarei-Hanzaki, S. M. Fatemi-Varzaneh and A. A. Roostaei, “The semi-solid tensile deformation behaviour of wrought AZ31 magnesium alloy,” *Material Design,* vol. 31, p. 4386, 2010.

[370] P. Changizian, A. Zarei-Hanzaki and A. A. Roostaei, “The high temperature flow behavior modeling of AZ81 magnesium alloy considering strain effects,” *Material Design,* vol. 39, p. 384, 2012.

[371] D. Samantaray, S. Mandal and A. K. Bhaduri, “A comparative study on Johnson Cook, modified Zerilli–Armstrong and Arrhenius-type constitutive models to predict elevated temperature flow behaviour in modified 9Cr–1Mo steel,” *Computational Material Science,* vol. 47, p. 568, 2009.

[372] D. T. Nguyen, T. L. Banh, D. W. Jung, S. H. Yang and Y. S. Kim, “A modified Johnson–Cook model to predict stress–strain curves of boron steel sheets at elevated and cooling temperatures,” *High. Temperature Material Process,* vol. 31, p. 37, 2012.

[373] Y. C. Lin, X. M. Chen and G. Liu, “A modified Johnson–Cook model for tensile behaviours of typical high-strength alloy steel,” *Material Science Engineering: A,* vol. 527, p. 6980, 2010.

[374] Y. C. Lin, L. T. Li, Y. X. Fu and Y. Q. Jiang, “Hot compressive deformation behaviour of 7075 Al alloy under elevated temperature,” *J. Material Science,* vol. 47, p. 1306, 2012.

[375] Y. C. Lin, Q. F. Li, Y. C. Xia and L. T. Li, “A phenomenological constitutive model for high temperature flow stress prediction of Al–Cu–Mg alloy,” *Material Science Engineering A,* vol. 534, p. 654, 2012.

[376] Y. C. Lin, L. T. Li and Y. Q. Jiang, “A phenomenological constitutive model for describing thermo-viscoplastic behaviour of Al–Zn–Mg–Cu alloy under hot working condition,” *Experimental Mechanics*, vol. 52, p. 993, 2012.

[377] H. J. Zhang, W. D. Wen and H. T. Cui, “Behaviours of IC10 alloy over a wide range of strain rates and temperatures: experiments and modelling steel,” *Material Science Engineering: A*, vol. 504, p. 99, 2009.

[378] M. Vural and J. Caro, “Experimental analysis and constitutive modelling for the newly developed 2139-T8 alloy,” *Material Science Engineering: A*, vol. 520, p. 56, 2009.

[379] J. B. Kim and H. Shin, “Comparison of plasticity models for titanium and a modification of the PTW model for wide ranges of strain, strain rate, and temperature,” *Int. J. Impact Eng.*, vol. 36, p. 746, 2009.

[380] Y. C. Lin and X. Chen, “A critical review of experimental results and constitutive descriptions for metals and alloys in hot working,” *Materials and Design*, vol. 32, p. 1733, 2011.

[381] Q. Y. Hou and J. T Wang, “A modified Johnson–Cook constitutive model for Mg–Gd–Y alloy extended to a wide range of temperatures,” *Computational Material Science*, vol. 50, p. 147, 2010.

[382] H.J. Frost and M.F. Ashby: Deformation-Mechanism Maps, Pergamon Press, New York, NY, 1982.

[383] F. A. Slooff, J. Zhou, J. Duszczyk, and L. Katgerman, “Constitutive analysis of wrought magnesium alloy Mg-Al4-Zn1,” *Scripta Mater.*, vol. 57, p. 759, 2007.

[384] N. Haghdadi, A. Zarei-Hanzaki, and H.R. Abedi, “The effect of thermomechanical parameters on the eutectic silicon characteristics in a non-modified cast A356 aluminum Alloy,” *Mater. Sci. Eng. A*, vol. 535, p. 252, 2012.

[385] F. Pilehva, A. Zarei-Hanzaki, M. Ghambari, H. Abedi, “Flow behavior modeling of a Ti–6Al–7Nb biomedical alloy during manufacturing at elevated temperatures,” *Mater. Des.*, vol. 51, p. 457, 2013.

[386] A. Marandi, A. Zarei-Hanzaki, N. Haghdadi, and M. Eskandari, “The prediction of hot deformation behavior in Fe-21Mn-2.5Si-1.5Al transformation-twinning Induced plasticity steel,” *Mater. Sci. Eng. A*, vol. 554, p. 72, 2012.

[387] Y.C. Lin and G. Liu, “A new mathematical model for predicting flow stress of typical high-strength alloy steel at elevated high temperature,” *Comput. Mater. Sci.*, vol. 48, p. 54, 2010.

Appendix A: Tensile test curves

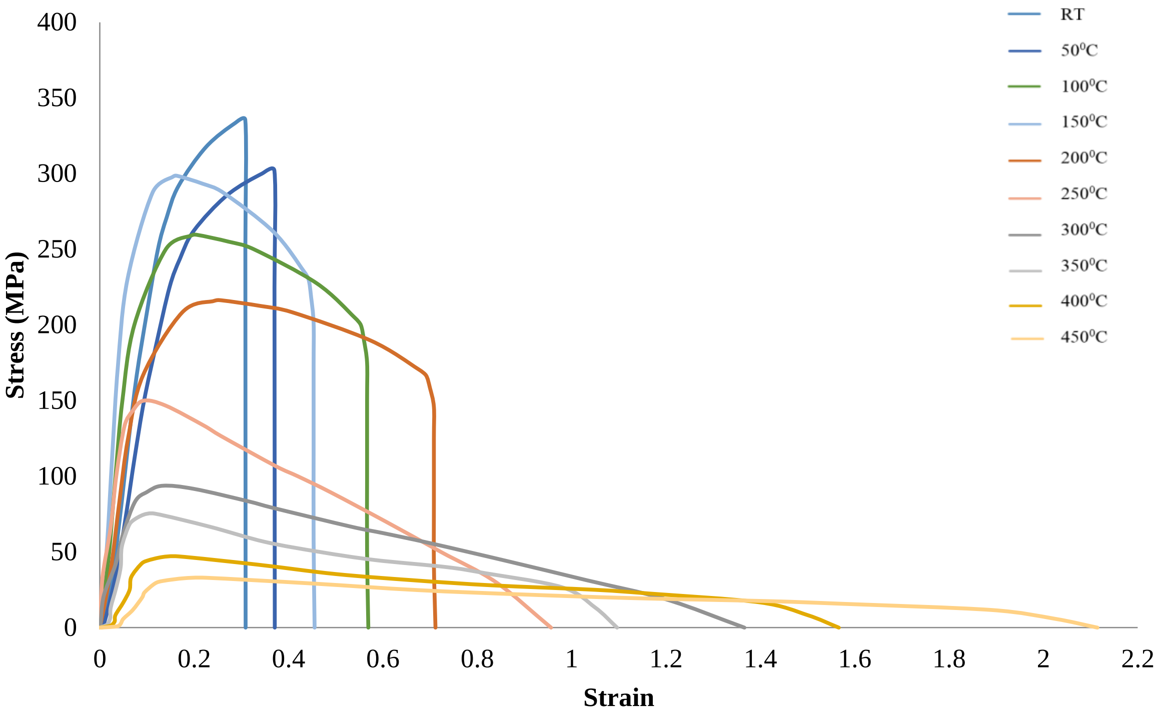

Stress-strain curves at various temperatures at a strain rate of $1x10^{-2}$ sec^{-1} for magnesium AZ80 - O

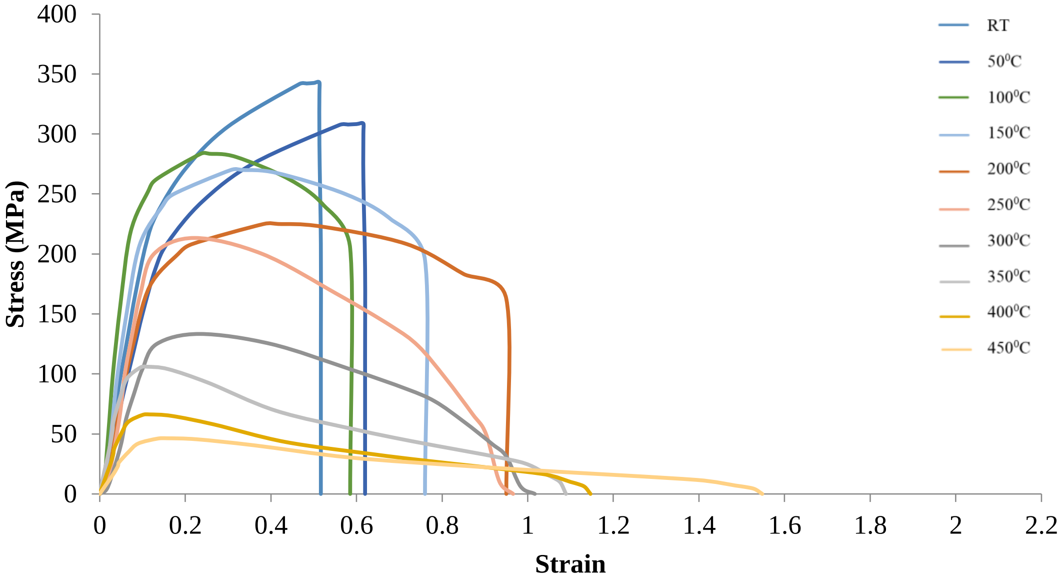

Stress-strain curves at various temperatures at a strain rate of $1x10^{-2}$ sec^{-1} for magnesium AZ80 - F

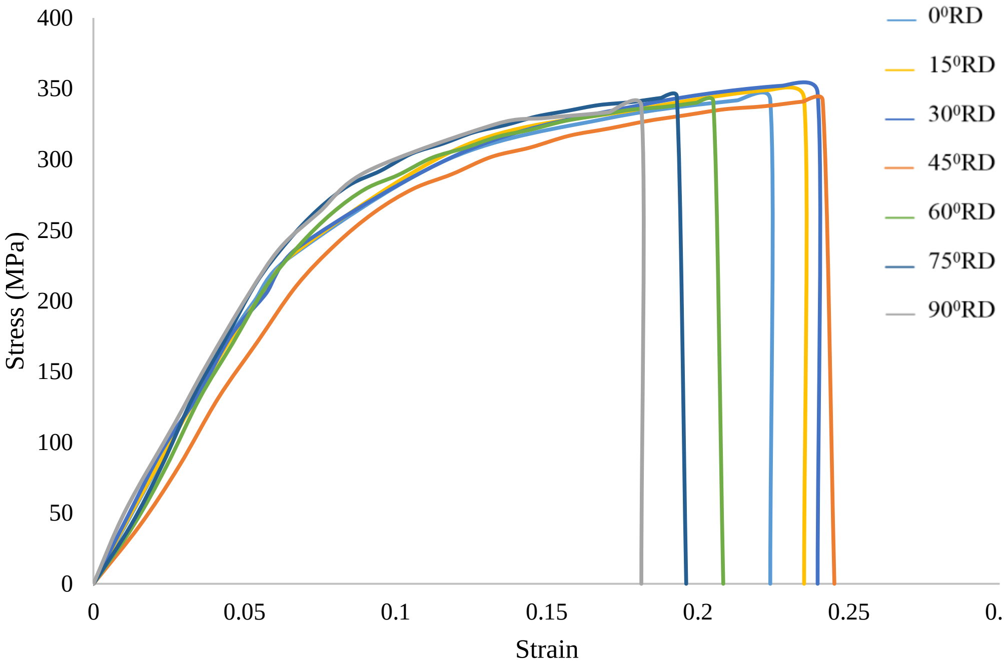

Stress-strain curves at room temperature at a strain rate of 1x10^{-2} sec^{-1} for magnesium AZ80 - O

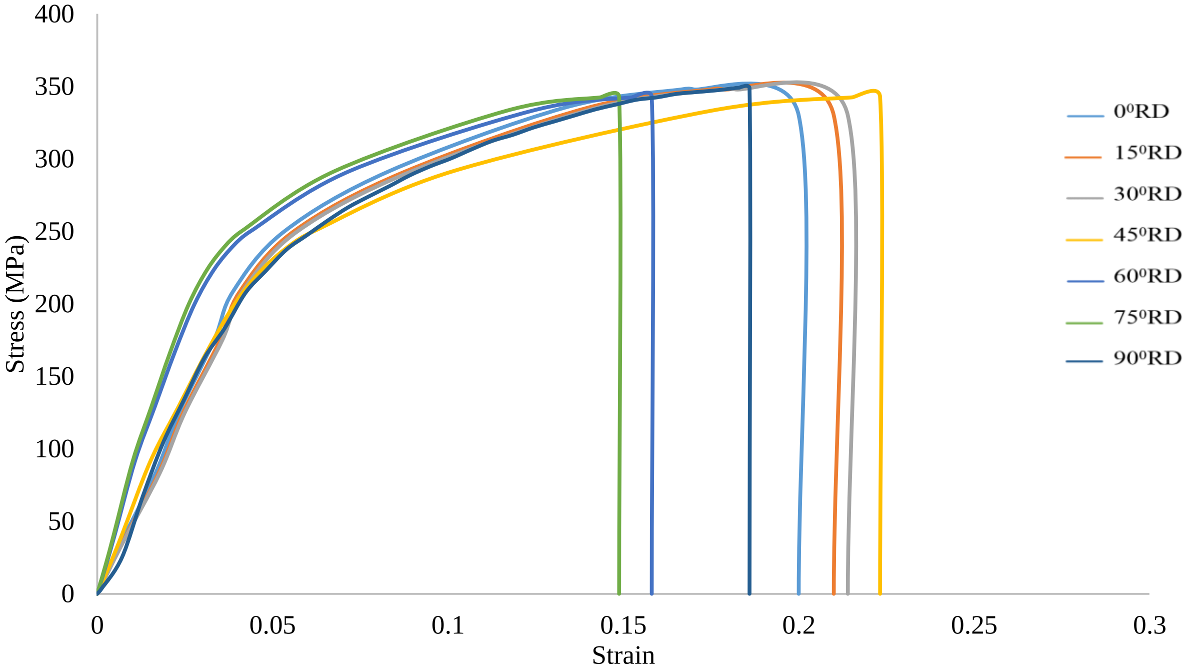

Stress-strain curves at room temperature at a strain rate of 1x10^{-2} sec^{-1} for magnesium AZ80 – F

Appendix B: Tensile test microstructure results at strain of 0.2

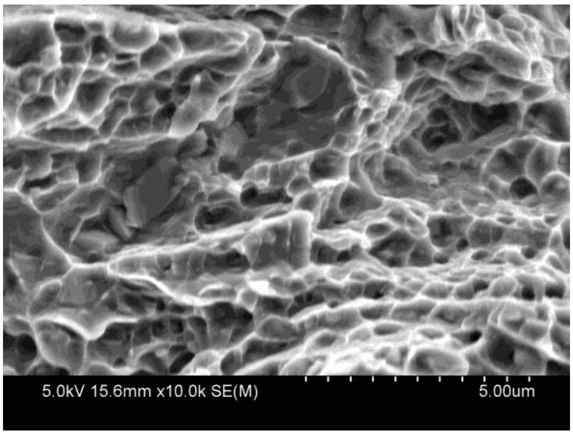
5.0kV 15.6mm x10.0k SE(M)
5.00um

AZ80 - O at RT and 10^{-2} sec^{-1}

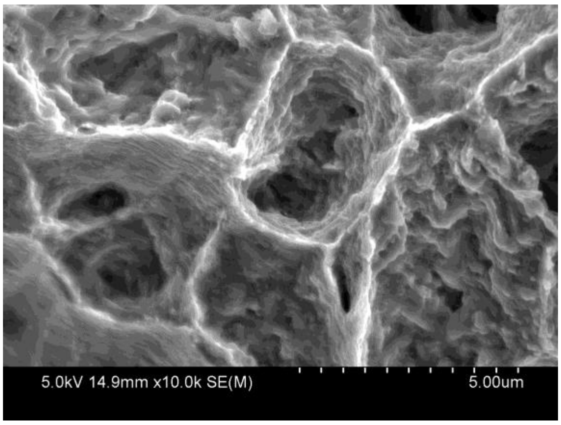
5.0kV 14.9mm x10.0k SE(M)
5.00um

AZ80 - O at 200^{0}C and 10^{-2} sec^{-1}

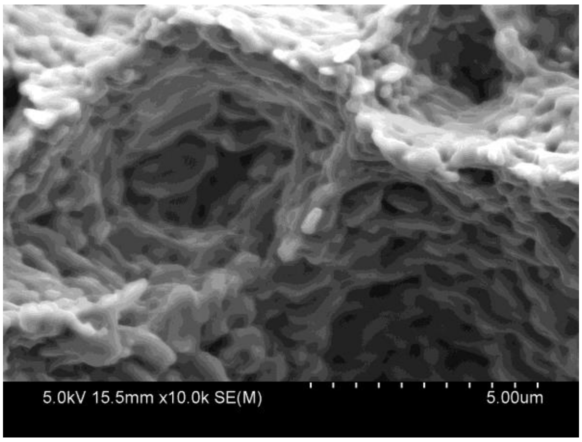
5.0kV 15.5mm x10.0k SE(M)
5.00um

AZ80 - O at 300^{0}C and 10^{-2} sec^{-1}

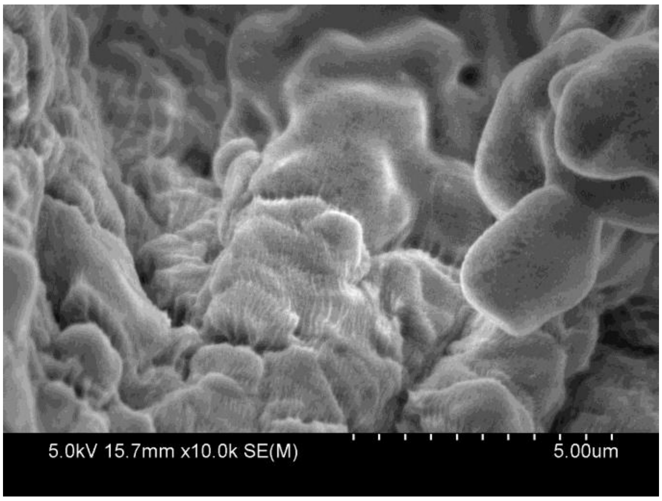
5.0kV 15.7mm x10.0k SE(M)
5.00um

AZ80 - O at 400^{0}C and 10^{-2} sec^{-1}

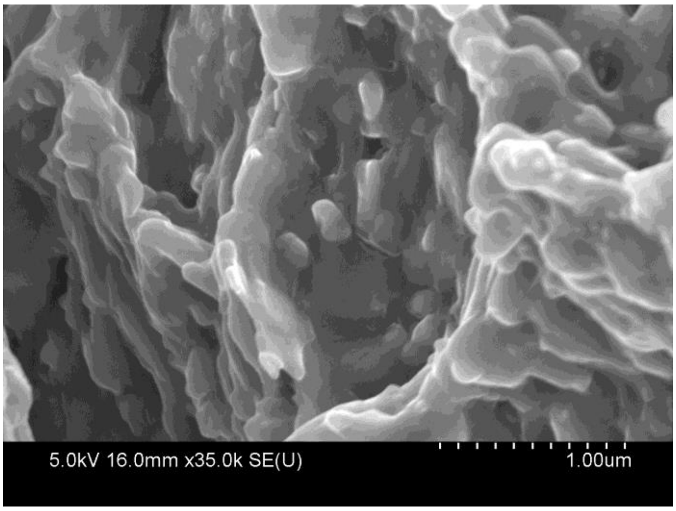
5.0kV 16.0mm x35.0k SE(U)
1.00um

AZ80 - F at 200^{0}C and 10^{-2} sec^{-1}

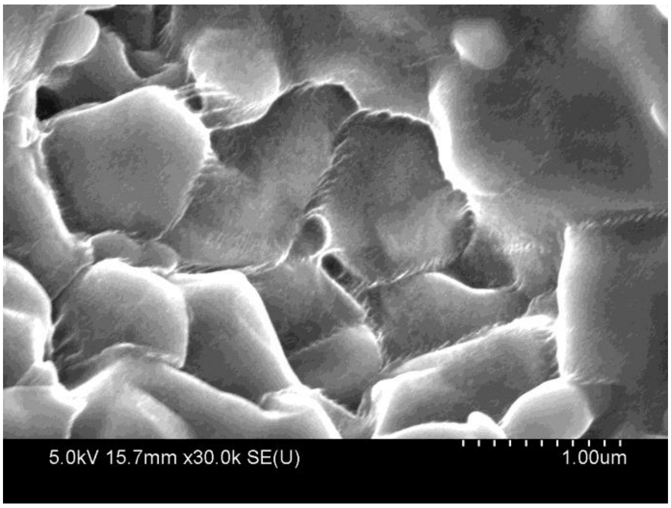
5.0kV 15.7mm x30.0k SE(U)
1.00um

AZ80 - F at 300^{0}C and 10^{-2} sec^{-1}

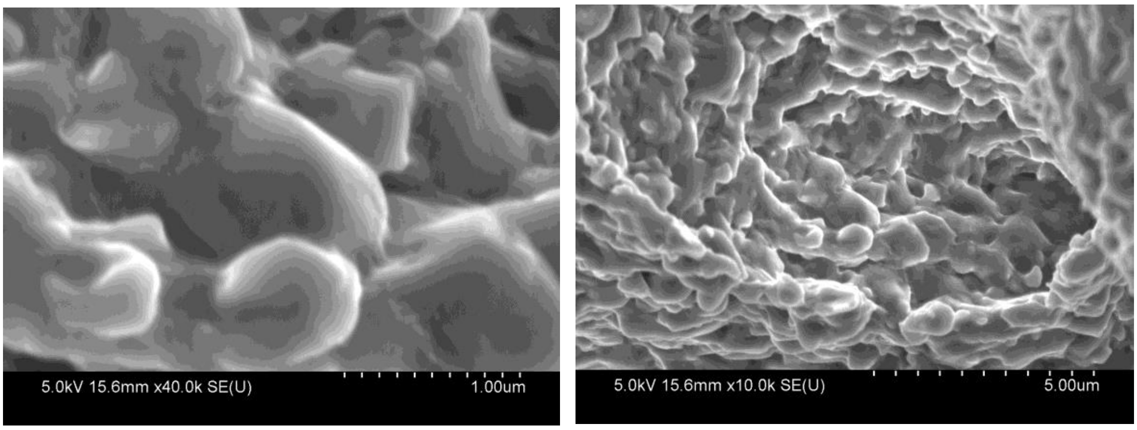
5.0kV 15.6mm x40.0k SE(U)
1.00um
5.0kV 15.6mm x10.0k SE(U)
5.00um

AZ80 - F at 200^{0}C and 10^{-4} sec^{-1}

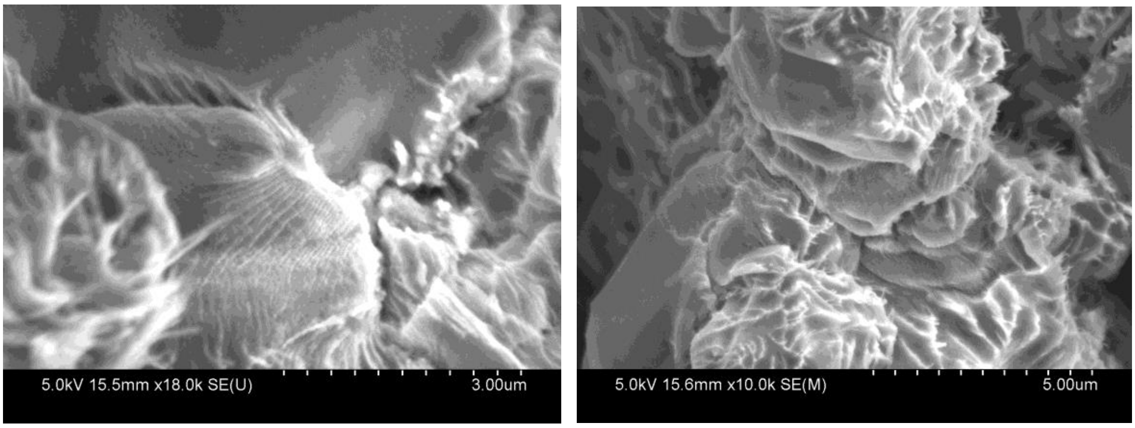
5.0kV 15.5mm x18.0k SE(U)
3.00um
5.0kV 15.6mm x10.0k SE(M)
5.00um

AZ80 - F at 300^{0}C and 10^{-4} sec^{-1}

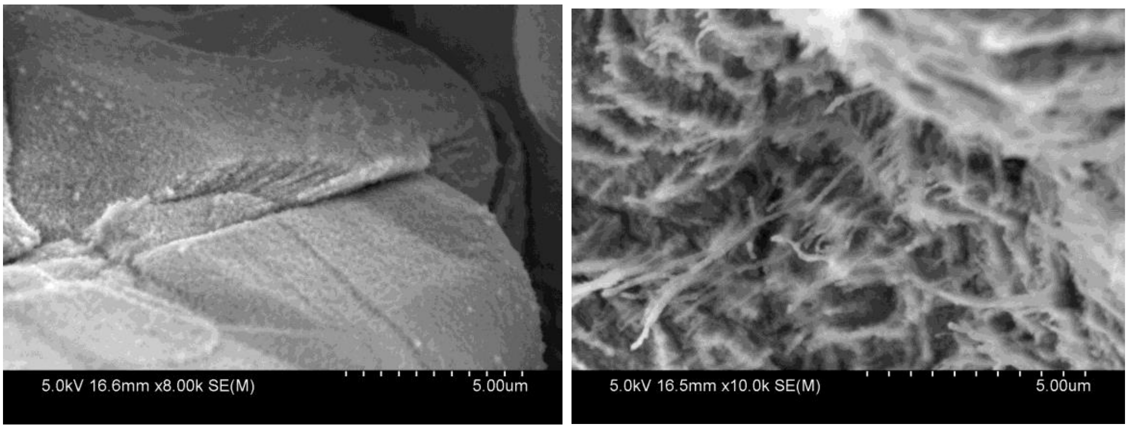
5.0kV 16.6mm x8.00k SE(M)
5.00um
5.0kV 16.5mm x10.0k SE(M)
5.00um

AZ80 - F at 400^{0}C and 10^{-4} sec^{-1}

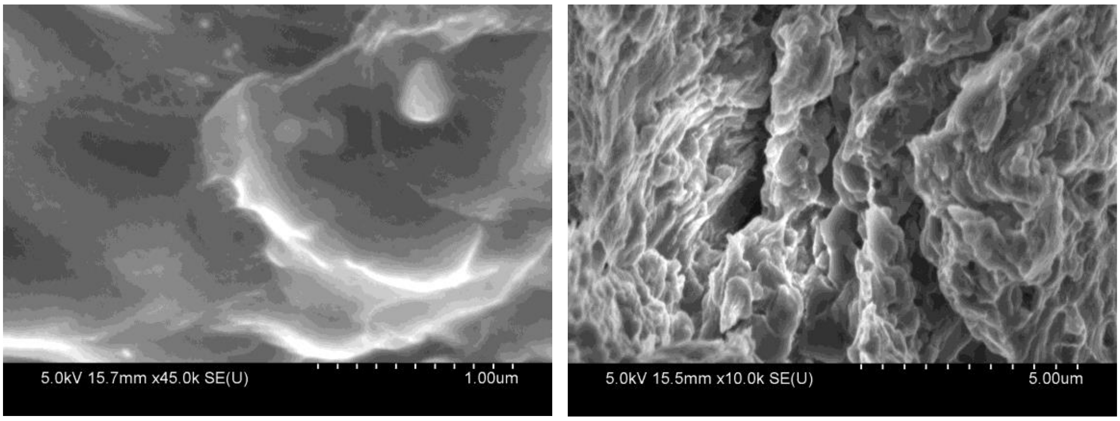
5.0kV 15.7mm x45.0k SE(U)
1.00um
5.0kV 15.5mm x10.0k SE(U)
5.00um

AZ80 - O at 200^{0}C and 10^{-4} sec^{-1}

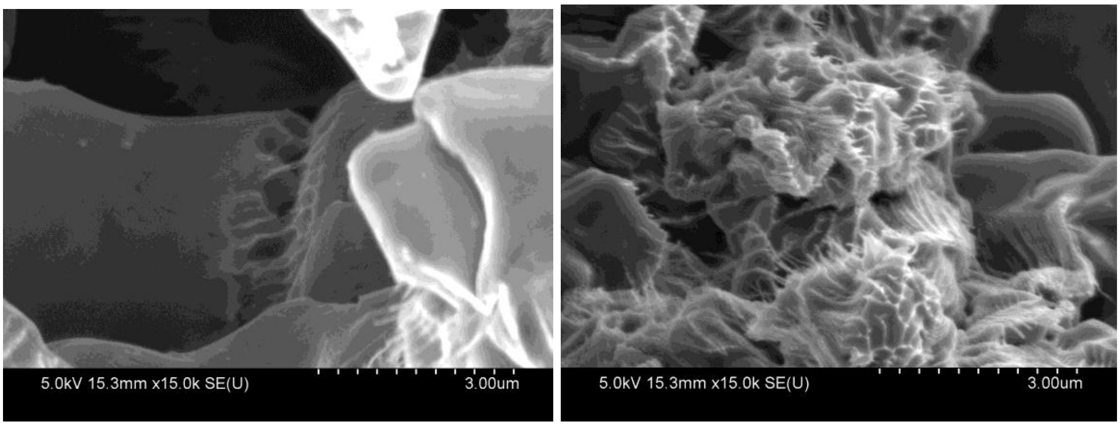
5.0kV 15.3mm x15.0k SE(U)
3.00um
5.0kV 15.3mm x15.0k SE(U)
3.00um

AZ80 - O at 300^{0}C and 10^{-4} sec^{-1}

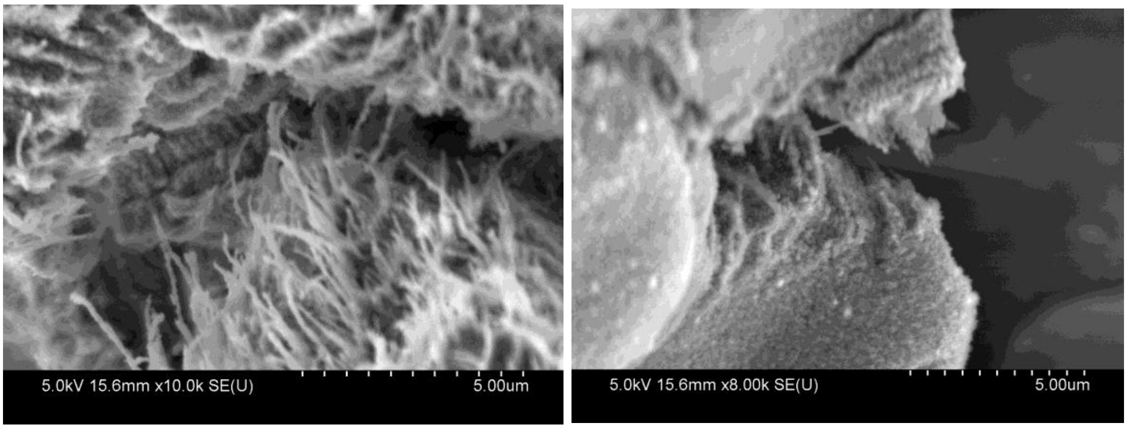
5.0kV 15.6mm x10.0k SE(U)
5.00um
5.0kV 15.6mm x8.00k SE(U)
5.00um

AZ80 - O at 400^{0}C and 10^{-4} sec^{-1}

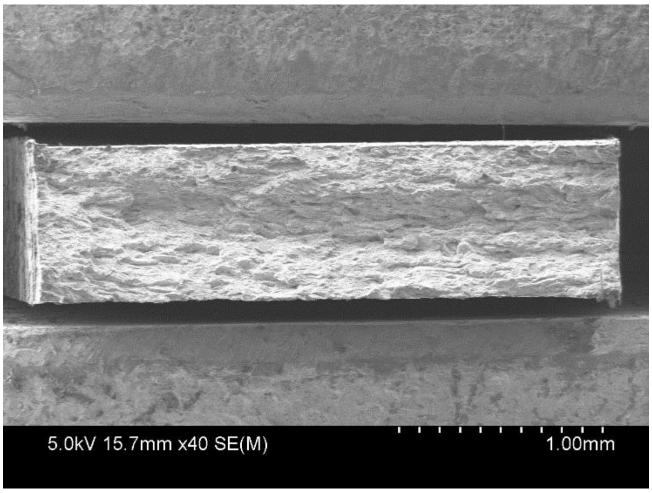
5.0kV 15.7mm x40 SE(M)
1.00mm

Surface morphology of AZ80 – O at RT and 10^{-2} sec^{-1}

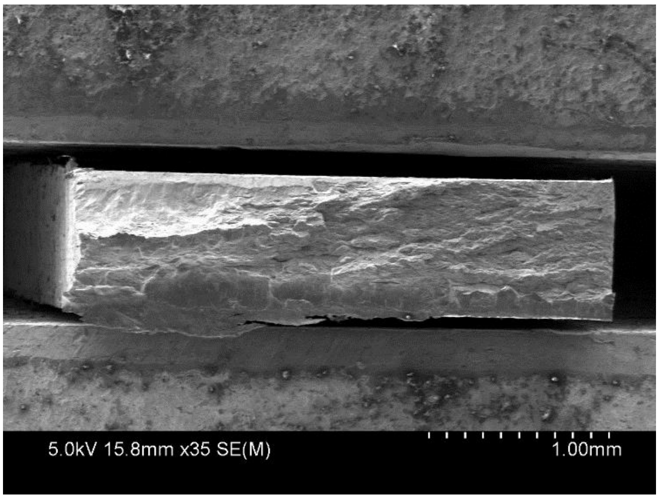
5.0kV 15.8mm x35 SE(M)
1.00mm

Surface morphology of AZ80 – O at RT and 10^{-3} sec^{-1}

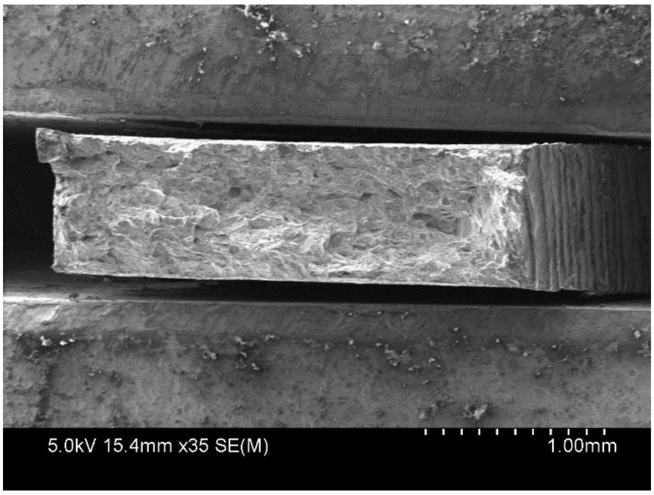
5.0kV 15.4mm x35 SE(M)
1.00mm

Surface morphology of AZ80 – O at RT and 10^{-4} sec^{-1}

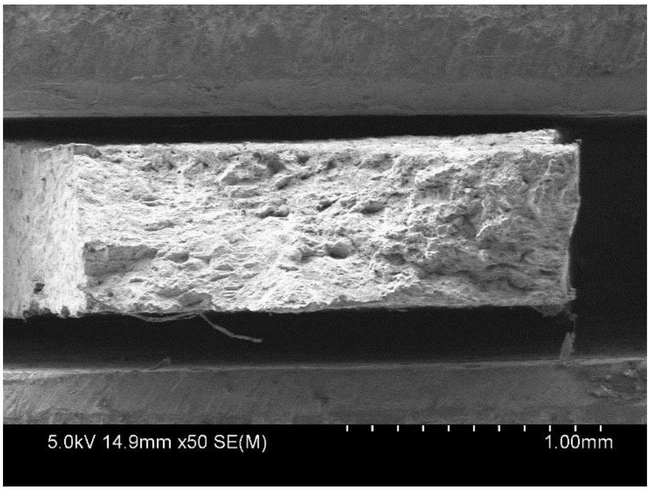
5.0kV 14.9mm x50 SE(M)
1.00mm

Surface morphology of AZ80 – O at 200^0C and 10^{-2} sec^{-1}

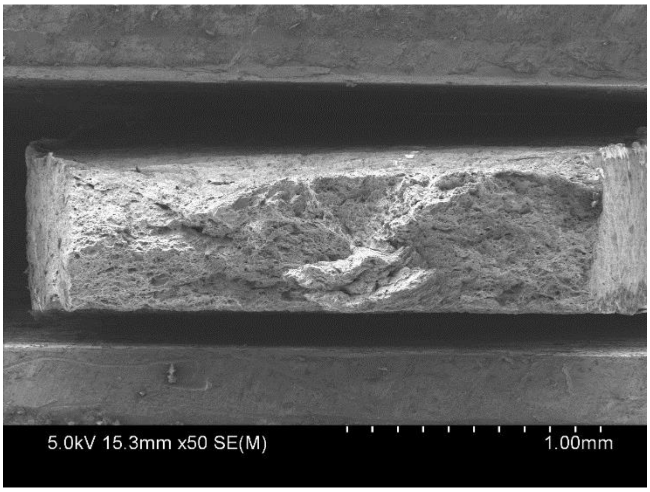
5.0kV 15.3mm x50 SE(M)
1.00mm

Surface morphology of AZ80 – O at 200^0C and 10^{-3} sec^{-1}

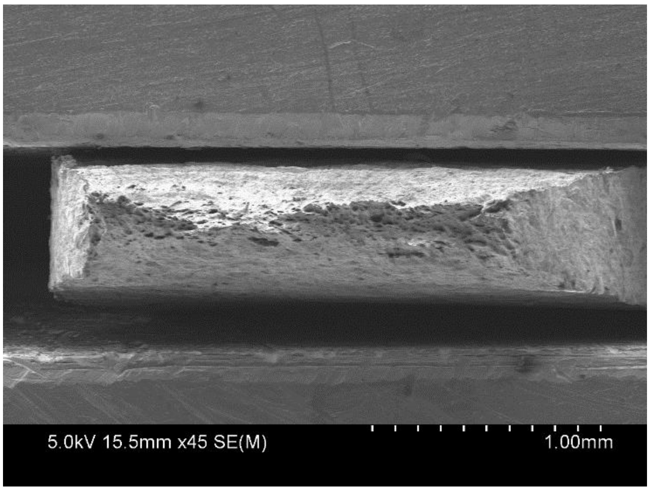
5.0kV 15.5mm x45 SE(M)
1.00mm

Surface morphology of AZ80 – O at 200^0C and 10^{-4} sec^{-1}

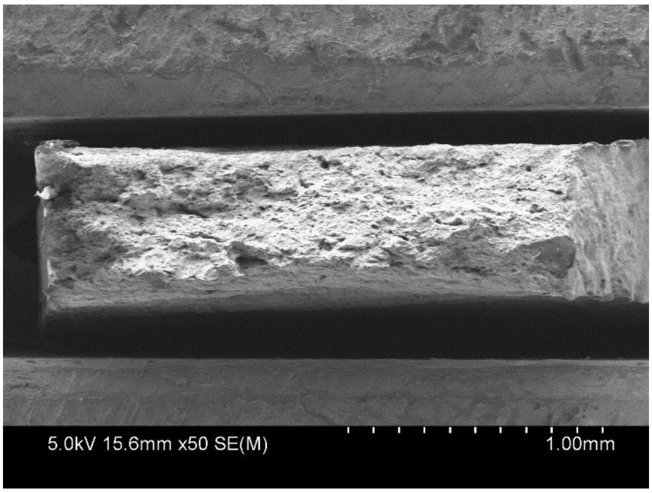
5.0kV 15.6mm x50 SE(M)
1.00mm

Surface morphology of AZ80 – O at 300^0C and 10^{-2} sec^{-1}

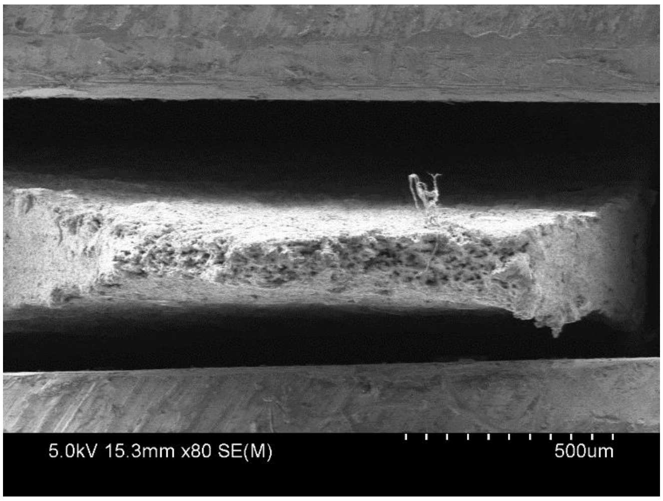
5.0kV 15.3mm x80 SE(M)
500um

Surface morphology of AZ80 – O at 300^0C and 10^{-3} sec^{-1}

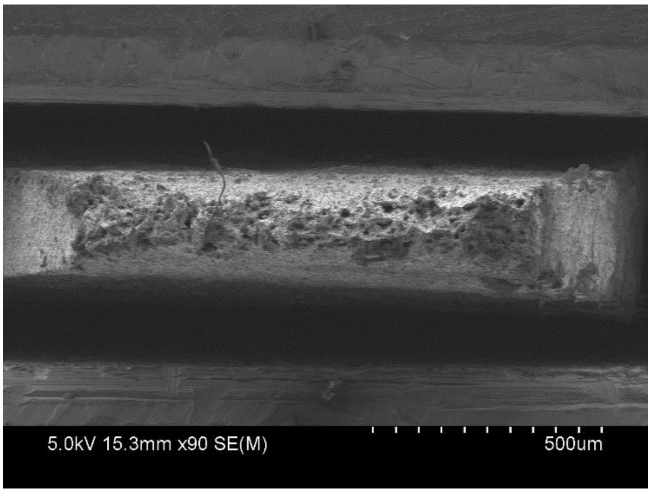
5.0kV 15.3mm x90 SE(M)
500um

Surface morphology of AZ80 – O at 300^0C and 10^{-4} sec^{-1}

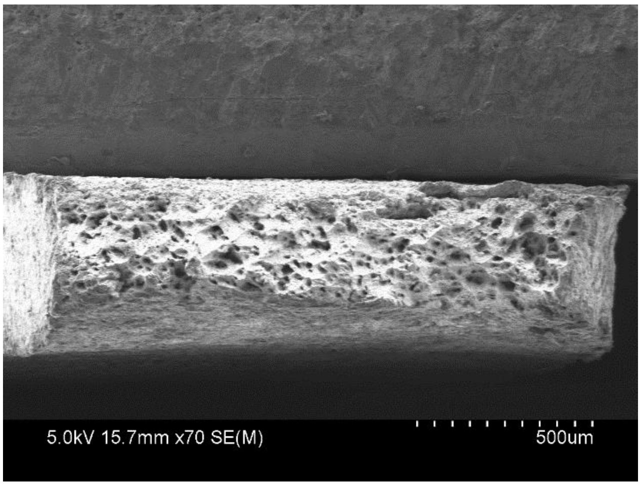
5.0kV 15.7mm x70 SE(M)
500um

Surface morphology of AZ80 – O at 400^0C and 10^{-2} sec^{-1}

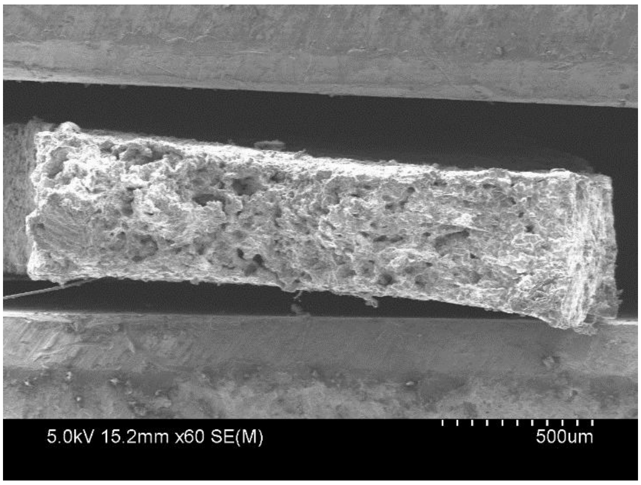
5.0kV 15.2mm x60 SE(M)
500um

Surface morphology of AZ80 – O at 400^0C and 10^{-3} sec^{-1}

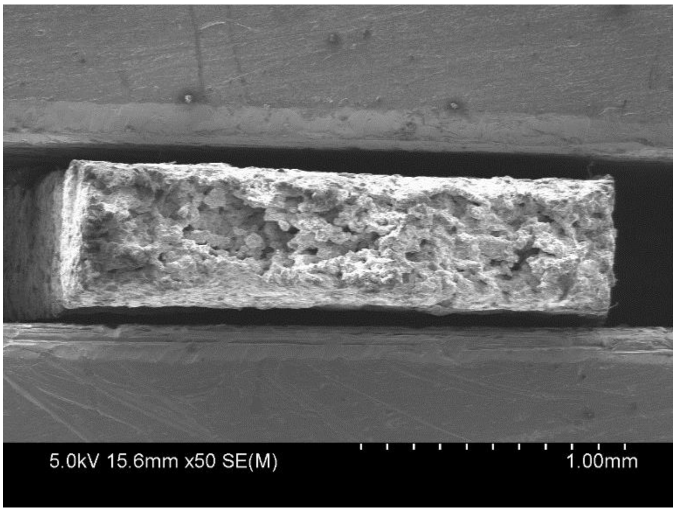
5.0kV 15.6mm x50 SE(M)
1.00mm

Surface morphology of AZ80 – O at 400^0C and 10^{-4} sec^{-1}

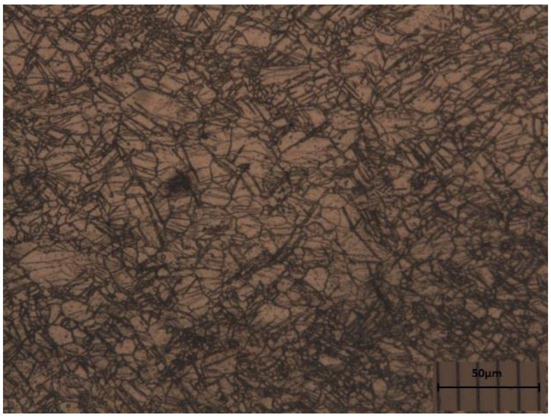

AZ80 – O at RT and 10^{-2} sec^{-1}

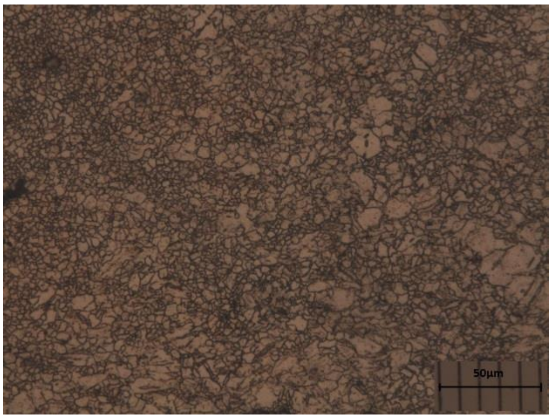

AZ80 – O at RT and 10^{-3} sec^{-1}

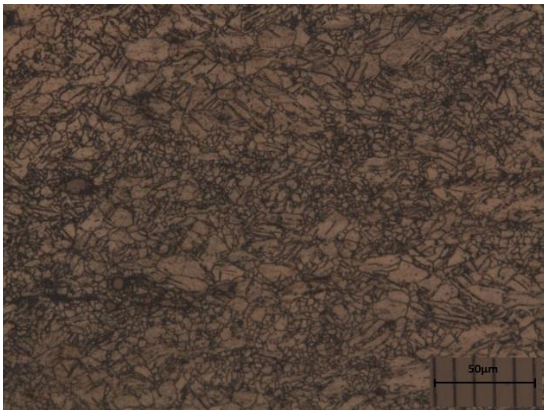

AZ80 – O at RT and 10^{-4} sec^{-1}

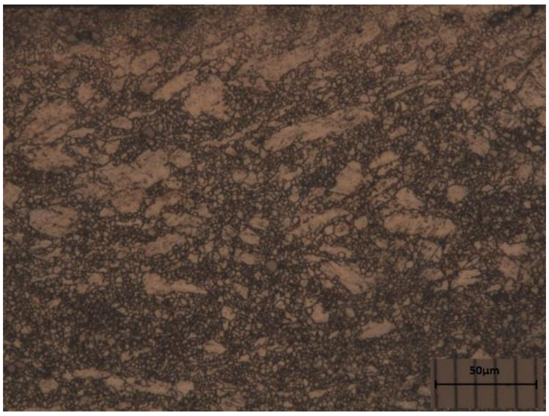

AZ80 – O at 200^{0}C and 10^{-2} sec^{-1}

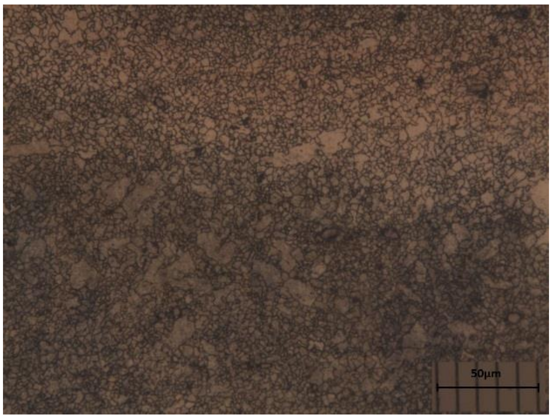

AZ80 – O at 200^{0}C and 10^{-3} sec^{-1}

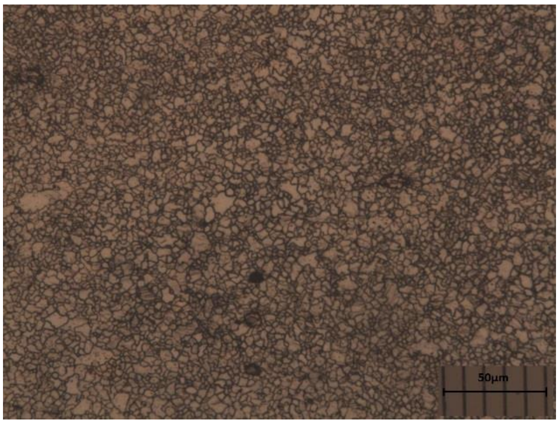

AZ80 – O at 200^{0}C and 10^{-4} sec^{-1}

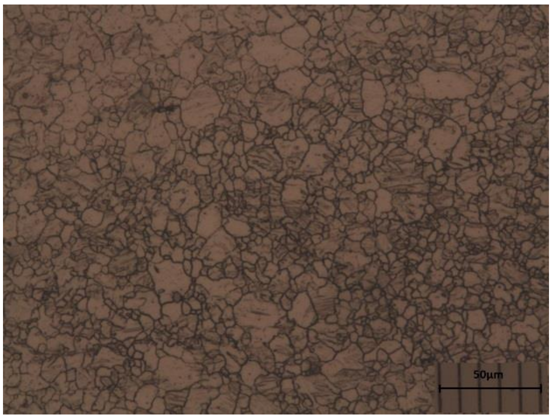

AZ80 – O at 300^0C and 10^{-2} sec^{-1}

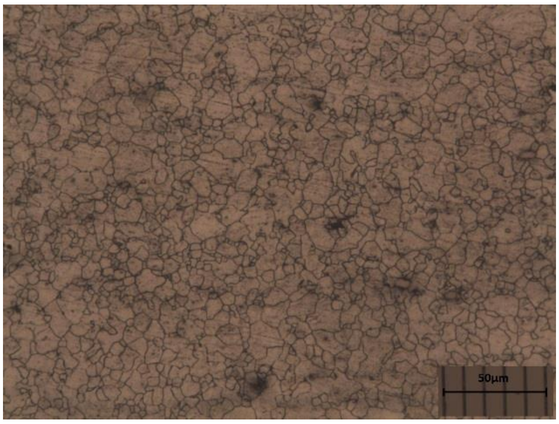

AZ80 – O at 300^0C and 10^{-3} sec^{-1}

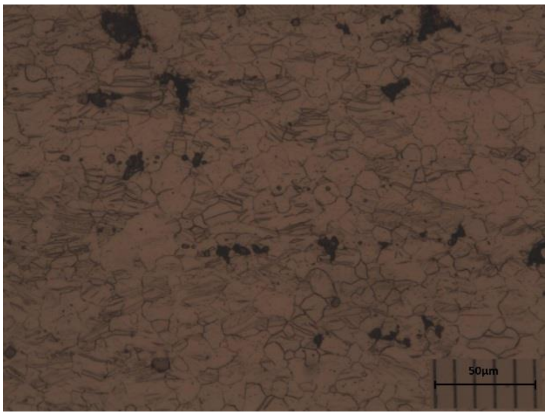

AZ80 – O at 300^0C and 10^{-4} sec^{-1}

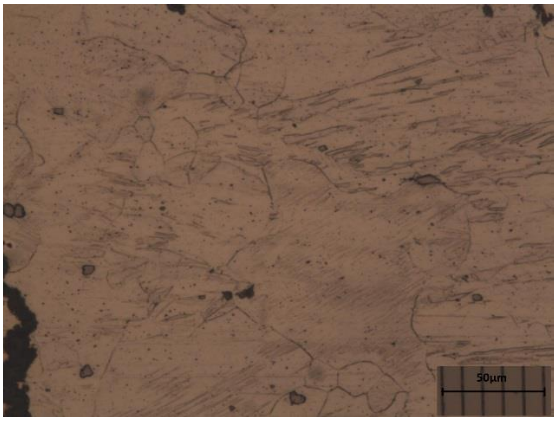

AZ80 – O at 400^0C and 10^{-2} sec^{-1}

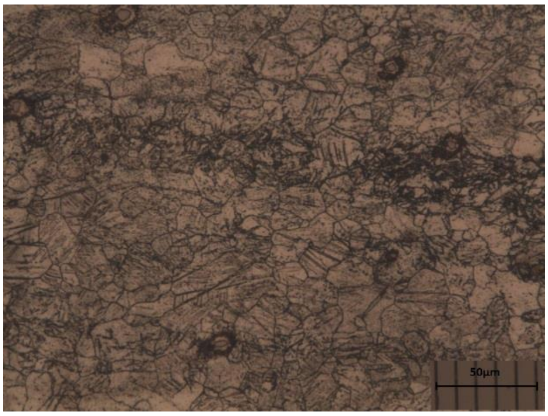

AZ80 – O at 400^0C and 10^{-3} sec^{-1}

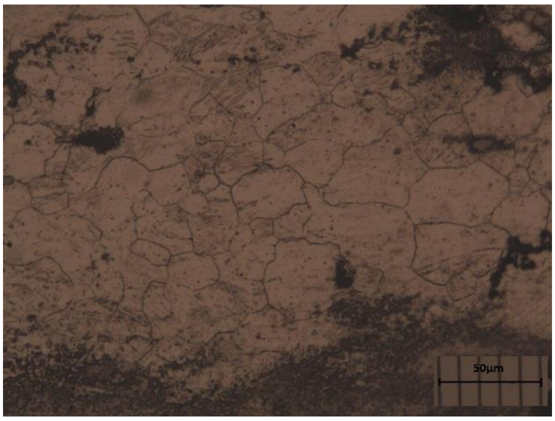

AZ80 – O at 400^0C and 10^{-4} sec^{-1}

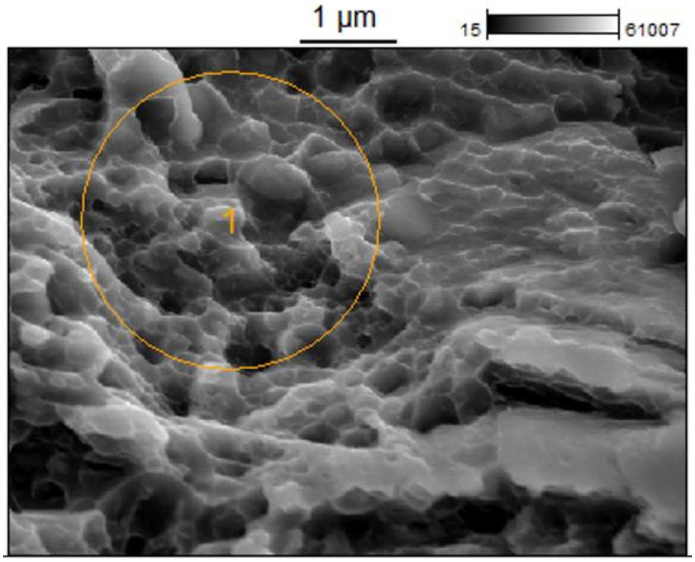
1 µm
15
61007
1

Data Type:	Counts
Image Resolution:	512 by 384
Image Pixel Size:	0.01 µm
Map Resolution:	256 by 192

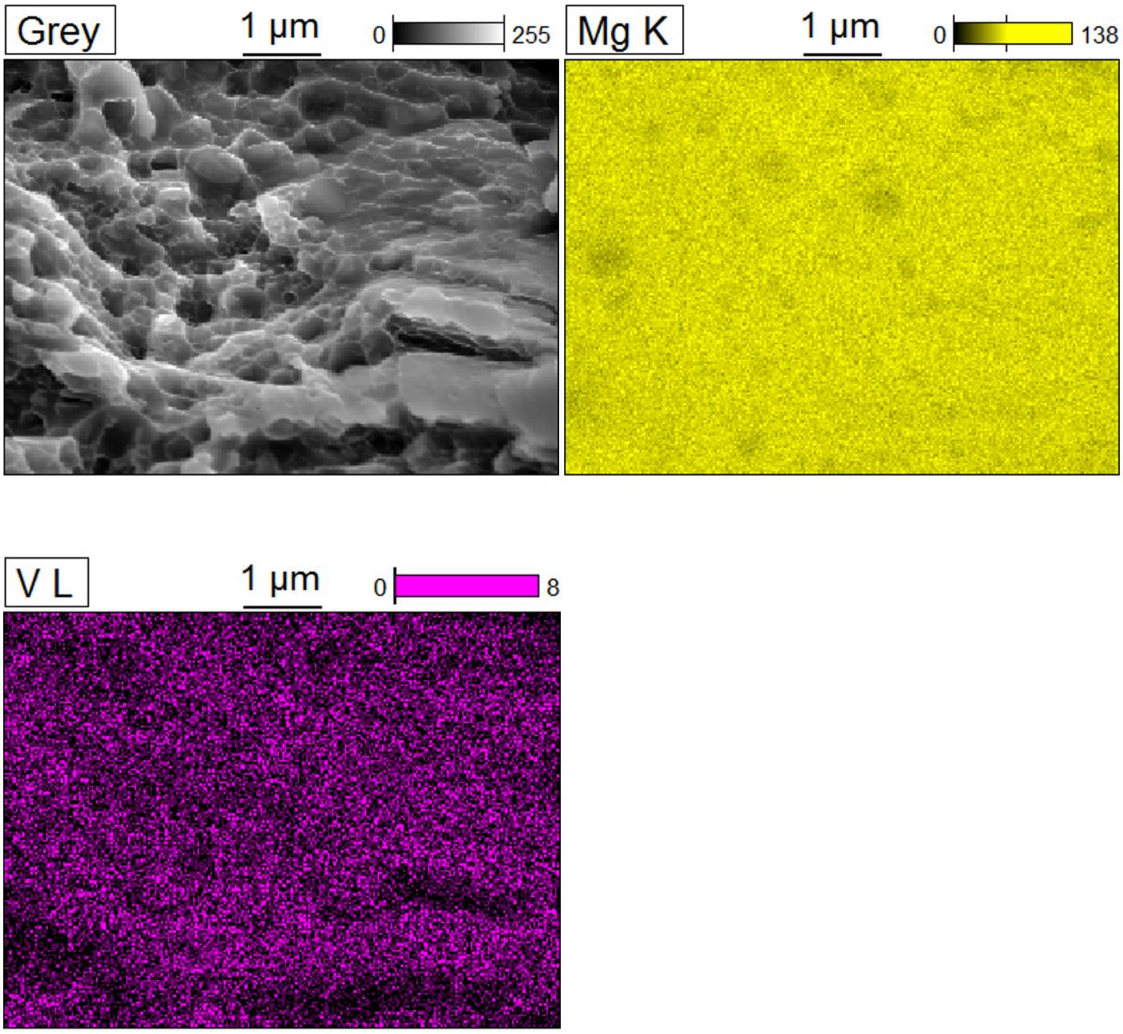
Grey
1 µm
0
255
Mg K
1 µm
0
138
V L
1 µm
0
8

EDS results of AZ80 – O at 300^{0}C and 10^{-4} sec^{-1}

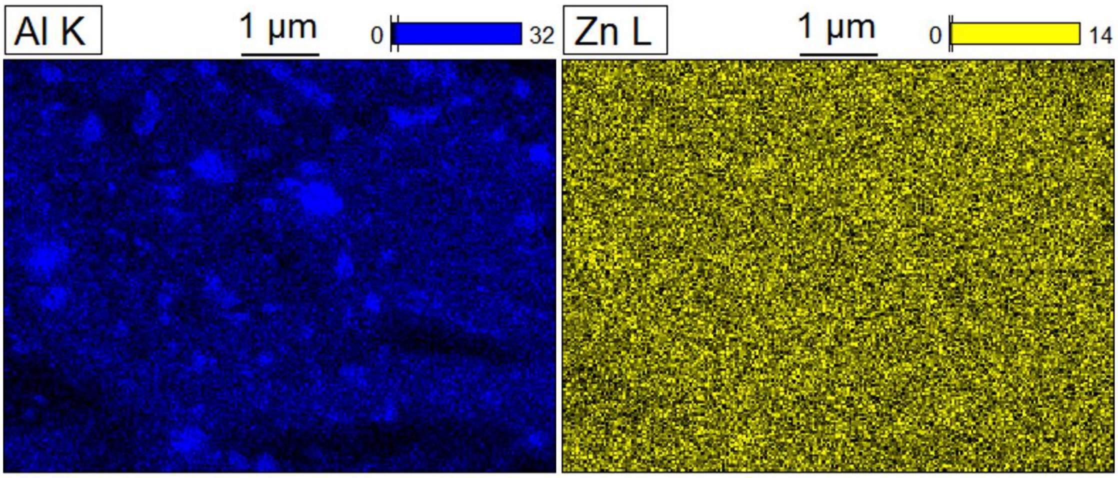
Al K
1 µm
0
32
Zn L
1 µm
0
14

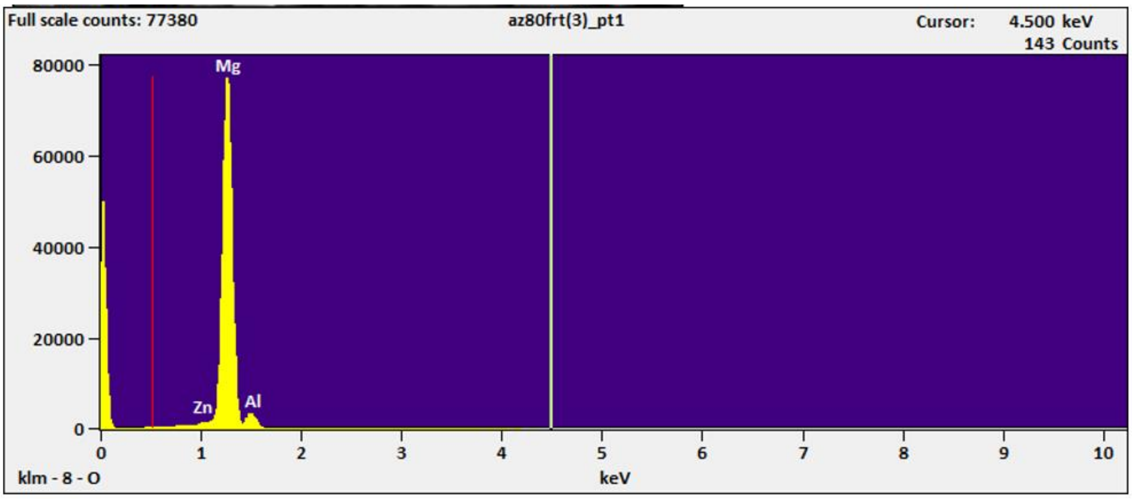

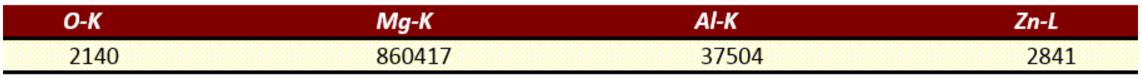

O-K	Mg-K	Al-K	Zn-L
2140	860417	37504	2841

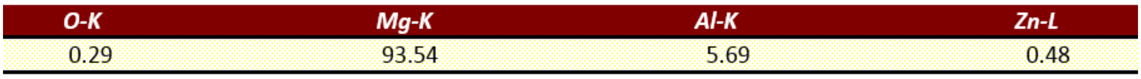

O-K	Mg-K	Al-K	Zn-L
0.29	93.54	5.69	0.48

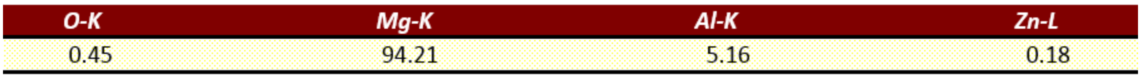

O-K	Mg-K	Al-K	Zn-L
0.45	94.21	5.16	0.18

EDS results of AZ80 – O at 300^{0}C and 10^{-4} sec^{-1}

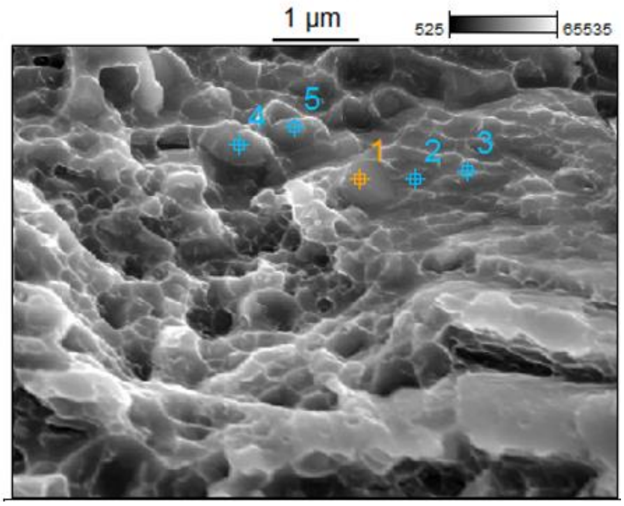
1 µm
525
65535
4
5
1
2
3

Image Name:	az80frt(5)
Image Resolution:	512 by 384
Image Pixel Size:	0.01 µm
Acc. Voltage:	5.0 kV
Magnification:	18000

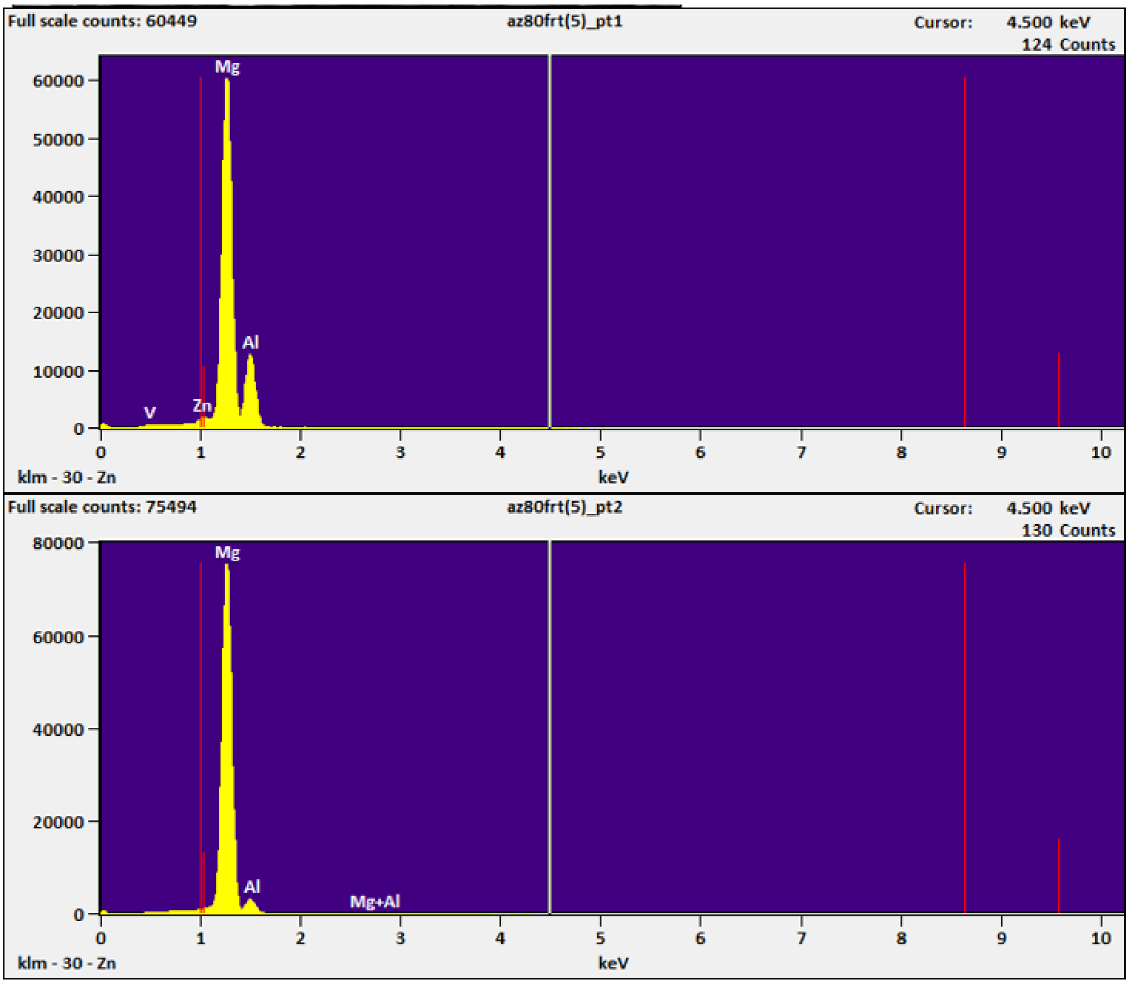

EDS results of AZ80 – F at 300^{0}C and 10^{-4} sec^{-1}

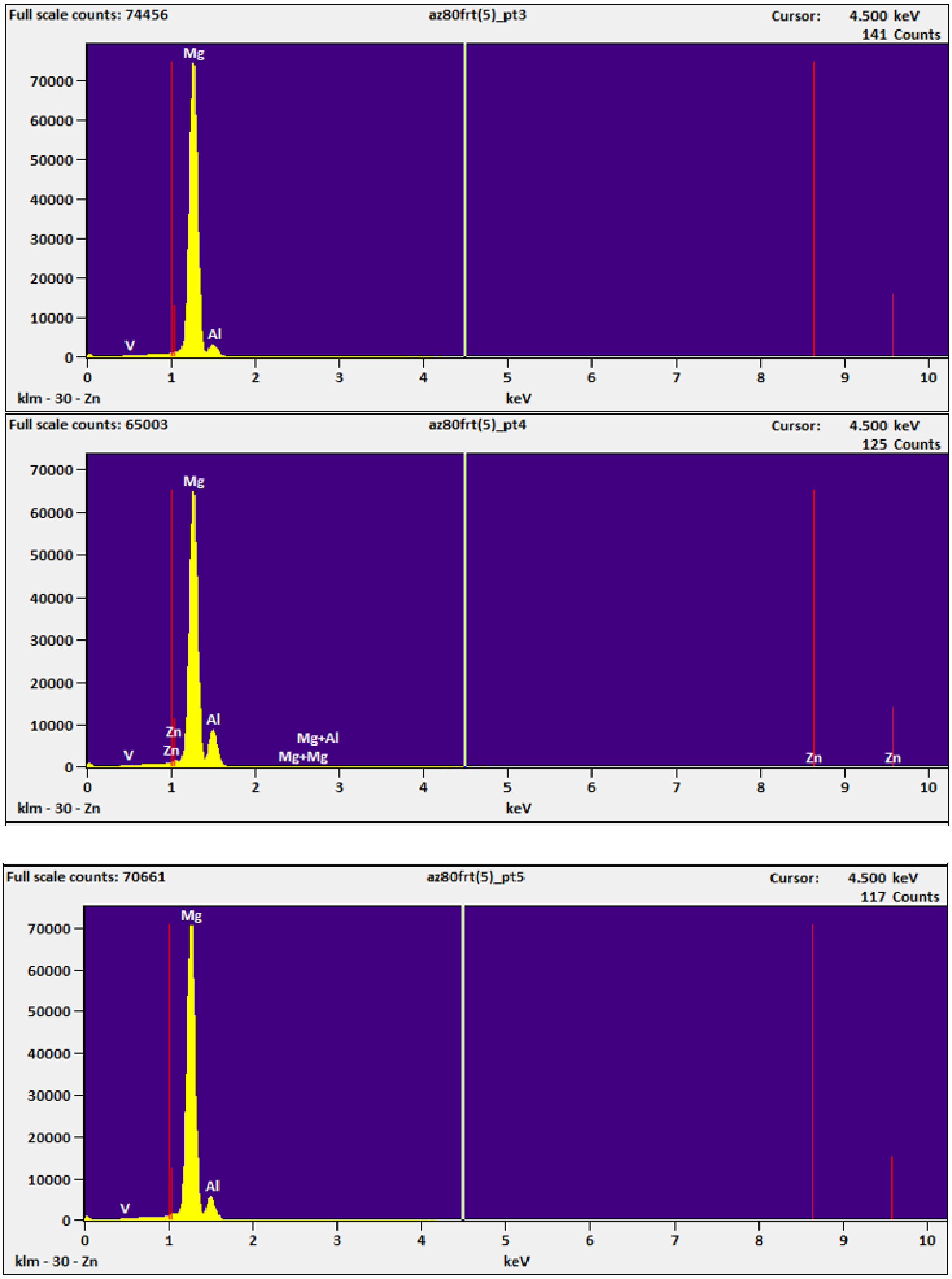

EDS results of AZ80 – F at 300^0C and 10^{-4} sec^{-1}